Non-Contacting Shaft Seals for Gas and Steam Turbines

James R. Aubry
St. Cross College



D. Phil. Thesis

Supervisor: Dr. D. Gillespie

Rolls-Royce UTP in Aerodynamics and Heat Transfer
Department of Engineering Science
University of Oxford

Michaelmas Term 2011

Abstract

Improvements upon current gas turbine sealing technology performance are essential for decreasing specific fuel consumption to meet stringent future efficiency targets. The clearances between rotating and static components of a gas turbine, which need to be sealed, vary over a flight cycle. Hence, a seal which can passively maintain an optimum clearance, whilst preventing contact between itself and the rotor, is extremely desirable.

Various configurations of a Rolls Royce (RR) seal concept, the Large Axial Movement Face Seal (LAMFS), use static pressure forces to locate face seals. Prototypes were tested experimentally at the Osney Thermofluids Laboratory, Oxford. Firstly a proof-of concept rig (simulating a 2-D seal cross-section) manufactured by RR was re-commissioned.

The simplest configuration using parallel seal faces induced an unstable seal housing behaviour. The author used this result, CFD, and analytical methods to improve the design and provide a self-centring ability. A fully annular test rig of this new seal concept was then manufactured to simulate a 3D engine representative seal. The full annulus eliminated leakage paths unavoidable in the simpler rig. A parametric program of experiments was designed to identify geometries and conditions which favoured best-practice design. The new seal design is in the process of being patented by Rolls Royce.

A ‘fluidic’ seal was also investigated, showing very promising results. A test rig was manufactured so that a row of jets could be directed across a leakage cross-flow. An experimental program identified parameters which could achieve a combined lower leakage mass flow rate compared with the original leakage. Influence of jet spanwise spacing, injection angle, jet to mainstream pressure ratio, mainstream pressure difference and channel height were analysed. It is hoped this thesis can be used as a tool to further improve these seal concepts from the parametric trends which were identified experimentally.

Acknowledgments

I am greatly indebted to my supervisor, Dr David Gillespie, for giving me this opportunity to pursue a D.Phil. and for his expert guidance, encouragement and support throughout. I would also like to thank Dr Andrew Owen, whose help and advice with the experimental test rigs was much appreciated.

Special thanks go to Leo Verling, the Seals group technician, who was heavily involved with the design, manufacture and commissioning of the two test rigs produced at Oxford, making this thesis possible. His friendship and generosity over the years have been a highlight of my time spent here in Oxford. Gratitude is also owed to Gerald Walker and Dominic Harris whose help also contributed to the success of these two test rigs.

I have enjoyed the benefit of excellent industrial direction and technical support by researching on a joint Rolls-Royce and Alstom project. Funding was gratefully received from the two industrial partners.

I also wish to thank my colleagues at the Osney Laboratory, many of whom have also been great friends, especially Chris Hambidge, Orpheas Tapanlis, Rod Lubbock, James Batstone, Salvador Luque-Martinez, Richard Fawcett, Matthew McGilvray and Noel Morris. Without their presence, this D.Phil. would not have been so enjoyable.

Above all, I am extremely grateful for the endless support and encouragement from my family. They have been instrumental throughout all my years and it is to them whom I owe this achievement.

Nomenclature

Symbols and units as described, unless stated otherwise.

A	Leakage path cross sectional area (m^2)
B	Slider pad length (m)
C	Constant of integration, LAMFS analytical model ($\frac{\dot{m}}{L}RT$)
C_D	Discharge coefficient
$C_D{}^*$	Zero cross flow discharge coefficient
C_f	Coefficient of friction
c_p	Specific heat capacity (J kg^{-1} K^{-1})
D_H	Hydraulic Diameter (m)
d	Jet hole diameter (m)
e	Effective clearance (m)
F	Force (N)
f_n	Seal housing natural frequency (Hz)
G_m	Mainstream mass velocity (kg m^{-2} s^{-1})
Gj	Jet mass velocity (kg m^{-2} s^{-1})
H	Load bearing capacity (N)
h	Leakage path gap height (m)
h_u	Minimum height in upstream seal gap (µm)
h_d	Minimum height in downstream seal gap (µm)
h_{step}	Radial-step height (µm)
h_{tsg}	Total seal housing axial movement: $h_u + h_d$ (µm)
h_0	Reference seal gap height (m)
I	Moment of Inertia (kg m^2)
KE	Kinetic energy (J)
L	Leakage path length (m)
L_{pc}	Jet potential core length (m)
L_w	Channel width (m)
M	Mach number
m	Mass (kg)
$\dot{m}$	Mass flow rate (kg s^{-1})
p_{atm}	Atmospheric pressure (Pa)
Δp	Pressure difference across mainstream leakage path (Pa)
p_0	Total pressure (Pa)
p	Static pressure (Pa)
q_{in}	Heat input (J)
R	Specific gas constant (J kg^{-1} K^{-1})
Re	Reynolds number
Re_c	Reynolds number based on channel hydraulic diameter
Re_h	Reynolds number based on seal gap height
r	radius (m)
s	Jet spanwise spacing (number of jet diameters (d))
T_0	Total temperature (K)
T	Static temperature (K)
t_{step}	Time step (s)
U	Radial surface speed (m s^{-1})
u	Radial flow velocity component (m s^{-1})
u^*	Frictional velocity (m s^{-1})
V	Axial surface speed (m s^{-1})

v	Axial flow velocity component (m s^{-1})
W	Circumferential surface speed (m s^{-1})
w	Circumferential flow velocity component (m s^{-1})
w_c	Work required by compressor (J)
w_t	Work extracted by turbine (J)
x	Radial direction
x_{step}	Radial position of radial step (m)
y	Axial direction
y^+	Wall y plus
z	Circumferential direction

Subscripts

u	Upstream
d	Downstream
in	At the inlet plane
spd	Static pressure drop
$step$	At the step location
m	Mainstream
j	Jet
out	Outlet

Greek

α	Ratio of inlet to step position length over seal gap length (x_{step}/L)
β	Inlet static pressure loss coefficient
Γ	Torque (N m)
δ	Seal housing displacement (μm)
δ_{eq}	Seal housing displacement at equilibrium position (μm)
ε_m	Mixed out loss factor
ε_p	Power loss factor
ρ	Density of air (kg m^{-3})
τ	Shear stress (N m^{-2})
ω	Angular velocity (rad s^{-1})
θ	Jet angle to mainstream direction (degrees)
μ	Dynamic viscosity (Pa s)
ν	Kinematic Viscosity (m^2 s^{-1})
σ_y	Yield stress
σ_{UTS}	Ultimate tensile stress
η	Efficiency
γ	Ratio of specific heat capacities

Acronyms

CFD	Computational Fluid Dynamics
LAMFS	Large Axial Movement Face Seal
HP	High Pressure
IPC	Intermediate Pressure Chamber
LP	Low Pressure
TDC	Top Dead Centre

Contents

1 Introduction 1
1.1 The Gas Turbine Engine 1
1.2 Motivation for Seals Research 2
1.3 Existing Gas Turbine Sealing Technology 5
1.3.1 Labyrinth Seals 7
1.3.2 Brush Seals 8
1.3.3 Leaf Seals 10
1.4 Effective Clearance 11
1.5 Thesis Overview 12
2 Literature Review 14
2.1 Introduction 14
2.2 Sealing Challenges to Overcome 14
2.2.1 Wear 14
2.2.1.1 Rotor-Bristle Tip Contact Wear 14
2.2.1.1.1 Start-up Induced Wear 16
2.2.1.1.2 Rotor-Casing Relative Growth and Rotor Eccentricity Induced Wear 16
2.2.1.2 Inter-Bristle Contact-Induced Wear 17
2.2.2 Large Axial and Radial Relative Movement 18
2.3 Seals Which Potentially Satisfy Both Criteria 19
2.3.1 Rolls Royce Concept – Large Axial Movement Face Seal 19
2.3.1.1 Pratt & Whitney Seal Concept 20
2.3.2 Fluidic Seal 21
2.4 Other Sealing Technology 21
2.4.1 Hybrid Brush Seal (HBS) 21
2.4.2 Film Riding Face Seal 25
2.4.3 Compliant Foil Seal 27
2.4.4 Compliant Foil Thrust Seals 31
2.4.5 Finger Seal 34
2.4.6 Cantilevered Floating Ring Seal (CFRS) 38
2.5 Hydrostatic Lubrication 41
2.6 Hydrodynamic Lift 41
2.6.1 Effect of Surface Roughness 43
2.7 Literature Review Summary 44
3 Linear Large Axial Movement Face Seal 46
3.1 Introduction 46
3.2 LAMFS Concept 47
3.2.1 Principle of Operation 48
3.3 Experimental Work 52
3.3.1 The Linear LAMFS Test Rig 52
3.3.1.1 Seal Housing and Rotor Geometry 54
3.3.1.2 Seal Gap Static Pressure Tapping Positions 55
3.3.1.3 Secondary Leakage Paths 56
3.3.1.4 Test Rig Set Up and Air System 56
3.3.2 Instrumentation 57
3.3.2.1 Calibration 58
3.3.2.2 Data Capture and Experimental Procedure 59
3.3.2.3 Uncertainty 59
3.3.3 An Example of Typical Measurements 61
3.4 Parallel Seal Faces – Baseline Geometry 62

3.4.1 Geometry 63
3.4.2 Analytical model 64
3.4.2.1 Reynolds 1D equation 64
3.4.3 CFD 67
3.4.4 Two dimensional CFD 68
3.4.4.1 Geometry 68
3.4.4.2 Meshing 69
3.4.4.3 Solving 70
3.4.5 Three dimensional CFD 72
3.4.5.1 Geometry 72
3.4.5.2 Mesh 74
3.4.5.3 Solving 75
3.4.6 Results for Parallel Seal Faces - Seal Housing Resultant Force vs. Displacement 75
3.4.6.1 Experimental Data 75
3.4.6.2 Analytical Modelling 76
3.4.6.3 CFD 79
3.4.7 Results for Parallel Seal Faces - Seal Gap Static Pressure Distribution 82
3.4.7.1 Inlet Loss Coefficient 88
3.5 Radial Steps 90
3.5.1 Introduction 90
3.5.2 Geometry 92
3.5.3 Parameters Investigated 93
3.5.4 Analytical model 94
3.5.5 Linear LAMFS Results - Seal Housing Resultant Force vs. Displacement 95
3.5.5.1 Maximum Force 96
3.5.5.2 Equilibrium Position (δ_{eq}) 97
3.5.5.3 Force Gradient at δ_{eq}: $\mathbf{d}\boldsymbol{F}\mathbf{d}\boldsymbol{\delta}\boldsymbol{\delta}\boldsymbol{eq}$ 98
3.5.5.4 Linear LAMFS Results - Seal Housing Resultant Force: h_{step} = 800 µm 99
3.5.6 Linear LAMFS Results - Seal Gap Pressure Distribution 102
3.5.6.1 Variation of h_{step} and α 102
3.5.6.2 Gradient of Pre-Step Viscous Pressure Drop 104
3.5.6.3 IPC Pressure Variation 105
3.5.6.4 Analytical Model Seal Gap Pressure Distribution 106
3.5.6.4.1 h_{tsg} = 800 µm 107
3.5.7 Linear LAMFS Results - Leakage Mass Flow Rate 108
3.6 Summary 113
4 Annular Large Axial Movement Face Seal 116
4.1 Introduction 116
4.2 Annular LAMFS Test Rig 118
4.2.1 Key Components 119
4.2.1.1 Seal Housing 120
4.2.1.2 Disc 121
4.2.1.3 Secondary Seals 121
4.2.1.4 Linear Actuator 122
4.2.1.5 Motor 122
4.2.1.6 Base Plate 123
4.2.1.7 Pressure Vessel 124
4.3 Instrumentation 124
4.3.1 Pressure Tapping Locations 125
4.3.2 Data Capture 126
4.3.3 Uncertainty 127

4.3.3.1 Direct Measurements 127
4.3.3.2 Computed Measurements 127
4.3.4 Measuring Secondary Leakage 127
4.4 Three Dimensional CFD 128
4.4.1 Geometry 128
4.4.2 Mesh 130
4.4.3 Solving 130
4.5 Results 130
4.5.1 Parallel Seal Surfaces 130
4.5.1.1 Resultant Force 130
4.5.1.2 Seal Gap Pressure Distribution 132
4.5.1.3 Leakage 137
4.5.2 Radial Step Geometry in Seal Gaps 139
4.5.2.1 Resultant Force 139
4.5.2.2 Seal Gap Pressure Distribution 142
4.5.2.3 Leakage 148
4.5.2.4 Rotating Disc: Radial Steps 151
4.5.2.5 Rotating Disc: Radial Steps and Circumferential Steps 151
4.5.2.5.1 Seal housing Resultant Force 151
4.5.2.5.2 Leakage Mass Flow Rate 153
4.5.3 Dynamic Behaviour 154
4.5.3.1 Squeeze film effect 157
4.6 Summary 159
5 Fluidic Seal 162
5.1 Introduction 162
5.1.1 Jet and Mainstream Flow Interactions 163
5.2 Relevant Previous Work 164
5.2.1 Impingement Cooling 164
5.2.1.1 Discharge Coefficient 164
5.2.1.2 Channel Friction Factor 165
5.2.1.3 Potential Core Length 166
5.2.1.4 Impingement Jet Cross Sectional Geometry 166
5.2.2 Theoretical Jet Analysis 167
5.2.3 Fluidic Seals 167
5.2.3.1 Fluidic Labyrinth Seals 168
5.2.3.2 Shrouded Turbine Blade Tip Leakage Sealing 169
5.3 Experimental Test Rig 172
5.3.1 Test section geometry 174
5.3.2 Air System 174
5.3.3 Instrumentation 175
5.3.3.1 Test Section 176
5.3.3.2 Further Instrumentation 177
5.3.4 Parameters of interest 177
5.3.4.1 Pressure difference (Δp) 177
5.3.4.2 Pressure ratio (p_r) 178
5.3.4.3 Channel height (h) 178
5.3.4.4 Jet angle: (θ) 178
5.3.4.5 Jet spacing (s) 179
5.3.4.6 Other Parameters 179
5.3.4.7 Labyrinth Seal 179
5.3.5 Cases Tested 181
5.3.6 Uncertainty 182

5.4 Analytical Model 183
5.5 CFD 184
5.5.1 Circular Holes 184
5.5.2 Console 184
5.5.3 Labyrinth-fluidic Seal 186
5.6 Results 186
5.6.1 Circular Jets - Mass flow rate 187
5.6.1.1 Jet Angle (θ): 90° 187
5.6.1.2 Experimental Data vs. Analytical Model 188
5.6.1.2.1 h = 3 mm 188
5.6.1.2.2 h = 2 mm 189
5.6.1.2.3 h = 1 mm 190
5.6.1.3 Normalised Mass Flow Rate 191
5.6.1.3.1 Normalised Mass Flow Rate: 3D CFD 194
5.6.1.3.2 Interactions: Normalised Mass Flow Rate 196
5.6.2 Circular Jets - Centreline static pressure distribution 199
5.6.2.1 Unexploited Jet Momentum: θ = 90° 200
5.6.2.2 Jets Angled Upstream 201
5.6.3 An Alternative Method to Evaluate Fluidic Seal Performance 202
5.6.3.1 Power loss results 204
5.6.3.1.1 Power Loss vs. Mass Flow Rate 206
5.6.3.1.2 Power Loss Interaction Plot 209
5.6.4 Console Jets 211
5.6.5 Labyrinth-fluidic seal: Jets upstream – Mass flow rate 214
5.6.5.1 Δp = 0.5 bar 214
5.6.5.2 Δp = 1 bar 215
5.6.6 Labyrinth-fluidic seal: Jets upstream – Static pressure distribution 216
5.6.6.1 Δp = 0.5 bar 216
5.6.6.2 Δp = 1 bar 218
5.6.7 Labyrinth-fluidic seal: Jets upstream – Flow field analysis (CFD) 219
5.6.7.1 Flow Vectors - Δp = 0.5 bar, p_r = 1.2 219
5.6.7.2 Flow Vectors - Δp = 0.5 bar, p_r = 2.6 220
5.6.7.3 Path Lines - Δp = 1 bar, p_r = 1.2 & 2.6 221
5.6.8 Labyrinth-fluidic seal: Jets downstream – Mass flow rate 221
5.6.8.1 Δp = 0.5 bar 221
5.6.8.2 Δp = 1 bar 223
5.6.9 Labyrinth-fluidic seal: Jets downstream – Static pressure distribution 224
5.6.9.1 Δp = 0.5 bar 224
5.6.9.2 Δp = 1 bar 226
5.6.10 Labyrinth-fluidic seal: Jets downstream – Flow field analysis (CFD) 227
5.6.11 Labyrinth-fluidic seal – Power Loss 228
5.7 Summary 230
6 Summary and Further Work 234
7 Bibliography 241
8 Appendix 247
8.1 Derivation of Reynolds 1D Flow Equation 247
8.2 Seal Housing Resultant Force 252
8.3 Linear LAMFS Primary Leakage Path Static Pressure Distribution 256
8.4 Rotating Component Containment 258
8.5 Fluidic Seal Analytical Model 260

List of Figures

Figure 1.1: *T-s* diagram of the Brayton cycle 1

Figure 1.2: Sealing Locations in a Gas Turbine Engine – Trent 1000 (Rolls Royce plc) 6

Figure 1.3: Variation in Seal Gap Height over Engine Flight Cycle (Chupp, Hendricks, et al. 2006) 6

Figure 1.4: Labyrinth Seal Configurations (Chupp, Hendricks, et al. 2006) 7

Figure 1.5: (a) – brush seal cross section, (b) – brush seal incorporated into a multiple-tooth labyrinth seal, schematic (Chupp, Hendricks, et al. 2006) and photo (Neef, et al. 2006) 10

Figure 1.6: Leaf Seal Design (Jahn, Franceschini, et al. 2011) 11

Figure 2.1: Rotor-seal contact wear after 30 months continuous service (Neef, et al. 2006): (*a*) – Brush seal bristle tips, (*b*) – Labyrinth seal teeth tips 15

Figure 2.2: Bristle cross section after 30 months continuous service (Neef, et al. 2006): (*a*) – bristles close to back plate, (*b*) – bristles close to front plate 17

Figure 2.3: Bristle condition after 30 months continuous service (Neef, et al. 2006) 18

Figure 2.4: Schematic of the Rolls-Royce LAMFS concept (J. Webster 2007) 19

Figure 2.5: Pratt and Whitney Self-Balancing Face Seal: (*a*) – Schematic, (*b*) – Schematic showing hydrostatic seals (Glahn and Munsell 2009) 20

Figure 2.6: HBS with Pad Elements Attached to Bristles (Chupp et al., 2006) 22

Figure 2.7: Next generation HBS: (*a*) – Schematic, (*b*) – HBS rear showing cantilever beams (San Andres, Baker and Delgado 2010) 24

Figure 2.8: Compliant foil seal schematic (Howard and Andres 2011) 28

Figure 2.9: Hydrodynamic pressure profile generated beneath foil pad (*a*) and film thickness profile (*b*) (Heshmat, Heshmat and Xu 2000) 32

Figure 2.10: Variation in rotational speed and coefficient of friction over a test cycle (Jahanmir, Heshmat and Heshmat 2009) 33

Figure 2.11: Hydrostatic and hydrodynamic induced pad pressure profile with orifice location at 33° from the leading edge, supply pressure at 4 times ambient pressure rotational speed at 40 krpm 34

Figure 2.12: Finger seal and detailed components (Chupp, Hendricks, et al. 2006) 35

Figure 2.13: Downstream finger element pad from a non-contacting finger seal (Chupp, Hendricks, et al. 2006) 37

Figure 2.14: Schematics of the cantilevered floating ring seal (Morgan 2004) 41

Figure 2.15: Infinite Slider Bearing Configuration (Brewe, et al. 1997) 42

Figure 2.16: Pressure Profile on Bearing Shoe with Varying *k* – (Brewe et al., 1996) 43

Figure 2.17: Variations in Surface Geometry to Create a Pressurised Fluid Film (Brewe, et al. 1997) 43

Figure 3.1: Schematic of LAMFS 48

Figure 3.2: (*a*) - Schematic of static pressure distribution on inner and outer seal housing surfaces, (*b*) - Static pressure variation through primary leakage path with seal housing position 51

Figure 3.3: Internal view of the linear LAMFS test rig 53

Figure 3.4: (*a*) - Seal housing and (*b*) rotor component dimensions (with partial cutaway section to show internal channels) 55

Figure 3.5: Schematic of pressure tapping axis locations in seal gaps (Note: centres of tappings at x/L = 0, 1 and 2 are in line with inlet and outlet planes 55

Figure 3.6: Test rig air system schematic 57

Figure 3.7: Typical data plots for parallel seal gaps (h_{tsg} = 400 µm, h_{step} = 0 µm, α = 0) at p_{HP} = 2.06 barg with error bars: (*a*) – Total leakage mass flow rate and seal housing resultant force vs. displacement, (*b*) – Primary leakage path static pressure distribution 62

Figure 3.8: Linear LAMFS baseline seal gap geometry: Parallel faces (Note: diagram not to scale) 63

Figure 3.9: (*a*) - CFD domain showing boundary condition definition, (*b*) – mesh within seal gaps and IPC 69

Figure 3.10: Piecewise-linear relationships for c_p, k and μ 72

Figure 3.11: Three dimensional CFD domain surfaces with endplate removed - Symmetry plane in light blue, endplate position indicated by dashed line 73

Figure 3.12: 3D CFD LAMFS leakage paths 74

Figure 3.13: Three dimensional CFD blocking (*a*) and mesh (*b*) 75

Figure 3.14: Experimental seal housing resultant force with displacement – Parallel gaps: h_{tsg} = 400 µm, h_{step} = 0 µm, α = 0 76

Figure 3.15: Analytical model seal housing resultant force with displacement – Parallel gaps: h_{tsg} = 400 µm, h_{step} = 0 µm, α = 0 77

Figure 3.16: Analytical model triple equilibrium analysis: (*a*) – positive and negative force components, (*b*) – seal gap static pressure distribution, (*c*) – seal gap entry losses for upstream and downstream gaps 78

Figure 3.17: 2D CFD seal housing resultant force with displacement – Parallel gaps: h_{tsg} = 400 µm, h_{step} = 0 µm, α = 0 79

Figure 3.18: 3D CFD seal housing resultant force with displacement –Parallel gaps: h_{tsg} = 400 µm, h_{step} = 0 µm, α = 0 80

Figure 3.19: 2D CFD seal housing resultant force with displacement - Parallel gaps: p_{HP} = 0.69 bar, h_{tsg} = 400 µm, h_{step} = 0 µm, α = 0 81

Figure 3.20: Intermediate pressure chamber velocity contours with laminar (*a*) and *k-ε* (*b*) turbulence models used in the simulation 82

Figure 3.21: Static pressure distribution in parallel seal gaps from experimental, analytical and CFD data - Displacement = –150 µm 85

Figure 3.22: Static pressure distribution in parallel seal gaps from experimental, analytical and CFD data – Displacement = 0 µm 86

Figure 3.23: Static pressure distribution in parallel seal gaps from experimental, analytical and CFD data – Displacement = +150 µm 87

Figure 3.24: Variation of inlet loss coefficient, β, with Reynolds number, Re_h 89

Figure 3.25: Log plot of variation of inlet loss coefficient, β, with Reynolds number, Re_h 89

Figure 3.26: Linear LAMFS analytical model with $\beta = f(\mathrm{Re}_h)$ against experimental data and analytical model with $\beta = 1$: p_{HP} = 0.69 bar 90

Figure 3.27: Simplified pressure distribution through primary leakage path with varying δ ... 92

Figure 3.28: Converging radial steps within seal gaps of LAMFS (Note: $\alpha = x_{ustep} / L = x_{dstep} / L$) 93

Figure 3.29: Analytical and experimental resultant force with displacement: h_{tsg} = 400 µm, h_{step} = 300 µm, α = 0.90 96

Figure 3.30: Peak positive (*a*) and negative (*b*) forces for experimental data: h_{tsg} = 400 µm .. 97

Figure 3.31: Seal housing equilibrium position (δ_{eq}) vs. inlet pressure for experimental data: h_{tsg} = 400 µm 98

Figure 3.32: Gradient of force-displacement relationship at δ_{eq}: h_{tsg} = 400 µm 99

Figure 3.33: Experimental data for seal housing resultant force - h_{tsg} = 400 µm and 800 µm: h_{step} = 300 µm, α = 0.90 100

Figure 3.34: Experimental data for δ_{eq} with p_{HP} (a) and $\mathbf{d}\boldsymbol{F}\mathbf{d}\boldsymbol{\delta}\boldsymbol{\delta}\boldsymbol{eq}$ with p_{HP} (*b*): h_{tsg} = 800 µm, α = 0.90 101

Figure 3.35: Experimental data for maximum positive (*a*) and negative (*b*) forces: h_{tsg} = 800 µm, α = 0.90 102

Figure 3.36: Static pressure distribution in seal gaps (p_{HP} = 0.69 barg, h_{tsg} = 400 µm) – Full range of step locations, h_{step} = 100 µm (row (*a*)) and full range of step heights, α = 0.90 (row (*b*)) 103

Figure 3.37: Gradient of viscous pressure drop pre-step in seal gap with height tending to zero for range of h_{step}: (a) – Downstream seal gap (δ = -150 µm, h_d = 50 µm), (*b*) – Upstream seal gap (δ = 150 µm, h_u = 50 µm) 104

Figure 3.38: Variation in p_{IPC} value with inlet pressure, p_{HP}, at δ = +150 µm ($h_u << h_d$), h_{stg} = 400 µm, ... 105

Figure 3.39: Analytical model and experimental seal gap static pressure distributions, p_{HP} = 0.69 bar, h_{tsg} = 400 µm, h_{step} = 300 µm: (*a*) δ = -150 µm, (*b*) δ = 150 µm 107

Figure 3.40: $\boldsymbol{pIPCpHP}$ for h_{tsg} = 800 µm (δ = +250 µm and +350 µm) and h_{tsg} = 400 µm (δ = +150 µm): h_{step} = 100, 200 and 300 µm 108

Figure 3.41: Experimental leakage mass flow rate: h_{tsg} = 400 µm (α = 0.90 radial step cases) 109

Figure 3.42: Difference between h_{tsg} = 400 µm and h_{tsg} = 800 µm for experimental (total leakage) and analytical (primary only) leakage mass flow rates (difference in primary leakage) α = 0.90 110

Figure 3.43: Secondary leakage for h_{tsg} = 400 µm and 800 µm, α = 0.90 112

Figure 3.44: Linear LAMFS test rig secondary leakage profile: blue – secondary seal, green – side leakage, red – total secondary leakage 112

Figure 4.1: Schematic of annular LAMFS test rig 118

Figure 4.2: Fully assembled LAMFS test rig on base plate 119

Figure 4.3: Cross section of annular LAMFS key components 120

Figure 4.4: Internal view of the pressure vessel with pressure vessel annulus and base plate end-support 124

Figure 4.5: Static pressure tappings in seal gaps of annular self-centring seal test rig: (*a*) – top dead centre, (*b*) – 90° (shown), 180° and 270° 126

Figure 4.6: Annular sector CFD domain surface geometry (nearer periodic face removed) . 129

Figure 4.7: Annular sector CFD domain surface seal gap geometry – radial and circumferential steps 129

Figure 4.8: Experimental and CFD seal housing resultant force –Parallel faces: h_{tsg} = 400 µm, static disc 131

Figure 4.9: Static pressure distribution in annular seal gaps – Parallel faces: h_{tsg} = 400 µm, δ = -150 µm 134

Figure 4.10: Static pressure distribution in annular seal gaps – Parallel faces, h_{tsg} = 400 µm, δ = 0 µm 135

Figure 4.11: Static pressure distribution in annular seal gaps – Parallel faces, h_{tsg} = 400 µm, δ = 150 µm 136

Figure 4.12: Annular experimental leakage mass flow rate – parallel seal faces: (*a*) – total, (*b*) – separate primary and secondary components, h_{tsg} = 400 µm 137

Figure 4.13: Annular CFD leakage mass flow rate – parallel seal faces: (*a*) – total, (*b*) – primary and secondary, h_{tsg} = 400 µm 138

Figure 4.14: Effective clearance for primary leakage – Parallel seal faces: h_{tsg} = 400 µm 139

Figure 4.15: Experimental and CFD seal housing resultant force with displacement – Radial steps: h_{tsg} = 400 µm, h_{step} = 200 µm, α = 0.50, static disc 140

Figure 4.16: Experimental peak force magnitude 141

Figure 4.17: (a) Force-displacement gradient at δ_{eq} and (*b*) force-displacement gradient across displacement range with polynomial fit and δ_{eq} position shown 142

Figure 4.18: Static pressure distribution in annular seal gaps - Radial steps: h_{tsg} = 400 µm, h_{step} = 200 µm, α = 50 %, δ = -150 µm, static disc 145

Figure 4.19: Static pressure distribution in annular seal gaps - Radial steps: h_{tsg} = 400 µm, h_{step} = 200 µm, α = 50 %, δ = 0 µm, static disc 146

Figure 4.20: Static pressure distribution in annular seal gaps - Radial steps: h_{tsg} = 400 µm, h_{step} = 200 µm, α = 50 %, δ = +150 µm, static disc 147

Figure 4.21: Annular experimental leakage mass flow rate – Radial steps: (*a*) – total, (*b*) – separate primary and secondary components, h_{tsg} = 400 µm, h_{step} = 200 µm, α = 0.50, static disc 148

Figure 4.22: Annular CFD leakage mass flow rate – Radial steps: (*a*) – total, (*b*) – primary and secondary, h_{tsg} = 400 µm, h_{step} = 200 µm, α = 0.50 149

Figure 4.23: Effective clearance of primary leakage path – Radial steps: h_{tsg} = 400 µm, h_{step} = 200 µm, α = 0.50 150

Figure 4.24: Effective clearance of primary leakage path at δ_{eq} 150

Figure 4.25: Force-displacement relationships for LAMFS with radial and circumferential steps with (*a*) - a static rotor and (*b*) - a spinning rotor, ω = 1333 rads^{-1} 152

Figure 4.26: Static pressure on downstream seal face with position of circumferential step position indicated (p_{HP} = 3.45 bar, δ = -150 µm, $h_u >> h_d$) 153

Figure 4.27: Annular CFD leakage mass flow rate – Radial and circumferential steps: (*a*) – total, (*b*) – primary and secondary, h_{tsg} = 400 µm, h_{step} = 200 µm, α = 0.50, ω = 1333 rads^{-1} 154

Figure 4.28: Dynamic response of annular seal (based on experimental F(δ)) when displaced downstream from δ_{eq} at maximum possible velocity whilst avoiding disc contact..... 156

Figure 4.29: Normalised induced pressure for parallel seal surfaces – L = 0.011 m, 0.11 m, 1.1m 159

Figure 5.1: Jet and mainstream flow interaction for low, 0.25, (*a*) and high, 4.0, (*b*) momentum flux ratios (Andreopoulos and Rodi 1984)..... 164

Figure 5.2: Schematic of seal proposed by Klomp (1969): (*a*) – Original design, (*b*) – Design with diffuser instead of pump..... 168

Figure 5.3: General Electric Company Fluidic Seal Patent (Turnquist 2009)..... 169

Figure 5.4: Turbine tip sealing with fluidic concept (Minoda, et al. 1988)..... 170

Figure 5.5: Inlet and exit mass flow rates to the shroud cavity with jet mass flow rate (*a*) and turbine efficiency with jet mass flow rate (*b*) (Curtis, et al. 2009)..... 171

Figure 5.6: Labyrinth-fluidic concept used as interstage seals (Hogg 2010) 172

Figure 5.7 Fluidic seal test rig external view..... 173

Figure 5.8: Fluidic seal test rig cross-section at mid span (dimensions in millimetres) 174

Figure 5.9: Schematic of fluidic seal test rig air supply system 175

Figure 5.10: Test section pressure tapping layout (dimensions in mm)..... 176

Figure 5.11: (*a*) – Fluidic seal test rig test section (primary insert removed), (*b*) – Underside of primary insert 177

Figure 5.12: Labyrinth-fluidic seal insert geometry tested at Oxford (Skouby 2011) 180

Figure 5.13: Possible sealing flow locations and flow field in a fluidic-labyrinth seal 181

Figure 5.14: Analytical model control volume..... 183

Figure 5.15: Console Geometry..... 185

Figure 5.16: Labyrinth-fluidc seal CFD domain (Skouby 2011) 186

Figure 5.17: Experimental mass flow rate: h = 1 mm, θ = 90°, Δp = 0.5 bar, s = 4d..... 188

Figure 5.18: Experimental and analytical mass flow rates: h = 3 mm, θ = 150°, Δp = 1 bar, s = 4d 189

Figure 5.19: Experimental and analytical mass flow rates: h = 2 mm, θ = 150°, Δp = 1 bar, s = 4d 190

Figure 5.20: Experimental and analytical mass flow rates: h = 1 mm, θ = 150°, Δp = 1 bar, s = 4d 191

Figure 5.21: Normalised mass flow rate for experimental data 193

Figure 5.22: Normalised mass flow rate for CFD data..... 196

Figure 5.23: Normalised mass flow rate interaction plot 199

Figure 5.24: Centreline static pressure distribution – Δp = 0.5 bar, θ = 90°, h = 1 mm, s = 4d 201

Figure 5.25: Centreline static pressure distribution – Δp = 0.5 bar, θ = 150°, h = 3 mm, s = 4d 202

Figure 5.26: Power loss factor against pressure ratio: Δp = 0.5 bar 205

Figure 5.27: Power loss factor against pressure ratio: Δp = 1 bar 206

Figure 5.28: Power loss factor against normalised mass flow rate: Δp = 0.5 bar 208

Figure 5.29: Power loss factor against normalised mass flow rate: Δp = 1 bar 209

Figure 5.30: Power loss interaction plot 211

Figure 5.31: Streamlines for console jet geometry (circumferential view): p_r = 2.6, s = 2d, h = 3mm, θ = 150°, A_s/A_e = 0.8, L_s/L_l = 1 213

Figure 5.32: Streamlines for console jet geometry (axial view): p_r = 2.6, s = 2d, h = 3mm, θ = 150°, A_s/A_e = 0.8, L_s/L_l = 1 213

Figure 5.33: Mass flow rate for labyrinth-fluidic seal – jets upstream, Δp = 0.5 bar (Skouby 2011) 215

Figure 5.34: Mass flow rate for labyrinth-fluidic seal – jets downstream, Δp = 1 bar (Skouby 2011) 216

Figure 5.35: Static pressure distribution for labyrinth-fluidic seal – jets upstream, Δp = 0.5 bar (Skouby 2011) 217

Figure 5.36: Static pressure distribution for labyrinth-fluidic seal – jets upstream, Δp = 1 bar (Skouby 2011) 218

Figure 5.37: CFD flow velocity vectors for labyrinth-fluidic seal – Δp = 0.5 bar, p_r = 1.2 (Skouby 2011) 220

Figure 5.38: CFD flow velocity vectors for labyrinth-fluidic seal – Δp = 0.5 bar, p_r = 2.6 (Skouby 2011) 221

Figure 5.39: CFD path lines for labyrinth-fluidic seal – Δp = 1 bar, (*a*): p_r = 1.2, (*b*): p_r = 2.6 (Skouby 2011) 221

Figure 5.40: Mass flow rate for labyrinth-fluidic seal – jets downstream, Δp = 0.5 bar (Skouby 2011) 223

Figure 5.41: Mass flow rate for labyrinth-fluidic seal – jets downstream, Δp = 1 bar (Skouby 2011) 224

Figure 5.42: Static pressure distribution for labyrinth-fluidic seal – jets downstream, Δp = 0.5 bar (Skouby 2011) 225

Figure 5.43: Static pressure distribution for labyrinth-fluidic seal – jets downstream, Δp = 1 bar (Skouby 2011) 226

Figure 5.44: Path lines for labyrinth-fluidic seal: Jets downstream, Δp = 1 bar, p_r = 1.2 (Skouby 2011) 227

Figure 5.45: Path lines for labyrinth-fluidic seal: Jets downstream, Δp = 1 bar, p_r = 2.6 (Skouby 2011) 228

Figure 5.46: Fluidic-labyrinth seal and plain channel power loss: h = 1 mm, θ = 135°, s = 4d 229

Figure 5.47: Fluidic-labyrinth seal and plain channel experimental power loss vs. normalised mass flow rate: h = 1 mm, θ = 135°, s = 4d 230

List of Tables

Table 3.1: Cross sectional area of all linear LAMFS leakage paths 56
Table 3.2: Linear LAMFS test rig transducer uncertainties 60
Table 3.3: Experimental cases tested 94
Table 4.1: Annular self-centring radial seal test rig transducer uncertainties 127
Table 4.2: Seal housing maximum velocity from δ_{eq} 155
Table 5.1: Channel friction factor correlations (Florshuetz, et al. 1982) 166
Table 5.2: Maximum experimental pressure ratios tested at Δp = 0.5 bar 181
Table 5.3: Maximum experimental pressure ratios tested at Δp = 1 bar 182
Table 5.4: Maximum pressure ratios tested at on labyrinth-fluidic seal at Δp = 0.5 and 1 bar 182
Table 5.5: Oxford fluidic test rig transducer uncertainties 182
Table 5.6: Console jet geometry CFD cases (console baseline case: 3rd row) 185
Table 5.7: Total mass flow rates for console geometry normalised against circular hole equivalent geometry total mass flow rate 212

1 Introduction

1.1 The Gas Turbine Engine

A gas turbine engine is comprised of three major components; the compressor, the combustor and the turbine. The ideal thermodynamic cycle which describes the process within a gas turbine engine is known as the Brayton cycle and is shown in a temperature-entropy, *T-s*, diagram below in Figure 1.1.

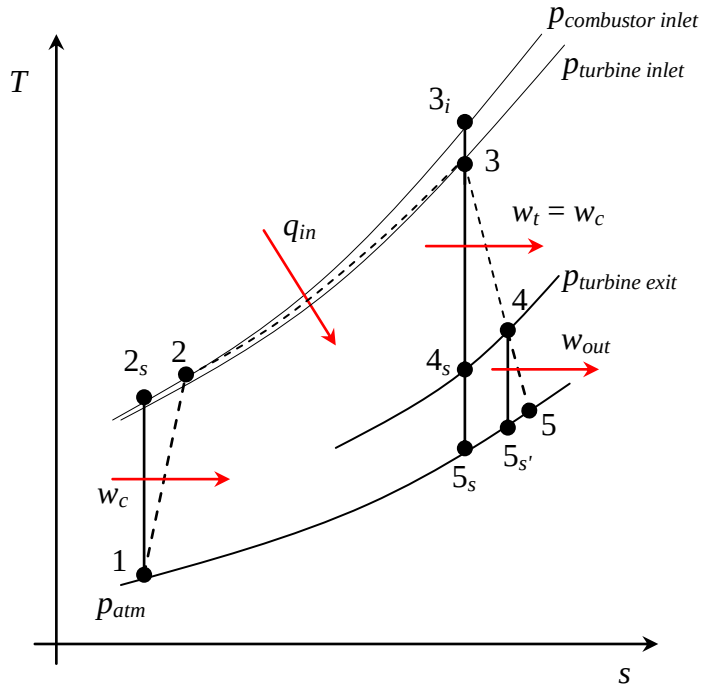


Figure 1.1: *T-s* diagram of the Brayton cycle

In an ideal process, ambient air is ingested into the engine and the pressure is raised by an isentropic and adiabatic process in the compressor (1 - 2_s). An isobaric rise in temperature follows in the combustor where fuel is added and burnt (2_s - 3_i). The combustion products are then expanded through the turbine where work is extracted to drive the compressor and the pressure falls (3_i - 4_s). This, as in the compressor, is an isentropic and adiabatic process. Finally, the remaining total pressure in the exhaust gases is used to accelerate the flow

through a nozzle back down to atmospheric pressure at 5_s (p_{atm}). It is the change in momentum of the exhaust gas as it accelerates through the nozzle which provides thrust. In a real engine however, losses are incurred from the compression and expansion processes due to the associated rises in entropy. For a given pressure ratio, the conditions at the compressor and turbine exits are points 2 and 4 respectively instead. The dashed lines indicate the non-ideal processes due to turbulence, frictional losses and heat transfer. Thus more work is required by the compressor and less work is extracted by the turbine than for their isentropic counterparts. The heat addition process is also non isobaric as there is a slight drop in pressure within the combustion chamber, due to mixing losses for example, and the actual process of heat addition is from points 2-3. The thermal efficiency for the Brayton cycle is given by

$$\eta_t = \frac{w_{net}}{q_{in}} \tag{1.1}$$

The non-ideal processes in the compressor and turbine therefore lead to a lower thermal efficiency. The high bypass ratio turbofan is currently the primary choice for commercial aircraft engines where efficiency is paramount. In the case of a turbofan, the core of the engine is effectively a turbojet, as described previously, and only sees a small portion of the total mass flow through the engine. The majority of the thrust comes from the fan, driven directly by the low pressure shaft. A larger mass of air is imparted with a smaller velocity change by a fan in comparison to a turbojet, leaving the accelerated gas with less energy once it has been exhausted from the engine, thus improving propulsive efficiency.

1.2 Motivation for Seals Research

The efficiency of gas turbine engines has become an increasingly important design consideration for engine manufacturers due to the demand from airlines and aviation authorities. This has resulted in greater turbine entry temperatures, cycle pressure ratios, bypass ratios and shaft speeds with each new generation of engine. Although increasing these

cycle parameters leads to higher thermal and propulsive efficiencies, the greater temperatures lead to more rapid degradation of high pressure and temperature components leading to increased specific fuel consumption (SFC) (Moore 1975).

Secondary leakages occur because the primary flow path within a gas turbine is not entirely sealed. Rotating and static components in close proximity which form part of a 'continuous' surface, such as a hub or casing endwall, must possess some clearance so as not to make contact during operation. Airflow used for coolant within the turbine is distributed from the compressor by internal passages, which is possible due to clearances between rotating and static components. Axial shaft load balance and bearings also contribute to clearances. These possible leakage paths occur in a vast number of locations within gas and steam turbines and it is essential that these secondary flows are controlled such that pressure differences across leakage paths are maintained and flow containing extractable work is not wasted.

Until recently, the majority of engine research time and funding resources has been concentrated on improving the main gas path engine components such as the fan, compressor and turbine vanes and blades. Now it is increasingly challenging to achieve cycle benefits from changes to these components due to trade-offs such as increased coolant flow required for the high pressure turbine. Regardless, increasing cycle pressures and temperatures remains a top priority and require continued development in these areas. However, the potential to make lower-cost, significant improvements to SFC now comes from relatively neglected components such as engine seals. For example, in an advanced high-bypass-ratio engine, a compressor efficiency increase of 0.91% would be required to produce the same increase in engine performance as would be achieved by a reduction in turbine seal component leakage of 1% of the engine airflow (Stocker, Cox and Holle 1977). Extracting an equivalent performance improvement with the compressor or turbine efficiency is 4 to 5 times more

expensive, in terms of research resources and manufacture of complex components, than by reducing the seal leakage (Stocker, Cox and Holle 1977, Smith 1994). Improvements in sealing alone could lead to an annual energy saving of the order of tens of millions of barrels of oil (Ludwig 1980) and hence a significant financial saving would also ensue. In terms of engine bleed, a 1% reduction in leakage could give a 0.4% reduction in specific fuel consumption (Moore 1975).

Thermal growths during operation and seal degradation over engine lifespan lead to larger seal clearances and hence increased leakage rates, having an adverse effect on the overall engine performance. Thrust is reduced for a given fuel consumption, hence requiring an increased throttle setting to obtain the original engine performance. This results in an increase in SFC, as well as higher combustor temperatures, reducing the lifespan of the high pressure turbine (HPT) components (Steinetz and Hendricks 1997). The life of HPT components is a strong function of operating temperature and hence the degradation of seals results in increased operating costs. Sealing has a marked effect on engine efficiency, performance retention, thrust, compressor pressure ratio and compressor stall margin (Zaretsky 1997). Industrial gas turbines and steam turbines are of a considerably larger scale than aircraft engines and thus seals used in this application are required to deal with greater rotor diameters and, subsequently, larger relative radial growth. The cycle pressure ratio for steam turbines is also much greater than those seen in aero gas turbine engines. Pressure drops to be dealt with can be up to 27 bar (Chupp, Ghrasripoor, et al. 2002) and to achieve this, multiple seals are used all with less than desirable leakage performance and lifespan from the wear mechanisms described in section 1.3.1. The realisation for the potential of improved seals for both civil aircraft and industrial gas turbines has raised the interest in seal technology research.

1.3 Existing Gas Turbine Sealing Technology

Some key civil aircraft gas turbine engine sealing locations in the primary and secondary air flow systems are shown in Figure 1.2. These include fan, compressor and turbine shroud seals (primary air system), bearing seals and compressor and turbine inter-stage seals (secondary air system). A large number of seals are present in an engine, and hence their leakage performance significantly affects the overall efficiency and hence SFC. It is the secondary airflow system seals which comprise the areas of investigation to which this project is dedicated. Current technology in use is described in sections 1.3.1 to 1.3.3. The high mainstream gas temperatures in the turbine require that certain components such as the rotor blades and stator vanes are cooled. To achieve this, mainstream flow from the compressor is bled off and channelled through to the turbine. Coolant flows at a range of pressures are guided to different destinations via a multitude of paths, which is only possible with the application of seals.

The primary aspect of seal design is the ability to deal with large variations in the clearance between the rotating and static components from idle to operating conditions due to relative thermal growth of the rotor and stator and centrifugal growth of the rotor. Figure 1.3 shows how the relative diameter can vary between a rotating component and its casing over the course of a flight cycle, in this case a high pressure turbine blade tip and casing. At idle conditions, the temperatures and rotor speeds are far from the cruise conditions (design point) and hence the clearance is greatest. At take-off the clearance reduces as the rotor experiences centrifugal growth and, over the course of the cruise, thermal growths affect the clearance by varying amounts. The challenge is to provide geometric control while maintaining efficiency, integrity and long service life.

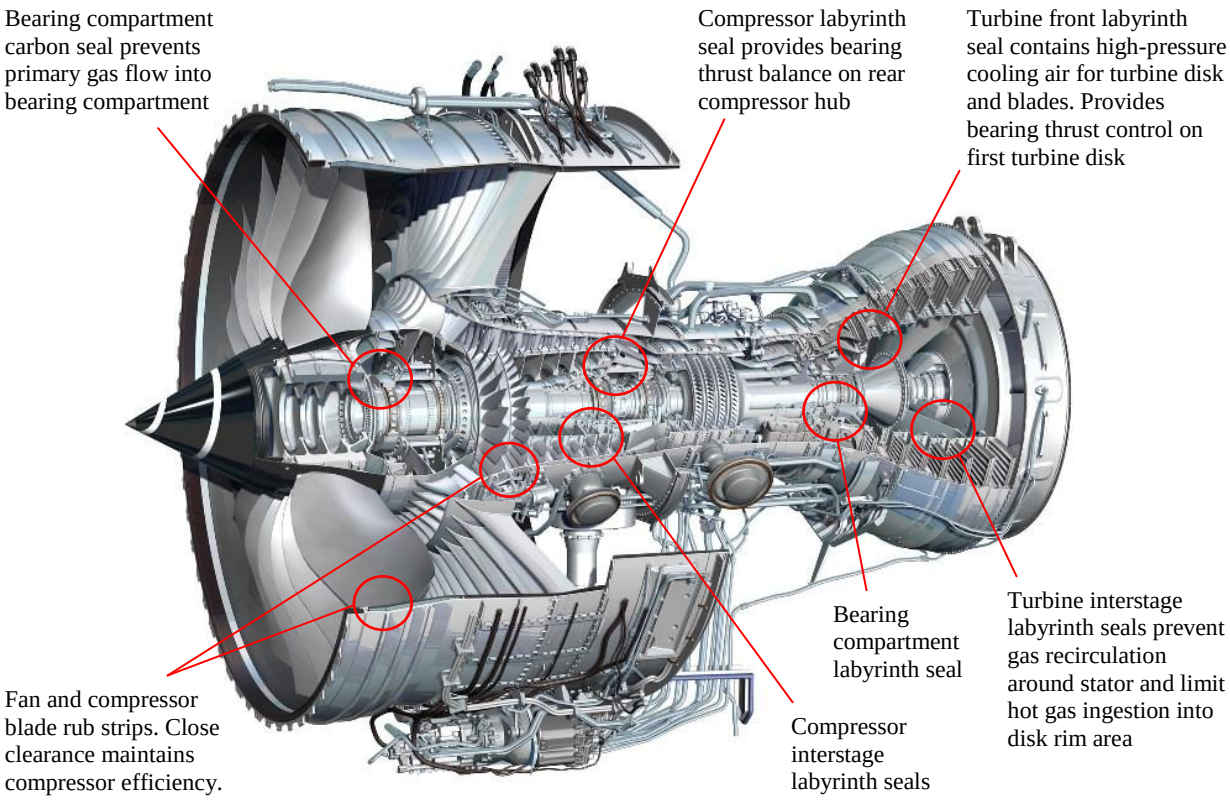


Figure 1.2: Sealing locations in a gas turbine engine – Trent 1000 (Rolls Royce plc)

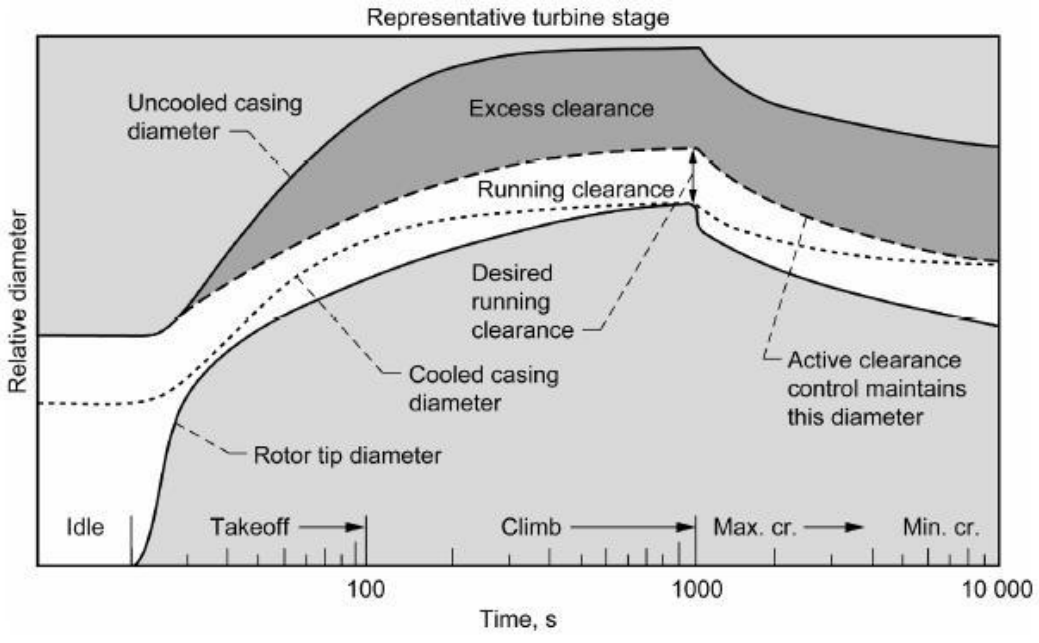


Figure 1.3: Variation in seal gap height over engine flight cycle (Chupp, Hendricks, et al. 2006)

1.3.1 Labyrinth Seals

Labyrinth seals and their principles are commonplace in gas turbine engines and come in a variety of configurations. The most commonly used configurations are straight, interlocking, slanted and stepped seals as shown in Figure 1.4. By their nature, labyrinth seals, the teeth of which are usually mounted on the rotor, are inactive clearance control seals i.e. the clearance will vary with rotor and casing relative growth. A labyrinth seal is designed to maintain a small clearance between the rotating and static surfaces and permit controlled leakages by the dissipation of flow energy through a series of abrupt expansions into inter-tooth cavities with minimum heat rise and torque, due to the non-contacting nature of the seal. Principle design parameters include clearance, throttle, cavity geometry and the number of teeth. The clearance is set to preclude contact with the shroud (unless the shroud is designed with an abradable surface) allowing for radial and axial excursions. The tooth thickness is as thin as is structurally feasible to mitigate heat propagation through the tooth-body into the shaft with a sharp edge at the leakage path throat, which is the primary flow restrictor (Willenborg, S. and Wittig 2001). The angle at which the flow approaches the teeth is usually perpendicular, allowing the seal to deal with undesirable flow reversals equally well.

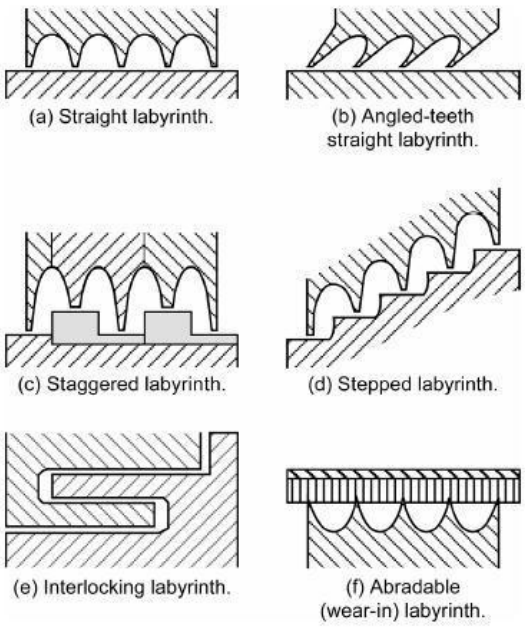


Figure 1.4: Labyrinth seal configurations (Chupp, Hendricks, et al. 2006)

Labyrinth seals have been used almost exclusively because of their low wear, very high running speed (460ms^{-1}), pressure (17 bar) and temperature (705°C) as well as their ability to accommodate shaft excursions. These figures are more representative of aero gas turbine applications but labyrinth seals can be subjected to higher speeds, pressures and temperatures in steam turbines, for example. Maintaining higher pressure drops (200 bar) requires more teeth and therefore the axial length of the seal can be significantly longer. To achieve increases in efficiency in future generation gas and steam turbines, increasingly harsh conditions are necessary and have resulted in higher leakage rates due to the larger clearances at which labyrinth seals must be run (Ferguson 1988). Although they are reasonable in restricting flow, they do not respond well to engine transients and often lead to instabilities in high pressure locations. Figure 1.4 shows possible labyrinth seal configurations which all require multiple teeth and cavities in order to sustain a desired pressure drop, leading to a considerable axial length required. In the case of an aero-engine where weight must be minimised, reducing the axial length of the seals, and in some locations the overall length of the engine, will result in significant performance gains. Industrial gas and steam turbines are of a significantly larger scale than aero gas turbines, which leads to much greater distances between bearings, resulting in more extreme relative movement to be dealt with. Pressure drops across seals can also be greater which are accommodated by the use of multiple tooth (as high as 10) labyrinth seals to dissipate the leakage energy, adding significant length to the shaft.

1.3.2 Brush Seals

The brush seal was the first simple and practical alternative to the labyrinth seal that offers extensive performance improvements and is now widely used in the gas turbine industry. Benefits of brush seals over labyrinth seals include a reduced leakage (up to 95%) and the ability to accommodate shaft excursions due to start-up, shut down and other transient conditions. Labyrinth seals require permanent seal clearances under all conditions, degrading

the seal and engine leakage performance. Brush seals also require significantly less axial space than a labyrinth seal to achieve an equivalent pressure drop. Brush seals consist of fine-diameter nickel-steel super-alloy bristles densely packed and welded to the inner circumference of a ring (Figure 1.5 (*a*)) between a backing ring (downstream) and a cover plate (upstream). The wire bristles protrude radially inward and are machined to fit the mating rotor with a slight interference (preload) in a cold geometry state. Preload interferences are carefully designed such that local overheating of the rotor and excessive thermal growths are prevented. To accommodate anticipated shaft movements the bristles must bend without axially buckling. Hence the wires are radially orientated at a lay angle (typically 45° to 55° where 0° = radial direction and 90° = circumferential).

The leakage of a newly installed brush seal has been shown to be only 4% of that of a vertical 5 toothed labyrinth seal with a 0.75mm clearance (Ferguson 1988), mainly because brush seals do not require an inherent operating clearance between the seal and the rotor surface. Hence in many industrial applications, they have been incorporated into labyrinth seal arrangements (Figure 1.5 (*b*)) to improve the leakage characteristics and reduce the overall axial length of the seal, which translates directly into reduced SFC (Hendricks, et al. 1994) or increased engine thrust. However, brush seals are contacting seals by nature and so in service can be susceptible to rapid wear caused by the 'blow-down' effect, which was first observed by Bayley et al. (1993). It was shown that a radial pressure gradient leads to a static pressure distribution over each bristle and a subsequent resultant force acting towards the surface of the spinning rotor. Brush seals have also been shown to undergo rapid wear due to pressure-induced distortions in the bristle pack and exhibit two phenomena: bristle 'hysteresis' and 'stiffening' from interlocking bristles shown by Basu et al. (1994). In parts of the engine where shaft speeds and temperatures are very high, brush seals are not deemed to be practical because of their short lifespan. They are also not greatly suited to large diameter rotor

applications where large growths and eccentricities occur, as they would be subjected to unsustainable bristle tip loads and rotor surface speeds causing rapid wear to both the seal and rotor.

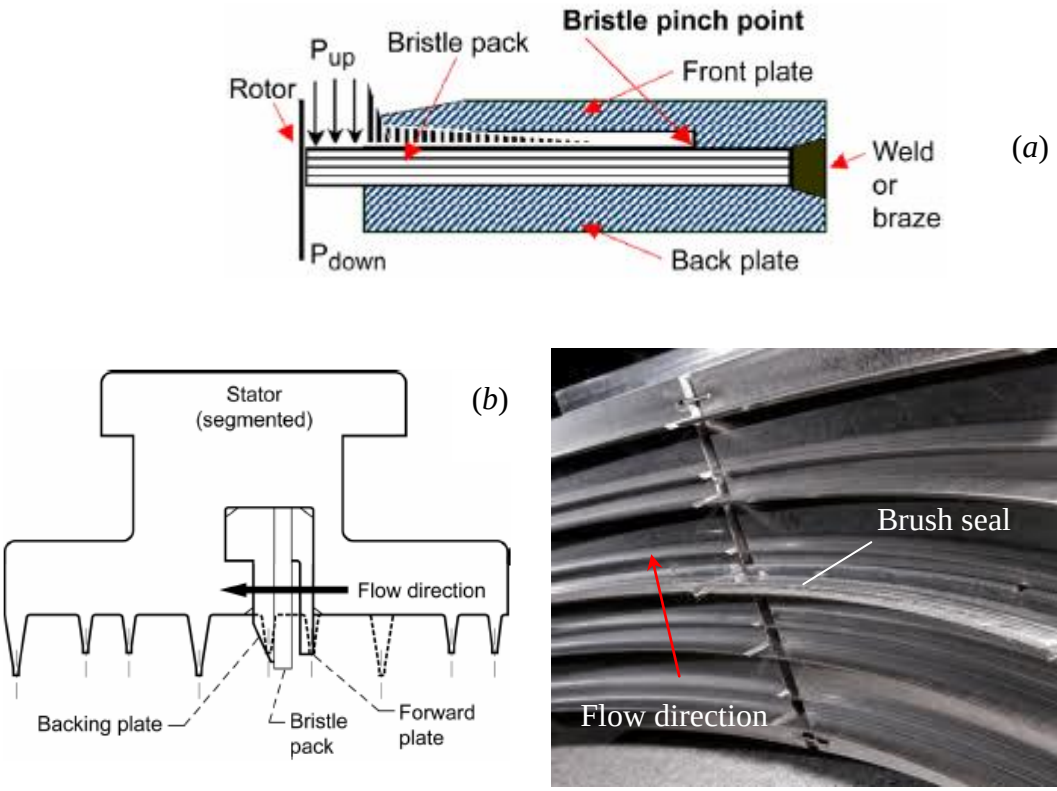


Figure 1.5: (a) – Brush seal cross section, (b) – Brush seal incorporated into a multiple-tooth labyrinth seal, schematic (Chupp, Hendricks, et al. 2006) and photo (Neef, et al. 2006)

1.3.3 Leaf Seals

Leaf seals are a similar type of seal to brush seals in that they make contact with the shaft surface permanently. They were invented (Wright 1999) to possess higher axial rigidity and more reliable performance than brush seals whilst producing similar leakage characteristics and addressing the problems of bristle stiffening and hysteresis. Bristles are replaced with leaves (thin plates), which are closely packed to obstruct the air flow and yet are able to deform radially to accommodate shaft growth and excursions. The leaf seal is a relatively young sealing technology and a design has been introduced successfully into service by Mitsubishi Heavy Industries in an industrial gas turbine (Nakane, et al. 2004). The

components that comprise a leaf seal, illustrated below in Figure 1.6, are multiple plates of thickness 50 – 200 µm, width 4 – 10 mm, and length 15 – 30 mm and are arranged around the circumference of the rotor and, like brush seal bristles, make contact with rotor surface at a lay angle. There are gaps between the leaves of the order of microns and hence radial movement of the rotor can be accommodated. The gaps lead to a leakage flow through the seal which may be desirable if controlling coolant flow. Although the leaf seal is also a contacting seal, wear rates at the interface between the shaft and leaf tips are less than for brush seals as the additional axial stiffness of the leaves prevents pressure stiffening of the seal and locking against the seal backing ring. Additionally, a hydrodynamic lift force generated by the fluid film moving with the rotating shaft may reduce the contact force (Nakane, et al. 2004). Although leaf seals appear quite promising, their behaviour and performance characteristics in engine conditions are relatively unknown as they have experienced very few hours in service. It is understood that leaf seals may suffer failure from the effects of high cycle flutter fatigue. Design methods to prevent this are currently being established (Jahn 2008).

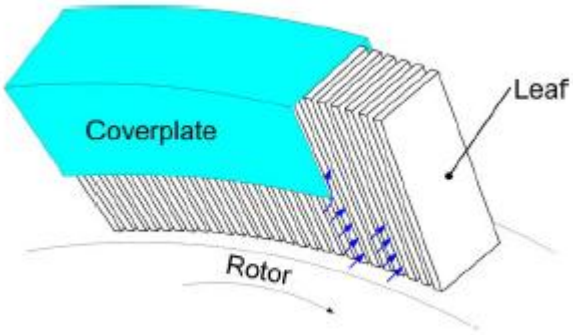


Figure 1.6: Leaf seal design (Jahn, Franceschini, et al. 2011)

1.4 Effective Clearance

A widely employed method of directly comparing the leakage performance of different seal types and sizes is to compute the effective clearance of a seal, shown below in Equation **(**1.2). This parameter is essentially the seal's capacity (mass flow rate normalised by the inlet

pressure and temperature: $\frac{\dot{m}\sqrt{T}}{p_{HP}}$) which has also been normalised by the circumference of the leakage path, πD, to leave the gap height. Calculating an effective clearance equates the mass flow rate of a seal to that of an axisymmetric ideal contraction of clearance e, which is given by

$$e = \frac{\dot{m}\sqrt{T}}{\pi p_{HP} D \epsilon} \tag{1.2}$$

where $\dot{m}$ is the mass flow rate, T is the upstream temperature, p_{HP} is the upstream total pressure, D is the rotor outer diameter and

$$\epsilon = \begin{Bmatrix} \sqrt{\frac{\gamma}{R}\frac{2}{(\gamma-1)}\left(\left(\frac{p_{HP}}{p_{LP}}\right)^{\frac{-2}{\gamma}} - \left(\frac{p_{HP}}{p_{LP}}\right)^{\frac{-(\gamma+1)}{\gamma}}\right)}, & \left(\frac{p_{HP}}{p_{LP}}\right) < \left(\frac{2}{(\gamma+1)}\right)^{\frac{-\gamma}{\gamma-1}} \\ \sqrt{\frac{\gamma}{R}\left(\frac{2}{(\gamma+1)}\right)^{\frac{\gamma+1}{\gamma-1}}}, & \left(\frac{p_{HP}}{p_{LP}}\right) > \left(\frac{2}{(\gamma+1)}\right)^{\frac{-\gamma}{\gamma-1}} \end{Bmatrix}$$

which is a coefficient that accounts for compressibility. Effective clearance will be referred to later in this thesis as a measure of a seal's leakage performance.

1.5 Thesis Overview

Two important aspects of future generation seal design are rotor-stator clearance and leakage. Ideally, a seal would not make contact between the rotating and static surfaces over an entire operational cycle whilst accommodating rotor eccentricities and relative radial growth preventing wear for longevity. This simultaneously maintains leakage characteristics over the seal's lifespan. The clearance would also be controlled to ensure a minimum gap and a desired leakage flow. A passive control system would be employed so as not to rely on an active one which could fail, leading to seal damage and possibly mechanical failure. The current shaft sealing methods, which have been outlined above, cannot achieve this. To address this issue, a new generation of non-contacting seals is being researched by the Shaft Seals group at the University of Oxford with the aim of developing new technologies that

satisfy both of the criteria discussed. The results in this thesis describe the progress made in analysing the feasibility and the development of two vastly different sealing methods and thus significantly contributes to the goal of achieving non-contacting sealing technology for gas and steam turbines. The majority of this research is concentrated on a Rolls Royce concept called the Large Axial Movement Face Seal; a non-contacting face seal for which experimental and computational fluid dynamics investigations and analytical modelling were undertaken. Importantly, the housing of this seal is designed to be rotor-following. The second seal concept of interest is a fluidic seal, involving flow injection from a row of jets across the leakage path to restrict the main leakage flow. The contents of each chapter in this thesis is briefly summarised below.

In chapter 2, the challenges facing seal design are elaborated upon. With this in mind, the two sealing technologies upon which this thesis is based are briefly described within the literature survey of current in-service seals, and seals under development. In chapters 3 and 4, the investigation of the Large Axial Movement Face Seal is fully reported. Chapter 3 describes all experimental and computational research carried out on a simplified, linear version (prismatic cross-section) of this seal. An effective passive clearance control system, using the static pressure loading on the seal housing, was designed and tested on this rig. Chapter 4 then describes the work conducted on a fully annular, three-dimensional test rig and the accompanying computational modelling, which were used to verify the design guidelines of the more extensive two-dimensional study. In chapter 5 the fluidic concept is described. Experimental, computational and analytical studies are reported and the feasibility of such a seal is discussed. In chapter 6, the conclusions of the research are reported and suggestions for further work are proposed.

2 Literature Review

2.1 Introduction

In this chapter, the author elaborates upon the two reasons behind the motivation for this research program. The issues of wear limiting seal lifespan and performance characteristics over time, as well as the need to accommodate large axial and moderate radial relative movement, are discussed in detail. The sealing concepts which comprise the bulk of the research presented in this thesis are also mentioned briefly and their attributes are discussed. Other next generation sealing methods are then reviewed and their abilities to overcome the issues described above are analysed. All are non-contacting seals, either by modification to an existing contacting seal, or are inherently non-contacting designs. Finally, some of the theory useful for modelling many of the non-contacting seals, which employ the hydrodynamic lift phenomenon, are shown.

2.2 Sealing Challenges to Overcome

2.2.1 Wear

2.2.1.1 Rotor-Bristle Tip Contact Wear

As described in chapter 1, seals which inherently make contact with the rotor suffer from undesirably high wear rates. This leads to a reduction in leakage performance over time and the short lifespan of the seal can influence the length of periods between engine maintenance. In fact, contacting seals such as brush seals are currently not used in ‘harsh environment’ regions within an engine as their lifespan would be unacceptably short, such as interstage seals where the surface speeds and temperatures are high. Though it is a considerable

problem, the issue of wear in brush seals has been relatively only briefly investigated compared with leakage characteristics, for example. It was shown by Wood et al. (1997) that the radial wear is dependent on the contact pressure between the two surfaces; the bristle tips and the rotor outer surface. The contact pressure is dependent on the brush seal's mechanical properties (the bristle stiffness and the level of the initial interference fit with the rotor) and pressure induced parameters (inter-bristle friction and 'blow-down', the latter of which is dependent on the cover plate and backing ring relative gap heights). The wear rate is also dependent on the tribological pair, *i.e.* the interaction between two different materials (Aksit and Tichy 1998). With a multitude of parameters to set, it can be difficult to achieve a contacting seal design which is relatively wear-free with acceptable leakage characteristics that are maintained over a desirable lifespan. Leaf seals, mentioned in chapter 1, are also susceptible to these issues, as are finger seals which are described in section 2.4.5. Figure 2.1 (*a*) shows a brush seal after service in an industrial gas turbine which has experienced significant bristle tip wear and noticeably some bristles are damaged. During extreme transient conditions, labyrinth seals, which are inherently non-contacting due to their lack of compliance, can also make contact with the rotor which can lead to significant wear of their tips – so called 'mushrooming' (Figure 2.1 (*b*)). The geometry of the sharp edges then becomes more flow compliant.

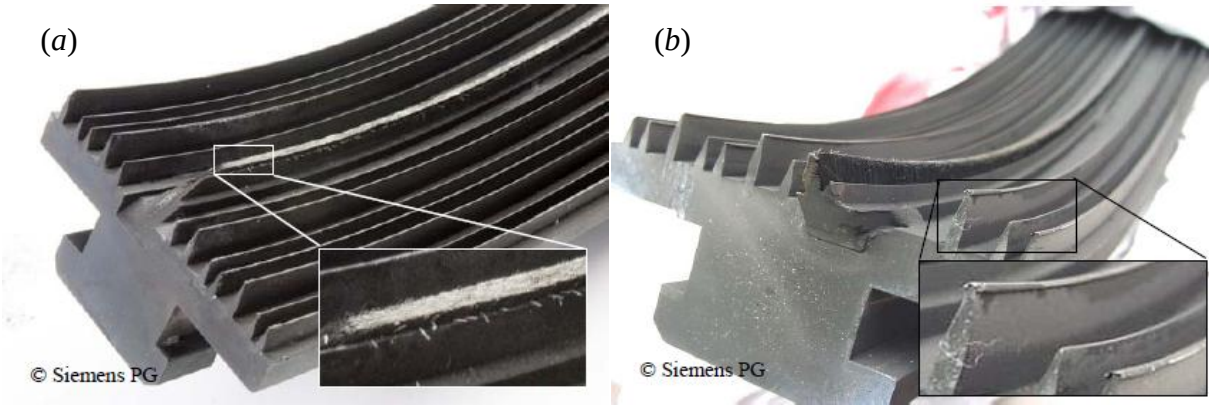


Figure 2.1: Rotor-seal contact wear after 30 months continuous service (Neef, et al. 2006): (*a*) – Brush seal bristle tips, (*b*) – Labyrinth seal teeth tips

Current seals extensively used in aero and industrial gas turbines, the labyrinth and brush seals, either have inherently poor leakage characteristics due to lack of clearance control or are compliant but their acceptable initial leakage performance degrades rapidly. Next generation seals will ideally be non-contacting but have a method of clearance control to maintain a minimum or desired gap height regardless of rotor-casing relative growth.

2.2.1.1.1 Start-up Induced Wear

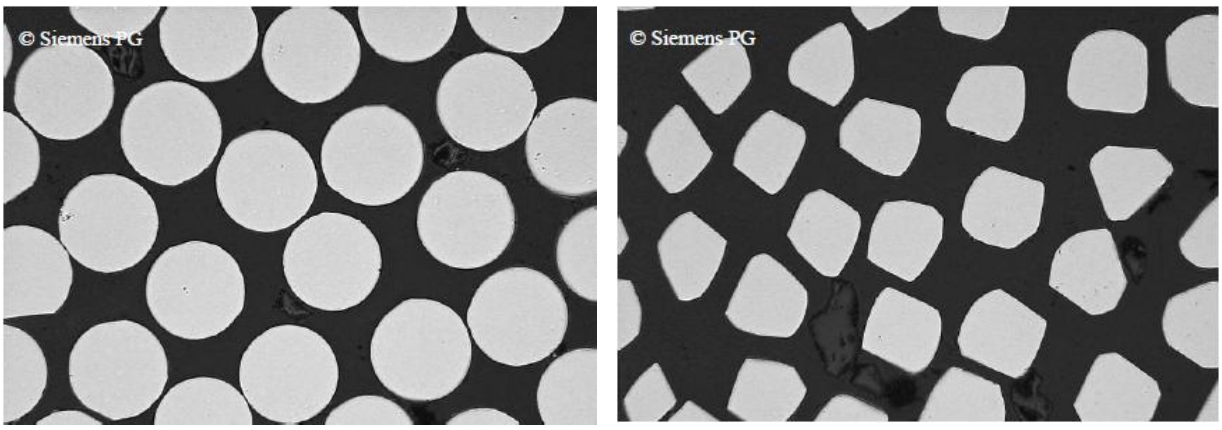
Work by Neef et al. (2006) reported the impact of wear incurred during start-up conditions, which was measured by the variation in leakage. A new brush seal was the focus of the test program and was subjected to multiple start-up simulations and the leakage under various pressure ratios was recorded between each cycle. The largest wear was experienced from the first cycle and increased the leakage considerably by 10%. After cycles two to five, more wear had been inflicted on the seal such that the leakage was 22% higher than when new. Further cycles had little effect on the seal's leakage performance as the shorter bristle length reduces the blow-down effect and the bristle wear saturates.

2.2.1.1.2 Rotor-Casing Relative Growth and Rotor Eccentricity Induced Wear

Further wear beyond what is experienced during start-up conditions can be inflicted by relative growth between the rotor and casing (by centrifugal rotor growth and/or thermal growth) or eccentricities (when the rotor and casing axes are non-concentric). Depending on the size of the relative movement, a significant increase in blow-down can occur due to the change in lay angle which increases the contact pressure on the bristle tips. This can lead to extremely high wear rates. These extreme conditions come from large transients, which are more likely to be experienced by aero-engines as oppose to industrial gas turbines, and are relatively infrequent, but an ideal seal would have the capability of enduring these without incurring wear and a subsequent reduction in leakage performance.

2.2.1.2 Inter-Bristle Contact-Induced Wear

In conjunction with the wear between the rotor surface and bristle tips, Neef et al. (2006) showed that wear also occurs between the individual neighbouring bristles. Contact forces arise from the pressure difference across each bristle forcing them downstream. By using a backing ring to prevent axial deflection, the bristles are therefore pressed together. Compliance to relative radial movement leads to inter-bristle rubbing and hence wear. Figure 2.2 shows how the bristles close to the back cover plate (*a*) have experienced negligible wear whilst the bristles close to the front cover plate (*b*) are considerably worn. The bristle diameters may eventually become extremely thin such that failure occurs as shown in Figure 2.3. This can result in debris being carried with coolant flow and could potentially block cooling passages in turbine blades and vanes, for example. A reduction in the effectiveness of cooling systems for these engine components must be prevented.



(*a*) (*b*)

Figure 2.2: Bristle cross section after 30 months continuous service (Neef, et al. 2006): (*a*) – bristles close to back plate, (*b*) – bristles close to front plate

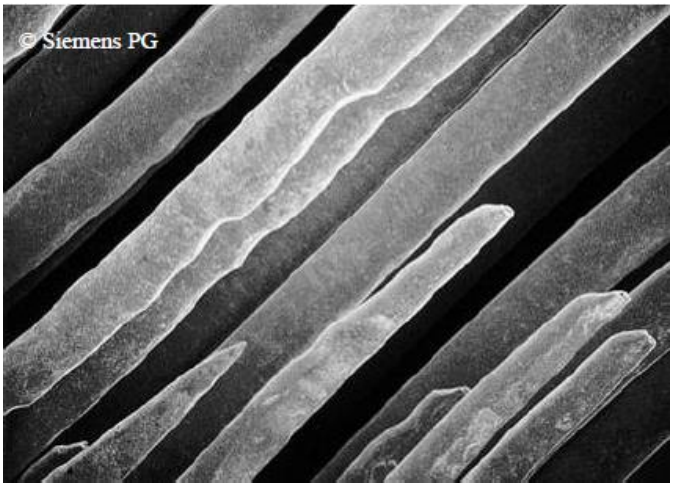


Figure 2.3: Bristle condition after 30 months continuous service (Neef, et al. 2006)

2.2.2 Large Axial and Radial Relative Movement

As described in section 1.3.1, industrial gas and steam turbines are of a larger scale than aero-engines and this leads to greater distances between bearings and the potential for greater relative radial excursions by the rotor. Aero gas turbines are much more compact but can be subjected to highly transient conditions such as a 'step-climb' (sudden maximum throttle) in emergency situations. For labyrinth seals to accommodate these large relative movements, an inherently large clearance is needed, which leads to poor leakage characteristics. Brush seals can experience significant wear from transient conditions such that there is no longer an interference fit at cold conditions and the blow-down force is no longer able to create rotor-bristle contact during operation as reported by Chupp et al. (2001) and Dinc et al (2002). This therefore reduces the leakage performance characteristics significantly. Dogu et al. (2008) modelled brush seals with clearances of 0.27 mm and 0.75 mm, resulting in the leakage through the clearance accounting for 65-95% of the total leakage, depending on the clearance and pressure difference across the seal. Private communication with Rolls-Royce reveals that the expected maximum radial and axial movements that seals are designed to accommodate in an aero-gas turbine are ± 0.5 mm and ± 5 mm respectively.

2.3 Seals Which Potentially Satisfy Both Criteria

Two seal concepts which are inherently non-contacting and can withstand large axial and moderate radial movement are described below. These two sealing methods are the focus of the author's research and are fully detailed in their respective chapters; the large axial-movement face seal in chapters 3 and 4 and the fluidic seal in chapter 5.

2.3.1 Rolls Royce Concept – Large Axial Movement Face Seal

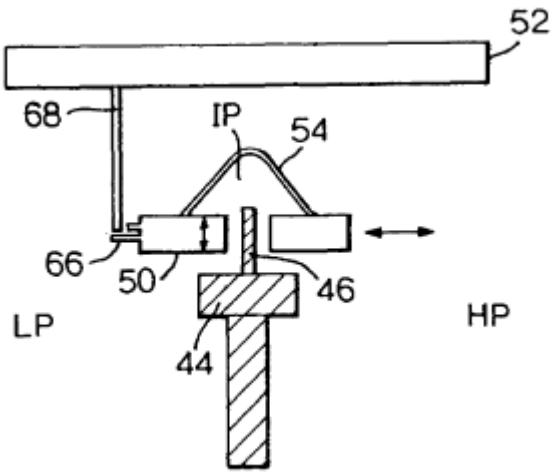
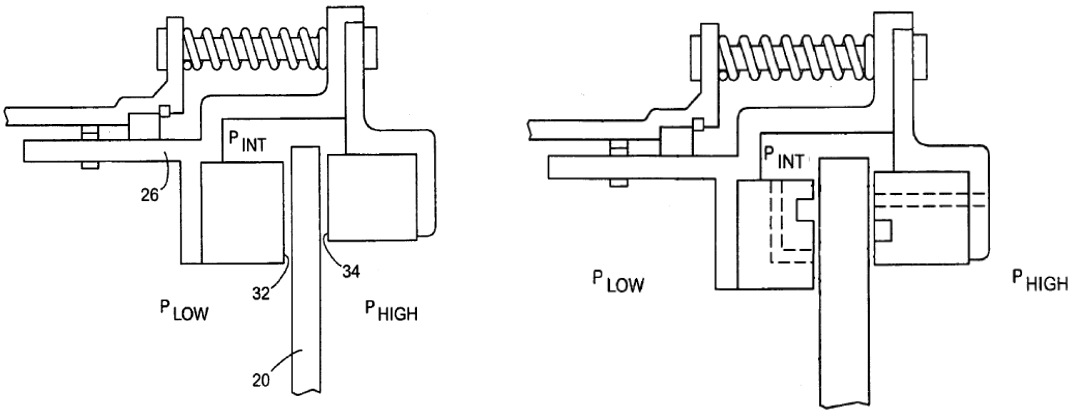


Figure 2.4: Schematic of the Rolls-Royce LAMFS concept (J. Webster 2007)

This seal concept is a Rolls-Royce patented idea (J. Webster 2007) which involves two sealing faces; on the upstream and downstream sides of a disc (46) shown in Figure 2.4. The seal housing (54) separates high and low pressure zones (HP and LP respectively). A secondary seal (66) allows axial movement of the seal housing and hence, if designed appropriately, a large axial movement of the disc can be accommodated. It also reduces the axial force on the seal housing in the downstream direction, due to the pressure difference across the seal, by allowing a portion of the downstream side to see high pressure, HP. This is explained fully in section 3.2.1. The cavity containing an intermediate pressure (IP) could easily allow for 0.5 mm relative radial growth and rotor excursions without compromising the seal's performance. Ideally the axial position of the seal housing relative to the rotor is

controlled by the axial component of the static pressure around the housing and it is demonstrated by the author that specific geometry is required within the seal gaps in order to achieve this. Relative axial movement that can be accommodated is dependent on the secondary seal, which must maintain its sealing ability at all times. The author spent the majority of the research program on this concept.

2.3.1.1 Pratt & Whitney Seal Concept



(*a*) (*b*)

Figure 2.5: Pratt and Whitney Self-Balancing Face Seal: (*a*) – Schematic, (*b*) – Schematic showing hydrostatic seals (Glahn and Munsell 2009)

A recent patent application by Glahn et al. (2009) from Pratt and Whitney was discovered, which is a very similar concept to the Rolls Royce large axial movement face seal. Two seal faces exist on either side of a rotating disc as shown in Figure 2.5 (*a*). The authors claim that the first (34) and second (32) seals are both hydrostatic and hydrodynamic seals though the types of hydrodynamic seals that would be utilised are not described. The hydrostatic sealing methods proposed are displayed in Figure 2.5 (*b*). A secondary seal is also employed and a biasing element, in the form of a spring, aids the self-balancing ability such that the clearances are maintained. This would be especially useful under start-up conditions where the hydrostatic and hydrodynamic induced pressure forces will be small. This seal concept could cope with moderate radial growth depending on the designed clearance between the disc outer

radius and the seal housing, though the extent of which this seal can cope with the axial relative movement may be limited by the inclusion of a biasing element. A maximum relative axial movement of 10 mm, as described in section 2.2.2, is a significant distance.

2.3.2 Fluidic Seal

The second sealing concept researched by the author is the fluidic seal, which employs a row of jets orientated normal to a leakage path aiming to reduce the leakage mass flow rate. For this seal to be beneficial, the sum of the jet mass flow rate and the mainstream leakage mass flow rate must be lower than the mainstream without the inclusion of the jet row under the same boundary conditions. Depending on how far the jets can penetrate through the mainstream flow, large clearances can potentially be left between the rotor and casing to accommodate radial growth, and the axial relative movement that can be withstood is essentially limitless. Literature on the research into this sealing method is summarised and contained within chapter 5 which concerns all fluidic seal related work from this research program. As will be shown in the fluidic seal chapter, relative radial growths of ± 0.5 mm and axial movement of ± 5 mm can be dealt with easily.

2.4 Other Sealing Technology

This section reviews other next generation sealing methods which are also non-contacting in nature. Their ability to overcome the current sealing issues, described in section 2.2, is assessed below.

2.4.1 Hybrid Brush Seal (HBS)

As described in section 1.3.2, the performance and life of brush seals degrade over time due to wear from contact with the rotor surface. An incremental improvement to current brush seals would be to provide air-riding capability to this technology for which a vast quantity of data already exists. Attempts have been made to use hydrodynamic lift to reduce the wear rate at

the bristle tips or eliminate it entirely (Justak 2004). He combined a brush seal with tilt pad bearing concepts. The design introduced is configured such that the bristle tips are attached to multiple pads which fit end-to-end along the inner diameter of the seal (Figure 2.6). All the seal leakage is controlled by the bristles and the lift force by the pads, but the leakage is more constant over time than for a conventional brush seal and can accommodate reverse rotor rotation with no bristle wear.

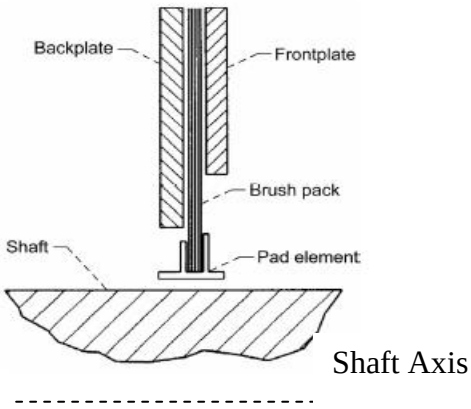


Figure 2.6: HBS with Pad Elements Attached to Bristles (Chupp et al., 2006)

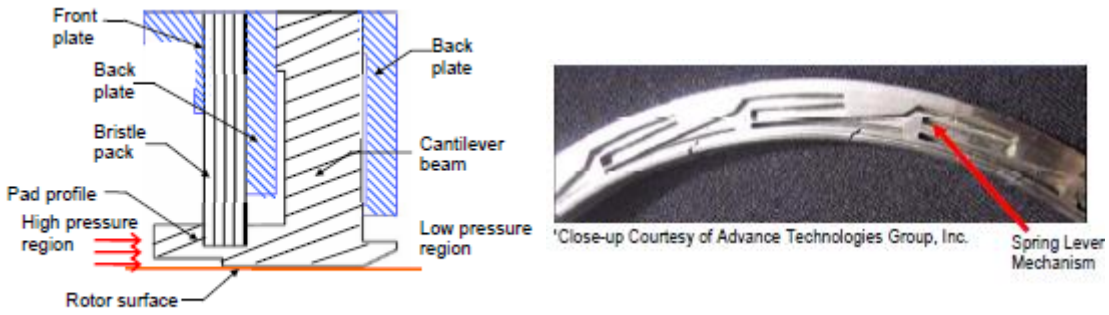
Experimental testing of the hybrid brush seal with rotor offsets of up to 0.51mm showed negligible wear or temperature rise occur and less than 1/3 of the torque is required to maintain rotational speed than that of a conventional brush seal. This would suggest that radial movement in aero-applications would be easily accommodated and axial movement would depend on the land (the length of the shaft of a constant radius with which the seal interacts). However, the main issue with the design shown was that the flexibility of the bristles allowed the pad elements to rotate about the circumferential axis, causing the upstream edge of the pad element to make contact with the rotor surface and hence wear, an issue which would need to be eliminated. Heat transfer studies would be required to understand the dissipation of heat created due to rotor-pad contact, which could occur from very large rotor growth or excursions. It would also be necessary to understand the effect and dissipation of heat generation in the air film due to viscous shear. Attaching the bristles tips to the pad may affect behaviour of the seal when accommodating shaft expansions and

movement, as the inter-bristle interactions may vary, affecting the stiffness and hysteresis characteristics compared to a standard brush seal.

Delgado et al. (2003) present a model and experimental data used to determine the static structural stiffness coefficient of a large diameter shoed brush seal (279 mm). The results indicated that the damping characteristics of the seal are influenced by the dry friction which occurs from the inter-bristle and bristle-to-backplate interactions. A computational study was performed by Delgado et al. (2004) to predict the rotordynamic force coefficients in a 20-shoe brush seal on a 169.2 mm diameter rotor. To create the model, the structural and mechanical properties of the bristles were coupled with the gas film pressure forces generated in the tight clearance between the rotor and the underneath of the shoes. The predictions suggest that the overall stiffness and damping characteristics from a shoed brush seal are not affected by either the operating gas film thickness or the pressure difference across the seal though small variations in bristle diameter can lead to large changes in the seal structural stiffness. The rotor speed also has a strong influence on the overall stiffness. It was shown that accurately modelling the damping relies upon the appropriate characterisation of the energy dissipation in the bristle pack and the damping type to be hysteretic (due to inter-bristle interactions). Delgado et al. (2007) conducted experimental research into the structural stiffness and damping coefficients of this shoed-brush seal and a good level of agreement was observed between this set of experiments and the computational data obtained in 2004.

San Andres et al. (2008) conducted experimental work on a second generation design of the HBS which aimed to eliminate pad rotation due to the pressure difference across the seal. This is achieved by supporting the pads with cantilever beams. A schematic of this seal design is shown below in Figure 2.7 (*a*) with an image of the rear of the seal detailing the cantilever geometry in Figure 2.7 (*b*). The pad design allows for hydrostatic lift-off when a pressure

difference is applied across the seal, including static shaft conditions, as well as hydrodynamic lift due to shaft rotation. The seal involved in the research consisted of 20 pads over a 167.1 mm diameter shaft. Bristles were orientated at a lay angle of 45° and the initial build interference of the pads with the rotor was 0.381 mm. Compared to the first generation HBS seal (Figure 2.6) this seal showed a 10% improvement in leakage at the highest pressure ratio of 3. Effective clearances for this seal are listed for the first generation HBS were between 0.4 mm and 0.6 mm. The second generation HBS shown below had measured effective clearances of between 0.25 and 0.45 at a pressure ratio of 1.3 and 3. The torque required to rotate the shaft from rest was recorded as being 7 times higher than the running torque at 1300 rpm, which suggests that there is still considerable friction due to pad-rotor contact at low rotational speeds. Wear to the pad surfaces is therefore possible under start-up and likely under large transients too, which may alter the pad profile and the ability to generate hydrodynamic lift. The life of this seal could therefore be limited. Further data, both experimental measurements and computational predictions, was obtained on this seal by San Andres et al. (2010) into the rotordynamic force coefficients. He reported that the overall stiffness reduced by up to 15% with increasing rotor speed from rest up to 1200 rpm as a result of the hydrodynamic-induced pressure fields.



(*a*) (*b*)

Figure 2.7: Next generation HBS: (*a*) – Schematic, (*b*) – HBS rear showing cantilever beams (San Andres, Baker and Delgado 2010)

2.4.2 Film Riding Face Seal

A film riding face seal is dependent on hydrodynamic lift where two annuli are in close proximity, one static and one rotating, both of which are subjected to a permanent bias force acting towards each other. When the rotor is in motion, they are prevented from making contact due to the surface geometry-induced above-ambient pressure field between them thus overcoming the bias force and causing the stator to lift off the rotor surface. As well as minimising the contact time and wear, another objective of equal importance is to minimise the leakage mass flow rate through the gap between the two surfaces separating the two pressure zones by operating the seal at a minimum clearance. Lipschitz (1984) created and investigated an early face seal design which made contact with the rotor when stationary but lifted off and separated from the rotor during operation due to the hydrodynamic pressure field created. Munson (1992) then developed the design further, assessing the risk of contact due to the variation in the induced pressure as the geometry of the annuli deforms with thermal growth from viscous heating. The surface geometries such as those shown in Figure 2.17 would only have a depth of the order of 100 μm and hence any wear could remove these features and the air riding ability of the seal entirely. The leakage characteristics of hydrodynamic face seals were compared to that of labyrinth and brush seals by Munson (1993) and it was reported that projected leakage mass flow rates for hydrodynamic seals were as low as 4 % of those of labyrinth seals and merely 10 % of those of brush seals at high differential pressures. A reason for the vast improvement in leakage performance over the labyrinth and brush seal is the ability to control the clearance between the rotor and stator surfaces, allowing the seal to maintain a gap height close to an optimum throughout an engine cycle.

A considerable quantity of research has been conducted by Zheng (2005), both experimentally and computationally, into the film riding face seal which achieved its air riding ability with

the use of spiral grooves. An endurance demonstration was performed lasting for over 51,000 hours and the seal showed very little signs of wear. The research reports a successful deployment of the seal in a field evaluation. A computational parametric study was also performed which attempted to optimise the geometry of the spiral grooves to maximise the magnitude of the induced pressure field. The parameters of interest were the number of grooves, the land to groove circumferential width ratio, the groove depth, the groove angle and the rotational speed of the rotor. The study showed that increasing the number of grooves from 20 to 70, having a groove depth of 10.2 μm (investigated between 2.54 μm and 19.05 μm), setting the groove angle at 10° (investigated between 6° and 30°) and having a land to groove ratio of 1 (investigated between 0.25 and 2) were the optimum values for the individual parameters. Similar computational work was performed on a spiral groove film-riding face seal by Zhou et al. (2007) where a thermal model was used to assess the viscous heating from the thin film and the associated thermal expansion of the spiral groove geometry and its effect on the pressure field generated. The relative surface speed increases with radius and hence does the viscous heating leading to distortion such that the gap between the two faces also increases with radius, leading to a drop in the load bearing capacity and an increase in leakage. Suggested methods to combat this were increasing the groove height towards the outer radius and designing the gap between the two parts in the cold build state to vary with radius opposing the inevitable thermal expansion.

From the literature available on this type of seal, preventing wear entirely would be a challenging task, especially when contact seems inevitable under start-up and shutdown conditions unless a hydrostatic pressure generation is employed by pumping the working fluid between the rotor and stator through small orifices. Although negligible wear was observed from the endurance demonstrations performed by Zheng (2005), the seal was subjected to few start-up conditions. A considerable amount of further research into the thermal deformation

due to the viscous heating is required to obtain a durable design with predictable behaviour, though it has been shown that although radial movement and growth would be easily accommodated, the 10 mm axial displacement may be beyond its capability.

2.4.3 Compliant Foil Seal

The compliant foil seal in the configuration displayed below in Figure 2.8 (circumferential interface as oppose to a face seal or thrust bearing) is essentially a journal bearing but with a flexible stator surface; a smooth top foil which is supported by an elastic foundation, the bump foil, which both deform to accommodate distortions and misalignments. Hence the tolerances required become less strict between the rotor and stator axes. This flexibility also provides resistance to loss in hydrodynamic pressure generation due to foreign particle ingestion within the film. The ability of the foils to deflect also allows for larger excursions of the rotor before the fluid film is ruptured, which may be favourable for larger diameter engine shafts. Flexibility in the foils also allows for vibration energy to be dissipated reducing the possibility of dynamic instabilities occurring. The hydrodynamic pressure field created between the shaft and the top foil due to the relative surface motion and the convergent-divergent gap between the two surfaces creates a resultant force to increase the minimum gap height. A throat for the circumferential flow occurs when the top foil and shaft axes are misaligned and the associated change in clearance with circumferential position leads to the generation of hydrodynamic lift.

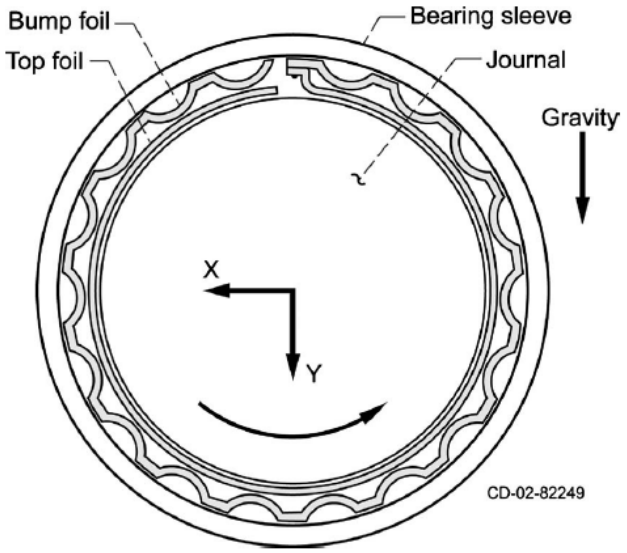


Figure 2.8: Compliant foil seal schematic (Howard and Andres 2011)

Salehi et al. (2001) performed an analytical and experimental study attempting to further understand the thermal characteristics of air lubricated compliant foil bearings. The analytical model employed a Couette approximation to the energy equation in conjunction with the compressible Reynolds equation to generate a theoretical temperature distribution in the lubricant (air). The experimental program was carried out on a 100 mm diameter foil bearing rotating at speeds up to 30,000 rpm and cooling air was pumped across the bearing. The temperature rise of this coolant gave a strong indication of the amount of heat energy that was being conducted through the top foil from the lubrication film. Tests were run at various mass flow rates of coolant, shaft rotational speed and bearing load and all showed that significant heat was generated purely from viscous heating within the fluid film. A peak temperature increase of 81° from ambient conditions was seen experimentally with a bearing load of 934 N, a shaft speed of 20,000 rpm and a coolant mass flow rate of $0.0133 kgs^{-1}$. This strongly suggests that thermal dissipation considerations are of great importance when designing a compliant foil bearing, or other air-riding sealing technologies, into an engine.

Saheli et al. (2002) also investigated the behaviour of the seal under dynamic conditions i.e. rotor eccentricities. A 144 mm diameter seal was tested up to surface speeds of 121 ms^{-1} and

to pressures of 3.5 bar, showing consistent leakage characteristics. The leakage was reported as a flow factor, the mathematical expression of which was not presented, and gives a value of 0.0135 at 0 rpm and 0.012 at 14,000 rpm, showing a slight reduction in mass flow rate due to the moving rotor. Rotor lift off was observed at rotor speeds above 1000 rpm and rotor eccentricities of 0.15 mm were accommodated. This would suggest that rotor-stator contact would occur at low rotational speeds and could lead to wear. This seal would also need the ability to accommodate higher radial excursions and relative growth than has been demonstrated here in order to be considered a viable option.

Although contact may be non-existent during operation between the rotor surface and the top foil inner surface, dealing with rotor excursions leads to rubbing at the contact points between the bump foil and the top foil outer surface. Le Lez et al. (2007) modelled the influence of the inter-foil friction coefficient and showed that the mechanical stiffness varies significantly with friction coefficient. Repeatedly accommodating large rotor excursions may lead to wear on the top foil outer surface such that the bumps would lie in grooves. This would reduce the ability of the two foil layers to deform. Endurance testing with multiple rotor excursions would need to be performed to gain a greater understanding of the inter-foil mechanical behaviour.

Investigations into the static and dynamic force characteristics under large loads were performed by Kim et al. (2008). Static loads of up to 200 N were applied in experimental tests and replicated in an analytical model, which used Reynolds equation for an isothermal, isoviscous ideal gas. The results showed that both sets of data were in excellent agreement when predicting the minimum thickness of the fluid film and shaft attitude angle. At the highest test load, the rotor eccentricities exceed, by approximately three times, the nominal clearance of the rotor and foil, though the presence of the bump strip allows for such

excursions and the top foil and bump strip deform accordingly. Under heavy load conditions where the gas film thickness was greatly reduced, a ‘hardening’ effect was observed in the fluid film stiffness.

The resistive torque from start-up contact and dynamic coefficients are of significant importance in such a seal and these parameters were investigated experimentally by Laurent et al. (2011) using a foil seal with a 38.1 mm diameter rotor driven up to 40 krpm. Test conditions consisted of static loads of between 10 N and 50 N and rotational frequencies ranging from 260 Hz to 590 Hz. Excitation frequencies to assess the damping coefficient etc. were between 100 Hz and 600 Hz which were applied by two shakers mounted orthogonally to one another. The natural frequencies, damping factors and stiffness were calculated from the complex impedances measured. Lift off speeds varied between approximately 3000 rpm to 5000 rpm depending on the static load applied. At this shaft diameter, these rotational speeds translate to between 6 ms^{-1} and 10 ms^{-1} which is relatively low in hydrodynamic applications. Start up frictional torque was reported as being between 0.07 Nm and 0.3 Nm showing that wear would potentially be an issue under this condition.

Howard et al. (2011) used computational modelling software for foil bearings developed by Kim et al. (2005), Kim et al. (2006) and San Andres et al. (2007) to compare to the experimental data they obtained on a 50.8 mm diameter shaft with eccentricities of 60 μm tested. Load versus rotor eccentricity relationships from the experimental and computational modelling were in good agreement, showing that the hydrodynamic pressure fields generated, coupled with the mechanical model of the foil and bump foil, can be predicted with reasonable accuracy. Again, larger radial accommodation would be necessary, though large axial movements would be easily dealt with.

2.4.4 Compliant Foil Thrust Seals

A compliant foil thrust seal comprises of multiple pads, which are sectors of an annulus, supported by bump foil which possesses compliant mechanical properties; a compliant version of a face seal with tapered sectors as the hydrodynamic lift-inducing geometry. A permanent force is applied to move the rotor and stator faces together, as in a film-riding face seal, and under operating conditions when the rotor is in motion, the sector pads generate hydrodynamic pressure fields between the rotor and compliant pads which act to separate the two components.

Some work has been done to understand the characteristics of thrust foil and seals, for example by Heshmat et al. (2000) where finite difference and finite element methods were combined to model the fluid film and the foil and bump strip deformation by solving the two dimensional, compressible Reynolds equation. Only one 45 degree sector pad was modelled to reduce the solution domain and the time required to solve each set of boundary conditions. A predicted pressure profile for the sector pad, displayed in Figure 2.9 (*a*), showed the induced pressure above ambient conditions to be zero at the pad boundary and increase up to a maximum of 2.06 bar (30 psi) at a rotational speed of 50 krpm, which would give a considerable separating force between the rotor and stator and hence a high potential load bearing ability. At the inner and outer diameters of the pad surface, the induced pressure rises quickly with position from the boundaries, though this gradient is steeper in the angular direction. The film thickness profile, Figure 2.9 (*b*), is shown to reach a maximum within 12° from the leading edge and subsequently reduce with the converging gap height and very little radial variation is observed.

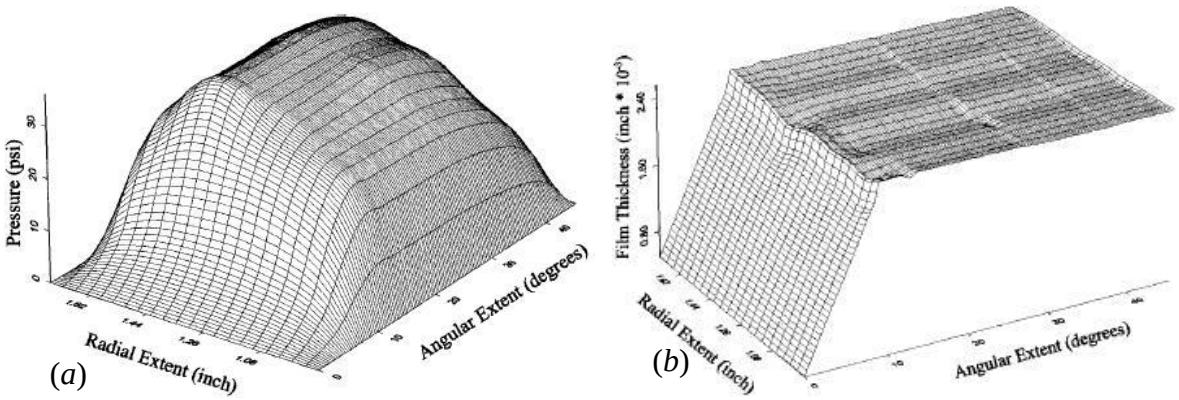


Figure 2.9: Hydrodynamic pressure profile generated beneath foil pad (*a*) and film thickness profile (*b*) (Heshmat, Heshmat and Xu 2000)

The finite element analysis assessed the deformation of the flexible pads due to the induced pressure loading and the predicted a load bearing capacity that was consistent with pre-existing experimental data. Experimental results indicate that seals of this type have been able to endure temperatures of 650°C and surface velocities of 620ms^{-1} and hence they may have potential moderate temperature applications shown by Heshmat et al. (1984) and Munson et al. (2002).

Jahanmir et al. (2009) performed an experimental investigation into wear-resistant materials to coat the pad surfaces to reduce the wear during start-up and shutdown conditions when contact occurs under high temperatures. An example of a test cycle and how the coefficient of friction varies is shown in Figure 2.10. The maximum coefficient occurs at shutdown, as oppose to start-up. This is due to the rotational kinetic energy of the rotor being dissipated by the dry rubbing of the rotor on the pad surfaces. A single sector pad with an inner diameter 23.5 mm, outer diameter 48.5 mm and angle 45° was tested at peak temperatures of 500°C and rotational speeds of just over 10 krpm. Three pad coating materials were subjected to these tests; Chrome, Diamondlike Carbon (DLC) and Hydrogenated-DLC. The average coefficient of friction for all three materials at full speed was approximately 0.002 at room temperature conditions, but an increase in viscosity at higher temperatures leads to higher

values. At start-up and shutdown when contact is made, however, the coefficient of friction values drop by around 30% with an increase in temperature. Interestingly, the H-DLC coating did not provide much hydrodynamic lift at high temperatures, which was reflected in average C_f at maximum speed increasing from 0.003 to 0.012.

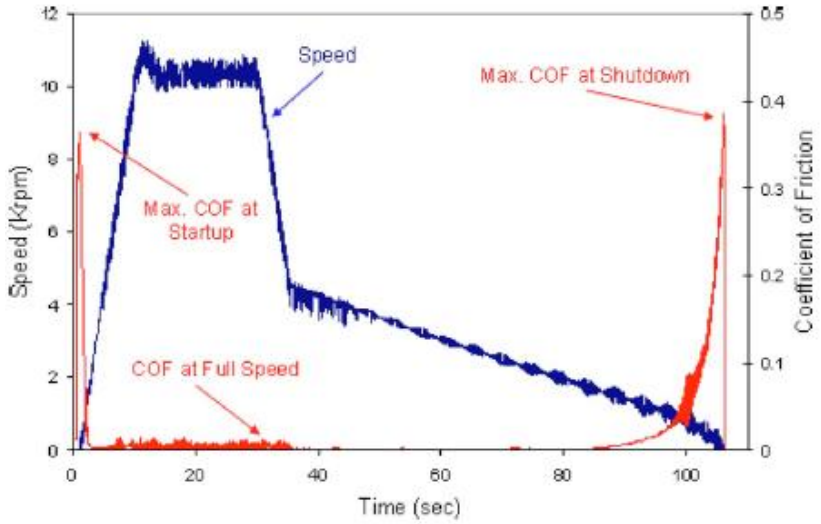


Figure 2.10: Variation in rotational speed and coefficient of friction over a test cycle (Jahanmir, Heshmat and Heshmat 2009)

Recent work by Lee et al. (2011) attempts to model a 6 pad, 55 mm inner diameter and 110 mm outer diameter, hybrid foil thrust seal which incorporates hydrostatic and hydrodynamic bearing technology to eliminate start-up and shutdown wear. Small orifices were placed on each pad allowing the working fluid to be pumped between the rotor and stator surfaces. Four orifice positions were tested at 11°, 33°, 38.5° and 44° from the leading edge. The pressure distribution on the sector pads is shown in Figure 2.11 and the location of the orifices can be seen clearly in the form of the peaks over small areas. It was observed that the hybrid seal has a higher minimum film thickness at zero rotational speed over a purely hydrodynamic seal at low rotational speed and hence would drastically reduce wear under low speed conditions. Experimental data to confirm this would be encouraging to prove that this type of seal can potentially be used to great effect in gas turbines.

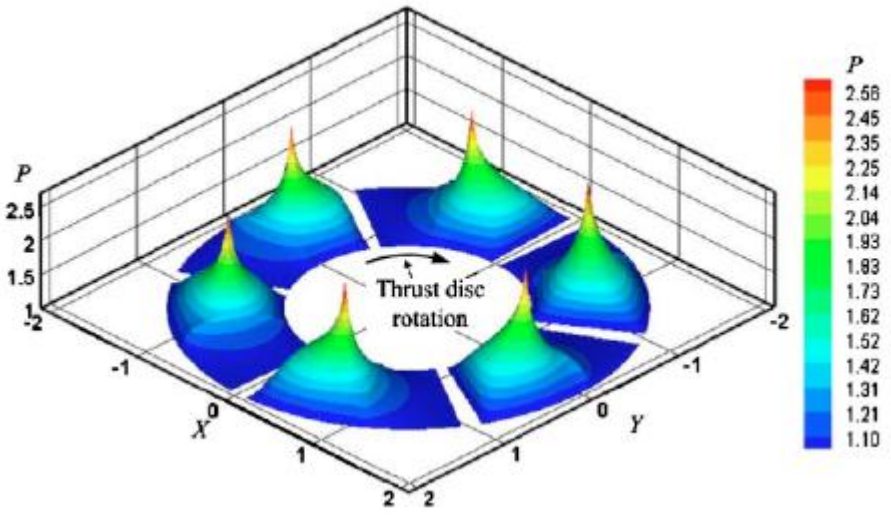


Figure 2.11: Hydrostatic and hydrodynamic induced pad pressure profile with orifice location at 33° from the leading edge, supply pressure at 4 times ambient pressure rotational speed at 40 krpm (Lee and Kim 2011)

2.4.5 Finger Seal

The finger seal, patented by Johnson et al. (1992), is shown in Figure 2.12. It comprises of a stack of sheet-like washers (finger elements) riveted together near the seal outer diameter as shown in Figure 2.12. The outer elements of the stack, called the forward and aft coverplates, are annular rings and a spacer is inserted between each of them and the stack. The finger elements are an annular ring with a series of cuts from the inner diameter to create slender curved beams or fingers with an elongated contact pad at the tip. The individual finger elements are rotated alternately such that the gaps between fingers are covered by the fingers of the next element immediately downstream, leading to a better seal. The gaps between the fingers give the seal its compliant property, acting as cantilever beams flexing away from the rotor during centrifugal or thermal growth.

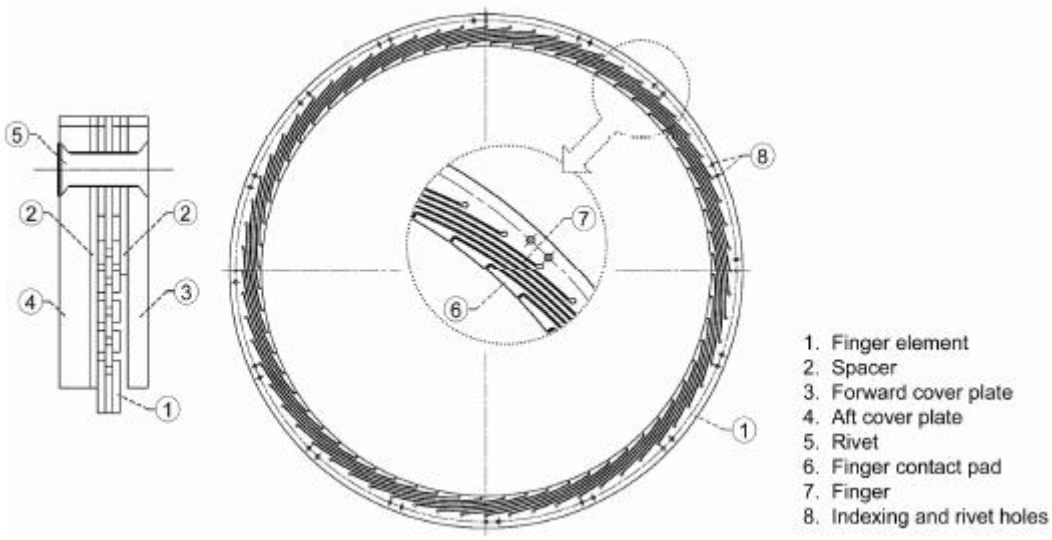


Figure 2.12: Finger seal and detailed components (Chupp, Hendricks, et al. 2006)

Pressure balancing can be applied to the finger seal in order to significantly reduce hysteresis due to the frictional forces between the finger elements and the backing ring, as done in brush and leaf seals, which was demonstrated by Arora et al. (1999). The seal was subjected to the following conditions; 4 to 6 bar pressure drop, up to 540 °C and surface speeds of between 250 and 325 ms^{-1}. Although consistent leakage flow was observed in all the endurance tests conducted (360 cycles, 35,000 rpm, 5.5 bar, 120 seconds each), the wear on the finger pads, determined as the change in the seal inner diameter, was a considerable 2.71 mm. Finger seals are also susceptible to the blow-down effect which leads to tip contact pressures that are higher than the interference fit and rotor growth may cause. The improvement in leakage flow is quoted as being 20% - 70% of that of a labyrinth seal under identical conditions. Although the leakage improvements are favourable, the wear rate for a standard finger seal is unacceptably high.

To reduce the contact loading, the geometry of the basic finger seal concept can be altered and was done so by Braun et al. (2003) and Proctor et al. (2004) where a self-acting lift pad is combined to the tips of the downstream finger element (Figure 2.13). The clearance between

the lift pads and the rotor outer diameter is set to be very small so as to ensure hydrodynamic lift is generated during shaft rotation. To improve the lift properties further, the designer can employ changes in surface geometry, such as the ones shown later in Figure 2.17, to either the underside of the pad or the rotor surface. These pads have only been designed into the downstream finger element and hence the remaining elements will make contact with the rotor and thus wear of the finger tips will still not be eliminated.

A computational study was performed on a finger seal design employing these pads on the tips of one finger element (downstream) of a twin element configuration (Li and Braun 2007). The seal was pressure balanced by having a cavity behind the majority of the radial span of the seal to reduce the hysteresis caused by friction from interacting with the backing plate. This study modelled the pads at predetermined, fixed positions and shaft vibrations were unaccounted for. The forces on the pad were obtained from steady state fluid flow (fixed geometry) instead of direct coupling of the fluid simulation and stress analysis in the finger (which has been attempted by Braun). It was reported that the leakage through the whole seal assembly has two components; the flow between the finger pad and the shaft and the flow through the finger elements, which, as expected, increase with axial pressure difference and the gap height between the pads and the rotor. Assessing the lift force, it was shown that the lift on the finger pads is a result of the hydrodynamic pressure generation and the axial pressure difference. It was found that the hydrodynamic effects reduce rapidly as the gap height increased whilst the axial force increased. When designing a non-contacting, compliant seal, the response to highly transient rotor excursions and growth is essential in maintaining consistently desirable leakage performance and hence, in the case of the finger seal, the hydrodynamic component must dominate the pad lift.

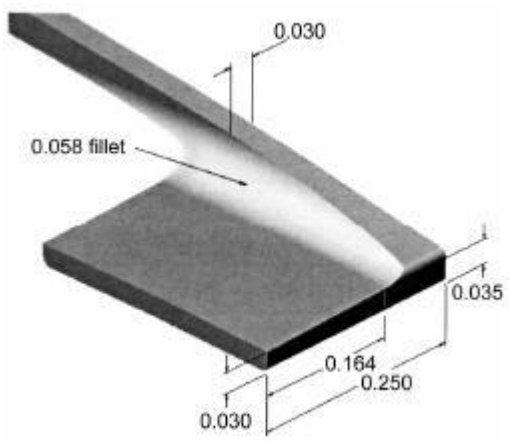


Figure 2.13: Downstream finger element pad from a non-contacting finger seal (Chupp, Hendricks, et al. 2006)

A comparative study was performed by Proctor et al. (2004) assessing the leakage and power loss characteristics of labyrinth, brush and standard finger seals without the pads described above. The generation and dissipation of heat is an important consideration in seal design as it is a result of power loss from the rotor. The thermal growth associated can have a negative impact on the seal performance and heating of the coolant flow reduces the ability to cool components further downstream which can significantly impact on the life span of those parts. Four test procedures were conducted to compare the three seal types starting with static tests, which were performed on all three seal types. The inlet feed was set up to a maximum 517 kPa and, under various temperatures, the leakage was recorded. Performance tests were then run on the brush and finger seals where the rotor was run at a selection of speeds, inlet pressures and temperatures whilst measuring the leakage. Endurance tests were carried on the brush and finger seals with data measured over time at a maximum temperature of 922 K, a peak pressure of 517 kPa and a maximum surface speed of 366 ms^{-1}. Finally, post-endurance performance tests were conducted on the brush and finger seals to assess the degradation as a result of the extended test runs. The leakage mass flow rate of the seal was assessed with the effective clearance parameter (Equation **(**1.2)).

Under static conditions it was shown that a brush seal with a 96.5 µm radial interference has a flow factor of 24 % less than a 4–fin labyrinth seal with a 229 µm radial clearance and only uses 38% of the axial length that is required for the labyrinth seal. The finger seal, however, exhibits under certain conditions a minimum flow factor of only 14 % of that of the brush seal, though on average the flow factor of the finger seal was 60 – 70 % of the brush seal, which is still a considerable reduction. Under the harshest conditions in the performance tests the finger seal only marginally reduced leakage mass flow rate over the brush seal. Overall the finger seals had a lower flow factor during the endurance tests than the brush seal. Initially, for the first two hours the difference in the flow factor was small but in the third and fourth hours, the finger seal flow factor was 36% less. The power losses for the finger and brush seal were very similar in magnitude at 9.72 and 10.48 kW suggesting that the interference fit and the blow down on the finger seal was comparable to that on the brush seal with that particular coverplate arrangement, though in terms of tip wear (measured as the change in inner diameter of the seal) the finger seal wore 21 times more than the brush seal. This level of wear would be unacceptable for a seal in service and would need to be addressed. Despite extensive research into the finger seal concept, this particular sealing method would not satisfy the criteria outlined in section 2.2.

2.4.6 Cantilevered Floating Ring Seal (CFRS)

Details of the CFRS, a seal concept patented by Morgan (2004), are shown below in Figure 2.14. This seal was intended to be used in regions within a gas turbine which are considered to be a harsh environment (high surface speeds, differential pressures and relative radial movement). A possible location for such a seal would be between an annulus of stator vanes (14) and a turbine rotor drum (52) as displayed on the right of Figure 2.14. The components within a CFRS include a seal pad (58), a cantilever (56), a seal housing (48), a piston ring seal (72) and a secondary seal (76). The cantilever connects the seal pad the seal housing, which is

rigidly attached to the stator. This then means the seal pad has a fixed axial location, despite the pressure difference across it, and is able to move radially within the limits imposed by the piston ring seal. The cantilever root is positioned such that the force exerted on the seal pad is towards the engine axis as, under operating conditions, forces from hydrostatic and hydrodynamic pressure will lift the seal pad off the rotor surface. Hydrostatic pressure can be generated by the release of fluid between the sealing pad inner surface and the rotor and the hydrodynamic pressure fields would be created from geometry, such as those shown in Figure 2.17, on the inner surface of the seal pad facing circumferentially. The secondary seal reduces leakage whilst giving the seal the ability to accommodate rotor growth/excursions. Axial excursions are easily dealt with by this seal. The main concern with this seal is the possibility of contact between the seal pad and the rotor during start up and shut down as the cantilever forces remain but the hydrostatic and hydrodynamic forces are small.

Research into the CFRS has been performed at the University of Oxford, which exploits the work carried out on the air-riding phenomenon firstly investigated by Wood (1998), which was continued by Lepetit (2001). Wood (1998) observed an air-riding property at the tip of large scale brush seal bristles but it was not understood well enough to incorporate into brush seal design. The research by Lepetit (2001) focussed on investigating the air-riding ability observed by Wood (1998). A series of experimental models of up to 40 times engine scale was designed using representative dimensionless groups to match those of a real seal under real conditions; a single bristle, small bristle packs and large bristle packs. These were tested together with different rotor surface geometries such as steps and chevron grooves (Figure 2.17). The seal-faceplate gaps ranged from 15 μm to 200 μm and surface speeds ranged from 1.4 ms^{-1} to 6.9 ms^{-1}, equivalent to clearances within an engine of approximately 1 μm to 2 μm and speeds from 63 ms^{-1} to 258 ms^{-1}. Lepetit (2001) reported that the flow field under the bristle tips comprises two components; the axial flow from the pressure drop across the seal

and the entrained flow in the circumferential direction from the moving rotor surface. He concluded that the interaction of these two flows, the result of changing pressure distribution within the gap between the pack and the influence of the porous nature of the underside of the bristle pack were all key to understanding the flow field at the bristle tip – rotor interface and, subsequently, the mechanisms that govern the air-riding phenomenon.

A detailed study was performed by Vasco (2009) into developing the CFRS itself. Many fundamental tests were conducted to investigate the pressure that can be generated between two surfaces in close proximity whilst in relative motion. Low speed, large scale tests with heavily instrumented pads were performed on many different pad orientations to assess the effect on the pressure generated. Reynolds 1D (see section A.1) and 2D models were created and compared to the experimental results with the 1D model results not matching well, primarily due to the inability to model side leakage from the pads. The 2D models performed significantly better. A 3D computational fluid dynamics model was also created which matched the experimental results closest. In depth analysis of the gap pressure profiles lead to development of the necessary components to ensure that the seal pad would air-ride under operating conditions. A 90° sector of the seal containing 3 pads was manufactured and tested as part of the design process. Rotating tests were unable to be performed and components such as the piston ring seal and secondary seal were not investigated due to time restrictions but a significant step towards optimising this seal has been achieved.

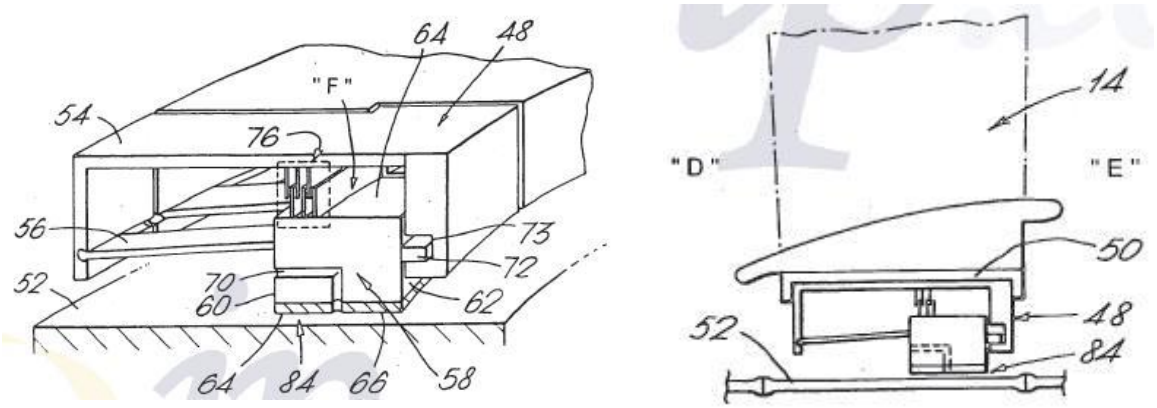


Figure 2.14: Schematics of the cantilevered floating ring seal (Morgan 2004)

2.5 Hydrostatic Lubrication

The application of external pressure can be used to supply a pressurised film between two surfaces which have no relative motion between them in the direction parallel to the surfaces. This results in a pressure above ambient conditions between the two surfaces and leads to a resultant force acting to separate them. Hence, hydrostatic lubrication can help to maintain a clearance during start-up conditions when incorporated into hydrodynamic seal.

2.6 Hydrodynamic Lift

Hydrodynamic pressure generation occurs from the relative motion between two surfaces where there is a change in gap height in the direction of motion. Below is an analysis of a rectangular pad of infinite width in the direction normal to the motion of the sliding component using Reynolds 1D equation by Brewe et al. (1997). This is the incompressible version of the equation but nevertheless shows how a pressure field above ambient conditions is induced. The compressible version is introduced and used in chapter 3. Equation **(**2.1**)** relates the pressure gradient between two surfaces to the film geometry, surface speed and gas viscosity and equation **(**2.2**)** shows that a converging wedge or taper geometry of a fixed angle is sufficient to produce a pressure field between the two moving surfaces above the ambient conditions.

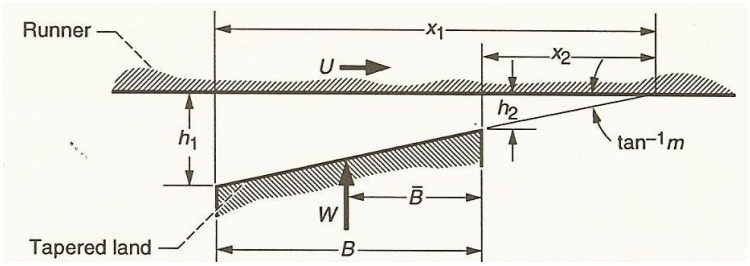


Figure 2.15: Infinite Slider Bearing Configuration (Brewe, et al. 1997)

The incompressible equation to be solved for an inclined pad of infinite length normal to the direction of motion is as follows:

$$\frac{\mathrm{d}}{\mathrm{d}x}\left(h^3\frac{\mathrm{d}p}{\mathrm{d}x}\right) = 6\mu U\frac{\mathrm{d}h}{\mathrm{d}x}, \tag{2.1}$$

which results in the following equation after the boundary conditions are applied and integrating twice:

$$p - p_{atm} = 6\mu UB\frac{(h_1 - h)(h - h_2)}{(h_1^2 - h_2^2)h^2}. \tag{2.2}$$

Due to $h_1 > h > h_2$, the expression above is always positive, which implies that the pressure in the fluid film is always greater than the ambient conditions. Figure 2.16 shows the pressure profiles generated on the wedge slider indicating that the position of the peak pressure translates further downstream from the leading edge as the gap height ratio (h_1/h_2) increases. For a maximum load bearing capacity, the figure suggests a gap height ratio of approximately 3. Many different options can be employed to achieve hydrodynamic lift by the use of converging cross sectional area. Some examples of these are shown below in Figure 2.17. The taper (a), analysed above, and (b), (c) and (d) are displayed as would be designed for relative linear motion, though they can be adapted to rotational motion cases, such as (e) and (f), within sectors of an annulus.

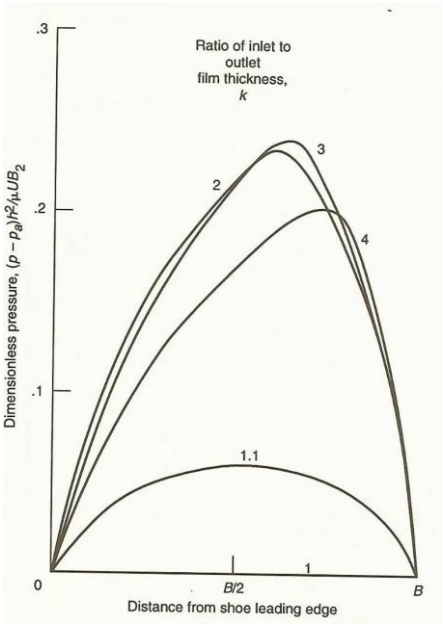


Figure 2.16: Pressure Profile on Bearing Shoe with Varying *k* – (Brewe et al., 1996)

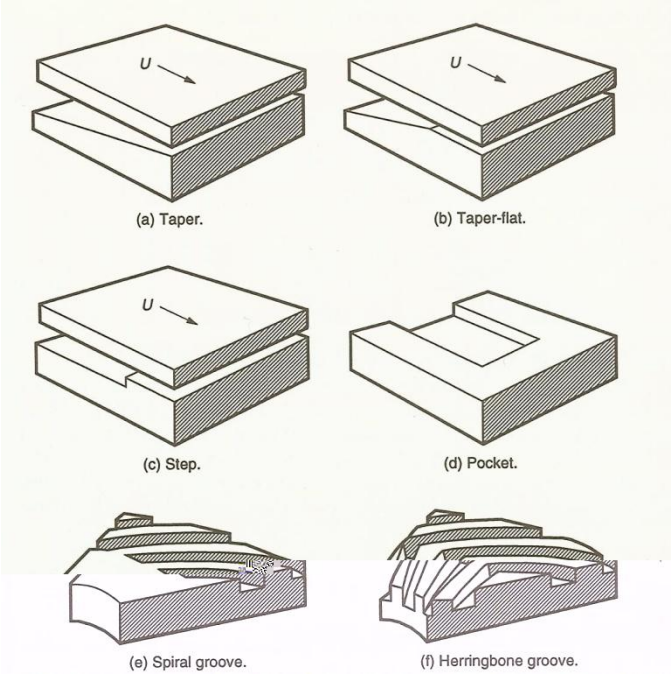


Figure 2.17: Variations in Surface Geometry to Create a Pressurised Fluid Film (Brewe, et al. 1997)

2.6.1 Effect of Surface Roughness

Air-riding seals operate with extremely small clearances of the order of 10μm and hence the effect of imperfections in the surface finish on the overall performance of the seal, due to

manufacturing faults or wear, must be evaluated. Guardino et al. (2004) investigated the effects of surface roughness with analytical and numerical solutions considering both compressible and incompressible flow. Two and three dimensional roughness patterns were applied to a step configuration. The relative surface velocity was set at $100ms^{-1}$. The surface roughness, ψ, was created with a sinusoidal wave with amplitudes ranging from 0.2 to 0.8 times the clearance after the step (minimum clearance). Numerical and analytical results were in good agreement over small values of ψ, though for larger values the results were less similar. A noteworthy result was that the film pressure generated increased with ψ and hence the non-dimensional load bearing capacity parameter as well. Compressible solutions displayed non linear pressure variations in the film while incompressible solutions predicted linear variation. This feature was also seen in the author's mathematical models in chapter 3 and 4.

2.7 Literature Review Summary

It is obvious from the literature that while engine SFC has dramatically reduced due to increasing thermal and aerodynamic efficiency over the last five decades, improvements in sealing technology have remained a low priority and hence labyrinth and brush seals remain the dominant sealing method in current generation gas and steam turbines. Some new sealing methods have reached the stage of being tested on demonstrator engines but almost none are ready to enter regular service at this point in time. With the reduction in SFC fast flattening out over the last few years, more cost effective ways of reducing the losses must be found outside the realms of compressor and turbine aerodynamic regimes. A major outcome of the literature review is that there is a relative dearth of any new design technologies or experimental programs before 2000 but there has been a frenzy of activity in the last 5 years

alone which highlights the sudden prominence with which this area of knowledge, or lack thereof, has emerged into the research spotlight.

In this thesis, a new seal concept first patented by Rolls Royce in 2007 is explored experimentally and developed further. The modifications to the seal design were carried out with an emphasis on elegance rather than complexity, passive clearance control rather than active, and the capability of self-adjusting. Another completely contactless form of sealing is investigated with some particularly exciting results in experiments involving fluidic seals. It is intended, in the light of this literature review, that the work presented in this thesis is put into context. That is, an attempt has been made to eliminate seal contact in a gas or steam turbine, thus eradicating wear, reducing maintenance costs and increasing overall efficiency in a cost-effective fashion.

3 Linear Large Axial Movement Face Seal

3.1 Introduction

A non-contacting concept seal with the ability to accommodate large axial and moderate radial rotor growth, whilst maintaining an optimum rotor-seal clearance, was proposed by John Webster at Rolls Royce plc. A test rig comprising of a linearly extruded, prismatic cross-section of an annular seal (or a sector of a seal of infinite radius) was manufactured by Rolls-Royce. The partial sector therefore required a static 'rotor' component. The purpose of this test rig then was to assess the behaviour of the seal when subjected to purely static pressure distributions induced by its geometry, and to gain a sufficient understanding of the resultant force against axial displacement relationships before incorporating any hydrodynamic effects from the induced flow fields due to a moving rotor. An equilibrium position for the seal housing is desired within the displacement range, with a restoring resultant force if it is perturbed from this position. For brevity, from this point onwards, this test rig shall be referred to as the 'linear LAMFS test rig'.

The baseline geometry within the seal gaps was tested at the Strategic Research Centre, Rolls-Royce at three inlet pressures (J. R. Webster 2001) and the results from these preliminary tests reported the seal housing to be unstable based on the axial resultant force due to static pressure distributions. Despite the undesirable seal housing behaviour, the large axial movement face seal (LAMFS) concept was patented (J. Webster 2007). The test rig was then delivered to the Osney Laboratory of Oxford University where it was re-commissioned and all further testing on this test rig was performed by the author in this research program.

Experimental, analytical and computational modelling was conducted on the linear LAMFS test rig. The unstable seal housing behaviour observed at the three pressures tested by Rolls-Royce on the baseline geometry was replicated and tests on two higher inlet pressures were also performed yielding similar results. The seal gap geometry was then modified to produce the desired behaviour, which is now being patented by Rolls Royce. The cross sectional geometry of this test rig and the results of this work are described in this chapter. The partial sector introduces additional leakage flows and these are also fully assessed. In Chapter 4, details of a test rig with a fully annular version of the seal are described. The linear LAMFS test rig is capable of operation at differential pressures somewhat lower than seen across some seals in a gas turbine application. Larger pressure drops, and especially those present within industrial steam turbines where this seal could also be beneficial, were not within the test rig's capability, however, it will be shown later that key flow physics are captured in a compressible flow regime, which depends on the pressure ratio across the seal.

3.2 LAMFS Concept

A 2D schematic of the LAMFS, labelling the components of which it is comprised, is shown in Figure 3.1. The seal separates a high pressure (HP) zone and a low pressure (LP) zone along a leakage path between a shaft and surrounding casing. A step change in the rotor radius, equivalent to a disc mounted on the shaft, allows the seal housing to be in close proximity to the rotor in two locations, the upstream and downstream faces of the disc, creating two tight clearance seal gaps. The primary path for the leakage mass flow is hence through the upstream seal gap into the cavity within the seal housing where some total pressure will be lost. This is therefore called the intermediate pressure (IP) chamber. The leakage flow then passes through the downstream seal gap to the low pressure region. In order for the LAMFS to accommodate relative axial movement between the shaft and the casing,

the seal housing has freedom to move in the axial direction with respect to the casing. A secondary static seal is therefore necessary to allow axial translation which is achieved by a secondary seal arm mounted to the seal housing. This is met by an existing seal, a brush seal, for example, attached to a radial extension of the casing. This static seal can be of very tight tolerance and can additionally provide damping for the movement of the housing. A very large radial gap can be tolerated between the seal housing intermediate pressure chamber surface and the rotor disc allowing large relative radial growth. Rotation of the seal housing is not required and, in fact, undesirable as relative movement within the seal gaps could allow hydrodynamic pressure distributions to be created. For successful operation, the 'seal gaps' must be small in clearance and the housing must move axially with respect to the disc on the shaft *i.e.* the seal housing and shaft axes must remain parallel.

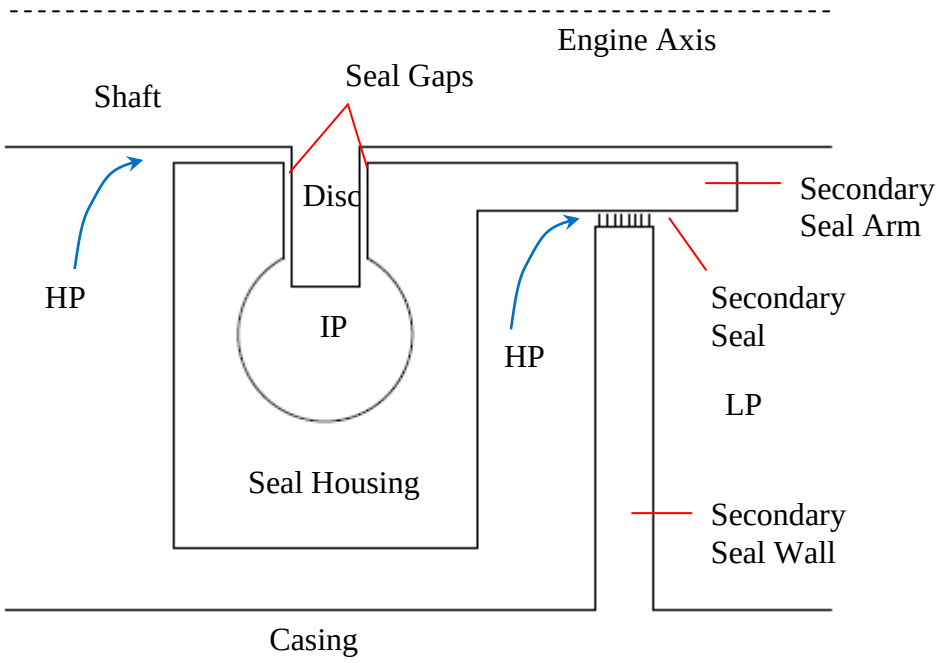


Figure 3.1: Schematic of LAMFS

3.2.1 Principle of Operation

Allowing the seal housing to translate axially requires a method of controlling the position of the seal housing relative to the disc surfaces such that contact is not made between the two components and wear does not occur. An active control system involving electronic systems

would be difficult to install in the desired locations within a gas turbine (*i.e.* between concentric shafts or in high temperature locations). Such a system would be complex and the possibility of failure would result in the axial position of the seal housing being influenced solely by the resultant hydrostatic and hydrodynamic loading. Hence the driving force behind the design of this experimental version of the seal was to create a fully passive system. This feature would ensure the seal housing remains at a set axial displacement relative to the disc purely due to the hydrostatic and hydrodynamic loading. This design is the most elegant solution as it would remain inherently stable.

Variation in Resultant Axial Static Pressure Force on the Seal Housing with Position

The housing of the LAMFS is intended to follow the rotor using the static pressure loading on the internal and external faces of the seal housing. The position of the secondary seal means that the high pressure is maintained over a large portion of the downstream external face of the seal housing. The proportion of that surface subjected to the upstream pressure is determined by the radial position of the secondary seal (Figure 3.2 (*a*)). The remainder of the downstream external face (i.e. the thickness of the secondary seal arm) sees low pressure. As high pressure acts on the entire of the upstream external face of the seal housing, there is a constant resultant force acting downstream from the external faces alone, which is independent of the position of the seal housing with respect to the disc.

As the leakage flow passes through the primary leakage path (seal gaps), the pressure drops through the upstream seal gap into the intermediate pressure chamber and similarly the remaining pressure drop occurs through the downstream gap to the low pressure region. The average pressure on the upstream internal seal housing face is therefore consistently higher than on the downstream internal seal housing face, leading to a resultant force acting upstream. As the seal housing translates axially with respect to the disc, the relative size of the

two seal gaps changes. A seal housing position which yields a relatively small upstream gap, h_u, and large downstream gap, h_d, will result in the majority of the pressure lost through the upstream seal gap and hence the pressure seen in the intermediate pressure chamber is close to the low pressure region and vice versa (Figure 3.2 (*b*)). The difference between the average pressures on the seal faces (internal), assuming non-linear pressure drops and including inlet losses etc., therefore varies with the seal housing position relative to the disc and hence the overall resultant load due to hydrostatic pressure distributions is dependent on the relative size of the seal gaps (seal housing axial position). The experimental program on the linear LAMFS test rig was designed to assess the effect due to variations in geometry within the seal gaps. Subsequent measurements were taken, with particular emphasis on the following criteria:

1. Assessing the ability of the seal housing to be balanced by the static pressure forces acting on it,
2. Determining the position of the equilibrium point,
3. Measuring the size of the restoration loads on the housing, the stability of the behaviour, and the leakage through the seal.

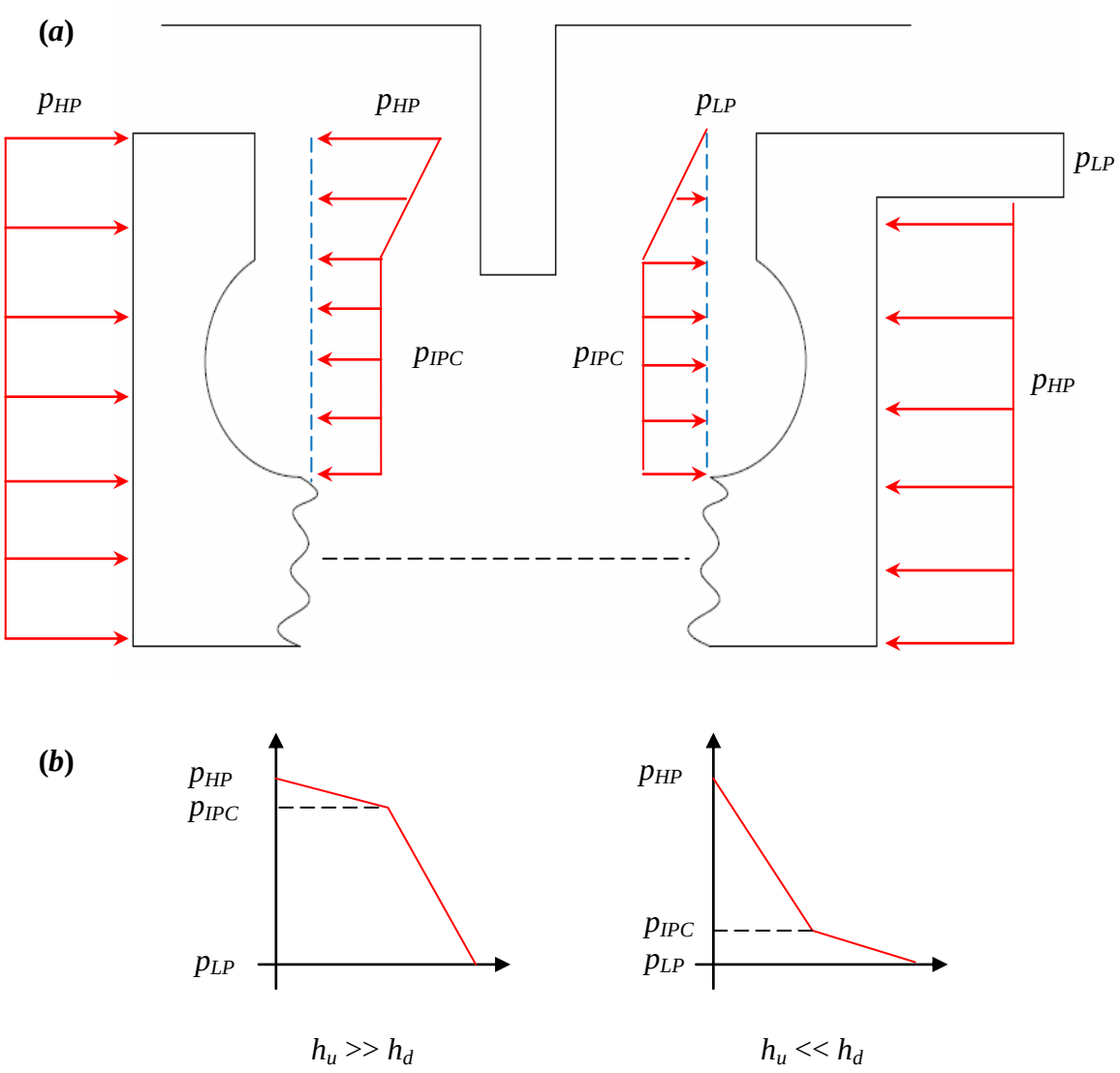


Figure 3.2: (*a*) - Schematic of static pressure distribution on inner and outer seal housing surfaces, (*b*) - Static pressure variation through primary leakage path with seal housing position

Hydrodynamic-induced pressure distributions could also assist in restoring the seal housing to an optimum position relative to the disc in the case of axial excursions of the rotor. These same forces can also be used to increase the resilience of the seal in transient conditions. As described in Chapter 2, the 'cushion' of air between the rotating and static surfaces in a hydrodynamic bearing for example, exhibits 'stiffness' such that as the two surfaces move closer together and the thickness of the film is reduced, the pressure field generated increases and hence the force acting to separate the surfaces increases accordingly (as described for the slider bearing in section 2.6). This effect would be beneficial if incorporated into this particular seal design as the hydrodynamic pressure would increase on the seal face as the

corresponding gap reduces in height and would subsequently decrease in the other gap as the clearance increases. However, it cannot be used as the sole driving mechanism in controlling the seal housing position as it would not be sufficient during the start-up and shut-down processes.

3.3 Experimental Work

3.3.1 The Linear LAMFS Test Rig

In the linear LAMFS rig for simulating 2D flow, all the key features required for this seal are incorporated using the simplest possible geometry. When designing a seal for an aero engine application, the weight penalty due to the components must not overshadow the improvements in leakage reduction. Thus for real engine applications, the seal housing cross sectional area would be reduced significantly. The rig was operated at inlet gauge pressures of up to 3.45 bar, which ensured that compressible flow effects were analysed. This therefore negated the need to run at engine conditions (40 bar total pressure) to assess the behaviour of the seal housing due to the static pressure loading on it. Although larger pressure differences than 3.45 bar may occur in real engine conditions, the pressure ratio, which determines the compressibility of the flow, is unlikely to be as high as 4.45:1 as was tested with this rig. The higher temperatures and pressures will affect the Reynolds number of the flow and this has been analysed in detail in section 3.4.7.1.

Figure 3.3 shows an annotated photograph of the internal view of the test rig. The radial and axial directions are indicated. The location of the engine axis lies arbitrarily above the top edge of the photograph. A linear ball slide supports the seal housing and hence allows axial freedom of movement. Air is supplied to the high pressure region through the upstream outer wall and passes through the seal gaps where it is vented directly to atmosphere as it vacates the downstream seal gap. The secondary seal is created by a clearance of the order 50 μm

between the secondary seal arm and the extension of the casing. To change the constant resultant axial force from the external surfaces of the seal housing, both the secondary seal arm and the casing extension radial positions could be altered. The rotor disc component was a separate replaceable part allowing various geometries to be easily interchanged and tested. Note that for all experimental tests, p_{LP} is atmospheric conditions, p_{atm}, and hence is equal to zero gauge pressure.

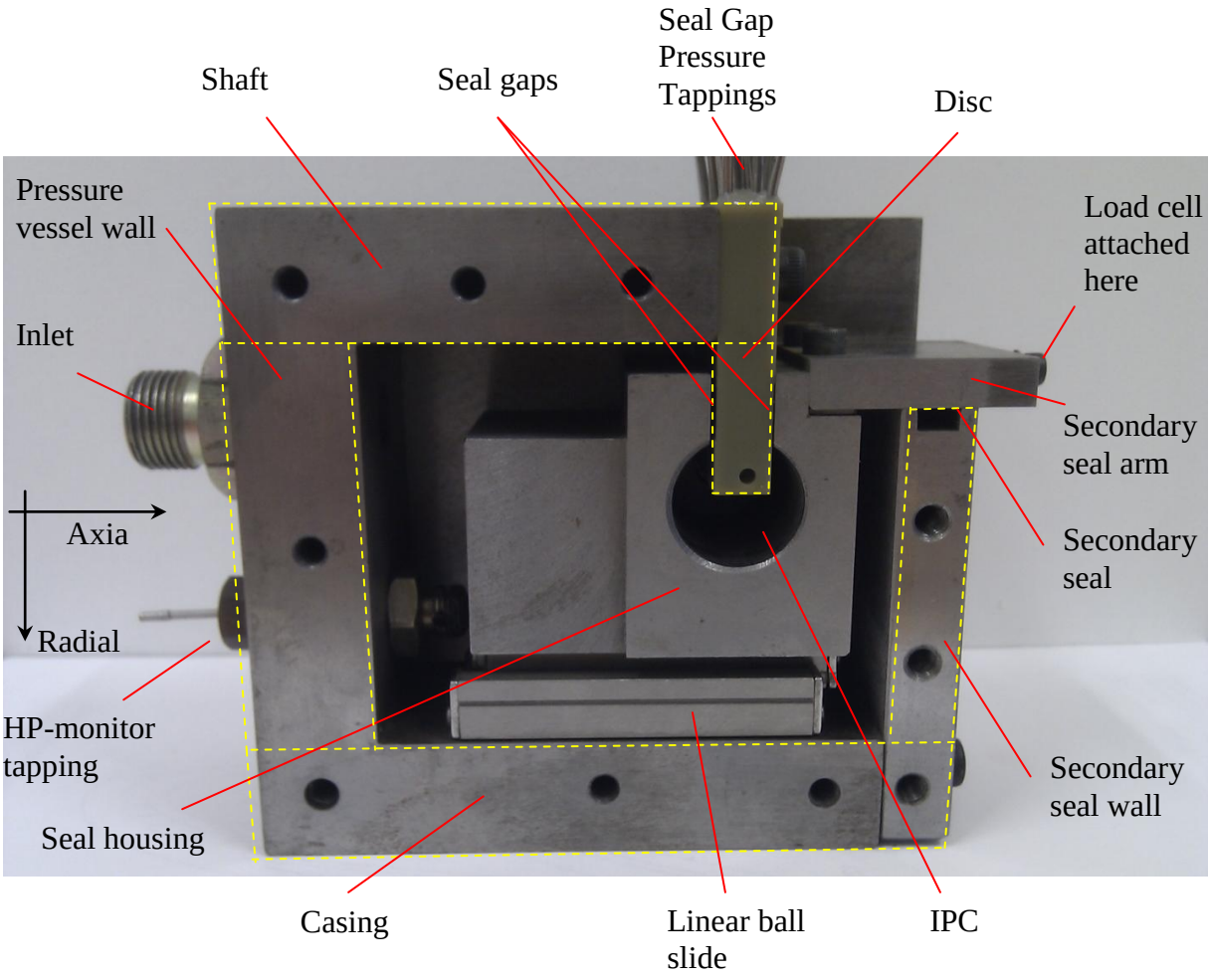


Figure 3.3: Internal view of the linear LAMFS test rig

Limitations of the linear LAMFS Test Rig

Because the seal is a linear segment rather than a full annulus, a gap exists between the endplates of the rig and the moveable seal housing. In order not to impede the axial movement of the housing, a tight tolerance gap of 50 µm is present at each sidewall. A leakage path between the high pressure zone and the intermediate pressure chamber resulted which would not be present in an annular case. This simple solution had a minimal effect on the axial load

on the seal housing, which was the highest priority parameter to be measured. Whilst the height of these gaps between the side plates may on occasion be of the same order as the primary leakage path seal gaps, their effects were characterised in a series of tests.

3.3.1.1 Seal Housing and Rotor Geometry

The dimensions of the seal housing and rotor component are shown below in Figure 3.4 (*a*) and (*b*) respectively. The length of the tight clearance faces and overall housing dimensions represent realistic engine scale, although they are not specific to any current or future model. The width of the seal housing is 41.3 mm. In order to measure the static pressure in the seal gaps, 11 pressure tappings of 1 mm diameter were created on each side of the rotor disc-representative block. The centres of the first and last tappings were aligned with the inlet and exit plane respectively of each seal gap. The tappings were arranged into two rows, one containing 6 tappings, the other containing 5, with the centres spaced equally along the 11 mm seal gap radial length. The only available exit for the tappings from the rotor geometry was through the top face of the plate and hence a network of paths was incorporated within the material. Multiple rotor blocks were manufactured from resin by Gemini Prototyping Ltd using stereolithography. These parts were machined post-manufacture to obtain several different seal gap geometries. In a real engine, the geometry design of rotating components is influenced by stresses induced due to rotation. Sharp corners, for example, are avoided as they result in high stress concentrations. Therefore in a real version of this seal, surface geometry for hydrostatic and hydrodynamic pressure fields would most likely be machined into the seal housing. This, however, has no effect on the seal gap aerodynamics.

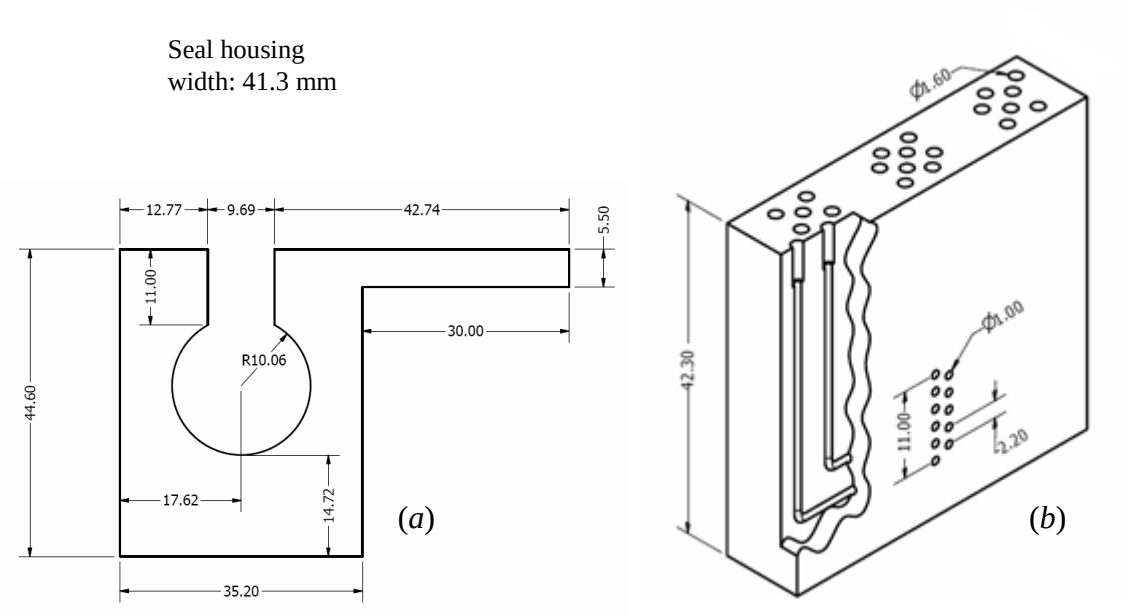


Figure 3.4: (*a*) - Seal housing and (*b*) rotor component dimensions (with partial cutaway section to show internal channels)

3.3.1.2 Seal Gap Static Pressure Tapping Positions

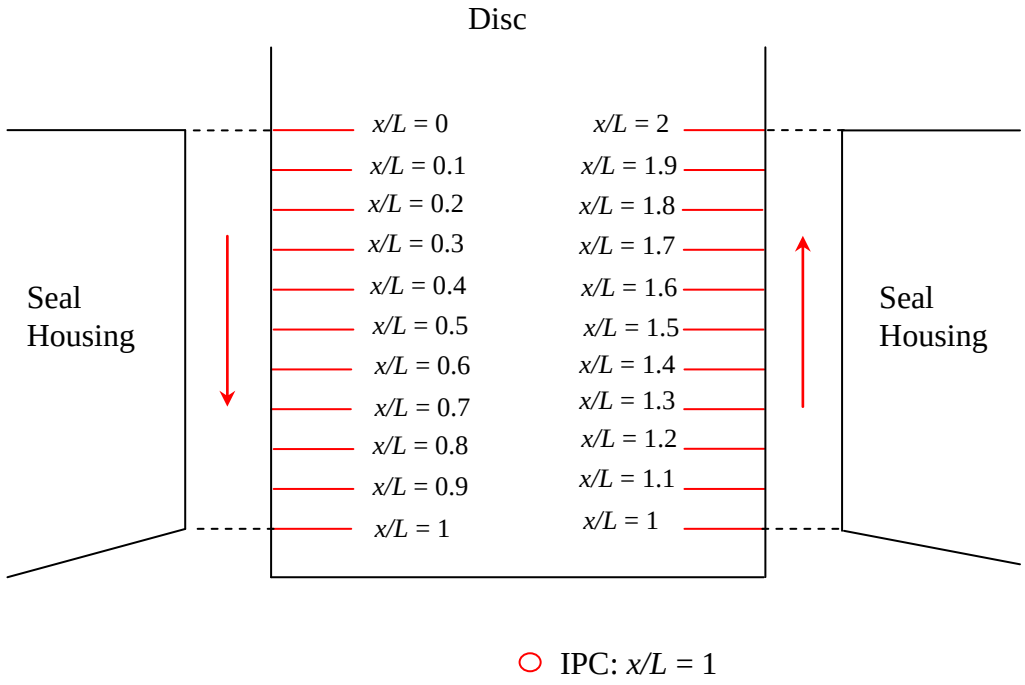


Figure 3.5: Schematic of pressure tapping axis locations in seal gaps (Note: centres of tappings at *x*/*L* = 0, 1 and 2 are in line with inlet and outlet planes

The radial positions of the static pressure tappings in the seal gaps are shown Figure 3.5. These are given as a non-dimensional parameter based on the seal gap radial length, *L*.

Tappings in the upstream seal gap have a value of $0 \leq x/L \leq 1$, the IPC is at $x/L = 1$ and the downstream seal gap tappings have a value of $1 \leq x/L \leq 2$.

3.3.1.3 Secondary Leakage Paths

Table 3.1 below shows the cross sectional area of the primary, secondary seal and side leakage paths. Taking the width of the side leakage paths to be the IPC perimeter, it can be seen that the combined secondary seal and side leakages areas are comparable to the primary leakage path area when in the maximum primary mass flow rate position i.e. the seal gaps are equal in height (seal housing displacement, δ, = 0). At large displacements, when the minimum primary seal gap is small, the combined secondary leakage flow area is much greater than the primary leakage area. This is shown in the leakage data in section 3.5.7.

Leakage Path	Minimum Gap Height (m)	Gap Width (m)	Area (m^2)
Primary (δ = 150 / -150 µm)	50 $x10^{-6}$	0.0413	2.065 $x10^{-6}$
Primary (δ = 0 µm)	200 $x10^{-6}$	0.0413	8.26 $x10^{-6}$
Secondary Seal	50 $x10^{-6}$	0.0413	2.065 $x10^{-6}$
2 x Side Leakage	50 $x10^{-6}$	0.0544	5.44 $x10^{-6}$

Table 3.1: Cross sectional area of all linear LAMFS leakage paths

3.3.1.4 Test Rig Set Up and Air System

Air was supplied to the test rig via a 7 bar (100 psi) laboratory air supply. A regulator was used to set the pressure within the main cavity (HP zone). In order to measure the pressure in this region, a tapping was located on the upstream face of the casing, adjacent to the inlet feed. The secondary seal arm was connected to a geared traverse mechanism via a load cell to allow a manual control of the seal housing's axial position. The resultant load on the seal housing could then be resolved at any housing position. The relative location of the seal housing with respect to the rotor component was monitored using a digital dial gauge in

contact with the secondary seal arm. Figure 3.6 shows a schematic of the components described.

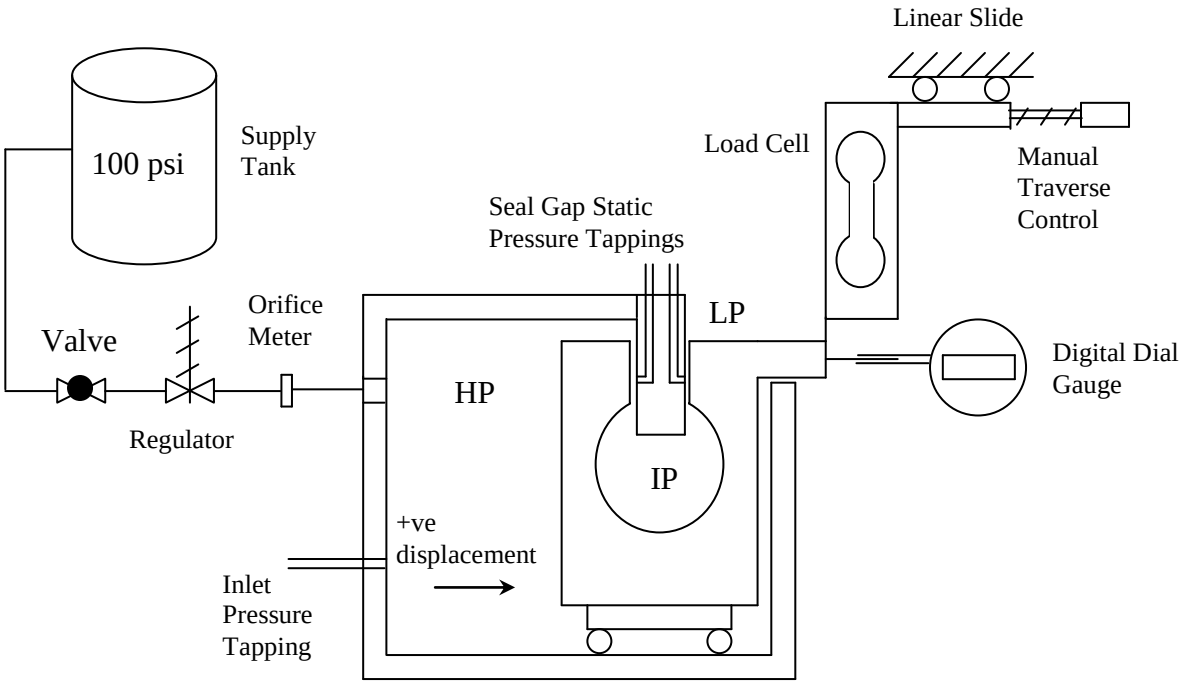


Figure 3.6: Test rig air system schematic

3.3.2 Instrumentation

A *Measurement Computing CIO-DAS802/16* 16 bit resolution data acquisition board was used to record the pressure, displacement and load data. To measure the pressure within the high pressure region, a *Sensor Technics CTE7005GP0* 0-5 bar range was used. The 22 tappings in the seal gaps were connected to a 24 channel *Scanivalve* pressure multiplexer unit allowing all channels to be measured with a single transducer. Depending on the inlet pressure, either a *CTE7005GP0* 0-5 bar range or a *PTE5015D1A* 0-15 psi range transducer was used in conjunction with the scanivalve box. Low range *PTE5000* series differential pressure transducers evaluated the pressure drop across an orifice plate. A selection of *Tedea Huntleigh* single point load cells of capacities 0.6 kg, 1.5 kg, 5 kg and 20 kg ensured an acceptable resolution for the seal housing resultant load which varied significantly with inlet pressure and the surface geometry in the seal gaps. A *Soemer LAC 65.1* load cell analogue

converter provided the excitation and power for the load cells and the signal to be read by the data acquisition card. The position of the seal housing relative to the disc was assessed with a *Mitutoyo Absolute* digital dial gauge. One K-type thermocouple channel was required for the orifice meter and this was read using an *Omega Monogram* multimeter with internal cold junction components. The accuracy of the gauges is shown in Table 3.2.

3.3.2.1 Calibration

A linear calibration of a pressure or load transducer comprises the computation of the gain and offset via linear regression of data obtained over the range of the transducer. While the gain is only likely to drift if the transducer has been over pressurised, the offset is a strong function of the ambient temperature. The offset is liable to fluctuate over time and so it is important to calibrate the offset before running each experiment. Automatic calibration of pressure and load cell offsets, which was programmed into the data acquisition software, was carried out prior to conducting each set of tests to account for this.

All transducers were calibrated *in situ* using the data acquisition system to minimise calibration errors. A *Fluke 718 100G*, calibrated to a national standard, was used to calibrate the pressure transducers. The accuracy of this device is stated at 0.1 mbar, which equates to a 0.4% error on the lowest range transducer used in this thesis (0 - 25 mbar). This uncertainty was incorporated into the individual pressure transducer uncertainties though this was negligible except when dealing with the lowest range transducer. Weights and a pulley system were employed to apply a force to the load cells, which could be reversed in order to calibrate them in the positive and negative axial directions. The resulting load was corrected for pulley friction. The conversion factors for the transducers were repeatable within acceptable margins (< 0.25 %) from the factory or nominal calibrations. Before large test schedules, the transducer calibration process was repeated and very little difference was observed (< 0.1 %).

3.3.2.2 Data Capture and Experimental Procedure

The graphical data acquisition programming language, *LabVIEW* [2007], was used to monitor and record the data from all the transducers on the test rig. 50 samples were taken at a rate of 20 Hz and averaged to give each data point. Separate tests were run depending on whether the seal housing resultant load or the seal gap static pressure distribution were being assessed. Data were acquired at 25 set locations across the full range of the seal housing displacement when measuring the resultant load, and at all these positions the leakage mass flow rate was also measured. The 22 seal gap static pressure readings were taken at 7 different axial positions of the seal housing. These provided a direct comparison to results obtained through CFD analysis. For each test, the process began by setting the regulator to achieve the desired pressure within the high pressure region of the test rig. The seal housing was then moved to the farthest position in the upstream direction providing a datum. The seal housing was then traversed downstream and data recorded at the predetermined locations. Once completed, the data were saved into a single-precision tab-delimited ASCII data file.

3.3.2.3 Uncertainty

An uncertainty analysis was performed in order to assess the level of confidence in the measured data. 95% confidence intervals were estimated for the measured and calculated results using procedures outlined in the following sources: Moffat(1982), Abernathy et al. (1985), Moffat (1988), Rolls-Royce guidelines (2005) and Performance Test Codes (2005). The uncertainty of a measurement can be considered to consist of two components; random and systematic uncertainties, which were treated separately. Overall uncertainties for particular measurements are a combination of both random and systematic uncertainties. For direct measurements coming from transducers, an estimate of the uncertainty could be computed from the transducer uncertainties listed in the respective data sheet and the uncertainty in the data acquisition system. For computed parameters, such as mass flow rate which require multiple measured input variables, the effect of each input's uncertainty on the

overall uncertainty is not so obvious. A jitter program (Moffat 1982) was employed to evaluate the uncertainty of computed parameters by perturbing each input variable from their measured value by their respective random and systematic uncertainty, assessing the combined effect of each input variable's uncertainty on the output. A central difference formulation was used and the contributions from the input uncertainties were combined using the Root-Sum-Square equation (suitable for independent and normally distributed uncertainties). For the coverage factor of 95% and the assumption of a normal distribution, the elemental uncertainty is simply twice the standard deviation: $u_i = 2\sigma$. When estimating the uncertainty of a direct measurement from the transducer's data sheet, a more conservative approach is to presume that a uniform distribution is appropriate. In many cases, it may only be possible to quantify the upper and lower bounds, usual symbol ± a, which contains 100% of the population of samples. If these bounds are the only information and there is no specific knowledge about the possible values within the interval, it is reasonable to assume that the potential uncertainty is equally probable to lie anywhere within the limits. For a coverage factor of 95%, the elemental uncertainty for the assumption of uniform coverage is: $u_i = 2a/\sqrt{3}$ (WP0875.104 2005). This criterion was applied where appropriate. Table 3.2 shows the uncertainties calculated for the transducers used in this test rig.

Measurement	Systematic Uncertainty	Random Uncertainty
Force (600 g)	1.731×10^{-3} N	7.887×10^{-4} N
Force (1500 g)	4.309×10^{-3} N	1.978×10^{-3} N
Force (5 kg)	0.011 N	9.812×10^{-3} N
Force (20 kg)	0.0427 N	0.039 N
Pressure (5 bar)	6800 Pa	925 Pa
Pressure (1.034 bar / 15 psi)	703 Pa / 0.102 psi	680 Pa / 0.0986 psi
Displacement	None quoted	0.0015 mm
Temperature	2.89 K	0.154 K

Table 3.2: Linear LAMFS test rig transducer uncertainties

Computed Parameters

An iterative scheme was employed to compute the mass flow rate, $\dot{m}$, using the pipe internal diameter, D, the orifice diameter, d, the value of the pipe surface roughness, k, the pressure upstream of the plate, p_u, the pressure downstream of the plate, p_d, the orifice temperature, T, and the atmospheric pressure, p_{atm}. The parameters for which only bias uncertainties exist when calculating $\dot{m}$ are D, d, k and p_{atm} as they are constants for a given experiment. The orifice meter was designed to British and European standards (ISO5167-2 2003) which included discharge coefficient and expansibility factor uncertainties. The jitter program was then employed to derive the uncertainty for each data point. The normalised static pressure distribution within the primary leakage path is derived from two pressure measurements: p / p_{HP}. The uncertainty for the static pressure data was therefore also calculated using a jitter program. The maximum mass flow rate uncertainty computed was 3.2% and the maximum normalised pressure uncertainty was 1.2%.

3.3.3 An Example of Typical Measurements

For clarity, an example of experimental data is presented in this section to enable the reader to better understand a discussion of analytical modelling and CFD before disclosure of the full set of experiments. The results of the baseline geometry research are in section 3.4.6 and 3.4.7. The results from the seal gap geometry modification are shown from section 3.5.5 to 3.5.7. A set of typical experimental data, along with uncertainties for derived quantities, is displayed below in Figure 3.7 for a particular case; parallel seal surfaces (geometry shown in Figure 3.8) with h_{tsg} = 400 µm and p_{HP} = 2.06 barg. Figure 3.7 (*a*) contains the leakage mass flow rate data (blue), with error bars calculated using the method described in section 3.3.2.3 and the seal housing resultant force data against seal housing displacement, δ. When δ = 0 µm, $h_u = h_d$. Note that the error bars have not been included on the force data as their magnitude is too small to be seen on the graph. Figure 3.7 (*b*) shows the static pressure

distribution through the primary leakage path. The x axis, x / L, represents the position, where 0-1 represents the upstream seal gap and 1-2 represents the downstream seal gap. The IPC is located at x / L = 1. The pressure is normalised by p_{HP}. Note that lines are added between experimental data points to show general trends and aid visual understanding and do not imply linear trends between points.

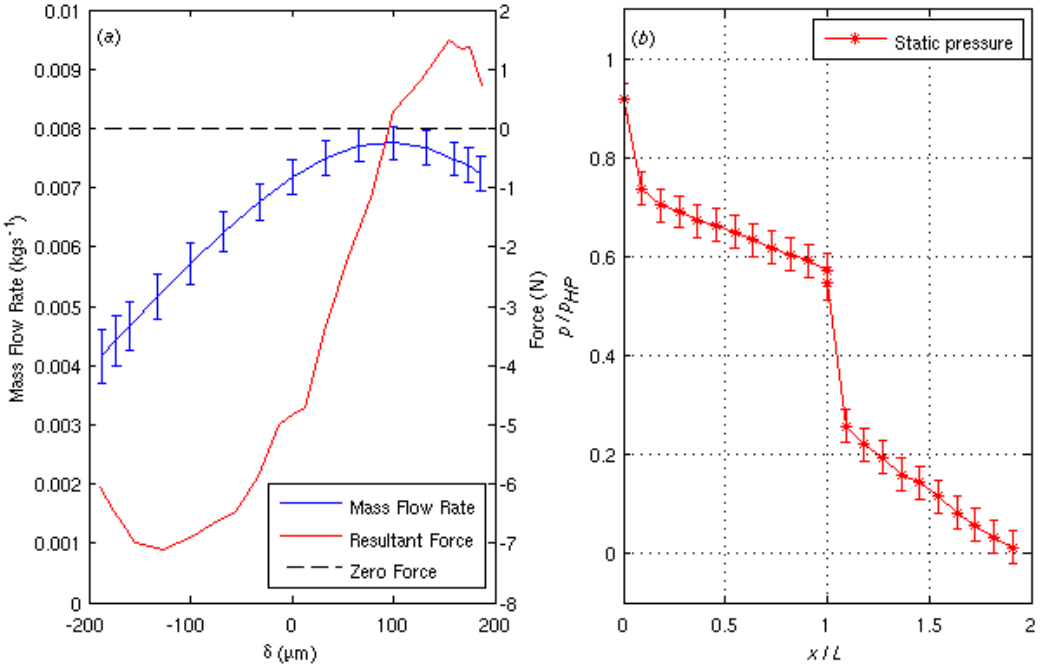


Figure 3.7: Typical data plots for parallel seal gaps (h_{tsg} = 400 µm, h_{step} = 0 µm, α = 0) at p_{HP} = 2.06 barg with error bars: (*a*) – Total leakage mass flow rate and seal housing resultant force vs. displacement, (*b*) – Primary leakage path static pressure distribution

3.4 Parallel Seal Faces – Baseline Geometry

This section contains the experimental and computational results obtained on the linear LAMFS test rig baseline geometry. First, the analytical and CFD models are described in detail. The results of the seal housing resultant force with displacement and the static pressure distribution within the seal gaps are presented for all experimental and computational data sets. For the tests on this geometry, the inlet pressure was set at five different values: 0.69 barg, 1.03 barg, 2.06 barg, 2.76 barg and 3.45 barg (10, 15, 30, 40 and 50 psig respectively).

The lowest three pressures, with this seal gap geometry, replicated preliminary tests performed by Rolls Royce plc (J. R. Webster 2001).

3.4.1 Geometry

The first seal gap geometry that was tested experimentally was the simplest case of parallel surfaces and hence this was replicated with the analytical model. Figure 3.8 shows the geometry and variables associated. The upstream and downstream seal gap heights are denoted by h_u and h_d respectively. The total seal gap height, h_{tsg}, and hence the range of seal housing displacement, is defined as the sum of the upstream and downstream seal gaps. The inlet, intermediate and outlet pressures are p_{HP}, p_{IPC} and p_{LP} respectively. The seal gap length (radial) is represented by L.

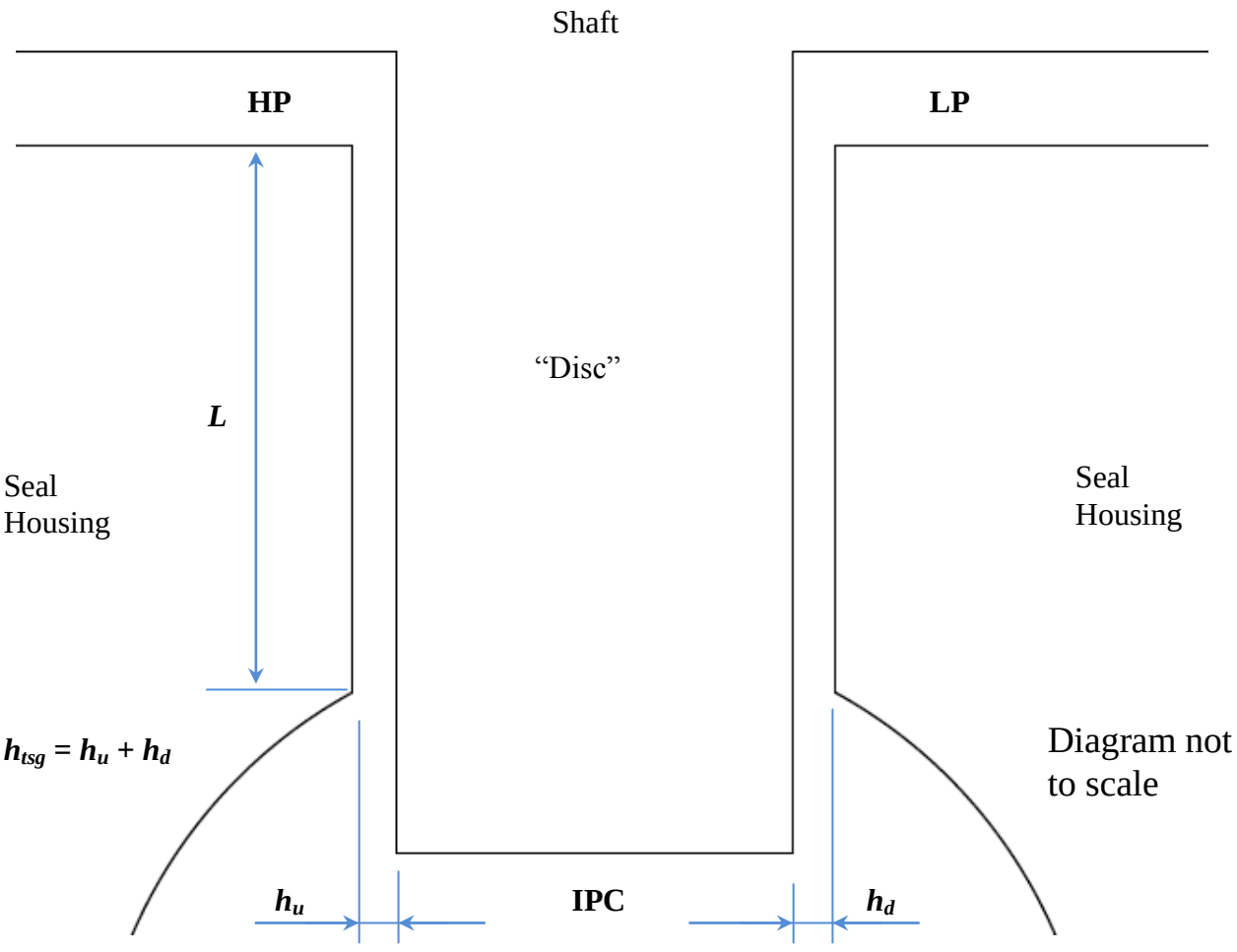


Figure 3.8: Linear LAMFS baseline seal gap geometry: Parallel faces (Note: diagram not to scale)

3.4.2 Analytical model

The flow through the seal gaps in the linear LAMFS can be modelled as one dimensional flow in the radial direction as the circumferential velocity component is zero and the pressure drop within the seal gaps is dominated by viscous loss in the radial flow. The seal gap flow is of primary interest since this determines the aerodynamic force on the seal faces and the overall resultant force on the seal housing. Hence the seal can be modelled as flow through the tight clearance upstream seal gap which passes into a relatively large cavity, the intermediate pressure chamber, where the dynamic head of the flow is dissipated before reaccelerating into the downstream seal gap. Entry effects as the flow enters the seal gaps are also taken into account although these are likely to be geometry dependent. The flow through the seal gaps is a one-dimensional viscous flow and thus may be described by a simplification of Reynold's equation.

3.4.2.1 Reynolds 1D equation

An analytical model for flow through the seal gaps is developed and discussed below. The current analysis is based on previous work on thin film flow in seals (Franceschini 2005). Reynolds equation relates viscosity, film thickness, pressure and volume flow rate. The following assumptions are made: the fluid is Newtonian, $\tau_{yx} = \mu \frac{\partial u}{\partial y}$; inertia forces are small relative to viscous shear forces and are neglected (Reynolds number is very low and as a result the flow is laminar); no slip exists at the fluid-solid interface as the Knusden number is < 0.07; the surfaces are infinitely wide in comparison to the film thickness; the pressure across the film thickness is constant i.e. $\frac{\partial p}{\partial y} \approx 0$. The compressible Reynolds 1D flow equation is shown below in Equation **(**3.1**)**. For the full derivation, see section A.1.

$$\frac{\partial}{\partial x}\left(\frac{h^3}{\mu}\frac{\partial p^2}{\partial x}\right) = 0 \,. \qquad \textbf{(3.1)}$$

This then becomes

$$\frac{\partial p^2}{\partial x} = \mathrm{C}\frac{\mu}{h^3}, \tag{3.2}$$

where C is a constant of integration, and evaluates to

$$p_2^2 - p_1^2 = \left[\frac{\mathrm{C}\mu x}{h^3}\right]_{x_1}^{x_2}, \tag{3.3}$$

giving the governing equation for one dimensional, compressible flow from an upstream pressure, p_1, to a downstream pressure, p_2, through a gap of height, h, and length, x. The units of C are as follows:

$$\mathrm{C} = \frac{p^2 h^3}{\mu x} \equiv \frac{\mathrm{Pa}^2\mathrm{L}^3}{\mathrm{Pa\ s\ L}}, \tag{3.4}$$

where Pa is Pascals, L is a length scale and s is time (seconds). This evaluates to

$$\frac{\mathrm{PaL}^2}{\mathrm{s}} = \mathrm{Pa}\frac{\mathrm{L}}{\mathrm{s}}\mathrm{L} \equiv puL, \tag{3.5}$$

which are pressure, velocity and length terms. Using the ideal gas equation

$$p = \rho \mathrm{R}T, \tag{3.6}$$

the constant C is equivalent to

$$\mathrm{C} = \rho u L \mathrm{R}T = \frac{\rho u A}{L}\mathrm{R}T = \frac{\dot{m}}{L}\mathrm{R}T \tag{3.7}$$

which is the mass flow rate per width (due to the 2D nature of the model) and the specific gas constant and temperature, which is assumed to be constant (isothermal). The constant C is therefore equal for both seal gaps in this seal to satisfy continuity. Applying equation **(**3.3**)** to the parallel wall seal gap geometry (Figure 3.8) then gives the following equations

$$\left(p_{HP} - p_{uin\ spd}\right)^2 - p_{IPC}^2 = \frac{\mathrm{C}\mu L}{h_u^3} \tag{3.8}$$

$$\left(p_{IPC} - p_{din\ spd}\right)^2 - p_{LP}^2 = \frac{\mathrm{C}\mu L}{h_d^3} \tag{3.9}$$

where $p_{uin\ spd}$ and $p_{din\ spd}$ are the static pressure drops at entry to the seal gaps as the flow accelerates and are defined as the dynamic head of the fluid based on the density, ρ, and the velocity, u. The equations for the inlet static pressure drops are

$$p_{uin\,spd} = \frac{1}{2}\rho_{uin}\overline{u_{uin}^2} \tag{3.10}$$

$$p_{din\,spd} = \frac{1}{2}\rho_{din}\overline{u_{din}^2} \tag{3.11}$$

where the subscripts *uin* and *din* correspond to the inlet plane for the upstream and downstream seal gaps respectively. The velocity, *u*, derived in section A.1 is

$$u = \frac{1}{2\mu}\frac{\mathrm{d}p}{\mathrm{d}x}(y^2 - hy)\,, \tag{3.12}$$

as the radial relative surface speed, *U*, is zero in this case. Therefore

$$u^2 = \frac{1}{4\mu^2}\left(\frac{\mathrm{d}p}{\mathrm{d}x}\right)^2 (y^2 - hy)^2 \tag{3.13}$$

and

$$\overline{u^2} = \frac{1}{h}\int_0^h \frac{1}{4\mu^2}\left(\frac{\mathrm{d}p}{\mathrm{d}x}\right)^2 (y^2 - hy)^2\,\mathrm{d}y\,. \tag{3.14}$$

From equation **(**3.3**)** the static pressure at a distance *x* downstream of the inlet to a seal gap is

$$p(x) = \sqrt{{p_{in}}^2 - \frac{\mathrm{C}\mu x}{h^3}}\,. \tag{3.15}$$

Hence

$$\frac{\mathrm{d}p}{\mathrm{d}x} = -\frac{1}{2}\left(\frac{\mathrm{C}^2\mu^2}{h^3(p_{in}^2 h^3 - \mathrm{C}\mu x)}\right)^{\frac{1}{2}} \tag{3.16}$$

The equation for the mean square of the velocity in a seal gap, dependent on the position through the gap, becomes

$$\overline{u^2} = \frac{1}{h}\int_0^h \frac{1}{16\mu^2}\left(\frac{\mathrm{C}^2\mu^2}{h^3(p_{in}^2 h^3 - \mathrm{C}\mu x)}\right)(y^2 - hy)^2\,\mathrm{d}y\,, \tag{3.17}$$

and then

$$\overline{u^2} = \frac{1}{16}\left(\frac{\mathrm{C}^2}{h^4(p_{in}^2 h^3 - \mathrm{C}\mu x)}\right)\int_0^h (y^4 - 2hy^3 - h^2y^2)\,\mathrm{d}y\,. \tag{3.18}$$

This evaluates to

$$\overline{u^2} = \frac{1}{480}\left(\frac{\mathrm{C}^2 h}{p_{in}^2 h^3 - \mathrm{C}\mu x}\right). \tag{3.19}$$

Therefore at the inlet, when $x = 0$, the mean square velocity is

$$\overline{u_{in}^2} = \frac{1}{480}\left(\frac{\mathrm{C}}{p_{in} h}\right)^2. \tag{3.20}$$

The density at the inlet to each seal gap is

$$\rho_{uin} = \frac{\left(p_{HP} - p_{uin\,spd}\right)}{\mathrm{R}T} \tag{3.21}$$

and

$$\rho_{din} = \frac{\left(p_{IPC} - p_{din\,spd}\right)}{\mathrm{R}T} \tag{3.22}$$

respectively. Once the pressure distribution through the seal gaps has been established, the resultant load per unit width on the seal housing can be obtained by

$$F = (p_{HP} - p_{LP})L_{SS} - \int_0^L p_u(x)\,\mathrm{d}x + \int_0^L p_d(x)\,\mathrm{d}x \tag{3.23}$$

where L_{SS} is the radial thickness of the secondary seal arm and the associated term is the offset force created by the presence of the secondary seal. The velocity of the flow between the seal housing inner radius and 'shaft' upstream and downstream of the disc is considered small (area ratio compared with seal gaps) and so momentum terms in the axial direction were neglected when evaluating the resultant force. The leakage mass flow rate per unit width, a fundamental measure of the seal performance, is

$$\dot{m} = \int_0^h \rho u\,\mathrm{d}y \tag{3.24}$$

3.4.3 CFD

Another tool available to the author was the Computational Fluid Dynamics (CFD) software, *Fluent*, and served as another means to analyse the test rig in conjunction with the analytical models. Provided that CFD data can be validated, it enables visualisation of the flow fields

more easily than from experimental data. Two-dimensional and three-dimensional CFD were simulated for the baseline geometry with parallel seal faces (no surface features).

3.4.4 Two dimensional CFD

3.4.4.1 Geometry

Assuming end effects from the side leakages are minimal, approximating the geometry to two dimensions should be representative of the test rig centreline. It should therefore be directly comparable to the analytical model. Seven seal housing positions were modelled in which the overall seal gap height was set to the test rig dimension (h_{tsg} = 400 µm). The seal housing was offset from the central position ($h_u = h_d$) over a range from δ = -150 µm to 150 µm in increments of 50µm including δ = 0 µm. Figure 3.9 shows the domain (white) with the seal housing and rotor solids in grey. The inlet and outlet to the domain are displayed in blue and red respectively whilst the conformal mesh boundaries are displayed in green. A typical mesh is shown in Figure 3.10.

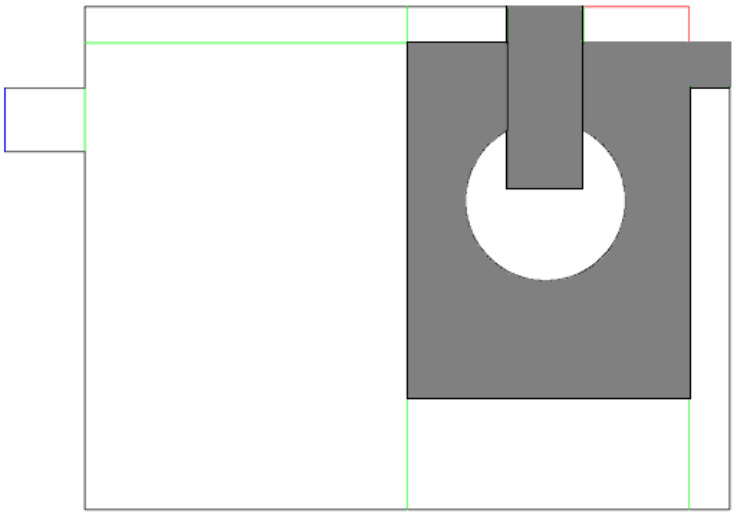


Figure 3.9: CFD domain showing boundary condition definition

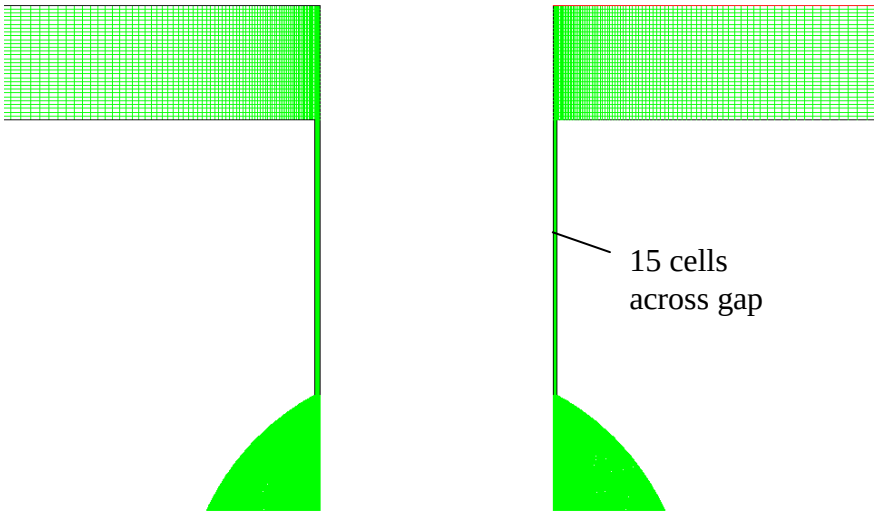


Figure 3.10: Mesh within seal gaps and IPC

3.4.4.2 Meshing

All meshes and geometry were created using the meshing tool, *Gambit*, an accompaniment to the *Fluent* CFD solver. A structured mesh was used to simulate most of this geometry as the majority of the surfaces are parallel to either of the two axes in the coordinate system, the 'axial' and 'radial' directions. The intermediate pressure chamber was the only region of unstructured meshing. The volume was split into various zones, shown by the green lines in Figure 3.10 (*a*), to allow greater control over meshing. All the meshed sections of the volume were conformal with each other i.e. the nodes on the interfaces between mesh zones were shared. Although capturing the flow fields in the seal gaps was essential to the performance of the model, the simple parallel wall geometry required only 15 nodes spanning the seal gap height to achieve grid independence. This was shown with a mesh sensitivity study, where the number of nodes was doubled to 30 and the number of nodes in the intermediate pressure chamber doubled: no change was seen in the resultant force produced or the leakage mass flow rates. All meshes were created to be as identical as possible to ensure comparability between the results and each contained 300,000 cells.

Turbulence Model

The standard *k*-ε model was employed as the turbulence model for this application being a simple, complete, robust, two-equation model allowing the turbulent viscosity and length scales to be independently determined. Although the correct values for these parameters were unknown, applying the model with the default settings for all cases would allow a reasonable comparison to be made.

Wall y^+

The meshes were developed so as to accommodate the use of a turbulence model in the seal gaps. Due to the very small gap heights, the first cell heights were inherently small and so y^+ values were aimed to be less than 1 in the seal gaps with the use of enhanced wall treatment in order to properly allow the laminar sub layer to be modelled (Fluent User Guide 2005). If it was desired to run laminar flow conditions within the seal gaps, the mesh was already partitioned into separate conformal zones and thus the turbulent viscosity could be set to zero in the required regions. This would effectively result in a hybrid turbulence model with the seal gaps containing laminar flow and turbulent conditions present elsewhere. The y^+ parameter is defined as:

$$y^+ = \frac{u^* y}{v} \tag{3.25}$$

where u^* is the frictional velocity (defined as $\sqrt{(\tau_w/\rho)}$), y is the distance of the first cell height from the wall and v is the kinematic viscosity. As the y^+ values depend on the first cell height and the flow velocity, they cannot be obtained until a solution has been produced and hence the mesh was adjusted after a preliminary case to give suitable y^+ values.

3.4.4.3 Solving

Solutions for each mesh were obtained with *Fluent* CFD version 6.3 solving the Reynolds Averaged Navier-Stokes equations for steady state conditions. As well as the momentum and

continuity equations, the energy equation was solved in order to achieve compressible flow solutions. The walls of the model were set to be adiabatic for energy considerations. A converged solution was assumed when the scaled residuals of the velocity, continuity and turbulence parameters fell below 10^{-3}, except for energy which was 10^{-6}, and had reached a plateau. A solution typically required 10,000 to 15,000 iterations to converge. To reduce the chances of divergence, the initial iterations were performed under the simplest conditions; laminar, constant density, first order accuracy and without solving the energy equation. Each setting was then changed sequentially, interspersed by sufficient iterations until the conditions most representative of the flow were being solved; the appropriate turbulence model (see Turbulence Model previously), compressible flow when appropriate (see Material Properties below) and second order accuracy.

Material Properties

A Rolls-Royce standard compressible flow air properties journal was read into Fluent to set the properties as shown below:

Density, ρ (kgm^{-3}): Ideal gas (compressible) or constant (incompressible)

Specific heat capacity, c_p ($Jkg^{-1}K^{-1}$): Piecewise-linear

Thermal Conductivity, k ($Wm^{-1}K^{-1}$): Piecewise-linear

Viscosity, μ ($kgm^{-1}s^{-1}$): Piecewise-linear

Molecular Weight ($kgmol^{-1}$): 28.96

The Piecewise-linear options, displayed in Figure 3.11, relate the properties of the fluid to its static temperature increasing the stability of the solver when high speed flows are present. In some seal housing positions, the velocity of the fluid at the seal gap exit planes was up to 220 ms^{-1} (≈ Mach 0.6) warranting the use of variable gas properties.

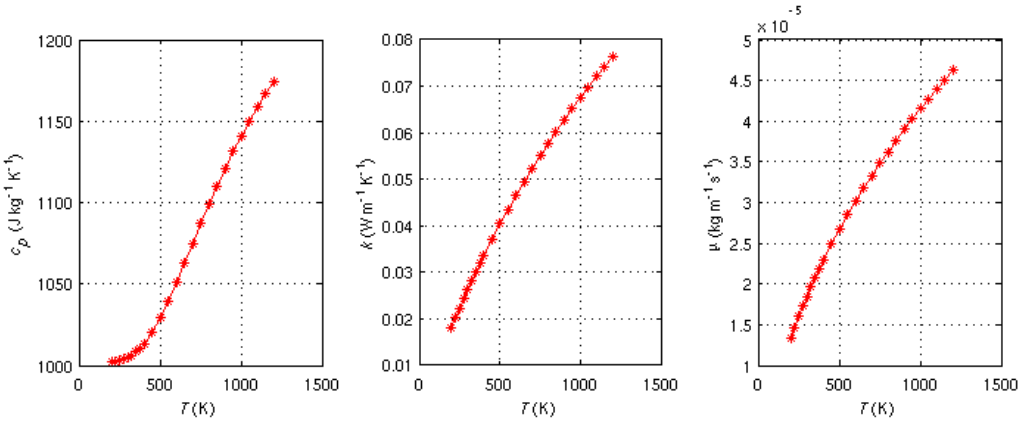


Figure 3.11: Piecewise-linear relationships for c_p, k and μ

3.4.5 Three dimensional CFD

The two-dimensional CFD effectively modelled an infinite-radius, annular version of the LAMFS. The influence of the side leakage flow in the linear test rig, between the seal housing side walls and the test rig end plates, necessitated the use of three dimensional CFD for a better comparison. Details of the geometry, mesh and solving methods are described below.

3.4.5.1 Geometry

The three dimensional CFD geometry modelled the primary leakage paths, the secondary seal and the side leakages between the seal housing side walls and the endplate. Figure 3.12 shows the solid surface geometry of the model with the endplate removed (the perimeter of its usual position is indicated with the white dashed lines). The seal housing side wall is displayed in orange and it is the clearance between this surface and the inner surface of the containment endplate that constitutes the side leakage path causing the flow to behave three dimensionally. This leakage path was modelled with a height of 50μm as measured. A symmetry plane boundary condition was set at the test rig centreline, thus only half the rig internal volume was modelled computationally allowing for a greater number of cells: a limit imposed by the resources available. Separate geometries, and hence meshes, were created for each of the seven displacements of the seal housing as in section 3.4.4.1 (δ = -150 μm to 150 μm in

increments of 50 μm). Figure 3.13 shows the leakage paths modelled with the paths equivalent to the 2D model shown in black and the side leakage paths displayed in red.

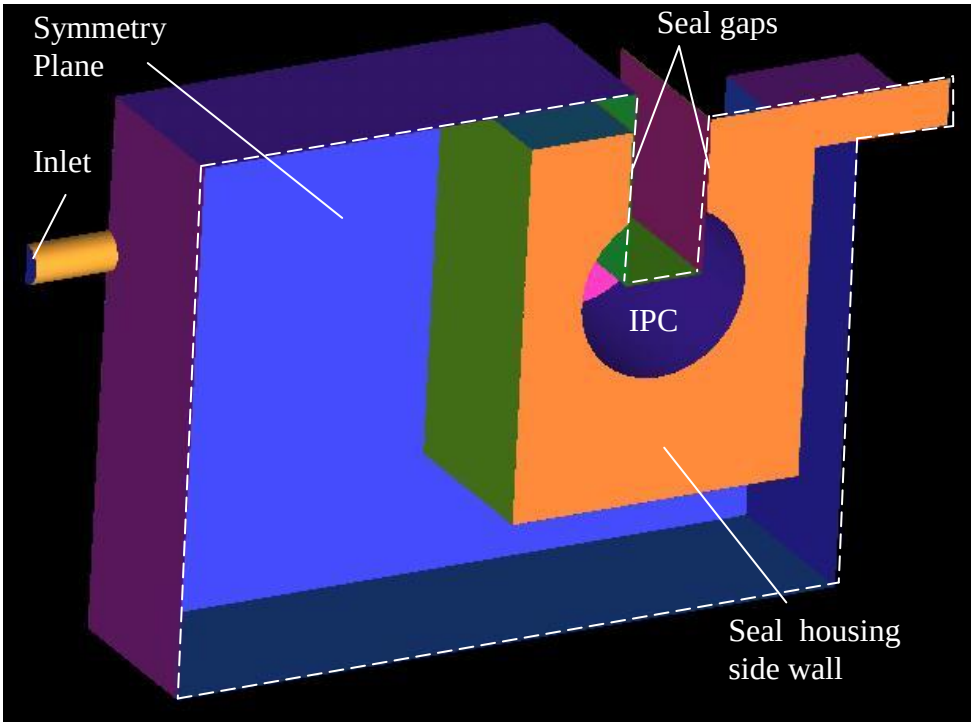


Figure 3.12: Three dimensional CFD domain surfaces with endplate removed - Symmetry plane in light blue, endplate position indicated by dashed line

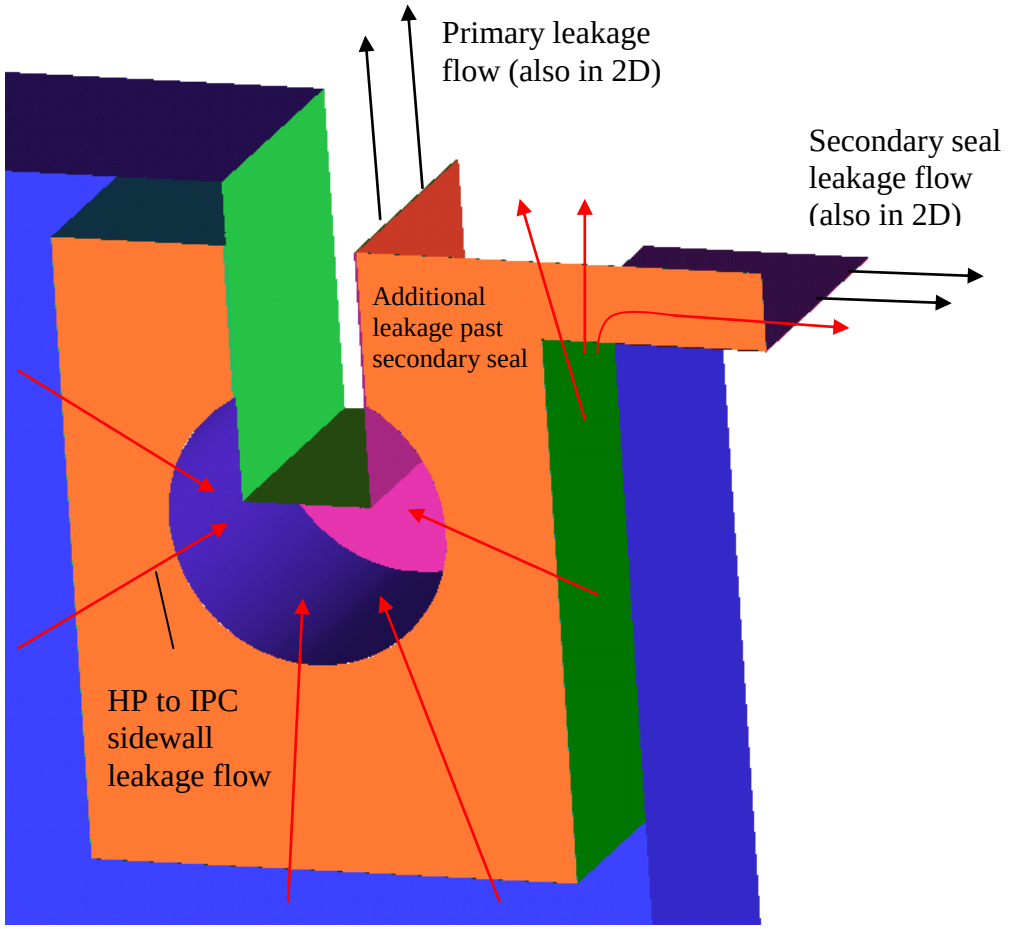
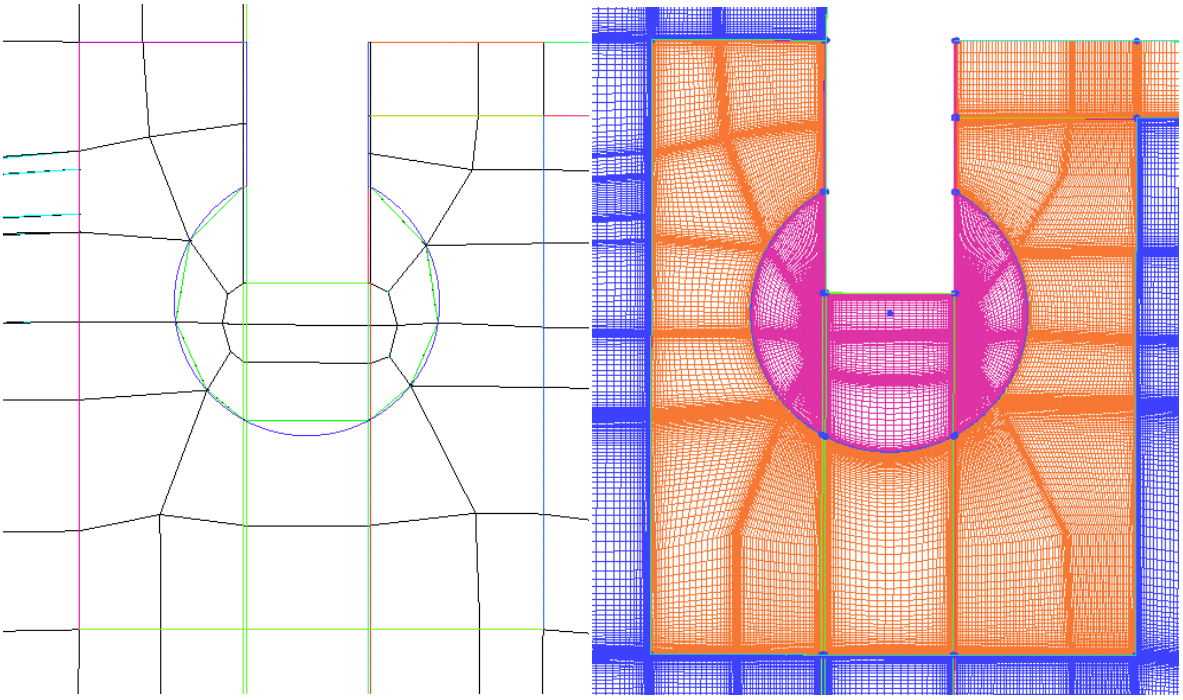


Figure 3.13: 3D CFD LAMFS leakage paths

3.4.5.2 Mesh

Three dimensional meshing was performed using *ICEM CFD 11* enabling the entire 3D domain to contain a structured mesh. Importantly, it allowed the simultaneous meshing of the primary leakage flow path and the secondary leakage paths. Figure 3.14 shows the method of splitting the domain into blocks, where the black lines represent the block edges and the coloured lines are the geometry of the domain. The node spacing was then determined on the block edges. This allowed for near identical meshes for each geometric case. The total cell count for each mesh was 3.5 million.



(*a*) (*b*)

Figure 3.14: Three dimensional CFD blocking (*a*) and mesh (*b*)

3.4.5.3 Solving

The approach used to arrive at a solution for the two dimensional CFD (section 3.4.4.3) was applied in an identical fashion to calculate converged results.

3.4.6 Results for Parallel Seal Faces - Seal Housing Resultant Force vs. Displacement

3.4.6.1 Experimental Data

From the seal housing resultant force measured experimentally for parallel seal surfaces, shown in Figure 3.15, an unstable behaviour is observed. Although an equilibrium point exists where the resultant force is zero (for p_{HP} = 0.69, 1.03, 2.07 and 2.76 barg), a perturbation in displacement from this point induces a force in the direction of motion and remains until the seal housing reaches the limit of its displacement range. For p_{HP} = 3.45 bar, the resultant force remains positive across the entire seal housing displacement range and hence an equilibrium

point does not exist. For the lowest three pressures, the force displacement relationships are reasonably similar but the seal housing behaviour then varies significantly when the inlet pressure increases to 2.76 and 3.45 bar, most likely due to compressibility affecting the flow at these pressure boundary conditions. For all values of inlet pressure, an undesirable behaviour would be observed. Contact would be made between the seal housing and rotor indefinitely, ultimately leading to structural failure through thermal loading and wear. The force displacement desired is one displaying a negative gradient, such that if the seal housing is moved from an equilibrium point existing, ideally, near the zero displacement location, the associated resultant force is in the opposing direction, thus exhibiting a stable behaviour.

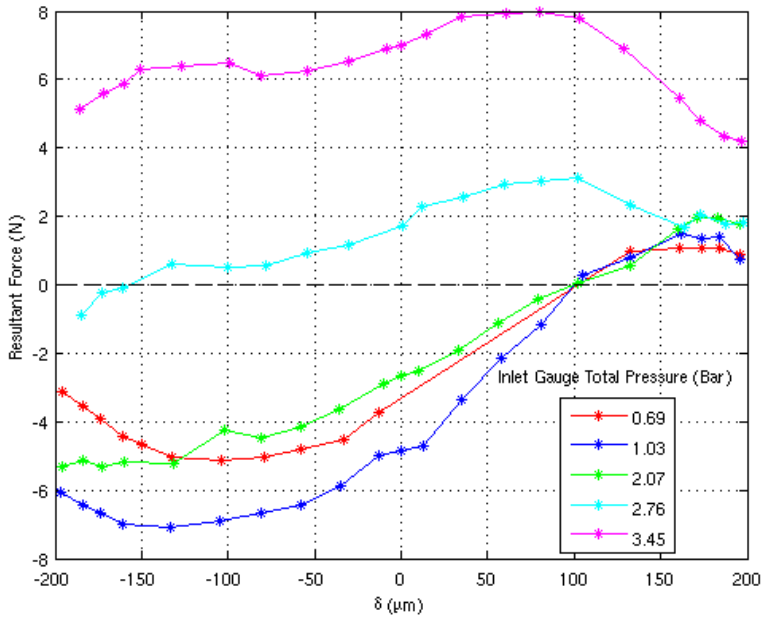


Figure 3.15: Experimental seal housing resultant force with displacement – Parallel gaps: h_{tsg} = 400 µm, h_{step} = 0 µm, α = 0

3.4.6.2 Analytical Modelling

The resultant force with displacement relationship predicted by the analytical model is shown in Figure 3.16. The overall trend is similar to a sinusoidal curve of approximately one period with the centre amplitude at zero resultant force and thus equilibrium points exist for all pressure cases and one is situated near zero displacement. Through the central equilibrium points, however, the gradient is positive and although the resultant force reaches a limit and

subsequently reduces in magnitude with further displacement in either direction, the behaviour of the seal housing would be unstable. At the very peripherals of the displacement range, the resultant force opposes the direction of increasing displacement, but this would be unable to prevent seal-disc contact as the seal housing would have acquired significant axial momentum by the point of reaching the peripheral equilibrium points (so called slap-through).The impact could also cause high stresses in the disc. The model does not replicate the experimental data adequately well in terms of the number of equilibrium positions, the peak magnitudes of the forces and the generally trends, but an unstable behaviour is still predicted. The reasons for these differences in behaviour are due to the static pressure distributions within the seal gaps. This is analysed in section 3.4.7.

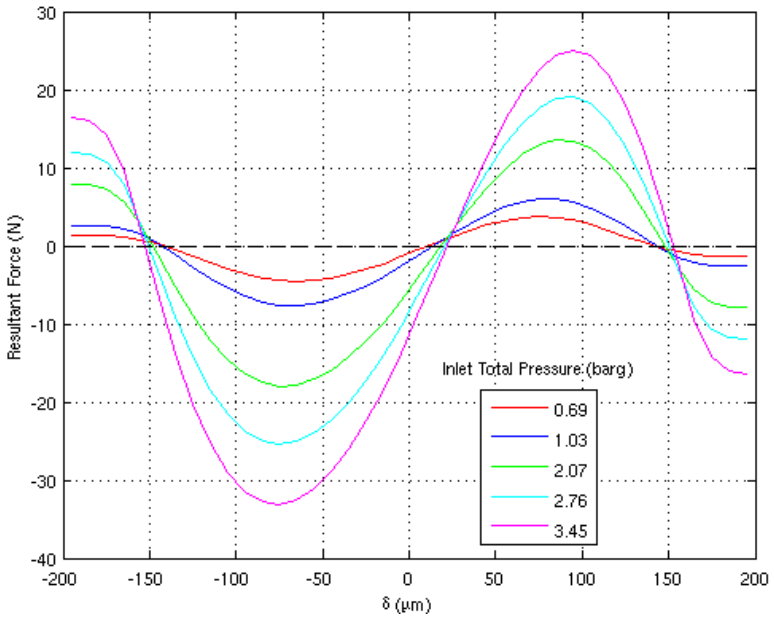


Figure 3.16: Analytical model seal housing resultant force with displacement – Parallel gaps: h_{tsg} = 400 µm, h_{step} = 0 µm, α = 0

Figure 3.17 is used to explain the triple equilibrium point seen in Figure 3.16. The *x*-axis in Figure 3.17 (*b*) represents the distance through the primary leakage path where 0 and 1 represent the upstream gap inlet and exit respectively, and 1 and 2 represent the downstream seal gap inlet and exit respectively. In Figure 3.17 (*a*), the positive force (downstream seal

gap and the constant offset from the outer surfaces) is plotted against the magnitude of the negative force (upstream seal gap). The positive force at δ = – 190 µm is greater than the negative force but the positive force magnitude drops at a higher magnitude of displacement (as the position of the seal housing is moved in the positive axial direction from δ = – 190 µm). This is due to the downstream seal gap inlet loss (Figure 3.17 (*c*)) being far greater in the negative displacement region, which is reflected in the static pressure distribution (x / L = 1 compared with x / L = 0 for the yellow, δ = – 190 µm, and green, δ = – 100 µm, lines). As δ tends to the zero position, the inlet losses are almost equal and hence the resultant forces reach a similar magnitude, leading to the meta-stable equilibrium position. In the positive displacement range, the inlet loss to the upstream seal gap dominates and hence the pressure on the upstream face is relatively low, resulting in the positive force being larger. However, as δ tends to its positive maximum (+190 µm) the inlet losses for both seal gaps are negligible as the mass flow rate through the primary leakage path tends to zero and therefore the pressure on the upstream seal face increases (comparing the blue, +100 µm, and black, +190 µm, curves in Figure 3.17 (*b*)).

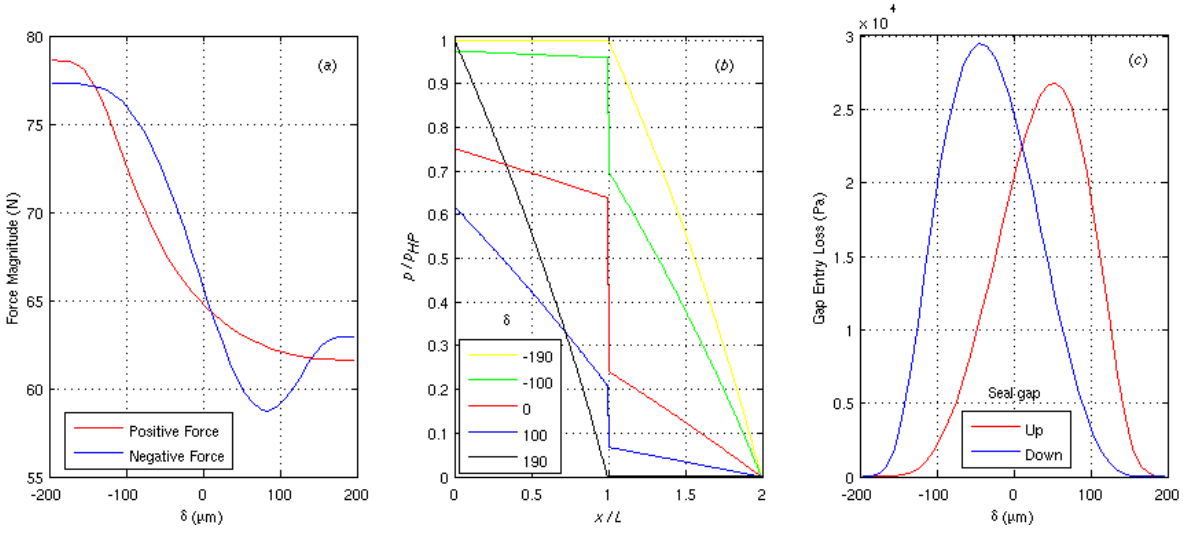


Figure 3.17: Analytical model triple equilibrium analysis: (*a*) – positive and negative force components, (*b*) – seal gap static pressure distribution, (*c*) – seal gap entry losses for upstream and downstream gaps

3.4.6.3 CFD

The resultant force-displacement data for the CFD is calculated by integrating the axial component of the seal housing static pressure distribution ($F = \int p \, dA$). The two dimensional CFD simulations do not predict a similar trend to the experimental data, but the results correspond well to the analytical model. This is most likely due to the forced laminar flow in the seal gaps, as in the analytical model. The reason for this is explained in 'Turbulence Model Effects' below. The magnitude of the resultant force, shown in Figure 3.18, generally increases with pressure. Though a negative gradient is observed at $|\delta| > 50$ µm, at a positive displacement, for example, the resultant force remains in that direction, and vice versa. Thus the seal housing dynamic behaviour would therefore be inherently unstable most likely leading to seal-disc contact.

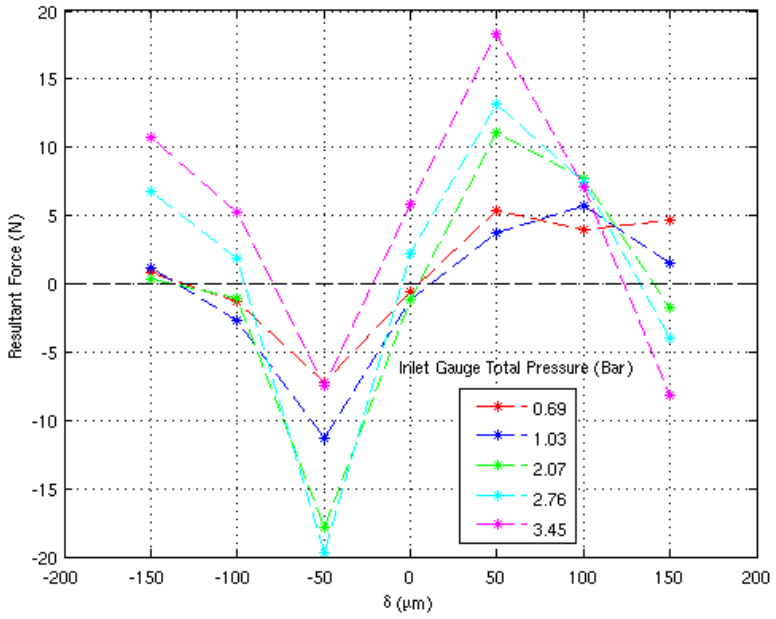


Figure 3.18: 2D CFD seal housing resultant force with displacement – Parallel gaps: h_{tsg} = 400 µm, h_{step} = 0 µm, α = 0

Despite an attempt to model the test rig more accurately by including the leakage paths between the seal housing and the end plates, the force-displacement relationship produced

from the three dimensional CFD (Figure 3.19) does not resemble the experimental data. For all inlet pressures, however, an unstable seal housing behaviour is still predicted. It can be inferred that introducing these leakage paths appears to affect the flow and pressure field significantly and hence the resultant force. However the correct flow field is still not captured by the 3D CFD. The magnitude of the resultant force increases with inlet pressure which is a trend also seen in the two-dimensional CFD and the analytical model data, all giving peak force magnitudes of between 20 N and 30 N. When compared to the experimental data, there is an over-prediction by a factor of 4.

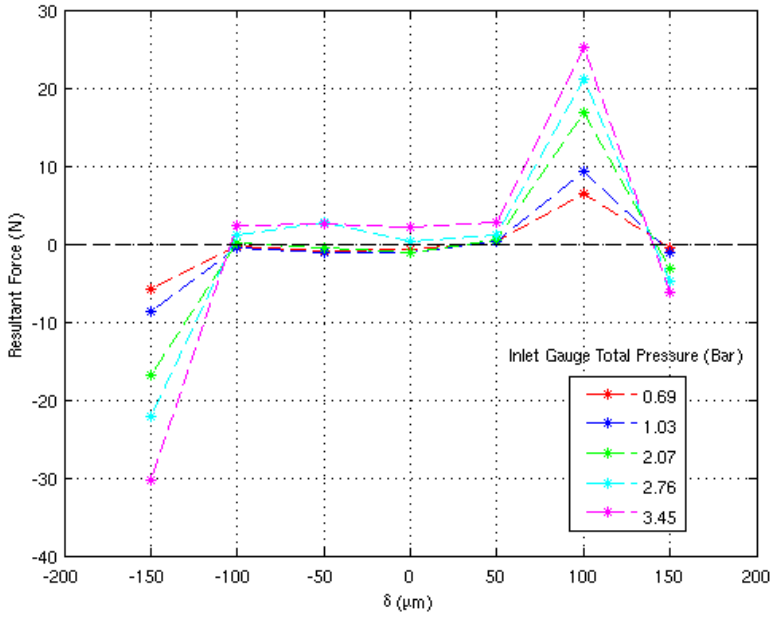


Figure 3.19: 3D CFD seal housing resultant force with displacement –Parallel gaps: h_{tsg} = 400 µm, h_{step} = 0 µm, α = 0

Turbulence Model Effects

Differences between the seal housing resultant force vs displacement predicted using different turbulence models is shown in Figure 3.20. This is the result of 22 simulations using the seven two-dimensional meshes representing various seal housing positions, with 4 turbulence models. These 4 options were: fully laminar throughout the domain, fully turbulent (k-ε), a hybrid with laminar flow in the seal gaps and turbulent elsewhere as described in section

3.4.4.3, or a fully laminar case using the *k-ε* model where the turbulent kinetic energy is set to zero. Only one data point was achieved for the laminar *k-ε* model to confirm that the hybrid model was necessary. Although the general trend is similar for all three cases, there are differences at some of the seal housing positions. On closer inspection of the intermediate pressure chamber (IPC) under laminar conditions (Figure 3.21 - (a)), it is apparent that the flow field predicted is far too complex to be a true time averaged representation of the flow. As the flow exits the upstream seal gap into the IPC, there are multiple vortices and the flow separates off the upstream face of the disc. Overall the time averaged flow field appears overly stable given its complexity and is unlikely to be seen in the test rig. The only region in the seal where the Reynolds number indicates laminar flow is in the seal gaps where the length scale is sufficiently small. The hybrid turbulence model was deemed most appropriate for the 2D and 3D CFD.

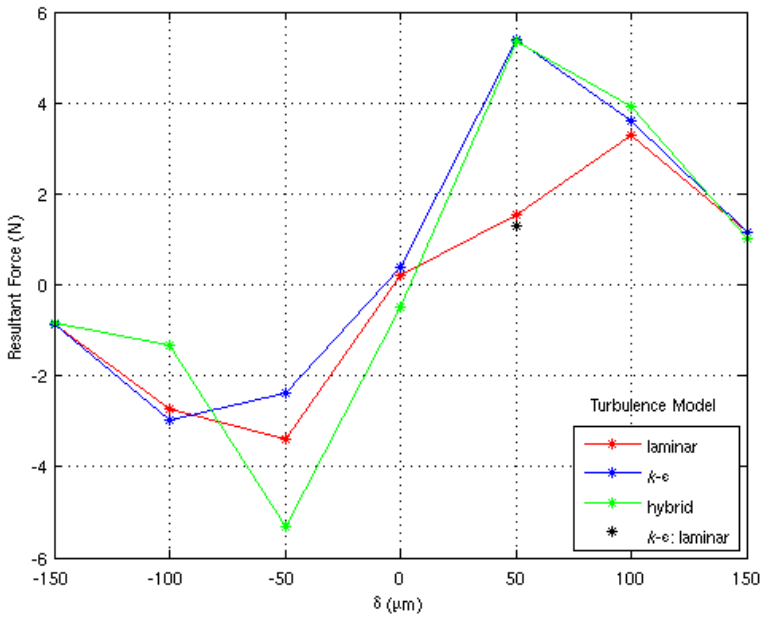


Figure 3.20: 2D CFD seal housing resultant force with displacement - Parallel gaps: p_{HP} = 0.69 bar, h_{tsg} = 400 µm, h_{step} = 0 µm, α = 0

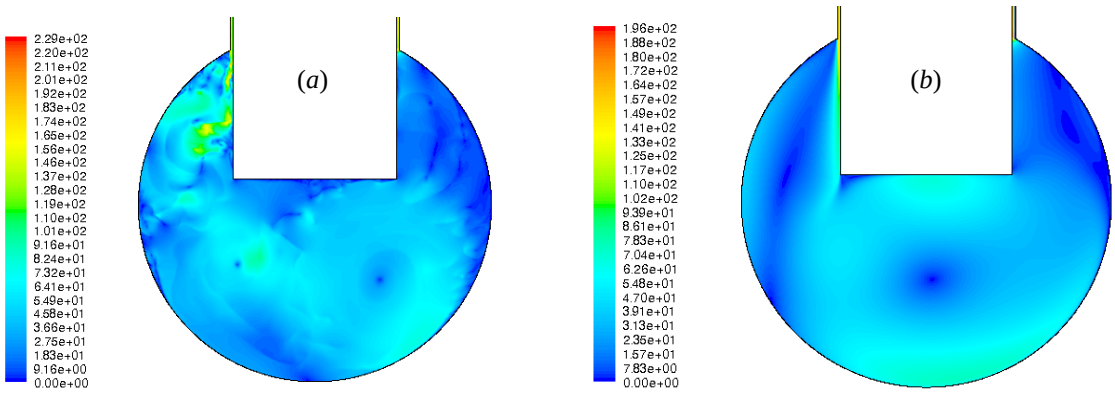


Figure 3.21: Intermediate pressure chamber velocity contours with laminar (*a*) and *k*-*ε* (*b*) turbulence models used in the simulation

3.4.7 Results for Parallel Seal Faces - Seal Gap Static Pressure Distribution

As described in section 3.3.1.2, the static pressure in the seal gaps was measured with 11 tappings on each face at a centre to centre streamwise spacing of 1.1 mm. As was performed for the CFD simulations, the static pressure throughout the primary leakage path was measured at 7 positions of the seal housing relative to the central position; –150 µm to 150 µm in increments of 50 µm. Figure 3.22, Figure 3.23 and Figure 3.24 show the pressure distribution for δ = –150, 0 and 150 µm displacements respectively: with experimental, analytical and 2D CFD data displayed. Each subplot within a figure represents a particular inlet pressure. The *x* axis represents the position through the primary leakage path where 0 is at the inlet plane of the upstream seal gap, 1 is at the exit plane of the upstream gap, the IPC and the inlet plane of the downstream gap, and 2 is at the exit plane of the downstream gap. The pressure in all plots is normalised by the upstream total pressure, p_{HP}.

Figure 3.22 shows the pressure distribution through the primary leakage path when the seal housing is displaced from the central location by –150 µm, such that $h_u >> h_d$. In this case the pressure throughout the upstream seal gap is $\approx p_{HP}$ and the vast majority of the pressure drop through the seal occurs in the downstream seal gap. The opposite occurs when the seal

housing is displaced by + 150 µm (Figure 3.24) where the pressure loss in the seal is through the upstream seal gap and the pressure within the entire length of the downstream gap is ≈ p_{LP}. When the seal is at zero displacement and $h_u = h_d$ (Figure 3.23), the proportion of the total pressure drop through each seal gap varies with p_{HP}; the normalised IPC pressure increases from ≈ 0.55 at p_{HP} = 0.69 bar up to 0.73 at p_{HP} = 3.45 bar i.e. the pressure drop through the upstream seal gap, as a proportion of the total pressure drop, reduces with increasing inlet pressure. For all seal housing displacements, the pressure drop as a function of seal gap position, *x*, changes with inlet pressure. At the lowest three inlet pressures, the pressure ratio across each gap is such that the flow regime is incompressible. The pressure drop through the seal gaps is therefore assumed linear for these cases. At the two highest inlet pressures, compressible effects are indicated by the nonlinear pressure drop; proportional to $\sqrt{\Delta x}$.

The static pressure loss at the inlet planes to the seal gaps varies depending on the pressure difference across the seal. As shown in Figure 3.5, the centre of the first (furthest upstream) of the 11 tappings on each seal face is in line with the inlet plane, and hence half the tapping area is exposed to either p_{HP} or p_{IPC} depending on the seal gap in question, heavily influencing the measured value in those tappings. The second tapping is also influenced by any inlet flow separations or the possibility of impingement of the flow at its position giving a higher reading. Calculating the inlet loss to a seal gap therefore becomes more complex and is described in detail in section 3.4.7.1. At p_{HP} = 0.69, 1.03 and 2.07 bar, the inlet losses, as a proportion of the pressure drop across the whole seal, are almost identical and are higher than those observed at higher pressure ratios where compressible effects are seen. A variation in the flow density at the higher-pressure, compressible conditions may be the cause of this reduction in static pressure loss at the seal gap inlets. According to the CFD models, the size

of the separation at the inlets reduces with increasing inlet pressure which may also contribute to the reduction in entry losses.

At δ = –150 µm and 150 µm seal housing displacement, the CFD and analytical models greatly under predict the static pressure loss at the entry to the smaller of the two seal gaps for inlet pressures of 0.69, 1.03 and 2.07 bar and subsequently do not match well with the experimental data, although near identical to each other. For inlet pressures of 2.76 and 3.45 bar where compressible conditions are seen experimentally, the seal gap inlet losses and overall distributions are well matched by the two models. At δ = 0 µm, the inlet losses and pressure drop gradients predicted by both models are in good agreement with the experimental data for inlet pressures of 0.69, 1.03 and 2.07 bar. The mass flow rate is higher at zero displacement than for both –150 µm and 150 µm and hence the inlet losses are greater. For inlet pressures of 2.76 and 3.45 bar, the CFD model remains reasonably close to the experimental data, but the analytical model over-predicts the inlet losses for both seal gaps and hence the pressure distributions are inaccurate.

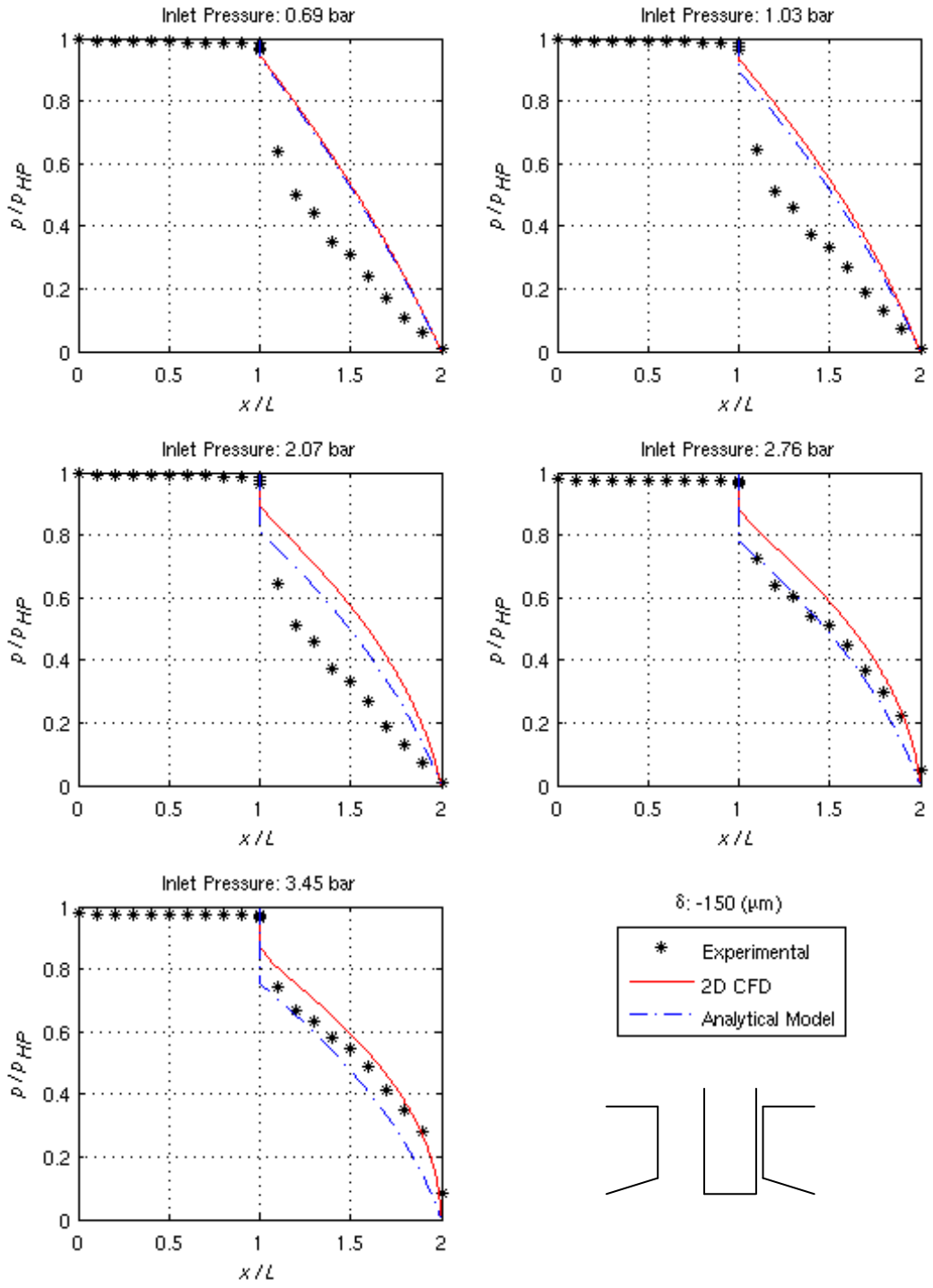


Figure 3.22: Static pressure distribution in parallel seal gaps from experimental, analytical and CFD data - Displacement = –150 µm

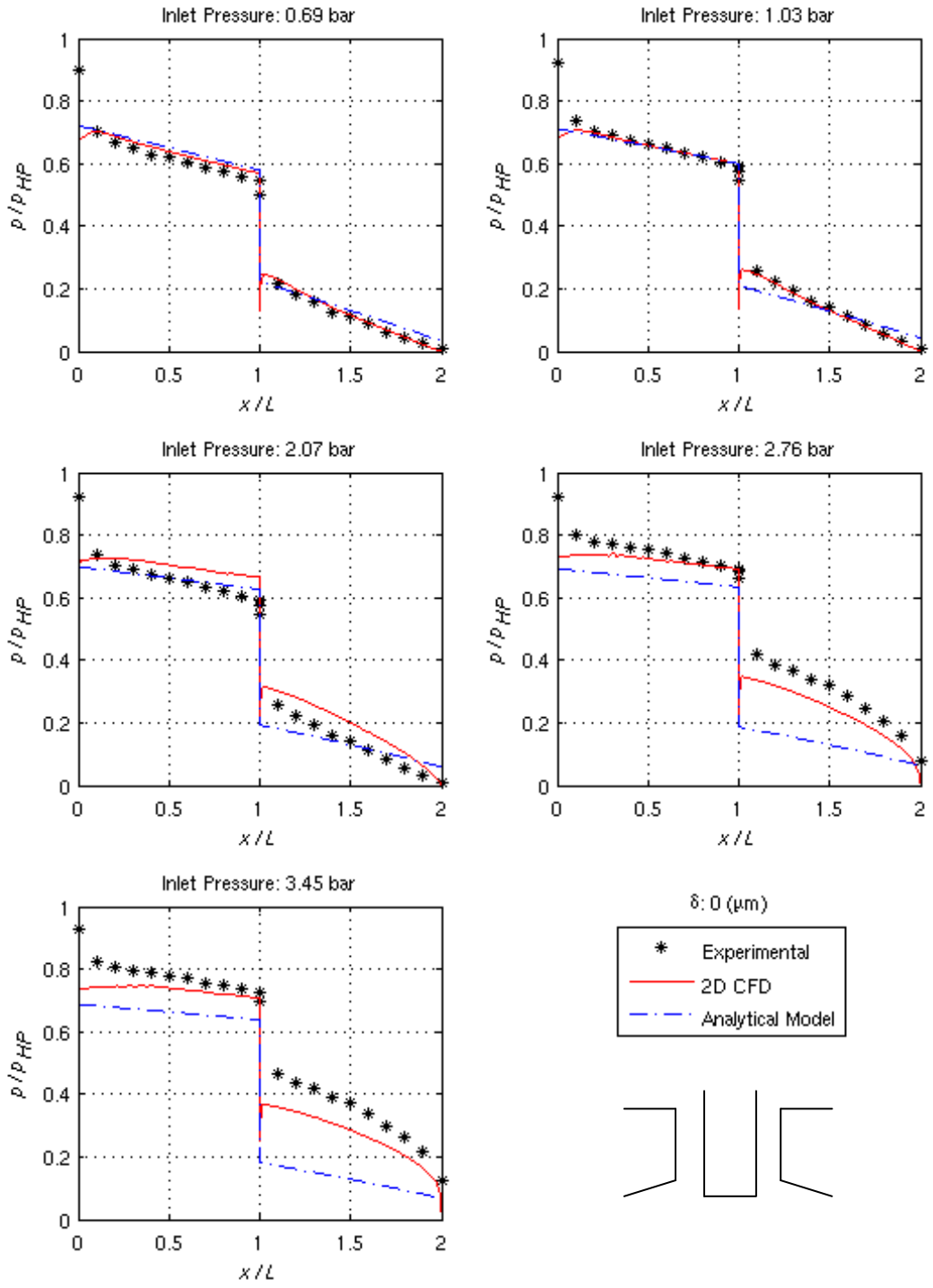


Figure 3.23: Static pressure distribution in parallel seal gaps from experimental, analytical and CFD data – Displacement = 0 µm

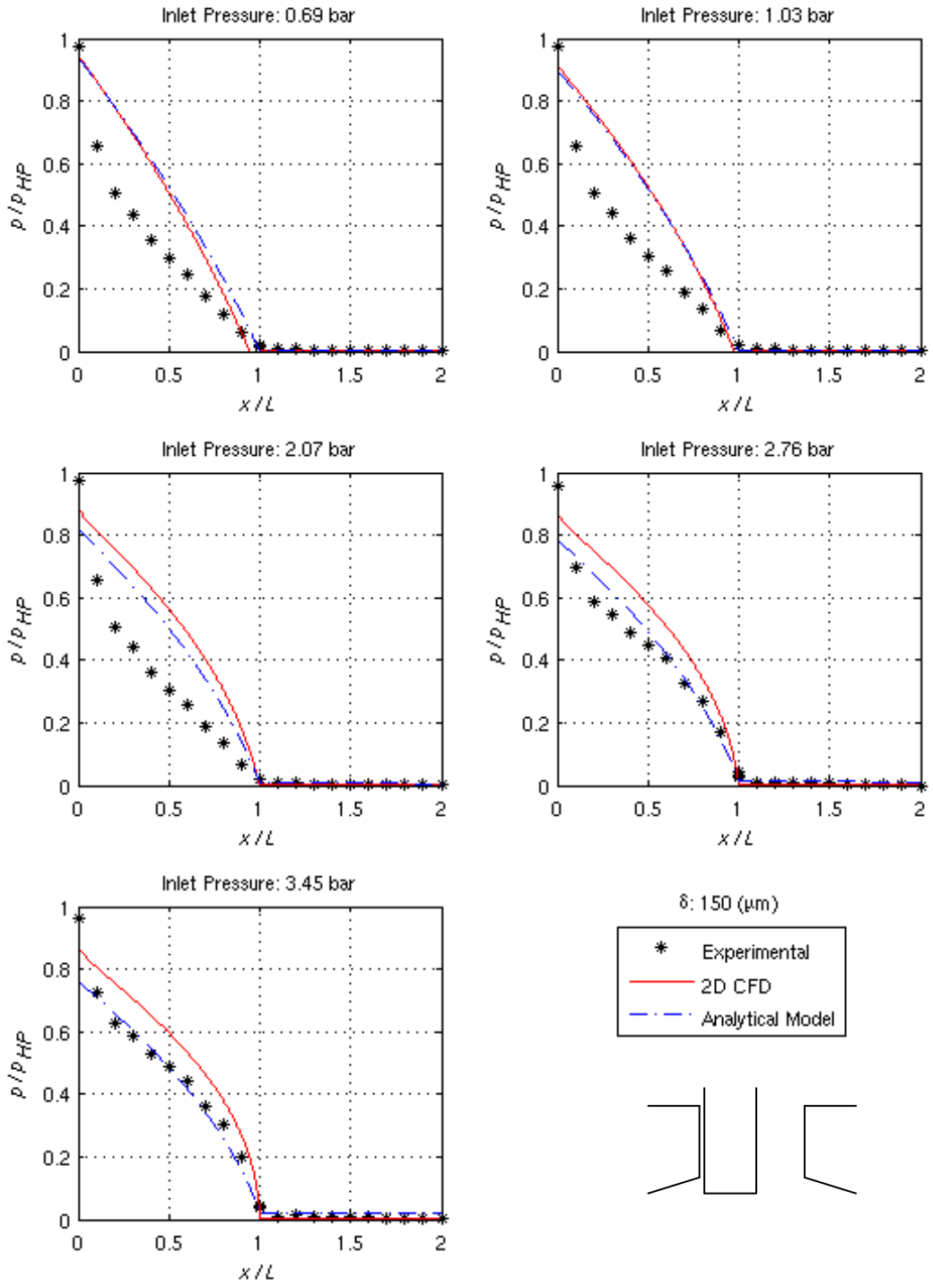


Figure 3.24: Static pressure distribution in parallel seal gaps from experimental, analytical and CFD data – Displacement = +150 µm

3.4.7.1 Inlet Loss Coefficient

The discrepancy between the seal gap static pressure distributions from the experimental and analytical data largely arise from the inaccuracy in predicting the magnitude of the loss at the seal gap inlets, which is determined as a function of the dynamic head at the inlet location. The original analytical model calculated the loss as one dynamic head but this was then modified such that the inlet loss is equal to $\beta \frac{1}{2} \rho u_{in}^2$, where β is the inlet loss coefficient. To assess the variation of β for both seal gaps empirically, a minimisation function in *Matlab* was employed to fit the analytical pressure drop equation **(**3.3**)** to the experimental data. Of the 11 data points per seal gap, only tappings 3 to 11 were used as half of tapping 1 is exposed to p_{HP} or p_{IPC} and the measurement at tapping 2 is influenced by the entry effects in the flow field. The analytical equations for the parallel seal face model become

$$\left(p_{HP} - \beta_u \frac{1}{2} \rho_{uin} \overline{u_{uin}^2}\right)^2 - p_{IPC}^2 = \frac{C\mu L}{h_u^3} \quad \textbf{(3.26)}$$

$$\left(p_{IPC} - \beta_d \frac{1}{2} \rho_{uin} \overline{u_{din}^2}\right)^2 - p_{LP}^2 = \frac{C\mu L}{h_d^3} \quad \textbf{(3.27)}$$

and the function is performed with initial guesses for β_u and β_d and minimises the error between the analytical solution and the experimental data points, returning optimal values of β_u and β_d. The variation of the inlet loss coefficients with Reynolds number based on gap height, Re_h, is shown in Figure 3.26. Deriving a correlation for β in terms of Reynolds number gives β as a function of gap inlet pressure (density term) and seal gap height, h (length scale). The form of the relationship is shown below in Equation **(**3.28**)**

$$\beta = a\, e^{bRe_h^c} \quad \textbf{(3.28)}$$

where a = 6.34 x 10^{-16}, b = 48.6 and c = – 0.0265. This is plotted (in black) against the experimental data. When scaled up to engine conditions (40 bar upstream pressure, 700 °C), any pressure ratio resulting in choked flow at δ = 0 (minimum gap height is 200 µm) yields a Reynolds number of approximately 34,000 which lies within the range that this correlation is

valid. Using this inlet loss coefficient, the analytical model can be applied to engine representative conditions with confidence.

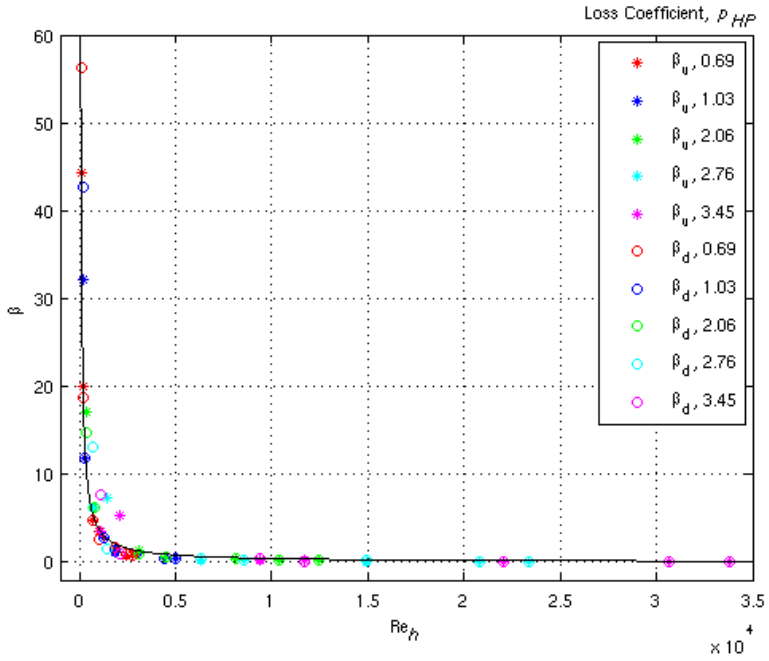


Figure 3.25: Variation of inlet loss coefficient, β, with Reynolds number, Re$_h$

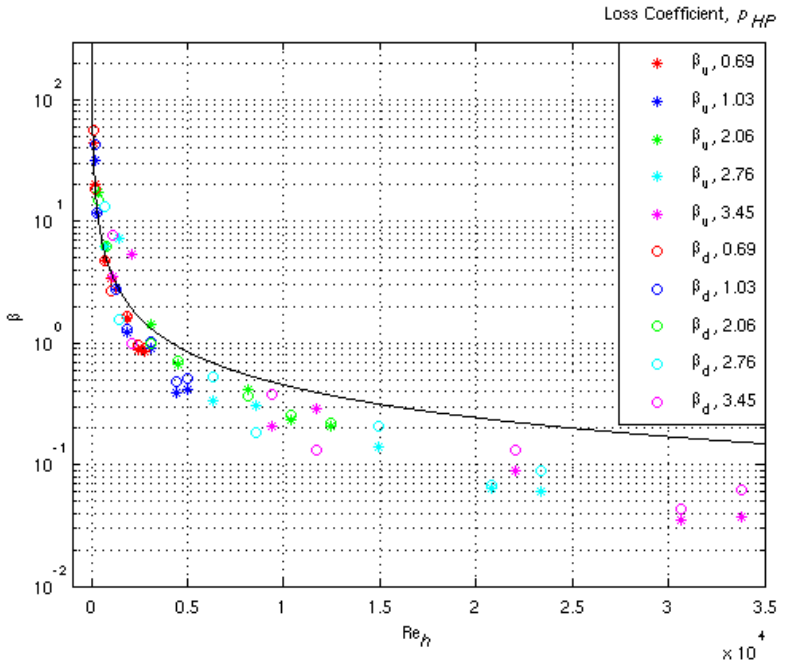


Figure 3.26: Log plot of variation of inlet loss coefficient, β, with Reynolds number, Re$_h$

When the analytical model is rerun on the parallel seal surface geometry with β dependent on the Reynolds number instead of equal to 1, the behaviour of the seal housing has significantly changed. The results are shown in Figure 3.27. The trend is now very similar to that of the

experimental data, which confirms that analysing the inlet losses is imperative for accurate modelling of the seal gap static pressure distribution and subsequently the seal housing behaviour.

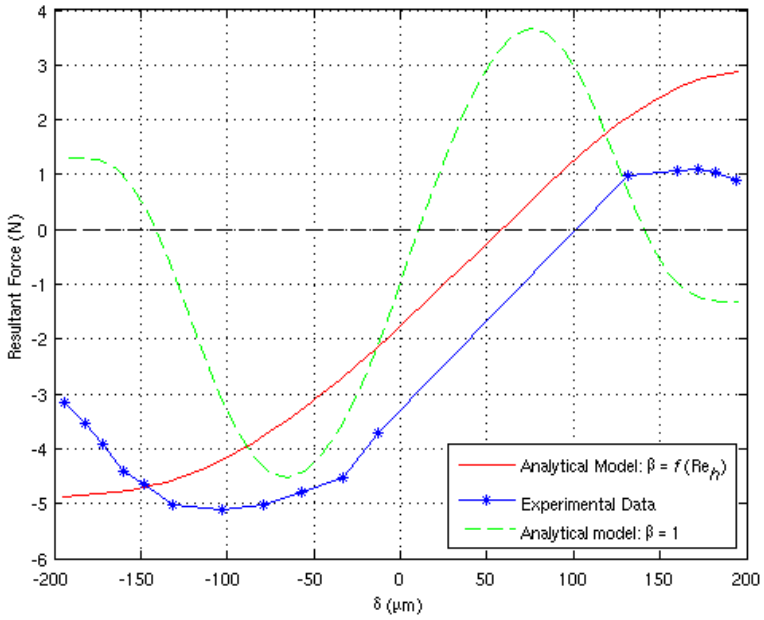


Figure 3.27: Linear LAMFS analytical model with $\beta = f$ (Re_h) against experimental data and analytical model with $\beta = 1$: p_{HP} = 0.69 bar

3.5 Radial Steps

3.5.1 Introduction

The baseline geometry of parallel faces produced an unstable seal housing behaviour, both observed experimentally and predicted computationally. The next step of the research program was to devise a seal gap geometry which would passively control the resultant force on the seal housing and restore its axial position to an equilibrium point. This would be done by controlling the static pressure distribution within the seal gaps. Figure 3.28 is used to explain the reasoning behind the geometry chosen to achieve this. Assuming that the secondary seal location is at the midpoint (radially) of the seal gaps, then the force per unit

width from the external surfaces is $(p_{HP} - p_{LP}) * L / 2$ in the downstream direction. Consider the seal housing is displaced –150 µm (upstream) such that $h_u >> h_d$ (left hand column of the figure), hence the majority of the pressure drop through the seal occurs in the downstream seal gap. If the pressure drop through the downstream seal gap is linear (red) and inlet losses are assumed negligible, then the force on the upstream face is $-p_{HP}L$, and $L*(p_{HP} + p_{LP}) /2$ on the downstream face. The resultant force for the internal surfaces is therefore $-p_{HP}L + (p_{HP} + p_{LP})L / 2 = -(p_{HP} - p_{LP})L / 2$, which balances with the external forces (this is also true when δ = + 150 µm). So, an average pressure on the downstream seal face less than the linear drop with no inlet losses will then give a resultant force in the upstream direction, closing h_d to zero, the undesired case (blue line – parallel faces). Similarly, when δ = + 150 µm, an average pressure on the upstream seal face less than the linear drop with no inlet losses (blue line) will then give a resultant force in the downstream direction, closing h_u to zero. Therefore an average pressure greater than for a linear pressure drop on a seal gap whose height is close to zero is required to provide a restoring resultant force (green dashed line). This can be achieved by delaying the pressure drop through the seal gap with the smallest height. A radial step was chosen to achieve this.

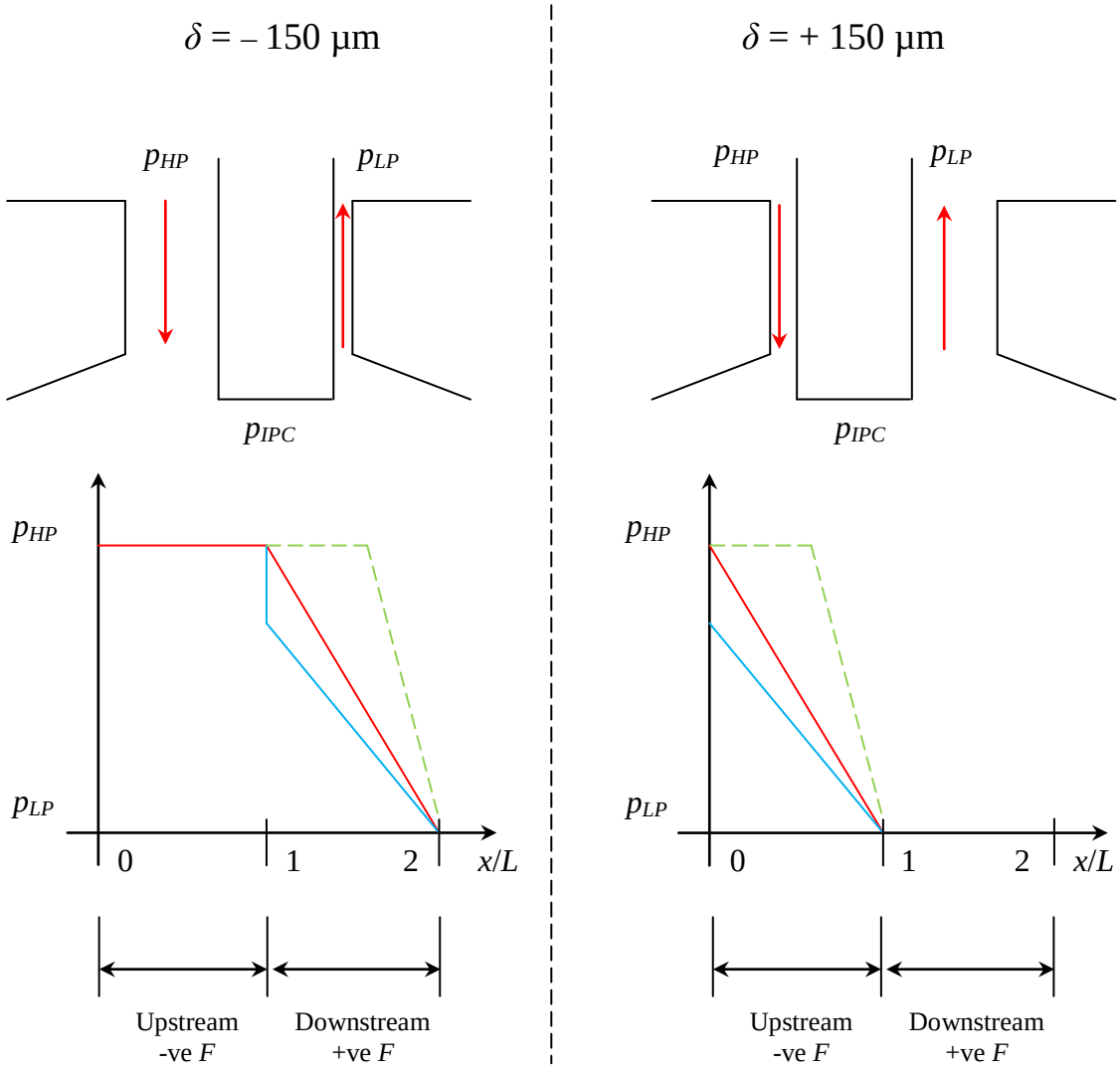


Figure 3.28: Simplified pressure distribution through primary leakage path with varying δ

3.5.2 Geometry

Figure 3.29 shows the radial step geometry incorporated into the LAMFS. In the case of the experimental test rig, this was done by machining the resin rotor component. The high, p_{HP}, intermediate, p_{IPC}, and low, p_{LP}, pressure regions exist as in the baseline parallel wall case. Due to the variation in gap height caused by the step, each section upstream and downstream of the step is analysed individually in the analytical model. The radial position of the step is represented by α as the proportion of the seal gap radial length. α determines x_{ustep} and x_{dstep}

such that $x_{u,dstep} = \propto L$. The total seal gap height, h_{tsg}, is again the sum of the minimum clearances, h_u and h_d. h_{ustep} and h_{dstep} are the respective heights of the steps in the upstream and downstream seal gaps.

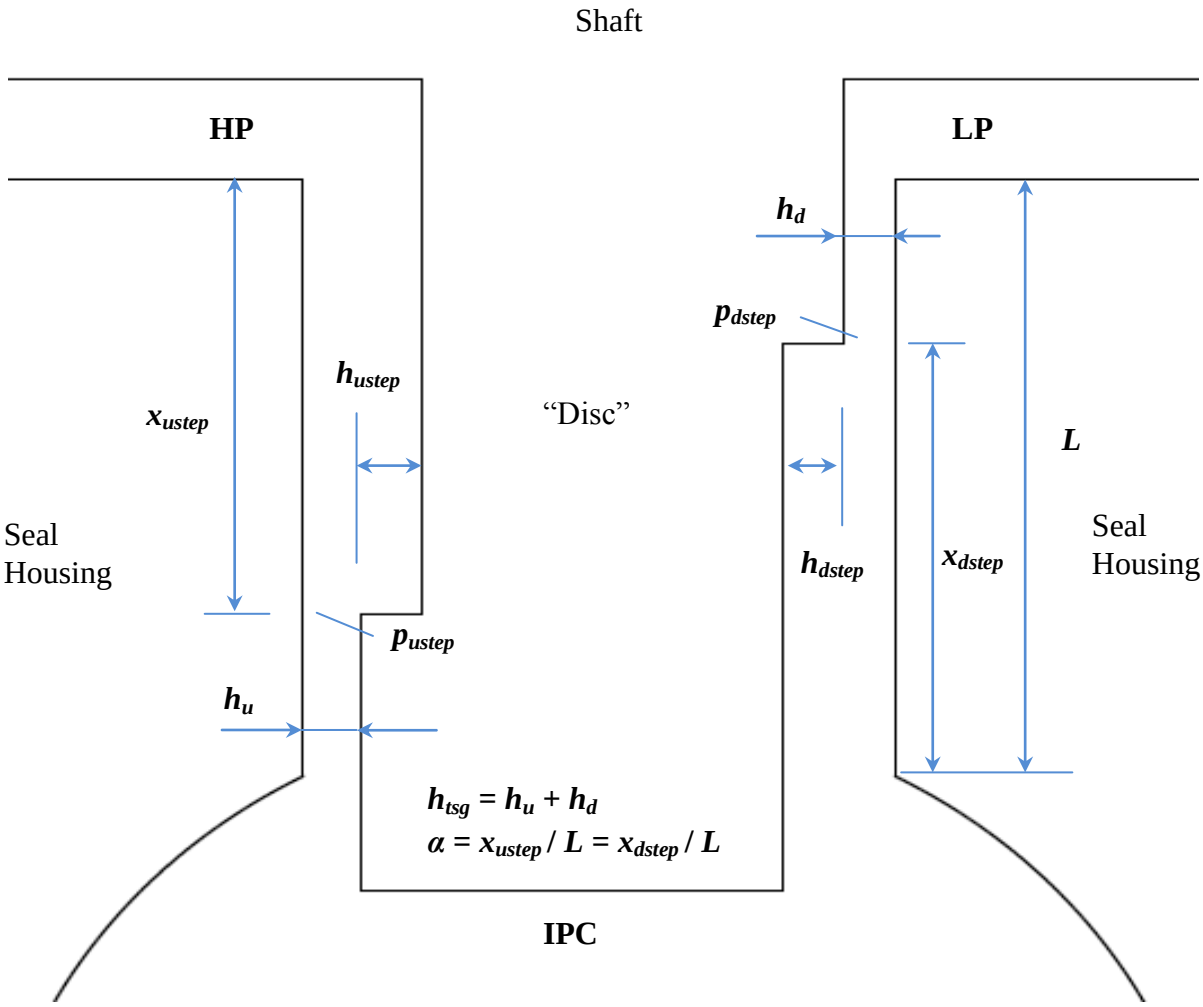


Figure 3.29: Converging radial steps within seal gaps of LAMFS (Note: $\alpha = x_{ustep} / L = x_{dstep} / L$)

3.5.3 Parameters Investigated

The change in seal housing resultant force due to alterations to the seal face surface geometry on the housing was the primary focus of the research performed on this test rig. Further experiments beyond the baseline geometry were performed where converging radial steps had been introduced into both seal gaps over the same range of inlet pressures. The steps are simply a change in gap height and can influence the pressure distribution depending on their

height relative to the minimum seal gap height and the radial position they are located at. Therefore the geometric variables chosen for investigation were the radial position of the step, α, step height, h_{step}, and the total seal gap height, h_{tsg}, i.e. the sum of the upstream seal gap minimum height, h_u, and the downstream seal gap minimum height, h_d. Note that $\alpha = x_{ustep}/L = x_{dstep}/L$. Step heights of 100, 200 and 300µm were tested at radial positions of 50, 75 and 90% of the seal gap length, L, at a total seal gap height h_{tsg} = 400 µm. In the case of the steps located at 90% of the seal gap length, additional tests were conducted with a total seal clearance of h_{tsg} = 800 µm. Table 3.3 lists the experimental data obtained with this test rig.

	x_{step} / L (α)		
	h_{step}: 100 µm	h_{step}: 200 µm	h_{step}: 300 µm
h_{tsg}: 400 µm p_{HP}: 0.69, 1.03, 2.07, 2.76, 3.45 barg	0.5 0.75 0.9	0.5 0.75 0.9	0.5 0.75 0.9
h_{tsg}: 800 µm p_{HP}: 0.69, 1.03, 2.07, 2.76 barg	0.9	0.9	0.9

Table 3.3: Experimental cases tested

3.5.4 Analytical model

The Reynolds 1D governing equations for the radial step case (Figure 3.29) are shown below. Pressures p_{ustep} and p_{dstep} represent the pressure at the locations of the steps in the upstream and downstream seal gaps respectively.

$$\left(p_{HP} - p_{uin\ spd}\right)^2 - p_{ustep}^2 = \frac{\mathrm{C}\mu\alpha L}{\left(h_{ustep} + h_u\right)^3}, \tag{3.29}$$

$$\left(p_{ustep} - p_{ustep\ spd}\right)^2 - p_{IPC}^2 = \frac{\mathrm{C}\mu(1-\alpha)L}{h_u^3}, \tag{3.30}$$

$$\left(p_{IPC} - p_{din\ spd}\right)^2 - p_{dstep}^2 = \frac{\mathrm{C}\mu\alpha L}{\left(h_{dstep} + h_d\right)^3}, \tag{3.31}$$

$$\left(p_{dstep} - p_{dstep\ spd}\right)^2 - p_{LP}^2 = \frac{\mathrm{C}\mu(1-\alpha)L}{h_d^3}. \tag{3.32}$$

The seal housing resultant force then becomes

$$F = (p_{HP} - p_{LP})L_{SS} - \left(\int_0^{\alpha L} p_{u1}(x)\,\mathrm{d}x + \int_{\alpha L}^{L} p_{u2}(x)\,\mathrm{d}x\right) + \left(\int_0^{\alpha L} p_{d1}(x)\,\mathrm{d}x + \int_{\alpha L}^{L} p_{d2}(x)\,\mathrm{d}x\right) \quad \textbf{(3.33)}$$

3.5.5 Linear LAMFS Results - Seal Housing Resultant Force vs. Displacement

The experimental and analytical seal housing resultant force with displacement is shown below in Figure 3.30 for a nominal case; h_{tsg} = 400 µm, h_{step} = 300 µm, α = 0.90. The full set of force-displacement results are shown in section A.2. The inclusion of radial steps within the seal gaps transforms the seal housing behaviour from unstable to a desirable, stable behaviour. The gradient throughout the displacement range is negative and an equilibrium point exists for all inlet pressures. A significant positive bias exists which moves the equilibrium position in the positive axial direction, which is more significant with increasing inlet pressure. This also reduces the magnitude of the negative restoring force (positive displacement) compared with the positive restoring force (negative displacement). Interestingly, the analytical model, which only assumed one dynamic head loss at the inlets, matches the experimental data well (compare this to the parallel case where the inlet losses varied greatly with Reynolds number). The positive bias seen in the experimental data has also been captured by the analytical model, although to a much lesser extent; all equilibrium points lie in the positive displacement region between 15 and 25 µm compared with 70 and 130 µm recorded experimentally. The positive bias, however, does not affect the peak resultant force of the analytical model at the peripherals of the displacement range as they are equal in magnitude. The peak forces of both sets of data at the maximum negative displacement are in excellent agreement but as the seal housing is moved in the positive direction, the discrepancy increases due to the positive bias described. The reason for this positive bias is explained in section 3.5.6.3.

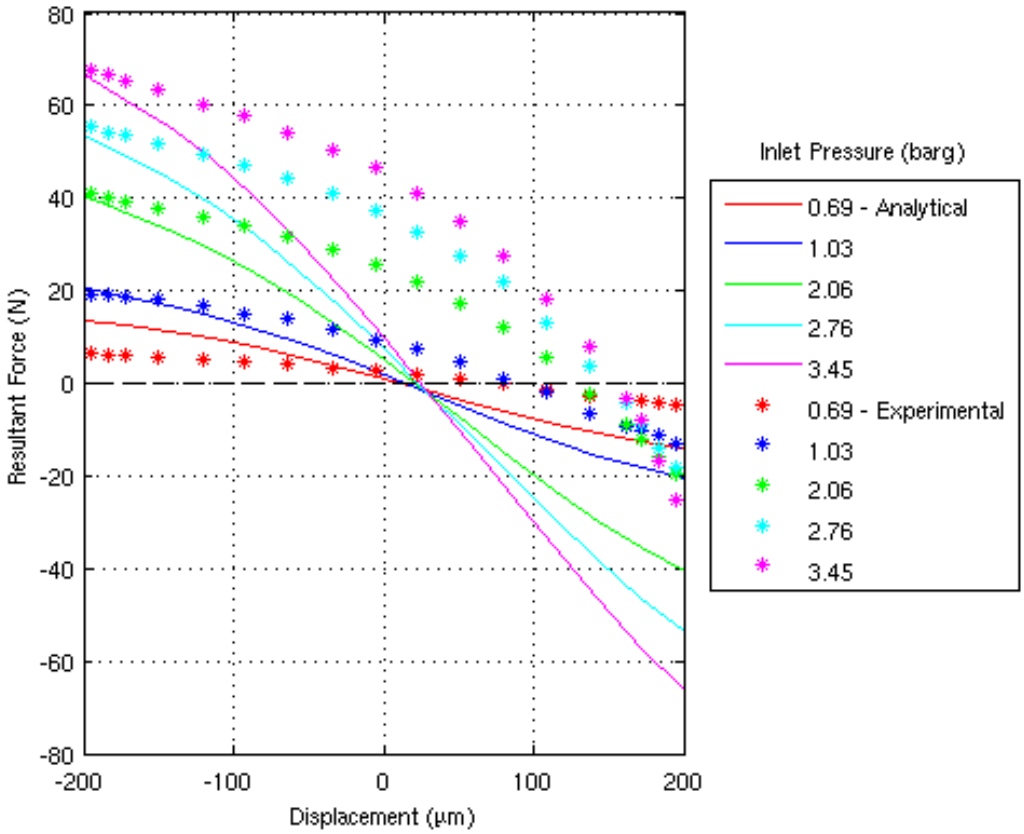


Figure 3.30: Analytical and experimental resultant force with displacement: h_{tsg} = 400 µm, h_{step} = 300 µm, α = 0.90

3.5.5.1 Maximum Force

All force-displacement trends with radial steps are similar in nature to the nominal case shown above. Therefore the features of interest are shown in figures below for all step heights and step positions. The peak positive and negative force magnitudes for all cases are shown in Figure 3.31. For a given step height and radial position, the magnitude of the resultant force increases with inlet pressure, however the peak negative forces increase less with inlet pressure than the positive restoring force due to the positive bias. The peak positive forces increase from 5–8 N at p_{HP} = 0.69 bar to 30–68N at p_{HP} = 3.45 bar, whereas the peak negative force magnitudes only rise from 4–7N at p_{HP} = 0.69 bar up to 16–47N at p_{HP} = 3.45 bar. The positive bias appears to be present across all cases. The increase in step height improves the

self-centring ability by increasing the magnitude of the resultant force on the seal housing, though this is most obvious on the negative side of the equilibrium position where the force is positive. From the peak positive force figure (left), it can be seen that moving the step position further downstream within the seal gap and increasing the step height lead to an increase in magnitude. This is less apparent in the peak negative magnitude results, but this is explained in section 3.5.6.3.

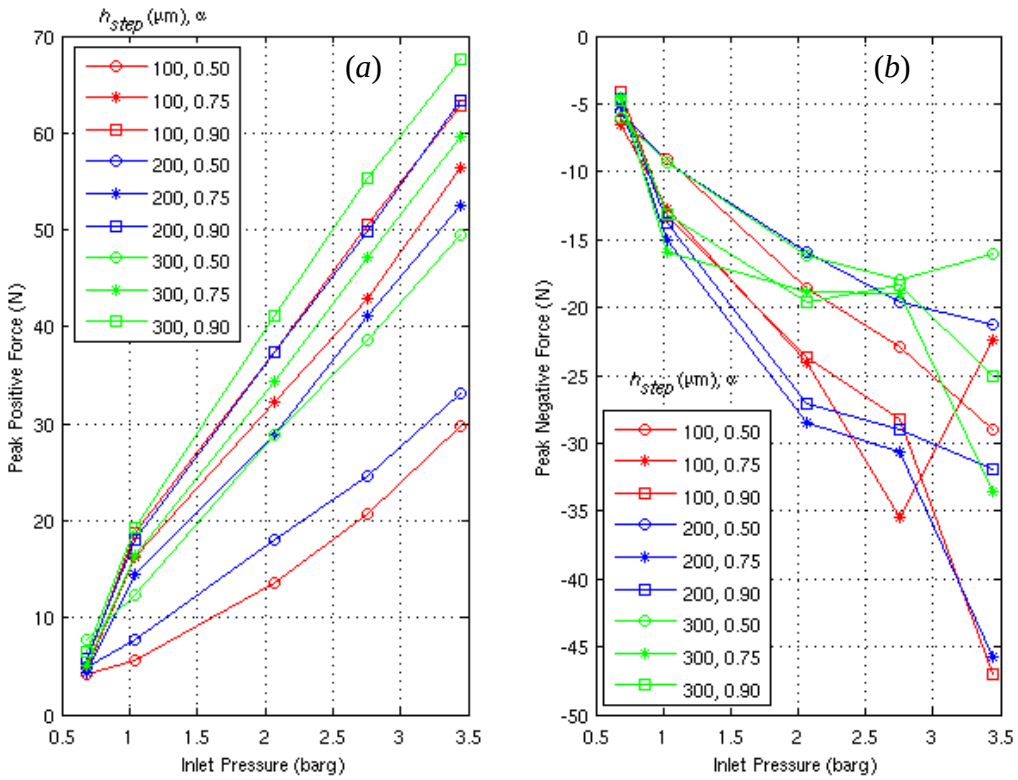


Figure 3.31: Peak positive (*a*) and negative (*b*) forces for experimental data: h_{tsg} = 400 µm

3.5.5.2 Equilibrium Position (δ_{eq})

The variation in seal housing equilibrium position with inlet pressure is shown in Figure 3.32. It can be seen for all values of h_{step} and α that the equilibrium position moves in the positive direction as the inlet pressure is raised. At p_{HP} = 3.45 bar, the equilibrium position lies between +100 µm < δ_{eq} < +150 µm such that $h_u << h_d$ (50 µm < h_u < 100 µm). It is important, then, that during transient conditions, the response of the seal housing is adequate enough to

move the seal housing to follow the disc before contact is made. The gradient of the force displacement relationship is of interest and is discussed below.

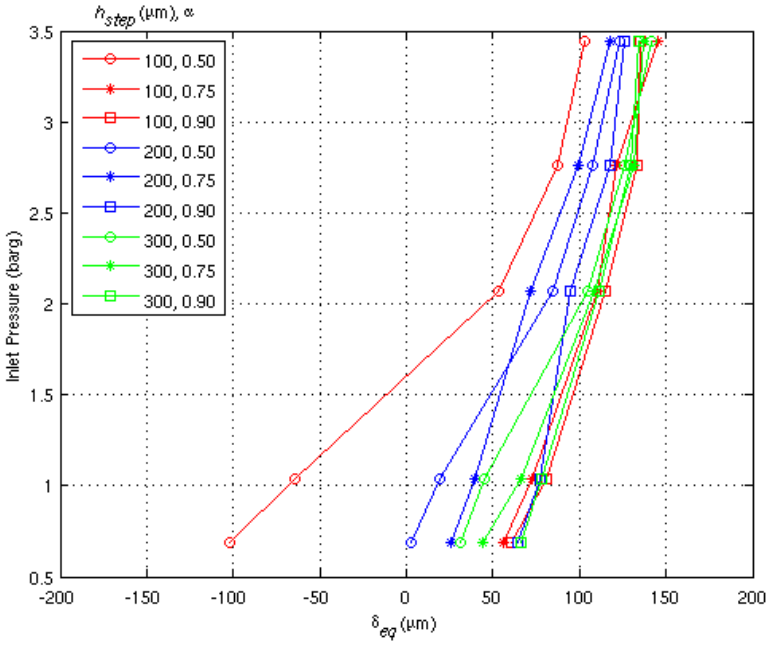


Figure 3.32: Seal housing equilibrium position (δ_{eq}) vs. inlet pressure for experimental data: h_{tsg} = 400 µm

3.5.5.3 Force Gradient at δ_{eq}: $\left(\frac{dF}{d\delta}\right)_{\delta_{eq}}$

Figure 3.33 shows how $\left(\frac{dF}{d\delta}\right)_{\delta_{eq}}$ varies with p_{HP}. As described above, δ_{eq} moves in the positive direction as p_{HP} increases, leaving the seal housing in a position where $h_u << h_d$. It is also the case that the negative gradient of $\left(\frac{dF}{d\delta}\right)_{\delta_{eq}}$ increases with inlet pressure. Thus for a given seal housing displacement from δ_{eq} the restoring force is larger for a higher p_{HP}. The pressure difference across the seal can change over a flight cycle, especially under step climb conditions (sudden max thrust) and hence increasing the seal's resilience during highly transient conditions would be favourable. The dynamic behaviour is modelled on the fully annular version of the seal in section 4.5.3. It can also be seen that the magnitude of the gradient also increases with h_{step} and α for a given p_{HP}.

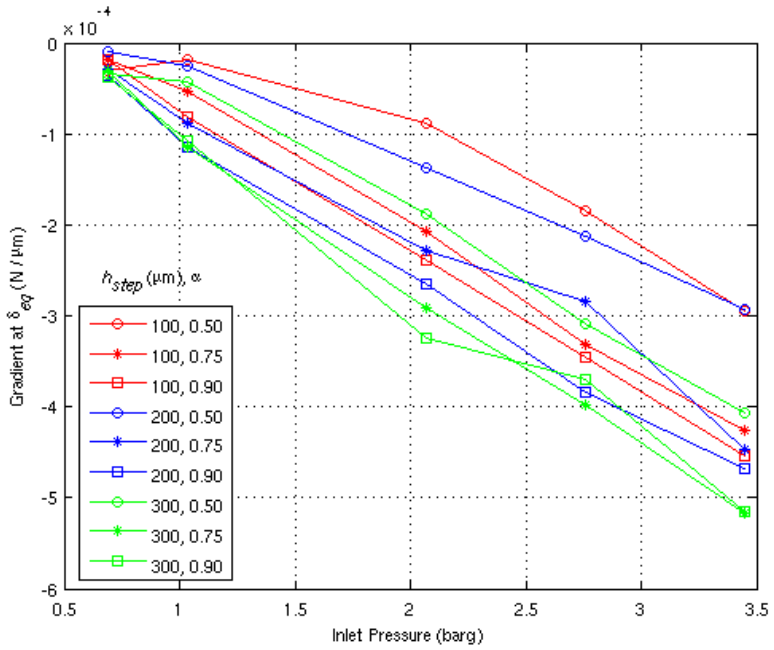


Figure 3.33: Gradient of force-displacement relationship at δ_{eq}: h_{tsg} = 400 µm

3.5.5.4 Linear LAMFS Results - Seal Housing Resultant Force: h_{step} = 800 µm

The total seal gap height was increased to 800 µm to assess whether the step heights tested would still be effective in controlling the seal housing behaviour at a larger clearance, should it be required. The force displacement results from the cases where h_{step} = 300 µm, α = 0.90 are shown in Figure 3.34 for h_{tsg} = 400 and 800 µm at various inlet pressures. The full set of force-displacement curves for h_{tsg} = 800 µm is shown in section A.2.The three step heights were investigated but only one step position of α = 0.90 was tested. The pressure boundary condition of 3.45 bar was unable to be tested as the air supply system was incapable of delivering the required mass flow rate for this case. For all inlet pressures, the radial steps ensure a stable seal housing behaviour. For the two values of h_{tsg}, the magnitude of the forces at the most negative displacement are quite similar but thereafter the htsg = 800 case experiences less positive bias. This is reflected in the δ_{eq} and maximum force magnitude figures below.

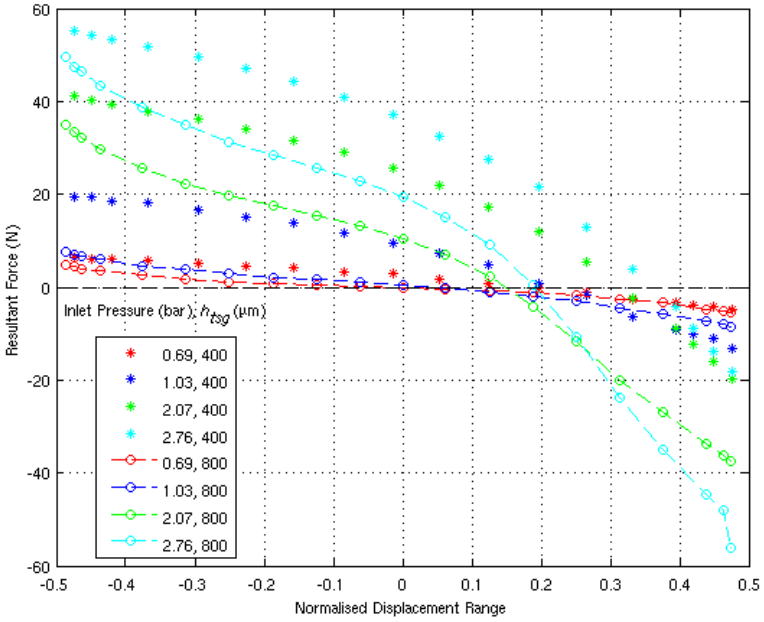


Figure 3.34: Experimental data for seal housing resultant force - h_{tsg} = 400 µm and 800 µm: h_{step} = 300 µm, α = 0.90

Equilibrium Position, δ_{eq}, and Force Gradient at δ_{eq}, $\left(\frac{dF}{d\delta}\right)_{\delta_{eq}}$

Figure 3.35 (*a*) below shows the variation of δ_{eq} with inlet pressure. The movement of the equilibrium point in the positive direction with inlet pressure occurs but to a lesser extent than when h_{tsg} = 400 µm. The value of δ at which δ_{eq} occurs is less than 200 µm, equivalent to less than 100 µm when h_{tsg} = 400 µm. The position of δ_{eq} is also shifted in the positive direction by increasing the step height. The magnitude of the negative gradient at δ_{eq} also increases with inlet pressure and is shown in Figure 3.35 (*b*). The increasing step height also leads to a steeper gradient, though it is far less influential.

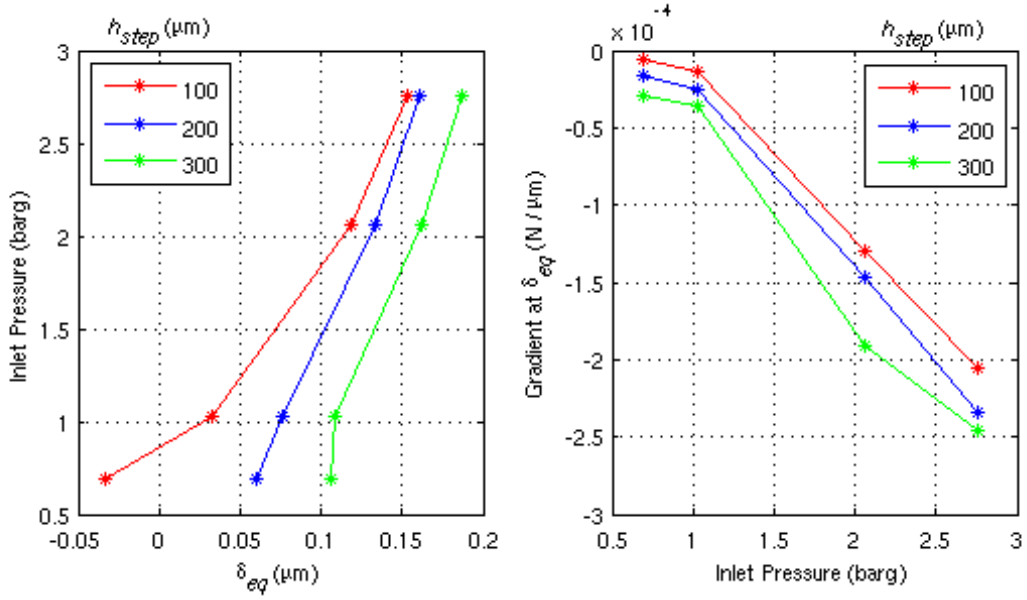


Figure 3.35: Experimental data for δ_{eq} with p_{HP} (a) and $\left(\frac{dF}{d\delta}\right)_{\delta_{eq}}$ with p_{HP} (*b*): h_{tsg} = 800 µm, α = 0.90

Maximum and Minimum Resultant Force

The maximum positive and negative resultant force values are shown in Figure 3.36 (*a*) and (*b*) respectively. For h_{tsg} = 800 µm, the positive bias has very little effect on the peak positive and negative forces reached as they are near identical. With a larger total seal gap height, h_{tsg} = 800 µm, the ratio of h_{step} / h_{tsg} decreases and hence the variation in step height has a negligible effect on the peak forces, but the importance of having a radial step for a self-centring ability and stable behaviour is nonetheless essential.

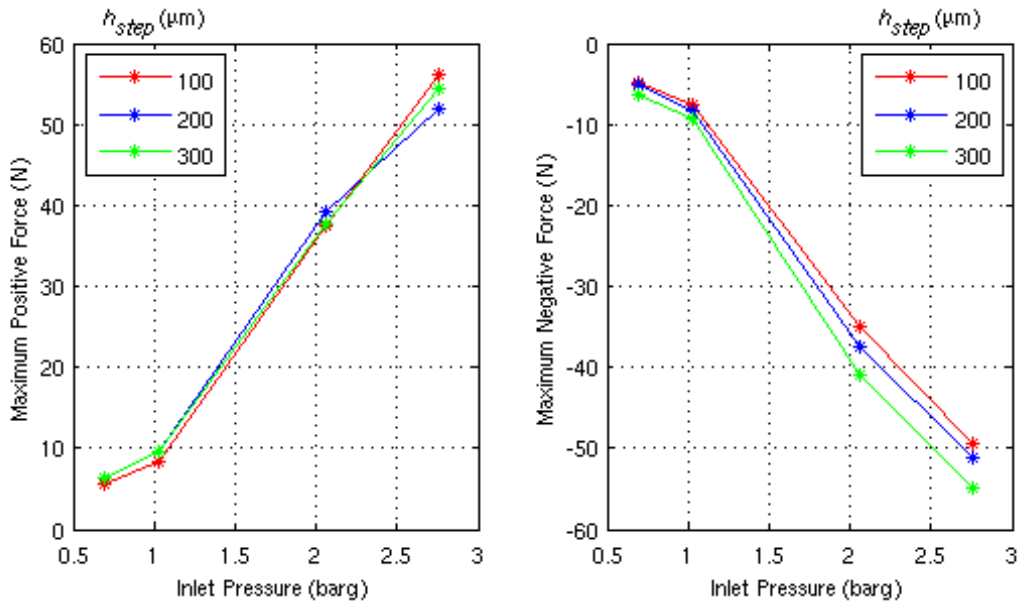


Figure 3.36: Experimental data for maximum positive (*a*) and negative (*b*) forces: h_{tsg} = 800 µm, α = 0.90

3.5.6 Linear LAMFS Results - Seal Gap Pressure Distribution

3.5.6.1 Variation of h_{step} and α

Figure 3.37 is used to explain the change in seal housing resultant force and behaviour from the inclusion of radial step geometry. The presence of radial steps reduces the pressure drop through the seal gaps until the step is reached due to the height ratio: (h_{step} + h_u) / h_u. The pressure is therefore maintained close to p_{HP} or p_{IPC}, depending on the seal gap in question, and the majority of the pressure lost through a particular seal gap occurs from the step onwards. The average pressure is therefore raised on a seal face, whose height is much smaller than the other, above what is required to perfectly balance the internal and external forces (linear drop – magenta line). This gives a resultant force to increase the gap height in the smallest gap.

At -150 µm displacement (left column), for example, h_d = 50 µm h_u = 350 µm and thus the majority of pressure is dropped through the downstream seal gap. In row (*a*), h_{step} is constant

at 100 µm and α is varied. The results show that increasing α delays the pressure drop further downstream within the gap. In row (*b*), α = 0.90 and h_{step} is varied. The main drop in pressure occurs at the same position for all step heights but the gradient upstream of the step lessens as the step height is increased. Increasing the values of h_{step} and α both lead to an increase in average pressure on that seal face and a greater restoring force on the seal housing. The variation in pre-step viscous pressure loss gradient is analysed below in section 3.5.6.2.

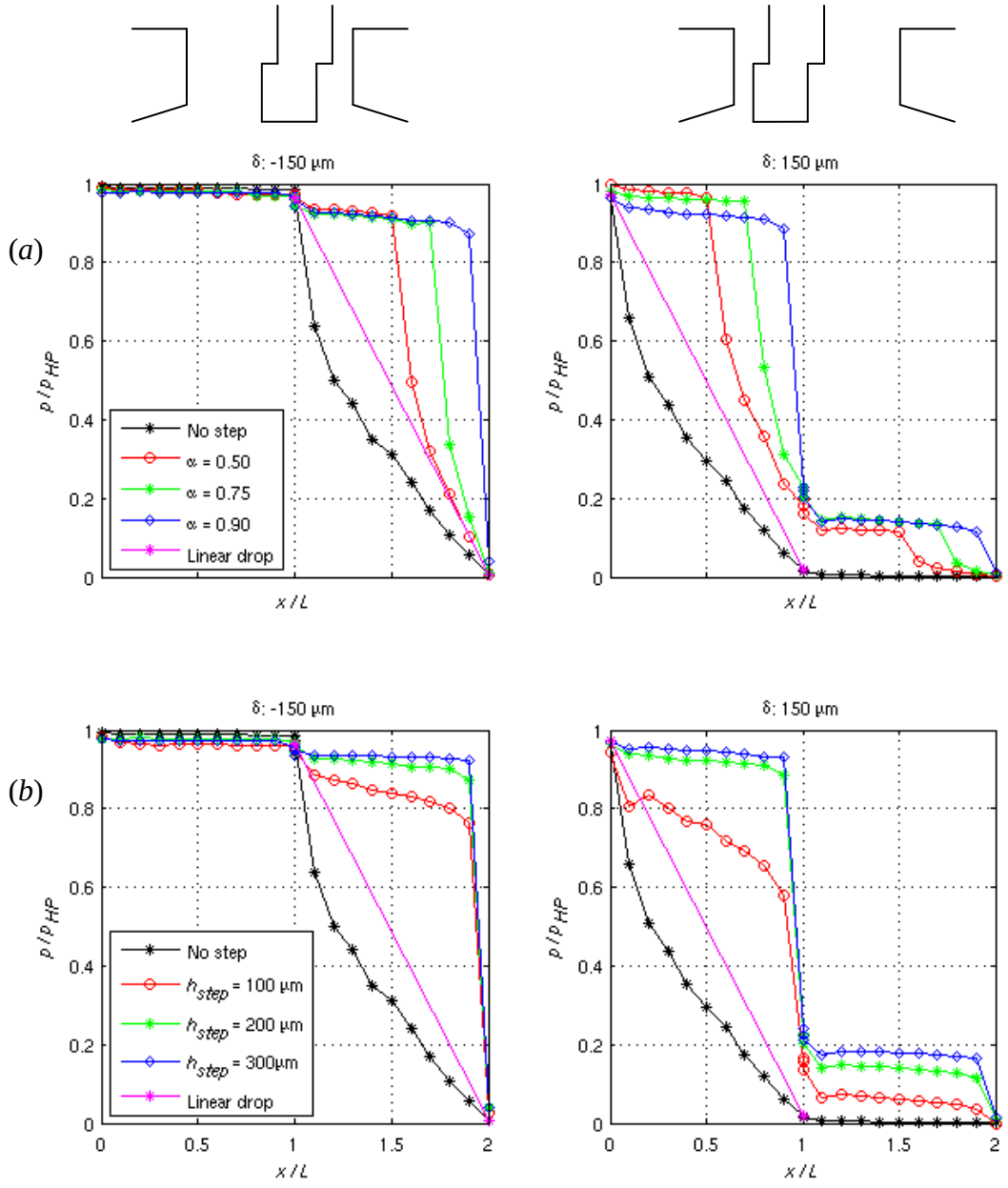


Figure 3.37: Static pressure distribution in seal gaps (p_{HP} = 0.69 barg, h_{tsg} = 400 µm) – Full range of step locations, h_{step} = 100 µm (row (*a*)) and full range of step heights, α = 0.90 (row (*b*))

3.5.6.2 Gradient of Pre-Step Viscous Pressure Drop

Figure 3.38 (*a*) and (*b*) show the pre-step viscous pressure drop in the downstream and upstream seal gaps respectively when the minimum clearance is equal to 50 µm. The ratio of the height of the gap before and after the step when the minimum clearance is 50 µm is: (h_d + h_{step}) / h_d = 3, 5 and 7 for h_{step} = 100, 200 and 300 µm respectively. As this ratio increases with step height, the gradient of the pressure drop upstream of the step reduces drastically as the viscous drop is proportional to $1/h^3$ (Reynolds 1D equation). The average pressure on the smallest clearance face is therefore increased with step height. This was reflected in the resultant force-displacement data. The influence of h_{step} on the leakage mass flow rate can be seen in section 3.5.7.

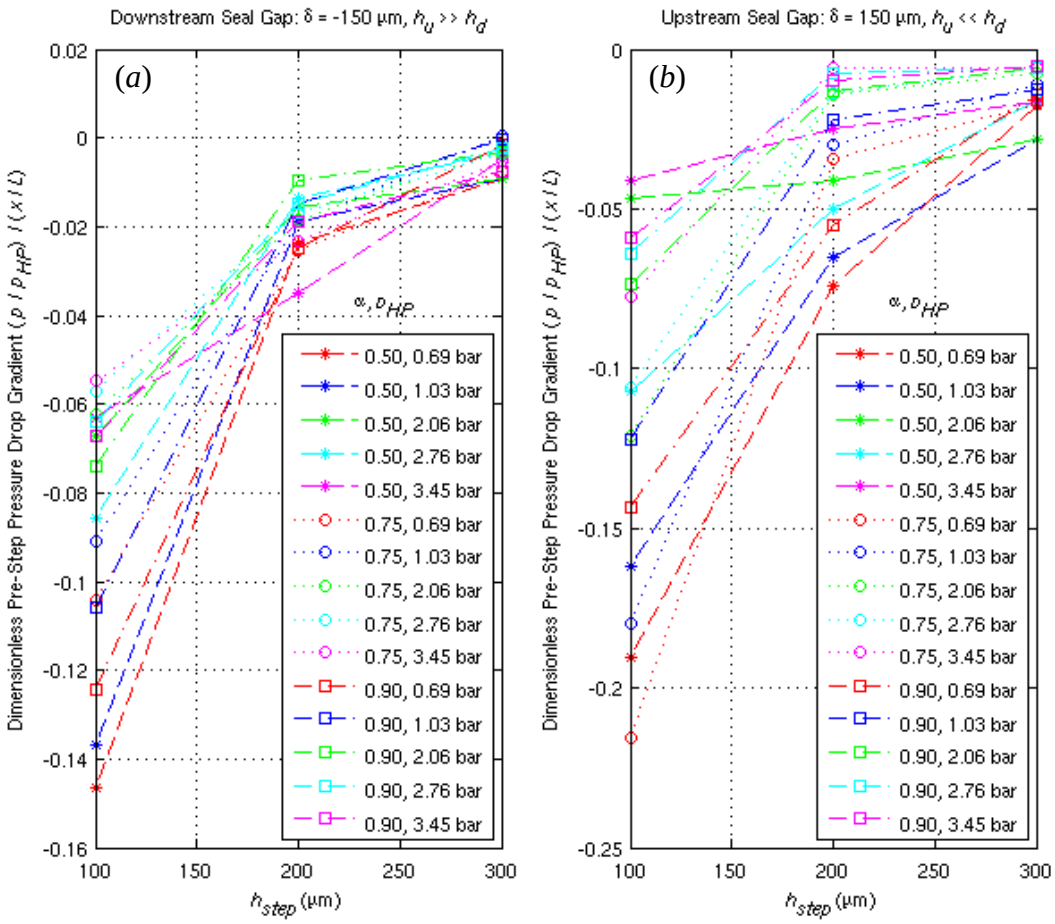


Figure 3.38: Gradient of viscous pressure drop pre-step in seal gap with height tending to zero for range of h_{step}: (a) – Downstream seal gap (δ = -150 µm, h_d = 50 µm), (*b*) – Upstream seal gap (δ = 150 µm, h_u = 50 µm)

3.5.6.3 IPC Pressure Variation

The positive bias observed in the force-displacement relationships for all cases is due to p_{IPC} being significantly higher than expected for the ratio of the gap heights. For example, when the seal housing is displaced downstream and h_u tends to zero, it is expected that the vast majority of the pressure drop across the seal occurs in the upstream seal gap. The pressure in the IPC should therefore be approximately the same value as p_{LP}, or roughly zero in terms of $\frac{p}{p_{HP}}$. Figure 3.39 shows the $\frac{p_{IPC}}{p_{HP}}$ value when the seal housing is displaced as described above (δ = +150 µm) and is hence expected to be close to zero. At p_{HP} = 0.69 bar, there is between 15% and 23% of the total pressure drop still to occur. This increases with inlet pressure to a peak of nearly 60%. This raises the pressure on the downstream seal face, which exerts a higher positive force on the seal housing and hence causes the positive bias. This corresponds to the increase in bias with inlet pressure. The reason for such a high value in the IPC could be attributed to the large side leakages present in the linear LAMFS test rig and compressibility requiring a higher pressure to satisfy continuity. The magnitude of the side leakages is shown in section 3.5.7.

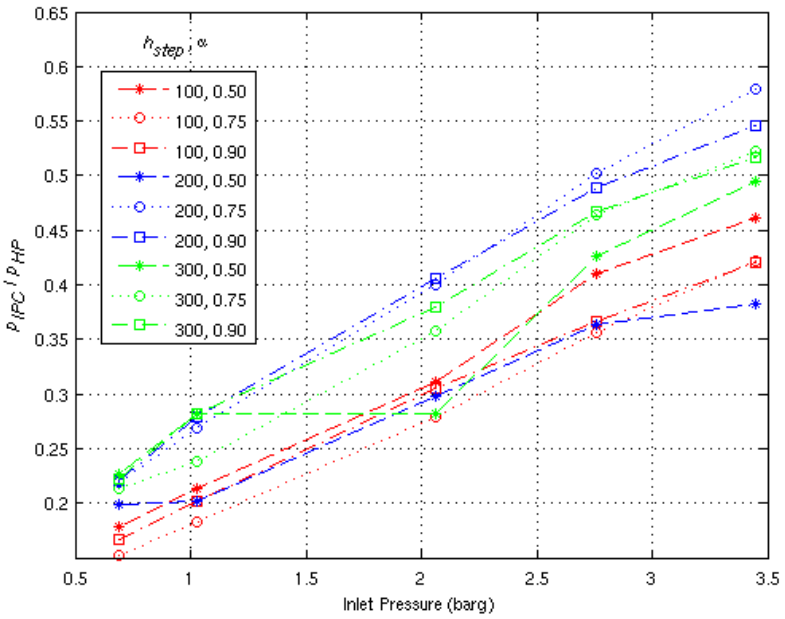


Figure 3.39: Variation in p_{IPC} value with inlet pressure, p_{HP}, at δ = +150 µm (h_u << h_d), h_{stg} = 400 µm,

3.5.6.4 Analytical Model Seal Gap Pressure Distribution

The static pressure distributions through the seal gaps predicted by the analytical model are shown in Figure 3.40 and are compared to the experimental data. Only one particular step height has been shown in order to demonstrate the ability of the model; h_{step} = 300 µm. The inlet pressure is 0.69 bar and h_{tsg} = 400 µm. Figure 3.40 (*a*) and (*b*) correspond to δ = –150 µm and +150 µm respectively. The three step positions of α = 0.50, 0.75 and 0.90 are shown in red, blue and green respectively and are plotted as solid lines for the analytical data and discrete data points for the experimental data. In Figure 3.40 (*a*), where $h_u >> h_d$, almost 100% of the pressure lost occurs in the downstream seal gap for all inlet pressures. The small percentage of loss that exists in the upstream gap is due to the acceleration of the flow into converging gap created by the step. As the flow accelerates into the downstream gap from the IPC, there is another small pressure drop, though this is relatively insignificant due to the relative size of the downstream gap before and after the step: $(h_d + h_{step}) / h_d = 7$. The acceleration, and hence dynamic head of the flow upstream of the step, is small. Once the flow reaches the step, there is an initial drop in pressure as the flow accelerates into the smaller gap height (occurring over a negligible distance), followed by a viscous-induced loss through the remainder of the downstream gap. This is almost identical to the experimental data. In Figure 3.40 (*b*), where $h_u << h_d$, the majority of the pressure loss is through the upstream seal gap from the step location onwards. The IPC value is almost zero, whereas experimentally it is approximately 0.2. A very slight positive bias is observed analytically, which is also seen in the resultant force data, but not to the extent of the experimental data. The model does not account for the influence on the p_{IPC} by the side leakage, as it was not modelled, but appears to replicate the experimental data well otherwise. The inlet losses are seemingly of a more acceptable order when radial steps are present. This may be due to the area change being less drastic as the flow enters the seal gaps.

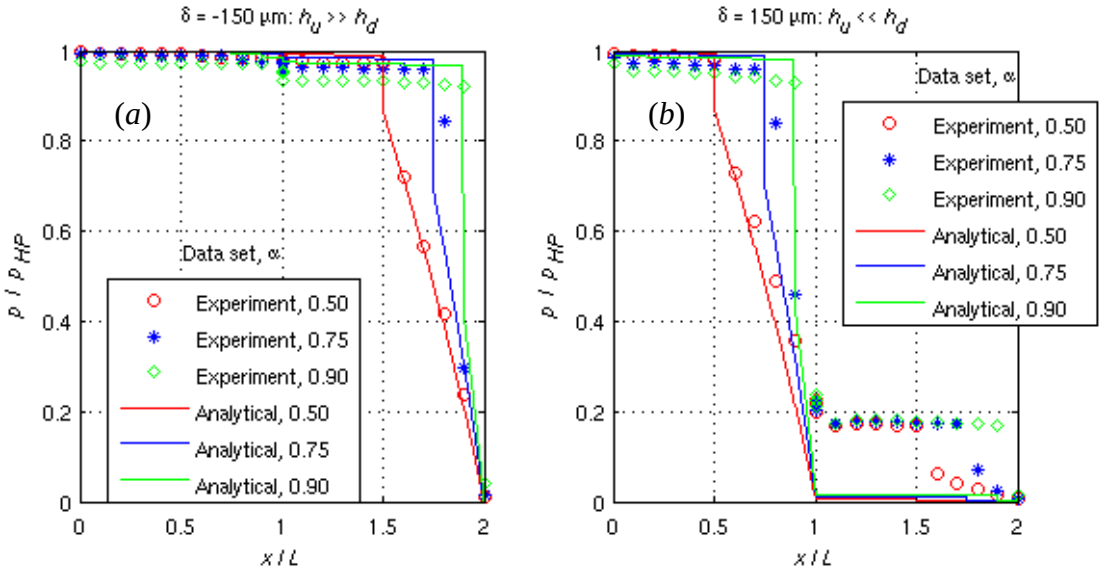


Figure 3.40: Analytical model and experimental seal gap static pressure distributions, p_{HP} = 0.69 bar, h_{tsg} = 400 µm, h_{step} = 300 µm: (*a*) δ = -150 µm, (*b*) δ = 150 µm

3.5.6.4.1 h_{tsg} = 800 µm

The full primary leakage path static pressure profiles for h_{tsg} = 800 µm are shown in section A.3. To explain the relative reduction in positive bias seen at this total gap height (compared to h_{tsg} = 400 µm) described in section 3.5.5.4, the $\frac{p_{IPC}}{p_{HP}}$ values are shown for all step heights across all inlet pressures when δ = 250 µm (100 * h_u / h_{stg} = 18.75 %) and δ = 350 µm (100 * h_u / h_{stg} = 6.25 %). Data is also plotted for h_{tsg} = 400 µm at δ = 150 µm (100 * h_u / h_{stg} = 12.5 %). The value of $\frac{p_{IPC}}{p_{HP}}$ is a function of h_u / h_{tsg} (as well as p_{HP}); as this height percentage decreases, so should $\frac{p_{IPC}}{p_{HP}}$. For the two different h_{tsg} values, there is no data at a position (δ) where the height percentage is equal. However, the height ratio of the h_{tsg} = 400 µm case (12.5%) plotted is mid way between the two h_{tsg} = 800 µm positions (6.25% and 18.75%). It would be expected then that the $\frac{p_{IPC}}{p_{HP}}$ trends for h_{tsg} = 400 µm should be approximately midway between the two h_{tsg} = 800 µm cases, but it is seen instead that they lie higher than anticipated at similar values to the h_{tsg} = 800 µm case, which is at a higher height ratio. This leads to a slightly less positive bias in the h_{tsg} = 800 µm case.

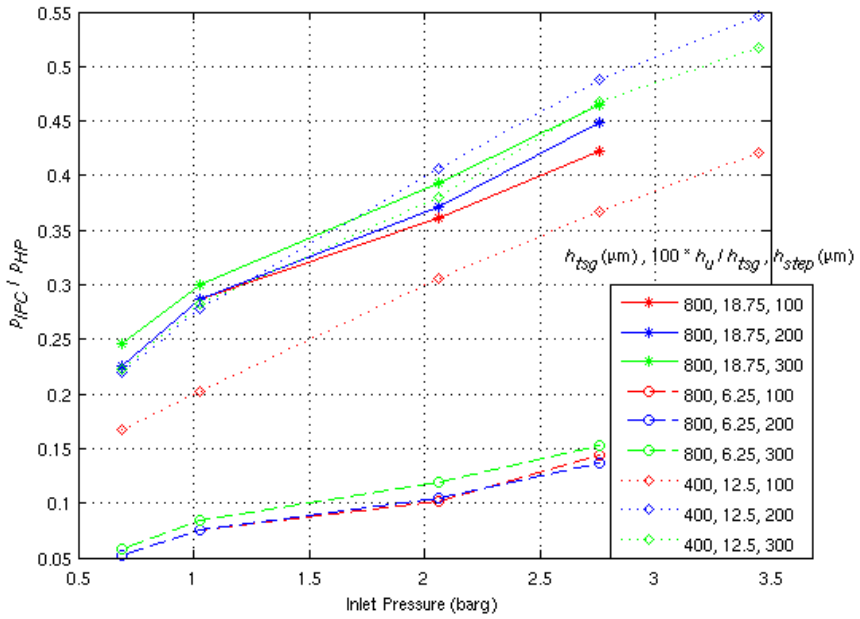


Figure 3.41: $\frac{p_{IPC}}{p_{HP}}$ for h_{tsg} = 800 µm (δ = +250 µm and +350 µm) and h_{tsg} = 400 µm (δ = +150 µm): h_{step} = 100, 200 and 300 µm

3.5.7 Linear LAMFS Results - Leakage Mass Flow Rate

The leakage mass flow rate was taken with respect to the axial position of the seal housing, δ. Figure 3.42 shows the experimental data. At the extremities of the seal housing displacement range, where one of the seal gap heights tends to zero, the mass flow rate is still high whereas analytically, the mass flow rate should also tend to zero.

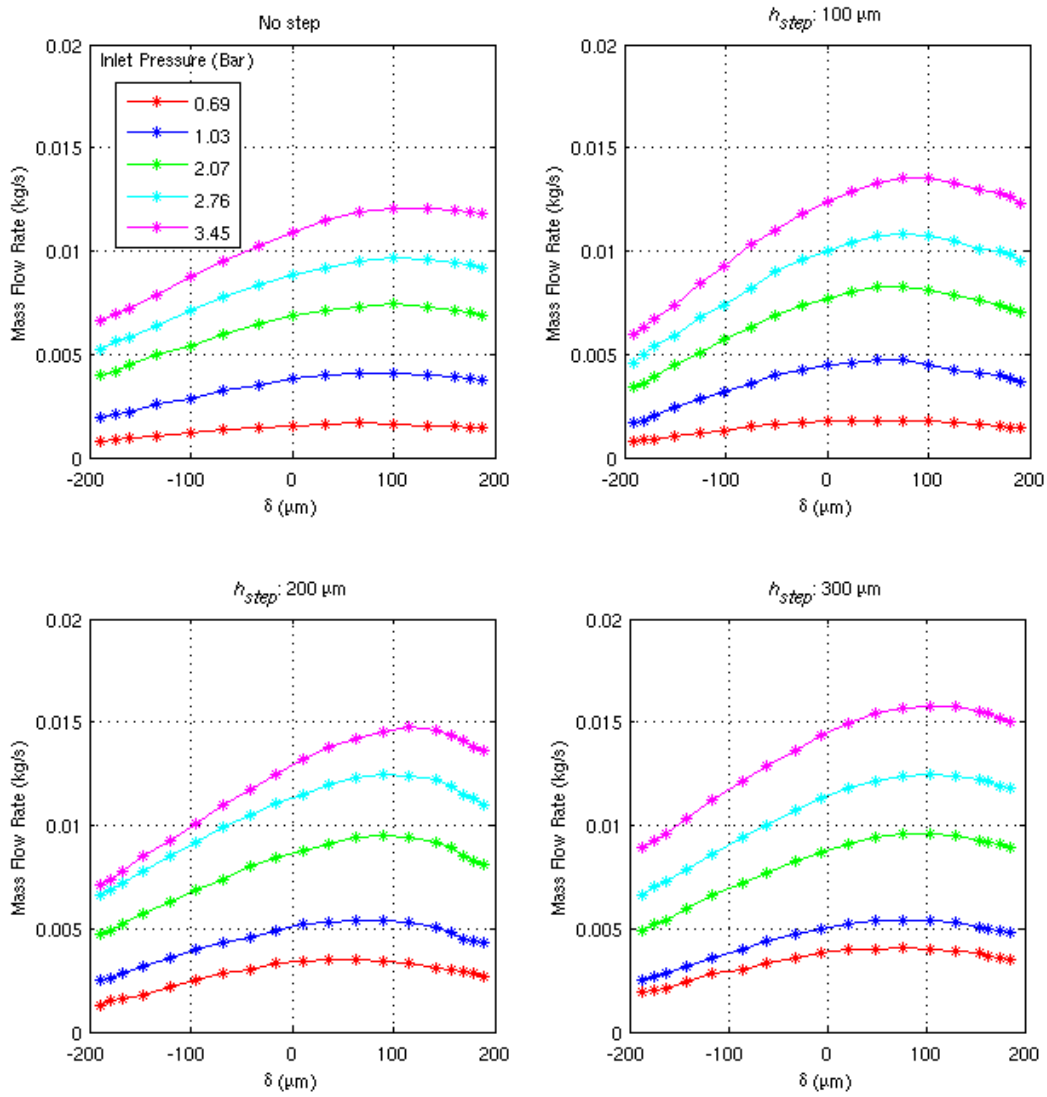


Figure 3.42: Experimental leakage mass flow rate: h_{tsg} = 400 µm (α = 0.90 radial step cases)

This is a result of the additional leakage paths; the side and secondary seal leakages. The mass flow rate is biased to the positive displacement range due to the side leakage as the IPC pressure reduces with increasingly positive δ, which leads to a larger pressure differential driving the side leakage. The secondary leakage flow could be characterised by the use of the analytical model mass flow rate predictions of the primary leakage. To assess the validity of the analytical model, a comparison was made between the experimental and analytical data. The difference was taken between the mass flow of the h_{tsg} = 400 µm and the h_{tsg} = 800 µm cases for each data set where a direct comparison could be made i.e. p_{HP} = 0.69, 1.03, 2.07, and 2.76 bar. h_{step} = 100, 200 and 300 µm and α = 0.9. The side leakage is dependent on the value of IP, which is itself dependent on the relative size of h_u and h_d (δ). Therefore the two

cases of h_{tsg} = 400 µm and 800 µm are compared by normalising their displacement. The secondary seal leakage is constant (independent of δ).

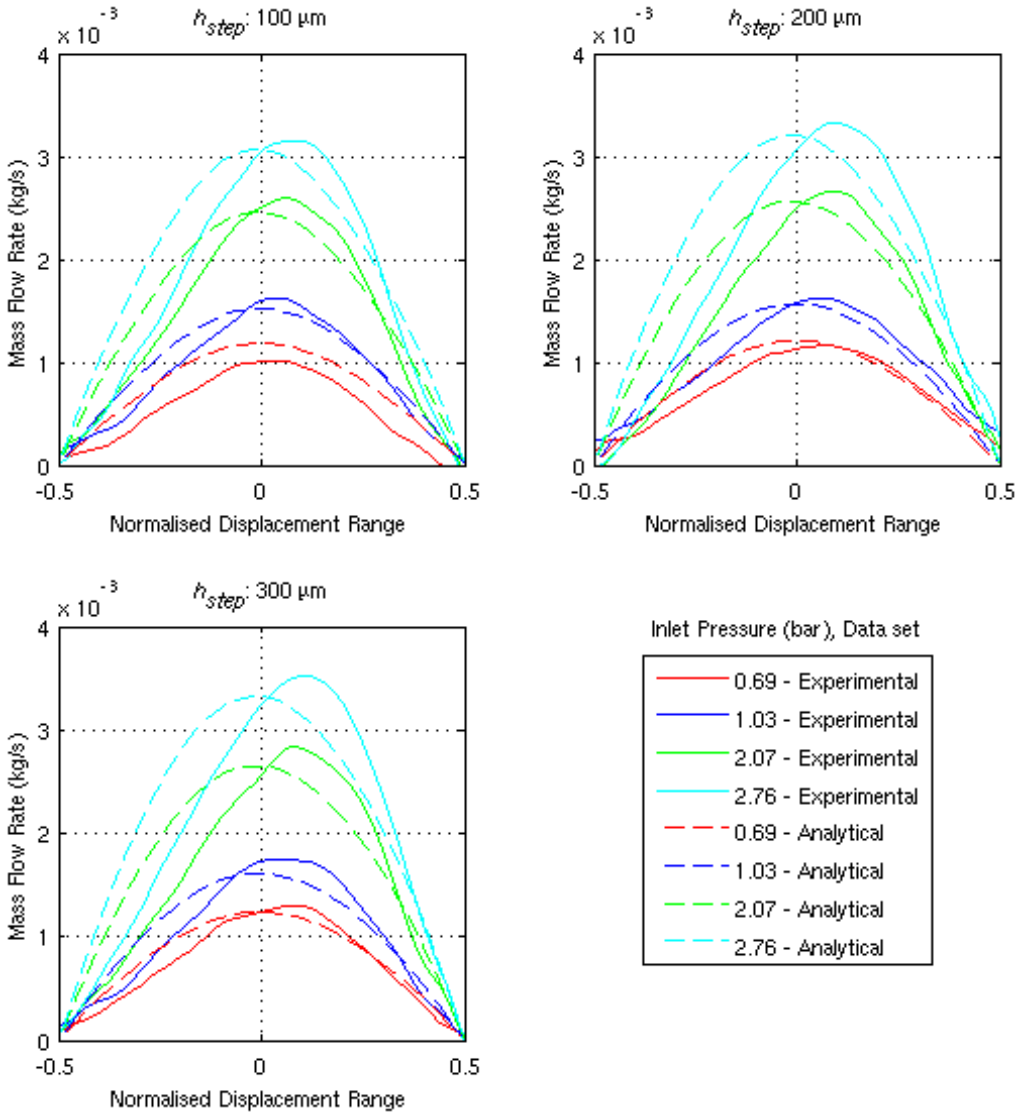


Figure 3.43: Difference between h_{tsg} = 400 µm and h_{tsg} = 800 µm for experimental (total leakage) and analytical (primary only) leakage mass flow rates (difference in primary leakage) α = 0.90

The curves for the difference in mass flow between the h_{tsg} = 400 µm and the h_{tsg} = 800 µm cases for experimental (total mass flow rate) and analytical (primary leakage only) data are displayed in Figure 3.43. The analytical data shows that the difference in primary leakage mass flow rate between the two total gap heights yields a curve similar to what is expected for a primary leakage path; the maximum flow rate occurs when δ = 0 (h_u = h_d) and the flow tends to zero at the peripherals of the displacement range. This is also seen, almost identically,

in the experimental data when the difference in total mass flow rate is taken for the two total gap heights, which indicates that the secondary leakages for both h_{tsg} = 400 µm and h_{tsg} = 800 are near identical across the normalised displacement range. What remains from the experimental data is a difference in the primary leakage, which correlates well to the analytical solution. Hence, the secondary leakage magnitude is independent of h_{tsg} and this also shows that the analytical model can accurately predict the primary leakage mass flow rate. From the three graphs in this figure it is also noticed that the difference in primary leakage increases with step height, which is to be expected as the average gap height is increased.

If the analytical model can accurately predict the primary leakage mass flow rate, then the secondary leakage can be evaluated by taking the difference between the total leakage from the experimental data and the primary leakage (analytical solution). The secondary leakage for h_{tsg} = 400 and 800 µm is shown below in Figure 3.44 and as expected, the magnitude of the secondary leakage is independent of the total seal gap height, h_{tsg}. It is also independent of the step height, h_{step}, and hence shows that the total secondary leakage depends on the relative gap heights h_u and h_d, not primary leakage path geometry. The variation in mass flow rate with displacement is due to the associated variation of p_{IPC} and subsequently the pressure difference driving the side leakage. The leakage through the secondary seal remains constant with displacement. Figure 3.45 below shows the total secondary leakage broken down into the two secondary leakage components. The secondary seal leakage (blue) is constant with displacement, whilst the side leakage (green) increases from zero at the maximum negative displacement to its peak at the maximum positive displacement. The sum total is shown in red.

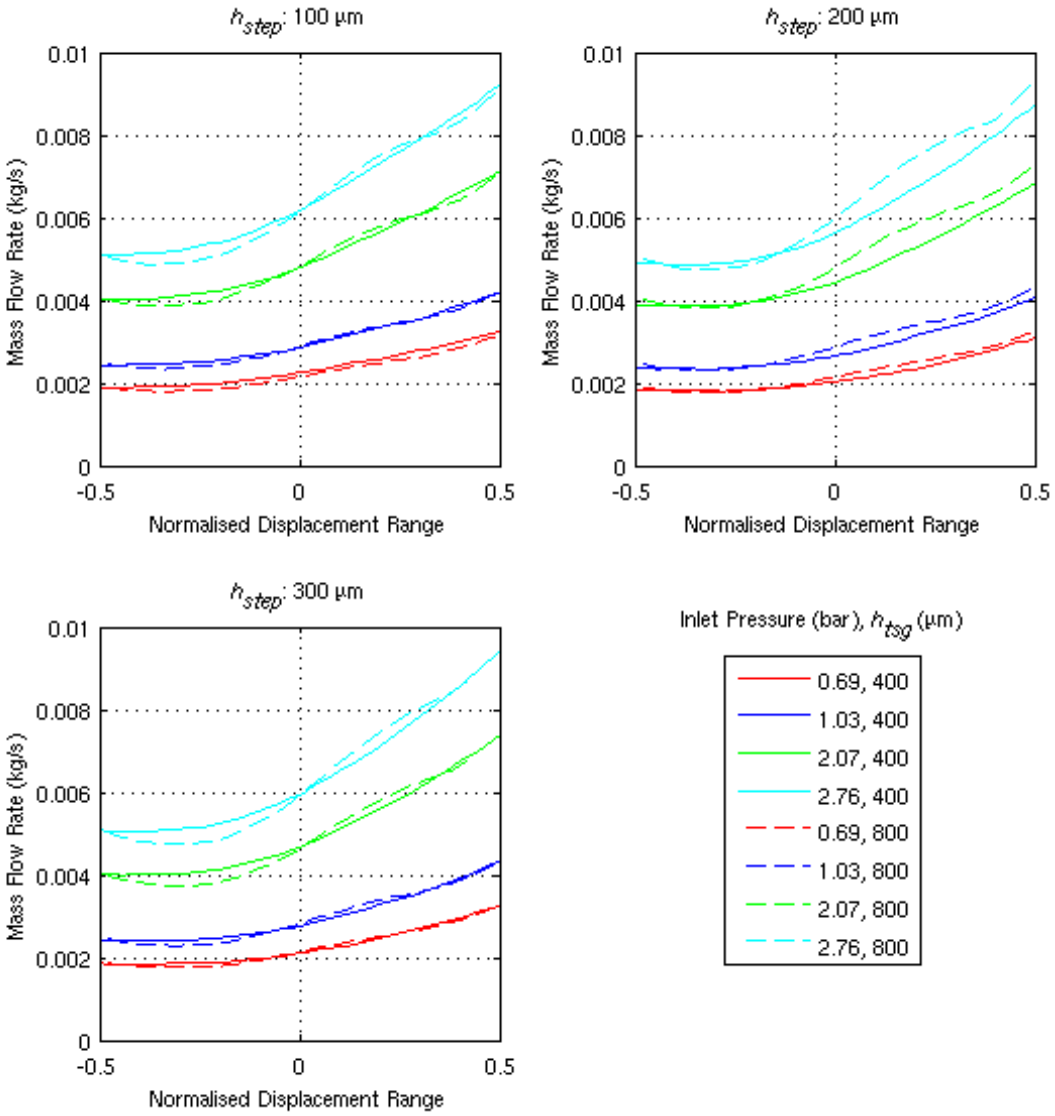


Figure 3.44: Secondary leakage for h_{tsg} = 400 µm and 800 µm, α = 0.90

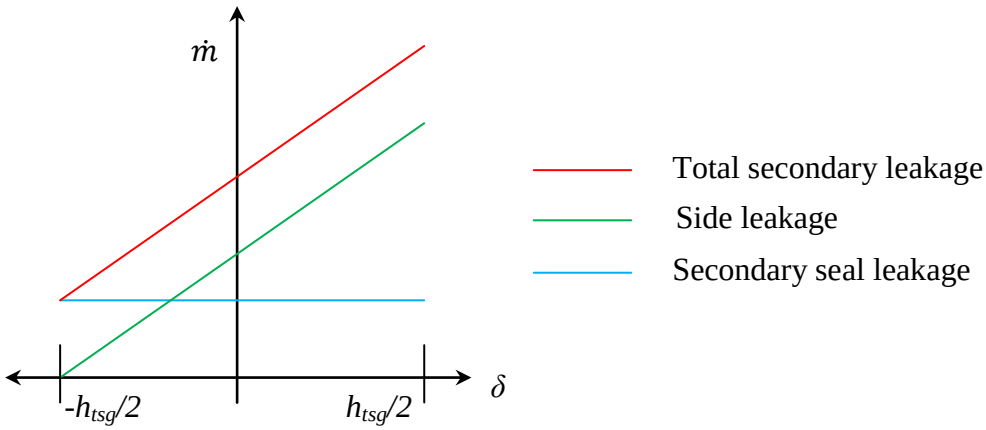


Figure 3.45: Linear LAMFS test rig secondary leakage profile: blue – secondary seal, green – side leakage, red – total secondary leakage

3.6 Summary

An extensive investigation has been carried out into the LAMFS concept devised by Rolls Royce plc using a test rig containing a linear version of this seal. The aim of the research in this chapter was to create a passive control system for the axial position of the seal housing relative to the rotor disc such that it is consistently and reliably a non-contacting sealing method. The concept then exhibits great potential to improve engine efficiency and boast a component life span significantly longer than the service period of an engine between major overhauls as wear will be negligible. Experimental data, CFD and an analytical model have all shown that an unstable seal housing behaviour will be observed with parallel seal faces (baseline geometry), although the trends of these three data sets did not match well. Acquiring a self-centring seal housing was then attempted by modifying the seal gap geometry to influence the static pressure distributions within the seal gaps which vary with the axial position of the seal housing relative to the rotor. It was then predicted analytically and confirmed experimentally that a stable, self-centring seal housing behaviour can be achieved by the use of radial steps. The agreement between these two data sets was significantly better for this seal gap geometry.

The parameters investigated with regards to the converging step geometry were the step height, h_{step}, at 100, 200 and 300 μm and the step position downstream of the gap inlet as a percentage of the radial gap length, α, at 50, 75 and 90%. The inclusion of a step in the gap determines the radial position at which the majority of the pressure drop occurs within a seal gap due to the relative size of the gap height upstream and downstream of the step. By delaying the pressure drop through a given seal gap by positioning the step further downstream, the average pressure on that seal face is effectively raised. As the step height increases and hence does the pre-to-post-step gap height ratio, the viscous pressure drop pre-step is reduced and nearly the entirety of the loss ensues post-step, which also leads to a

further small increase in the average pressure on a seal face. Data showed that the magnitude of the restoring resultant force increased with h_{step} and α. The step has relatively little effect on the pressure distribution within a seal gap whose minimum height is much larger than the other and is most effective when the minimum height is smallest of the two gaps. This is when the increase in average pressure, and hence the force, on a seal face is most desirable; to move the faces apart.

A positive bias, which was dependent on inlet pressure, was observed on the force displacement relationships whereby the equilibrium points traverse in the positive displacement direction. This was confirmed by the static pressure distributions showing that the IPC pressure rises with inlet pressure. This was partly attributed to the side leakage inherent in the linear test rig. The total seal gap height, h_{tsg}, was also investigated at 800 μm, double the original height, and the three step heights were all tested at a position of α = 90%. This also produced a self-centring seal housing and showed that if a larger total seal gap height is required for a particular location in a gas turbine where a particular mass flow rate is desired, the converging radial step geometry in the seal gaps will still provide the desired seal housing behaviour.

The analytical model derived to predict the static pressure distribution throughout the primary leakage path was based on Reynolds 1D equation. When compared to the experimental data, it emerged why the discrepancies occurred between the two sets of data for the force-displacement relationship. The static pressure losses at the seal gap inlets greatly affect the primary leakage path static pressure profile. Equating these losses to one dynamic head of the flow entering the seal gap proved to be generally inaccurate. A correlation was devised between an inlet loss coefficient and the inlet Reynolds number based on the gap height and pressure at the seal gap inlet which greatly improved the analytical model predictions.

The leakage mass flow rate with respect to seal housing position, δ, was obtained experimentally and compared to the analytical model's prediction. Due to the considerably large secondary seal and side leakages, the leakage profile was heavily influenced and differed from a leakage profile solely from the primary leakage flow. The analytical model was used to characterise the secondary leakage of the linear LAMFS test rig as its prediction of the primary leakage was highly accurate. This was taken from the experimental total leakage to give a secondary leakage which was not constant with displacement as the variation in the IPC pressure directly affects the driving pressure gradient for the side leakage flow.

To prove the LAMFS concept, a fully annular version of the seal, which eliminates side leakage, needed to be tested. Confirmation of the ability of the converging step geometry to heavily influence the seal housing behaviour in the desired way was required. A test rig was designed and manufactured for this purpose and the details of this test rig and experimental data obtained from it are provided in chapter 4.

4 Annular Large Axial Movement Face Seal

4.1 Introduction

An annular version of the LAMFS was manufactured to assess the seal in 3D space. The purpose of this is to eliminate side leakage inherent to the linear test rig and develop a facility to allow testing with shaft rotation to assess rotational effects and hydrodynamic-induced pressure fields. When the seal is converted from the linear LAMFS test rig geometry to an annular version there are two inherent differences that occur. Firstly, the leakage paths between the linear LAMFS test rig end plates and the sides of the seal housing no longer exist as the annular geometry is a continuous volume created by revolving the seal housing cross-section 360° about the engine axis. The other difference is in the seal gap geometry and arises from the change in radius as the flow travels through the primary leakage path. The seal gap cross sectional area varies with radius for a set of parallel seal surfaces as the area of a leakage path at a radius of r and clearance h is $2\pi rh$. Hence the relationship between the leakage path cross-sectional area and radius is linear, thus for parallel seal faces, and from the flow's point of view, the upstream seal gap cross-sectional area increases whilst the downstream gap area decreases in the annular seal. The equivalent seal gap geometry for the linear seal is a diverging taper in the upstream gap and a converging taper in the downstream gap. The inner and outer radius of the annular seal gaps are 69.5 mm and 80.5 mm respectively which leads to an area change of approximately 15% over the 11 mm long seal gap.

Initial tests were performed on the annular seal with the baseline geometry with a static rotor. The total seal gap height was the same as investigated with the linear LAMFS test rig (h_{tsg} = 400 µm) for the same range of inlet pressures. This was done to confirm that this geometry was unable to provide the desired seal housing behaviour. The seal gap geometry was then modified to contain converging radial steps and was also tested under static rotor conditions to compare with the linear LAMFS test results. Only one of the step heights and step positions from the linear LAMFS investigation was tested on this rig by the author. The results from this seal gap geometry are extremely promising. Concerns about the effect of the change in seal gap cross-sectional area with radius were no longer applicable as these were insignificant in comparison to the area change with steps present. The experiment was designed to originally to include a spinning rotor and the setup is described in the following sections. However safety issues could not be overcome for the high rotational speeds required for the experiment, and so this aspect of the experiments was abandoned. CFD was used instead to quantify the hydrodynamic effects. For possible future work, the rig capable of spinning is described in detail regardless, should the rig be commissioned with rotational capability.

3D CFD was performed on the test seal for the two seal gap geometries described above under static rotor conditions and the force-displacement results were in good agreement with the experimental data. The rotor was then modelled as spinning at engine representative surface speeds for both the baseline and radial step seal gap geometries and the difference in the resultant force was negligible. This is confirmed by Reynolds equation. Circumferential geometry features to generate hydrodynamic lift were also incorporated into the CFD model but were ineffective. Leakage mass flow rates for the experimental and CFD data are presented along with effective clearance values for the experimental primary leakage path flow, which are an improvement on current in-service brush seals. The dynamic behaviour of the seal housing was simulated, using the experimental force-displacement relationships

obtained, under transient rotor axial position conditions and shows a highly responsive behaviour and the ability to accommodate large step changes in relative velocity whilst preventing seal-rotor contact.

4.2 Annular LAMFS Test Rig

A schematic of the annular LAMFS test rig is shown in Figure 4.1. The seal housing encapsulates the rotor, which is a disc, and seal housing axial position is varied by a linear actuator. The resultant force exerted by the seal housing on the linear actuator is transmitted through a load cell and can therefore be measured. The double-headed arrows indicate that the seal housing and load cell can translate in the axial direction. The digital dial gauge records the position of the seal housing and is in contact with the seal housing upstream external face.

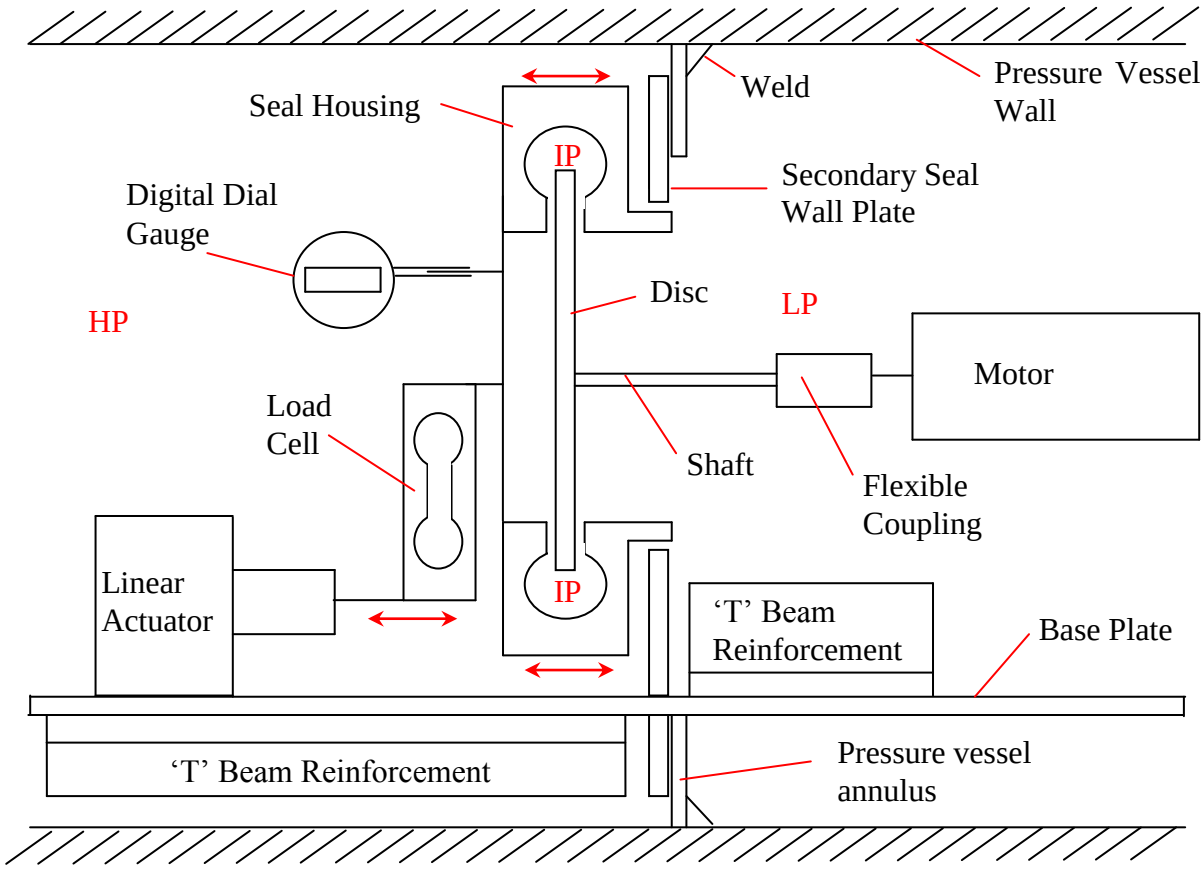


Figure 4.1: Schematic of annular LAMFS test rig

The disc is mounted on a shaft which is supported within a bearing housing and is driven by a motor. A flexible coupling and speed sensors are positioned between the disc shaft and the motor for safety reasons. The base plate to which the components are attached is reinforced by 'T' beams on the upstream and downstream side of the secondary seal wall plate position. The test rig was designed such that it could be assembled in its entirety externally before being inserted into the pressure vessel from the upstream end. The components that comprise the annular self-centring radial seal are described in detail below in section 4.2.1. Figure 4.2 displays the test rig in its fully assembled state.

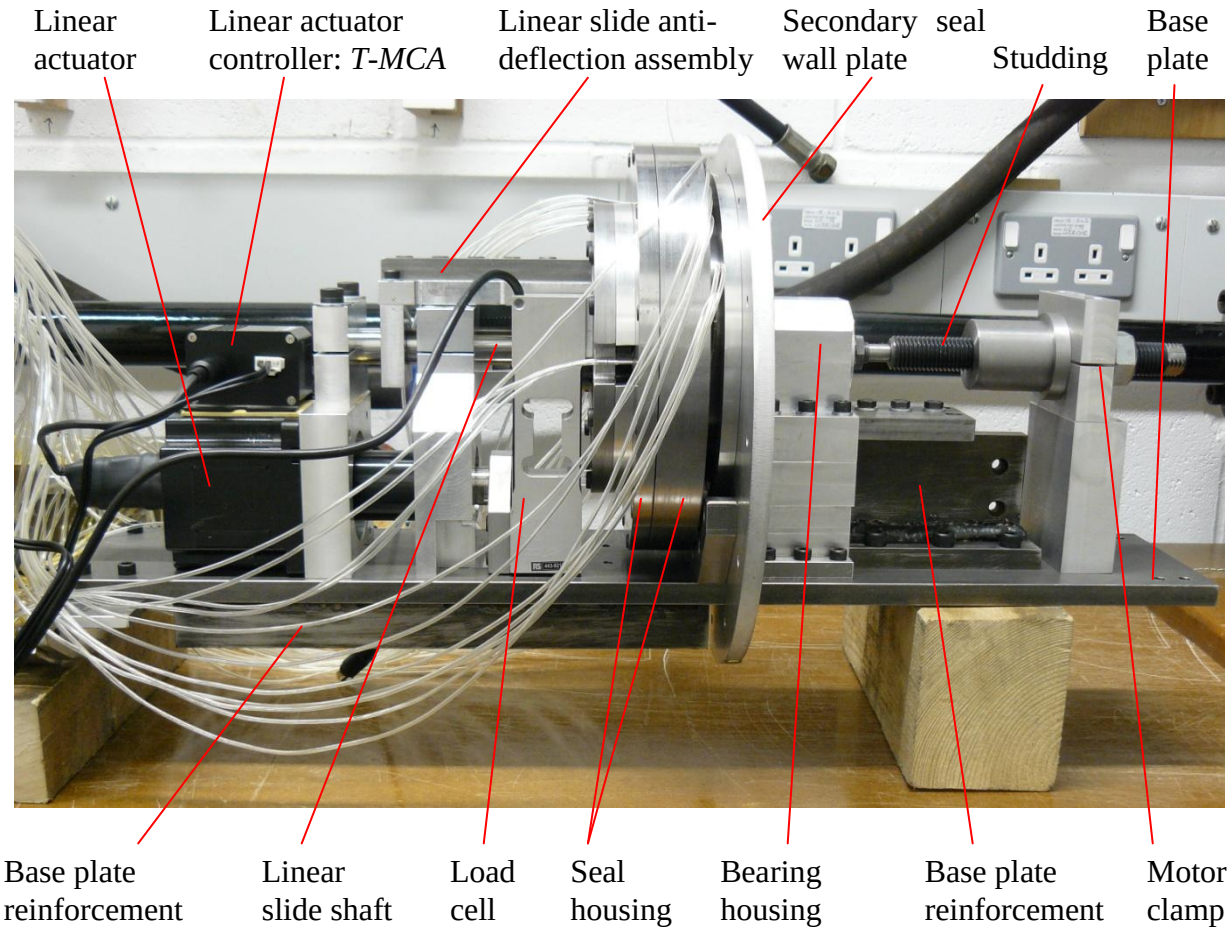


Figure 4.2: Fully assembled LAMFS test rig on base plate

4.2.1 Key Components

This section describes the major components involved in the annular LAMFS test rig and a more detailed diagram of some of these components is displayed in Figure 4.3.

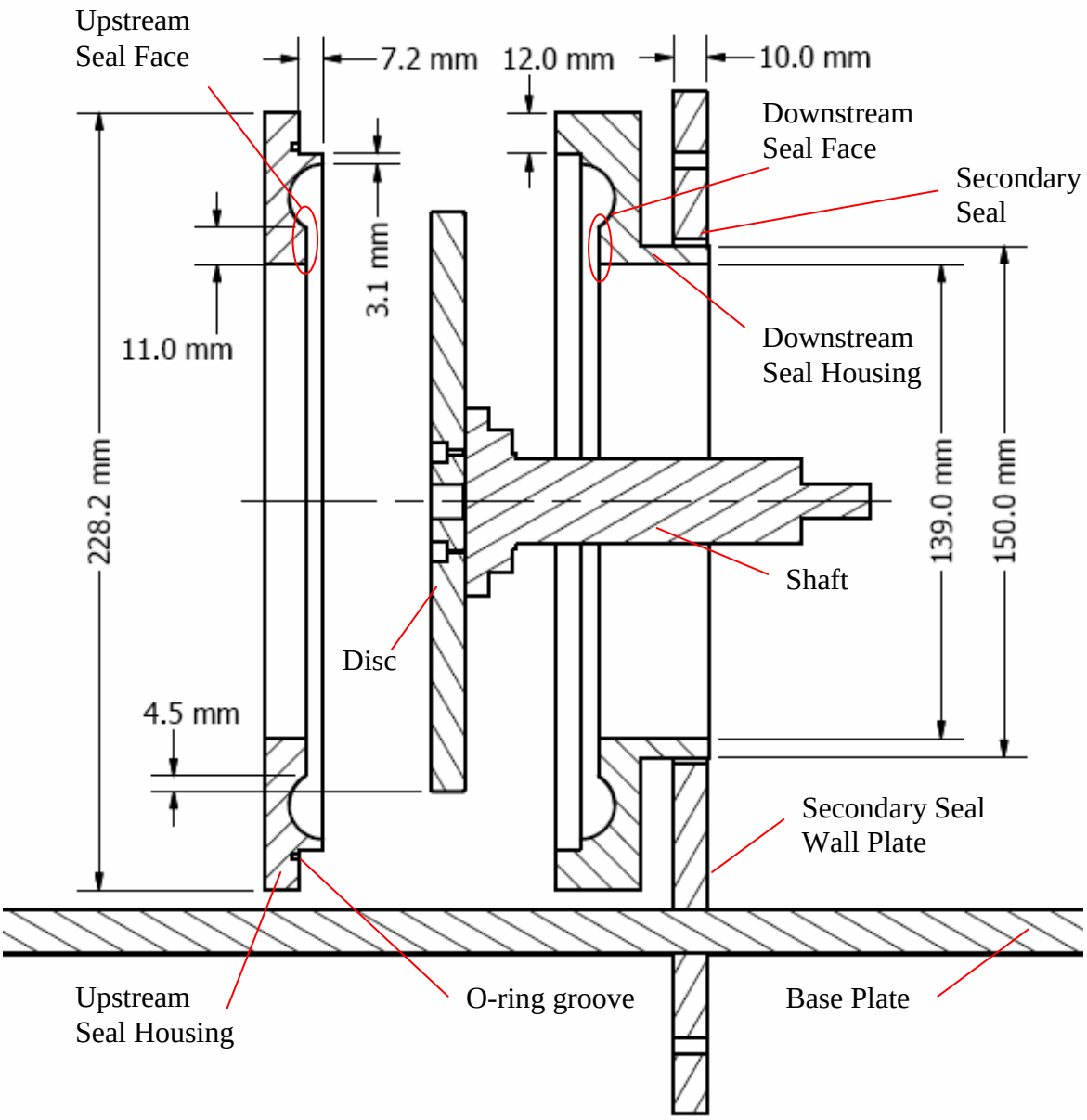


Figure 4.3: Cross section of annular LAMFS key components

4.2.1.1 Seal Housing

The seal housing was manufactured from mild steel and was created in two separate parts in order to allow the disc to be positioned between them. The dimensions of the cross section are detailed in Figure 4.3. When combined together into one component, the cross section is identical to that of the linear LAMFS test rig. The seal gap radial length remains at 11 mm. An O-ring is placed between the two parts in a groove cut out of the upstream seal housing part as shown to prevent leakage from the HP region directly into the IPC. The lip on the

upstream part at the interface region and dowel pins ensured the parts were repeatedly concentric. A *Bosch R072352086* linear slide supports the weight of the seal housing and allows it to be traversed in the axial direction. It is circular in cross section and placed concentrically with the seal housing. This linear slide model permits unrestricted axial movement but prevents rotation about its axis, which is a consideration for experiments if, in future, the disc is run up to high rotational speed where a torque may be induced on the seal housing. The linear slide shaft diameter is 20 mm which was chosen for its rigidity. The seal housing is attached to the flange on the linear slide bushing. An anti-deflection assembly was necessary to ensure the linear slide bushing and shaft axes remained parallel during operation.

4.2.1.2 Disc

The rotor disc was manufactured from Hykro steel (0.25% carbon, 3% chromium, 0.6% molybdenum) which had been hardened and tempered in order to cope with the stresses induced when rotating at high speed. The dimensions were 10 mm thickness and 170 mm diameter, which is 9 mm greater than the outer diameter of the seal surfaces and penetrated the IPC by 4.5 mm.

4.2.1.3 Secondary Seals

The secondary seal wall plate had a letterbox hole for the base plate to fit though and a circular hole for the secondary seal arm to fit within with ample clearance. The secondary seal was then mounted on the upstream face of the secondary seal wall plate. The two options for the secondary seals were a brush seal or a solid ring which formed a tight clearance around the secondary seal arm as in the linear test rig. The brush seal had an inner diameter (bristle tips) of 150 mm and the bristles were at a lay angle of 39°. The blow-down effect, described in 1.1.2, increases the contact pressure between the bristle tips and the secondary seal arm and

hence the friction on the secondary seal arm, which affects the force-displacement relationship, would need to be characterised. The alternative secondary seal was manufactured to exhibit a 100 μm clearance across the diameter of the secondary seal arm to give a gap height of 50 μm comparable to the linear test rig. The secondary seals were mounted to the secondary seal wall plate by a fitting which allowed a small degree of freedom to allow the chosen secondary seal to be concentric with the seal housing.

4.2.1.4 Linear Actuator

To traverse the seal relative to the rotor disc, a linear actuator was incorporated into the design as the test rig was enclosed within the pressure vessel and therefore the seal housing axial position could not be controlled manually. A *Zaber NA 34C60* was used which was capable of producing sufficient force to overcome the axial force magnitude generated by the seal and had a more than adequate linear resolution of 0.198 μm to allow any seal position to be obtained.

4.2.1.5 Motor

Although tests were not performed with a rotating disc, the motor which would drive the disc is described here. It is designed to be placed downstream of the secondary seal within the LP region. An *Isel Automation – UFM 1050* electric lathe motor was chosen for this application. It has an operating window of between 10 krpm and 25 krpm which is sufficient to achieve at least $100ms^{-1}$ surface speed at the seal surface radius to replicate engine conditions and evaluate any hydrodynamic effects. The motor torque is transmitted to the downstream end of the disc shaft via a *Huco* (part no. 466.33.3232) flexible coupling and a 32 fin slotted disc with an optoswitch as a speed sensor.

4.2.1.6 Base Plate

A base plate was used to assemble all the components before inserting them within the pressure vessel. A steel plate of length 650 mm and cross section 12.7 mm x 127 mm (0.5" x 5") was used. The plate had three supports to prevent deflection under the component weight and stresses transmitted to it from the forces measured by the load cell; one at each end and one provided by the flat surface of pressure vessel annulus (Figure 4.4). The upstream end-support bolted to the inner surface of the pipe whilst the downstream end-support was welded to the inner surface. To prevent any bending and deflection of the base plate, reinforcements were provided in the form of 'T' cross-section beams which were bolted by their top flat surface to the base plate. Due to the presence of the secondary seal wall plate, the reinforcement needed to be split into two sections. The section upstream of the secondary seal wall plate was placed on the underside of the base plate due to the presence of all the components on the top surface. The section on the downstream side of the secondary seal wall plate was restricted to the top side of the base plate as a result of the pressure vessel annulus during assembly (the test rig enters the pressure vessel from the upstream side). This reinforcement also provided an additional support to the bearing housing. Under the maximum pressure difference across the seal of 3.45 bar, the axial pressure force on the disc is almost 8 kN which applies a moment on the base plate at the location of the bearing housing supports. Despite these reinforcements to the base plate, the deflection downstream of the disc due to pressure loading was reduced to approximately 300 μm, instead of 1.2 mm, though this still resulted in the disc and seal axes being significantly non-parallel. To eliminate the deflection entirely during static tests, a screw mechanism (a length of studding) was clamped in the motor mount which could exert the necessary force on the downstream end of the shaft to return it to its original position. This method was extremely effective for performing static tests but the design prevented achieving a safety certificate for the test rig for a moving rotor.

4.2.1.7 Pressure Vessel

The pressure vessel, which effectively represents the casing as shown in Figure 3.3, was manufactured using a 660 mm length of 12” inner bore diameter standard section steel pipe rated to 40 bar was used. A *Victualic* endcap and an internal division ring (pressure vessel annulus) provided the high pressure cavity. The secondary seal wall plate mated with the upstream face of the internal division plate.

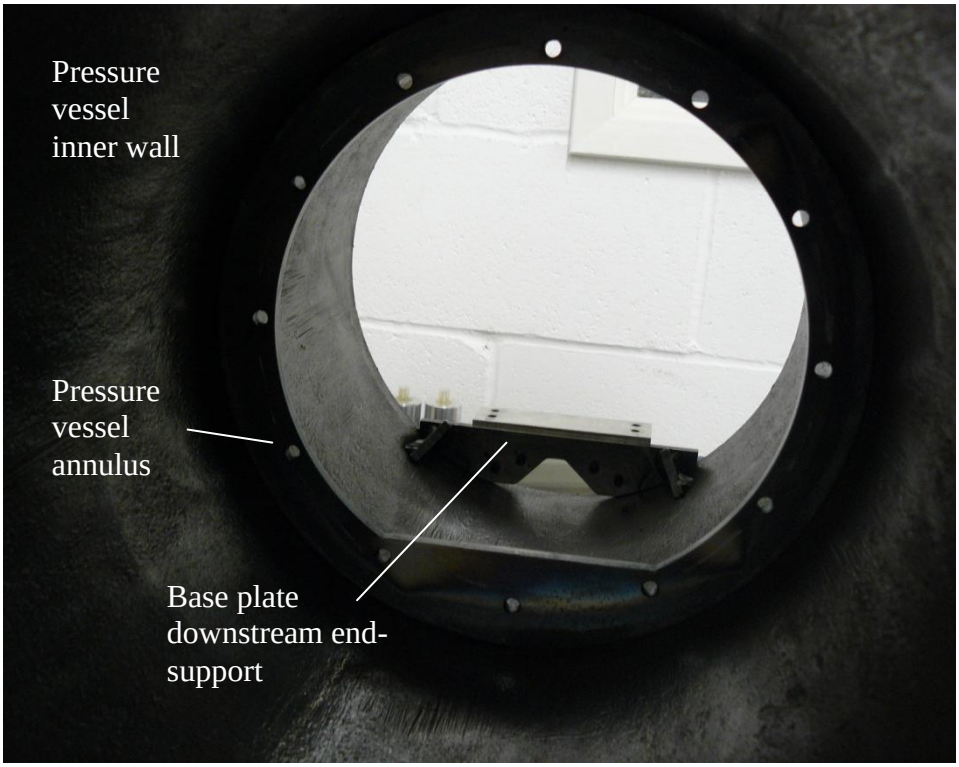


Figure 4.4: Internal view of the pressure vessel with pressure vessel annulus and base plate end-support

4.3 Instrumentation

To record the measurements from the various transducers, a *CIO-DAS802/16* 16 bit data acquisition board was used. One *Sensor Technics CTE7005GP0* 0-5 bar range was permanently used to measure the total pressure within the HP region. The 39 pressure tappings used to acquire the pressure distributions within the seal gaps were measured with either two *PTE5015D1A* 0-15 psi (0-1.034 bar) or two *PTE5005D1A* 0-5 bar range transducers. The orifice meter required a low range differential pressure transducer to capture

the pressure drop across the orifice plate which was achieved with a low range *PTE5000* series transducer. The pressure upstream of the orifice plate was measured with either a *PTE5015D1A* 0-15 psi (0-1.034 bar) range or *PTE5005D1A* 0-5 bar range transducer, depending on the inlet pressure. A 75 kg capacity *Tedea Huntleigh* single point load cell was used to measure the axial force on the seal housing. A *Soemer LAC 65.1* load cell analogue converter connected the load cells to the data acquisition card and provided the excitation. All pressure transducers and the load cell were connected to the data acquisition card via a NI *BNC 2110* shielded connector block with 8 analogue inputs. The orifice meter thermocouple was recorded by using a *NI USB-9211* 4 channel thermocouple reader which was transmitted to the data acquisition PC through a USB port. The position of the seal housing relative to the disc was monitored with a *Mitutoyo Absolute* digital dial gauge. The leads from the instrumentation within the high pressure cavity exited through a series of flanged plugs attached to the inside surface of the end cap.

4.3.1 Pressure Tapping Locations

The nature of the annular pressure balanced seal test rig is such that the pressure tappings within the seal gaps cannot be placed within the disc to allow it to rotate. The tappings are hence placed in the seal housing seal faces instead as shown in Figure 4.5. The seal gap static pressure was measured in four locations around the seal face circumference; 0° - top dead centre (TDC), 90°, 180° and 270°. The arrangement of the pressure tappings used in the linear LAMFS test rig was also employed at TDC whilst a lower resolution was applied to the other three locations which were used to assess whether the seal gap heights were consistent around the whole circumference. Due to the limitations for placing the tappings imposed by the seal housing geometry, only 10 tappings were placed in each of the seal gaps at TDC due to the inner radius location being unable to adequately support a tapping. This tapping reading was heavily skewed in the linear LAMFS test rig and so was not necessary. Three tappings were

placed on each seal face at 90°, 180° and 270° at the positions shown. One tapping was also taken from the IPC. This gave a total of 39 tappings; TDC – 20, 90° – 6, 180° – 6, 270° – 6, IPC – 1. A 2 x 24 channel scanivalve multiplexer was used, with the 20 tappings from TDC on one bank of 24 channels and the remaining 19 on the second bank of 24.

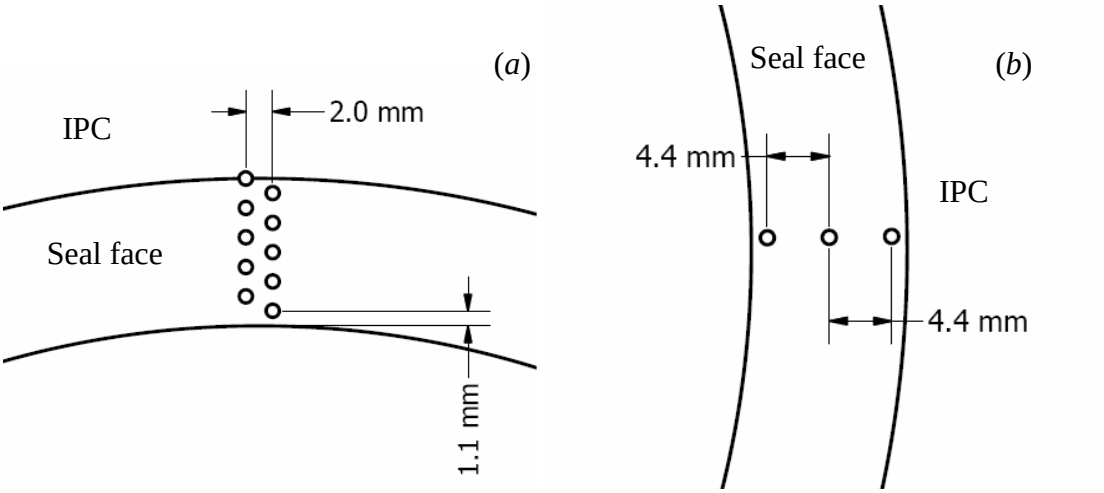


Figure 4.5: Static pressure tappings in seal gaps of annular self-centring seal test rig: (*a*) – top dead centre, (*b*) – 90° (shown), 180° and 270°

4.3.2 Data Capture

LabVIEW [2007] was used to monitor and record the data from all the transducers on the test rig. 50 samples were taken at a rate of 20 Hz and averaged to give each data point. Multiple data points were taken across the full range of the seal housing displacement when measuring the resultant load, and at all these positions the leakage mass flow rate was also measured. The 39 static pressure channels were recorded at 3 different positions of the seal housing in order to compare with the 3D CFD analysis (δ = –150 µm, 0 µm and +150 µm). The seal position was controlled by the *Zaber Console*; the accompanying software for the linear actuator. For each test, the process began by setting the regulator to achieve the desired pressure within the high pressure region within the test rig. The seal housing would be moved to the farthest position in the upstream direction, then the seal housing was traversed downstream and data would be recorded at the predetermined locations as done in the linear

tests. Once completed, the data was saved into a single-precision tab-delimited ASCII data file.

4.3.3 Uncertainty

4.3.3.1 Direct Measurements

Table 4.1 below displays the random and systematic errors associated with all transducers used in the annular LAMFS test rig. The method for calculating these uncertainties is described fully in section 3.3.2.3.

Measurement	Systematic Uncertainty	Random Uncertainty
Force (75 kg)	0.155 N	0.137 N
Pressure (70 mbar)	64.7 Pa	49.3 Pa
Pressure (350 mbar)	272.6 Pa	239.4 Pa
Pressure (5 bar)	6800 Pa	925 Pa
Pressure (15 psi)	0.102 psi	0.0986 psi
Displacement	None quoted	0.0015 mm
Temperature	2.89 K	0.154 K

Table 4.1: Annular self-centring radial seal test rig transducer uncertainties

4.3.3.2 Computed Measurements

Mass flow rates were computed, and the error associated, by the methods described in described in section 3.3.2.3. The maximum mass flow rate uncertainty was calculated at 3.6%.

4.3.4 Measuring Secondary Leakage

Leakage through the secondary seal was quantified by eliminating the primary leakage flow. This was achieved by covering the upstream side of the disc with a layer of neoprene thicker than h_{tsg} (≈ 1 mm) such that the seal housing clamped this between the disc and the upstream seal face. The assumption is made that flow velocity in the HP region is approximately zero

and hence the secondary seal leakage is independent of the primary leakage. Mass flow rates were then measured for the five inlet pressures to obtain values for the secondary leakage. These were subtracted from the total leakage data to give the primary leakage mass flow rate which could then be more directly compared to the CFD data.

4.4 Three Dimensional CFD

4.4.1 Geometry

The geometry modelled with 3D CFD was based on that of the annular pressure balanced seal test rig, in that the dimensions of the seal are identical, but the inner radius on either side of the disc represents the shaft as in an engine case. In the test rig the shaft surfaces do not exist, merely a disc is present but this will have a negligible effect on the flow field as the velocity of the flow in the main volume will be close to zero and h_{uin} is much smaller than the distance between seal housing and shaft. A 20° sector of the full annulus was created to reduce the mesh size required to model the seal with sufficient accuracy and hence periodic boundary conditions were applied as shown in Figure 4.6. The cross-sectional geometry of the domain revolved around the axis was near identical to the cross section of the linear test rig. The secondary seal was modelled as a tight tolerance fit, as was used in place of the brush seal, with a clearance of 50 μm. The whole of the upstream face of the domain was given a pressure inlet boundary condition, whilst the two pressure outlet boundary conditions were as shown. Three seal displacements were created and solved for: –150, 0 and +150 μm. Three different geometries within the seal gaps were investigated; the baseline case of parallel seal faces, radial steps to create converging flow paths as in the research conducted for chapter 3, and circumferential steps for hydrodynamic pressure generation in conjunction with the radial steps described. The geometry of the radial steps were as follows; h_{step} = 200 μm and α = 0.5 as was tested experimentally. The circumferential geometry was a 100 μm deep step removed

from a 10° sector with radial limits equal to that of the seal gaps. These were 'cut' from the rotor surface. Figure 4.7 shows the radial and circumferential steps in the CFD domain.

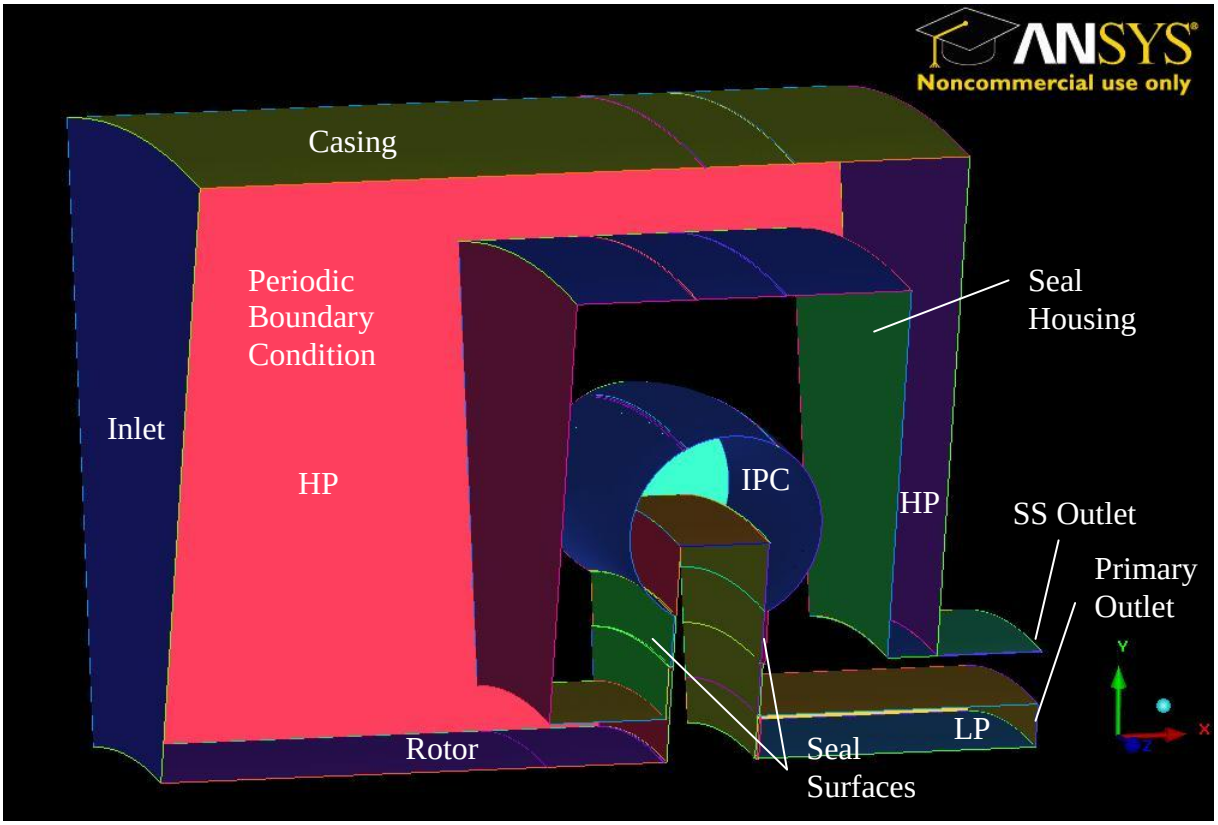


Figure 4.6: Annular sector CFD domain surface geometry (nearer periodic face removed)

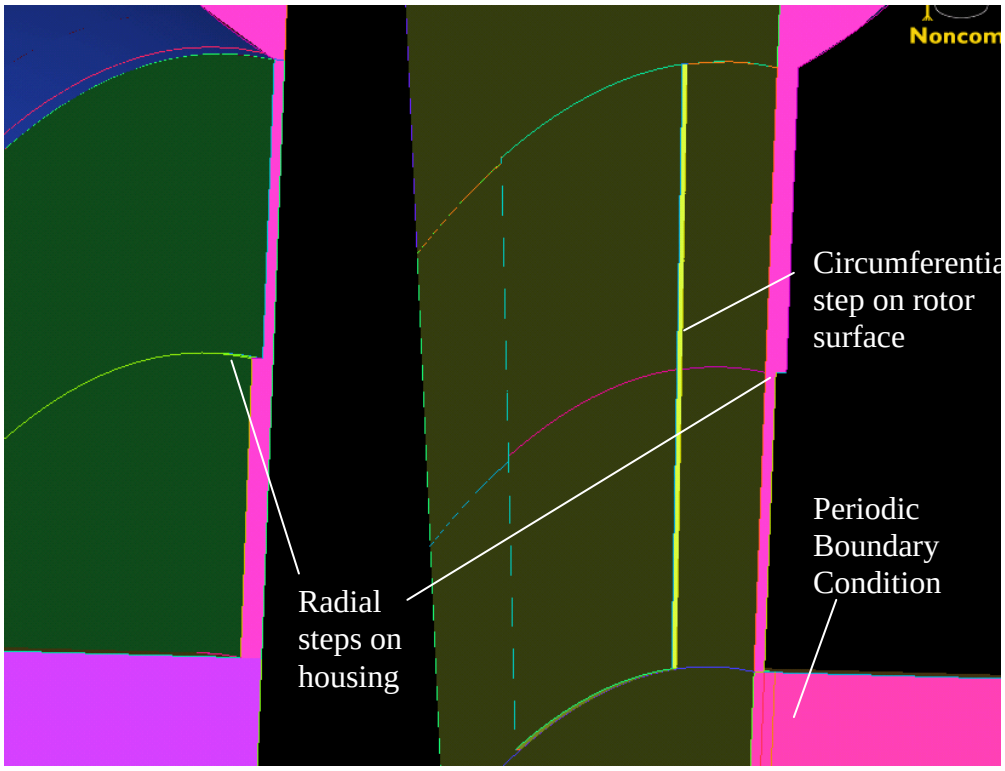


Figure 4.7: Annular sector CFD domain surface seal gap geometry – radial and circumferential steps

4.4.2 Mesh

Meshes were created using *ICEM 11* and were structured due to the axisymmetric nature of the geometry. A mesh sensitivity study was performed to determine the quantity of cells and hence the resolution required. A mesh size of 500,000 elements was deemed to be sufficient with a mesh sensitivity study.

4.4.3 Solving

The method to solve the CFD simulations was the same as described in section 3.4.4.3.

4.5 Results

In this section, the results of the experimental and CFD research are presented. All data related to the baseline geometry (parallel seal walls) is discussed first followed by the radial step geometry within the seal gaps. For each seal gap geometry investigated, the seal housing resultant force, primary leakage path static pressure distribution and leakage mass flow rate data is shown. Effective clearance values are also given for the radial step case.

4.5.1 Parallel Seal Surfaces

4.5.1.1 Resultant Force

The seal housing force-displacement relationship from the annular test rig for parallel seal gaps is shown below in Figure 4.8. The two lowest pressures of 0.69 bar and 1.03 bar display very similar trends. Starting from the most upstream position of the seal (δ = –200 µm) and traversing downstream, the force is initially positive (restoring) and exhibits a negative gradient as would be desired. An equilibrium point is reached where the force changes direction. However, from -100 µm onwards, a minimum exists and the gradient becomes positive until a second equilibrium point is experienced, though the positive gradient leads to an unstable behaviour and the seal housing snaps to its downstream limit imposed by the disc. This force-displacement would be entirely undesirable. The 2.07 bar and 2.76 bar cases

display similar trends which differ in magnitude by approximately 75 N across most of the range of displacement. An inlet pressure of 3.45 bar gives the highest magnitude of force of all cases at 330 N. The highest three pressure cases all experience a force that is permanently positive and no equilibrium position exists which would lead to the seal housing permanently forced against the upstream surface of the disc. The force-displacement relationship for the parallel seal faces clearly shows that a modification to the geometry within the seal gaps is required to produce a stable, self-centring behaviour.

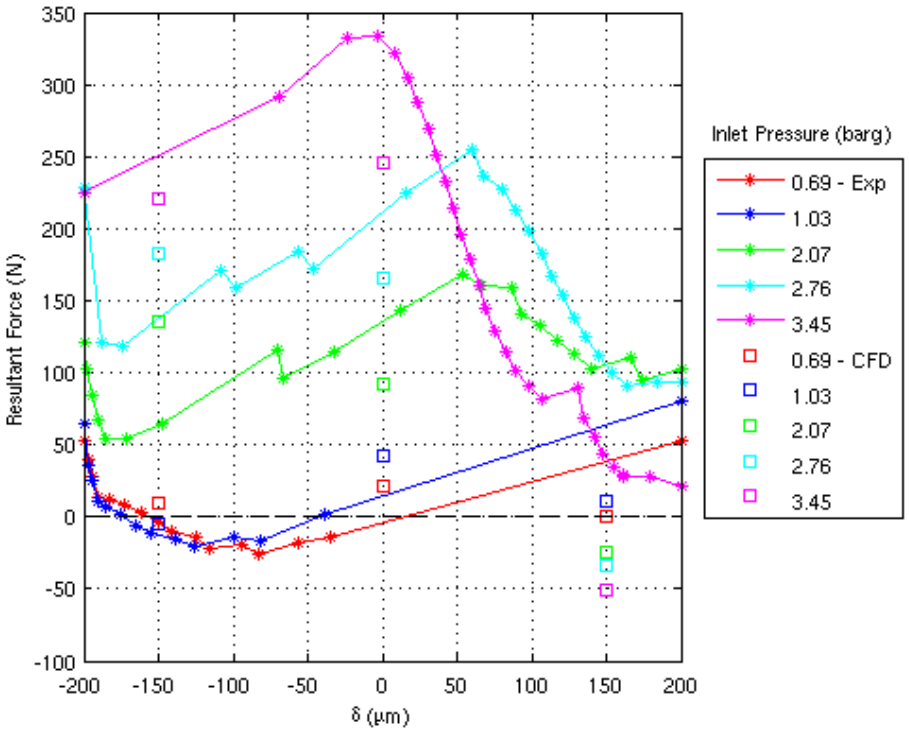


Figure 4.8: Experimental and CFD seal housing resultant force –Parallel faces: h_{tsg} = 400 µm, static disc

The force-displacement relationship predicted by the annular sector CFD is also shown in Figure 4.8. For the two lowest pressure cases, the force is positive across the displacement range except briefly for the 1.03 bar inlet pressure case at -150 µm. Both pressures exhibit a non-ideal behaviour. When the inlet pressure is 2.07 bar and above, the trends appear to be self-centring as the overall gradient is negative and they contain an equilibrium position at approximately 120 µm displacement. When compared to the experimental data, the general trend across the range of pressures is very similar where the magnitude of the resultant force

increases with inlet pressure in the positive (downstream) direction. The 3.45 bar inlet pressure case is in best agreement with the experimental data but the equilibrium point predicted by the CFD would change the behaviour from purely unstable to possessing a self-centring ability.

4.5.1.2 Seal Gap Pressure Distribution

Experimental (black) and CFD (red) seal gap pressure distributions for parallel seal surfaces from the annular test rig are shown in Figure 4.9, Figure 4.10 and Figure 4.11, which correspond to –150 µm, 0 µm and 150 µm seal housing displacement. The position through the primary leakage path is defined by x / L as in the linear LAMFS data where 0-1 on the x-axis represents the upstream seal gap and 1-2 represents the downstream seal gap. The IPC pressure is plotted at $x / L = 1$. The y-axis is the static pressure normalised to the inlet pressure (p_{HP}). At –150 µm displacement, Figure 4.9, $h_u >> h_d$ and hence very little pressure is lost through the upstream seal gap, which can be seen for all pressures and in both sets of data. The pressure drop in the downstream gap is near linear for 0.69 bar and 1.03 bar, which was also seen in the linear experiments in section 3.4.7. The highest three inlet pressure cases see a nonlinear pressure drop in the downstream seal gap as the conditions required for compressible flow are met. Comparing the two sets of data, the agreement between the two is extremely good for 0.69 bar and 1.03 bar. The inlet losses are negligible and the viscous pressure drop is linear which leads to a near-zero resultant force, as is reflected in Figure 4.8. There is very little inlet loss at entry to the upstream seal gap as the mass flow rate should be low. As the inlet pressure increases and hence does the mass flow, the inlet loss appears to increase for both the experimental and CFD data though they differ in the magnitude.

At $\delta = 0$ µm , where $h_u = h_d$, the discrepancies between the two sets of data are greater. At this seal housing position, the mass flow rate is at a maximum and hence the inlet losses are greater. Under incompressible conditions (p_{HP} = 0.69 bar and 1.03 bar) the predictions by the

CFD for the inlet losses to the upstream seal gaps are quite inaccurate. The inlet losses to the downstream gaps, however, are of a similar size but in general the pressure profiles do not match well for these inlet pressures. The inlet losses for the highest three inlet pressure cases are more accurately predicted by the CFD though the gradient of the pressure drop through the upstream seal gap is much steeper. The cross-sectional area of the upstream seal gap in the annular version of this seal increases with distance downstream (radius) and hence the pressure drop after the initial inlet loss should be minimal as shown by the CFD. This may be due to a slight misalignment between the disc and seal housing leading to constant or converging area seal gap cross-sectional area. The pressure drop profile in the downstream seal gap, however, is very similar between the two sets of data.

When δ = +150 μm and $h_u << h_d$, almost all of the pressure drop occurs through the upstream seal gap. Viscous pressure drops are linear for p_{HP} = 0.69 bar and 1.03 bar and non linear for the remaining inlet pressures. As for when δ = –150 μm, the inlet losses to the smaller seal gap height are far less than at δ = 0 μm as the mass flow rate is significantly lower.

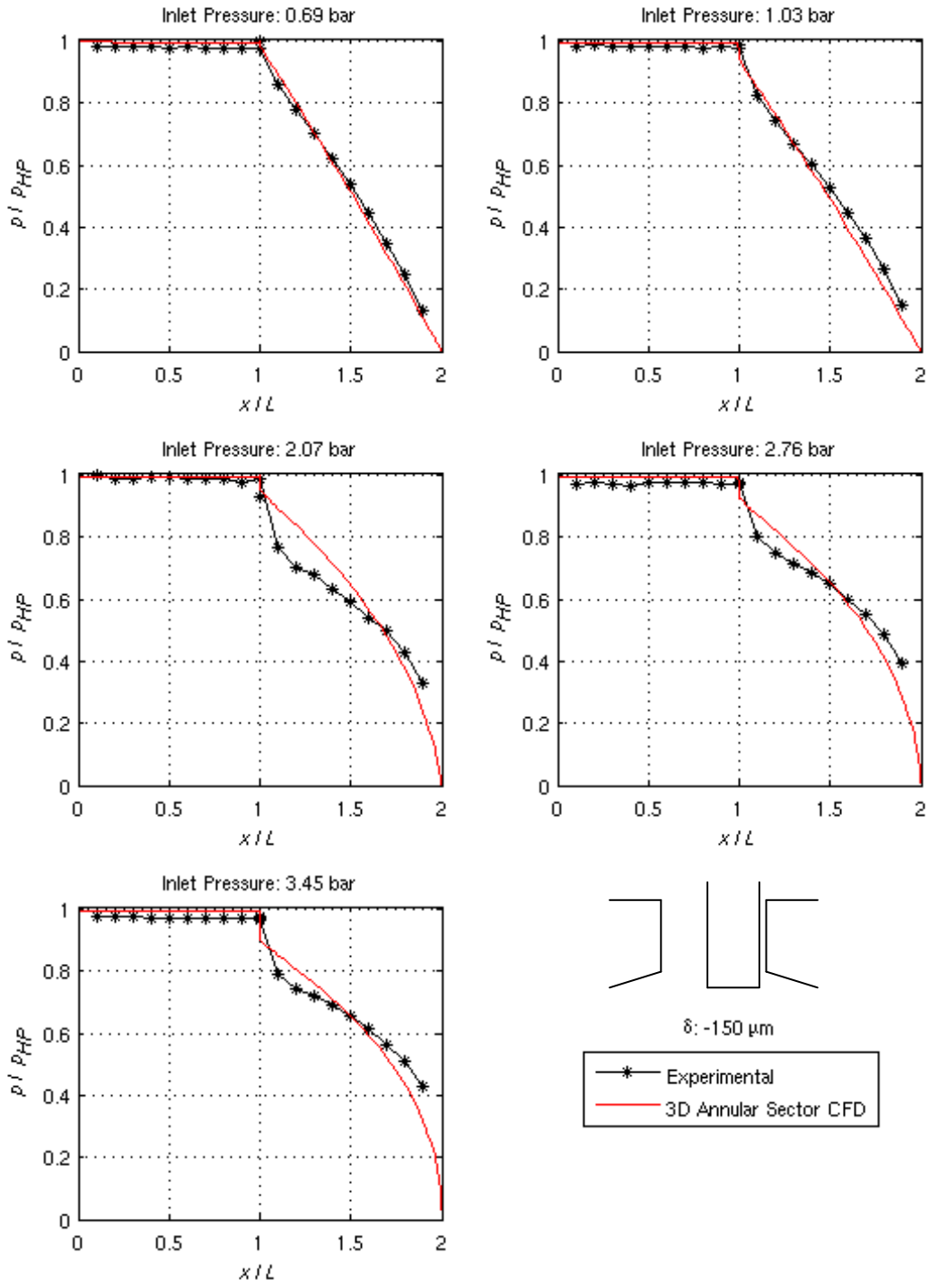


Figure 4.9: Static pressure distribution in annular seal gaps – Parallel faces: h_{tsg} = 400 µm, δ = -150 µm

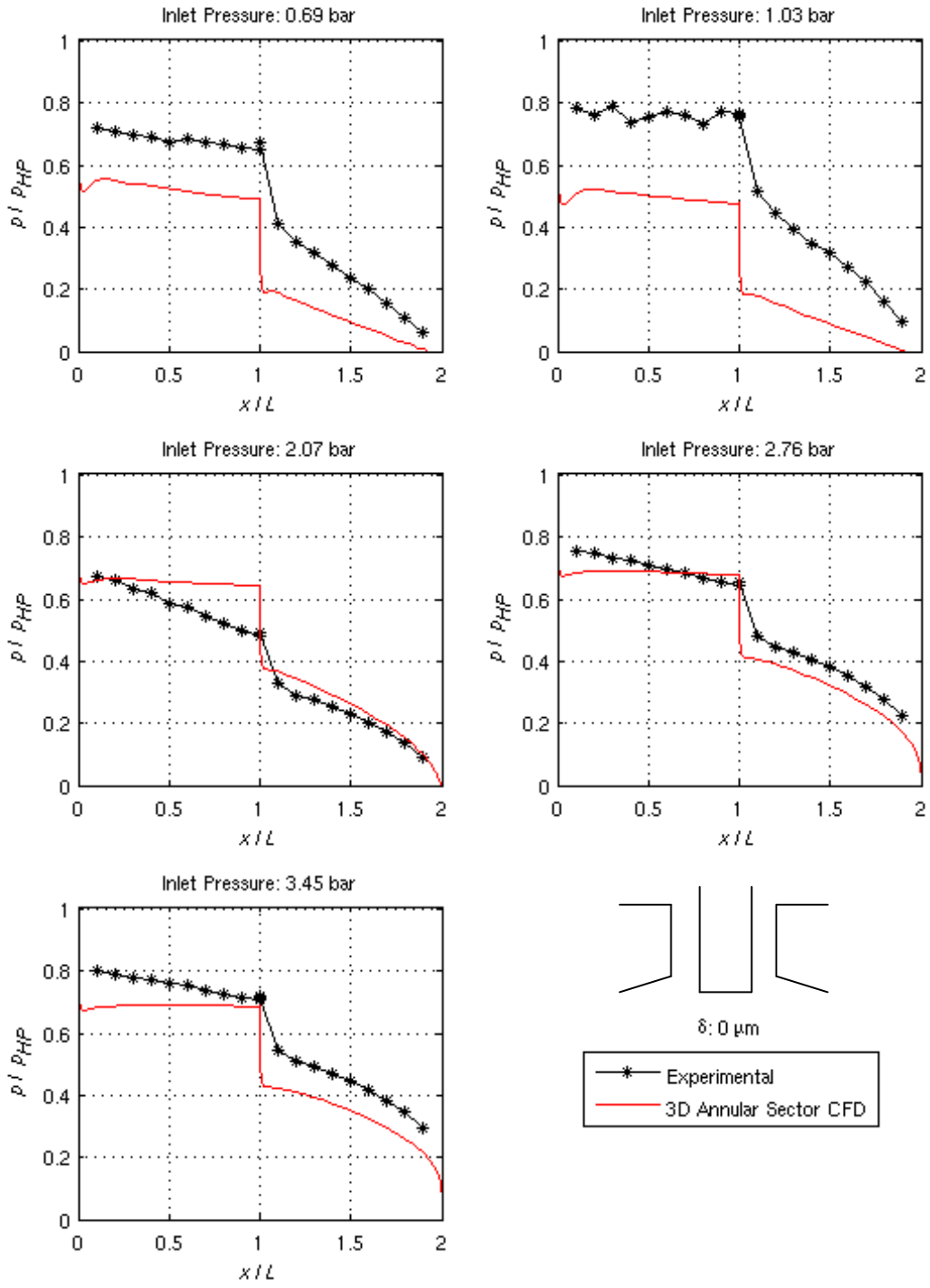


Figure 4.10: Static pressure distribution in annular seal gaps – Parallel faces, h_{tsg} = 400 µm, δ = 0 µm

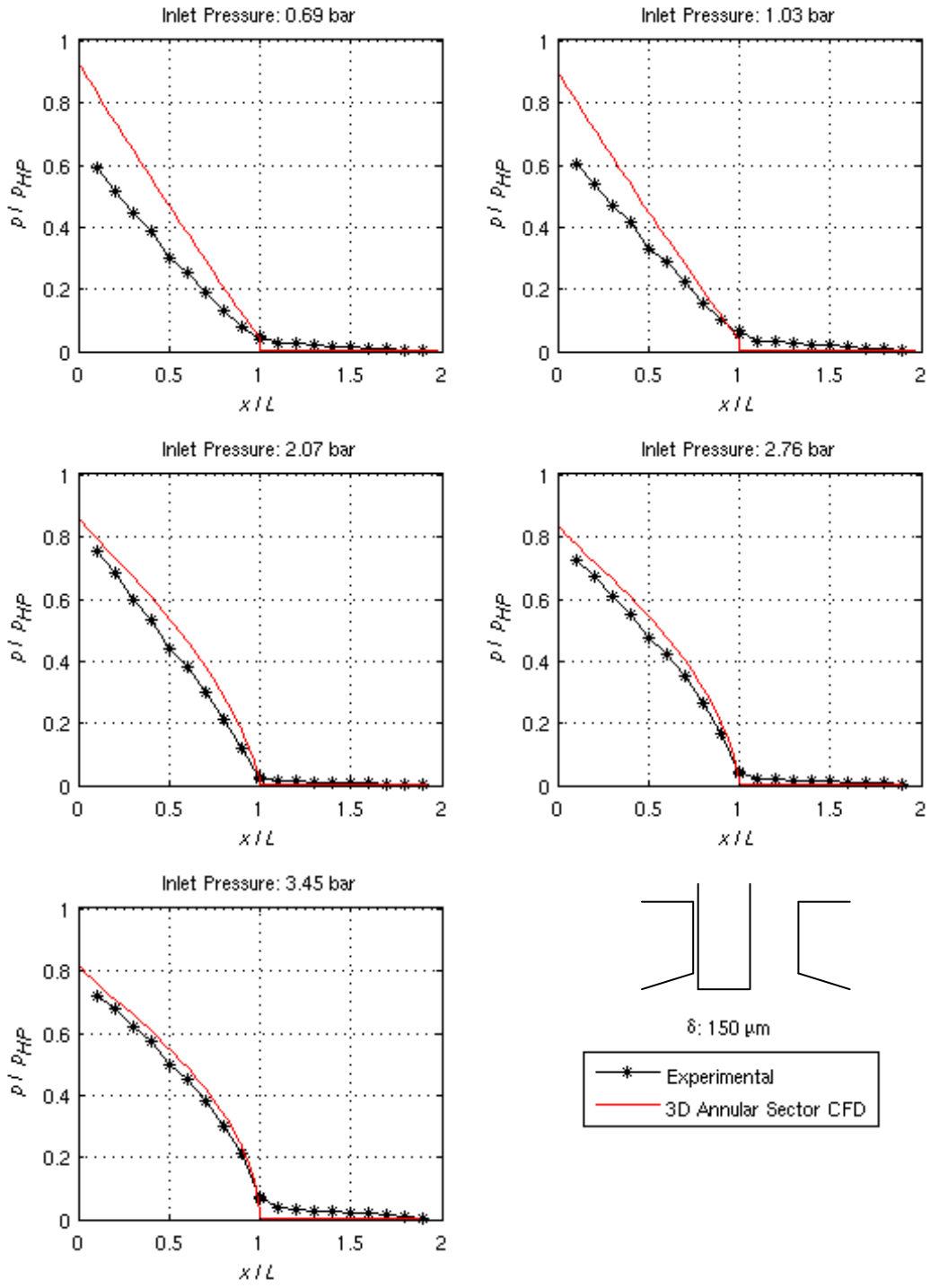


Figure 4.11: Static pressure distribution in annular seal gaps – Parallel faces, h_{tsg} = 400 µm, δ = 150 µm

4.5.1.3 Leakage

The experimental leakage data for the annular LAMFS is displayed below in Figure 4.12. The trend is such that the minimum mass flow rate occurs at the maximum displacements of the seal housing where either h_u or h_d tends to zero. The peak flow rate exists at, or very close to, the central position where $h_u = h_d$. As seen in the linear test rig, the total leakage is significantly influenced by the secondary leakage; the fully annular seal has no side leakage but the secondary seal (brass tight-clearance ring) and other leakage paths clearly permit significant mass flow. Replacing the brass secondary seal with the brush seal would reduce the secondary seal flow significantly (as in a brush seal compared to a labyrinth seal).

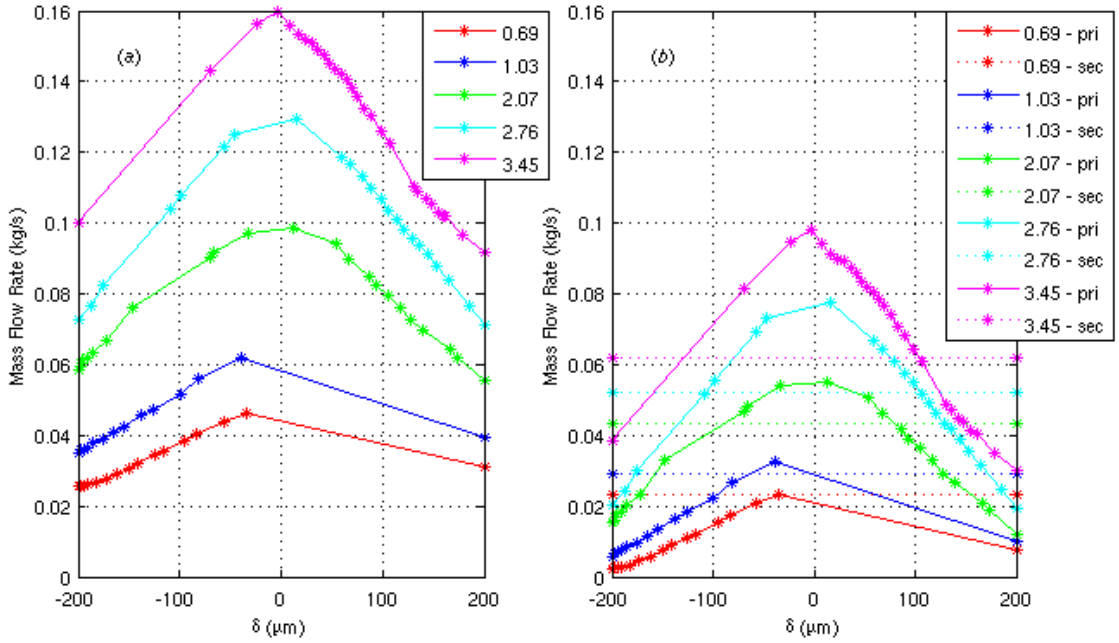


Figure 4.12: Annular experimental leakage mass flow rate – parallel seal faces: (*a*) – total, (*b*) – separate primary and secondary components, h_{tsg} = 400 μm

The total leakage mass flow rate is also significantly higher than that predicted by the CFD (Figure 4.12). Up to 4 times the mass flow rate is seen in secondary leakage which may be due to the other leakage paths as well as through the secondary seal. Primary leakage values are much more comparable where the mass flow is approximately 30% more than predicted by the CFD.

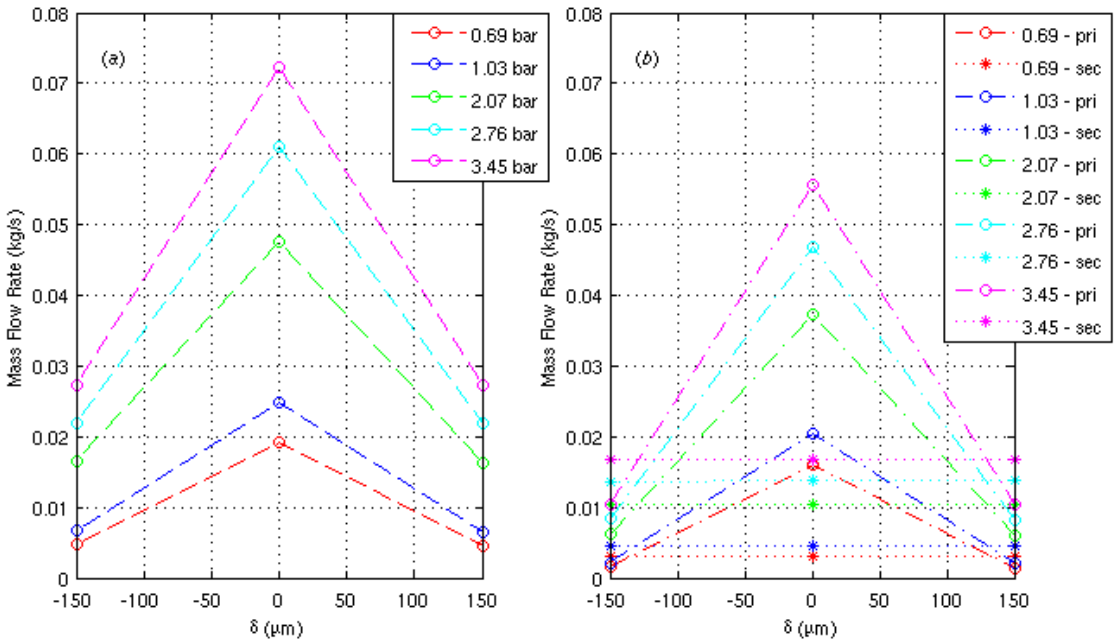


Figure 4.13: Annular CFD leakage mass flow rate – parallel seal faces: (*a*) – total, (*b*) – primary and secondary, h_{tsg} = 400 µm

As with the experimental data, the maximum mass flow rate occurs when the seal housing is at 0 µm displacement which corresponds to the minimum seal gap height being equal to $h_{tsg}/2$ (the largest possible). The total mass flow rate is considerably less when δ = either -150 µm or 150 µm. Figure 4.13 (*b*) shows the leakage mass flow rates of the primary and secondary leakage paths separately and, as expected, the secondary leakage is independent of seal housing position. The primary leakage tends to zero along with the minimum seal gap height at the peripherals of displacement and is greatest at 0 µm displacement where it dominates the total leakage mass flow rate. At the extremes of the displacement range, the secondary leakage is slightly greater than the primary leakage. The minimum seal gap height at these positions is equal to the secondary seal gap height at 50 µm but due to the longer path and the IPC where dynamic head is dissipated and lost, the primary leakage is lower.

The effective clearance for the primary leakage path, shown below in Figure 4.14, is near maximum for a given inlet pressure when δ = 0 µm ($h_u = h_d$ = 200 µm) and reduces as δ tends

to ± 200 µm. Only the mass flow rate term varies with changing δ and so this trend is to be expected. As described in section 2.4.1, hybrid brush seals have exhibited effective clearance values of between 0.25 and 0.6. Finger seals have been able to improve upon brush seals by around 30%. The effective clearance values for the LAMFS are comparable to the current and potential future sealing technologies. In fact, the peak e values occur at δ = 0 µm but the equilibrium position may be towards one extreme of displacement where effective clearance values are significantly lower.

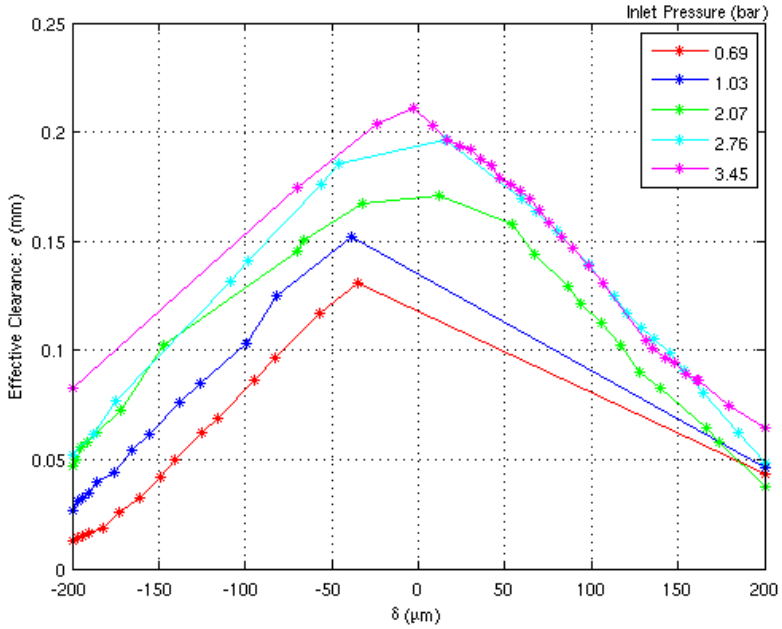


Figure 4.14: Effective clearance for primary leakage – Parallel seal faces: h_{tsg} = 400 µm

4.5.2 Radial Step Geometry in Seal Gaps

4.5.2.1 Resultant Force

The resultant force-displacement relationships obtained from the annular LAMFS test rig with radial steps in the seal gaps are shown below in Figure 4.15 along with the 3D CFD data. Comparing this to the linear LAMFS results for the same step height, h_{step}, and step position, α = 0.5 in section 3.5.5, the overall trends are very similar. A negative gradient is seen throughout the range of displacement for each inlet pressure and there is an equilibrium position. The seal housing therefore possesses a self-centring ability. As in the linear seal

results, a positive bias exists such that the equilibrium position lies in the positive displacement region; between + 60 µm and + 120 µm. This gives a maximum negative force which is between 50 N and 100 N less in magnitude than its positive counterpart (Figure 4.16). The maximum magnitude of the resultant force is near 500 N, which is extremely high considering the mass of the seal housing is 5.65 kg leading to large accelerations at displacements away from δ_{eq}. The dynamic behaviour of the seal based on this force-displacement data is modelled in section 4.5.3. These results indicate that the static pressure distributions alone can produce a highly responsive seal housing. This figure demonstrates that the use of converging radial steps in the LAMFS is capable of influencing the pressure distributions within the seal gaps to ensure a stable, self-centring seal housing behaviour. Based on the linear experimental results, the magnitude of the restoring force can be increased further by increasing the step height and positioning the step further downstream.

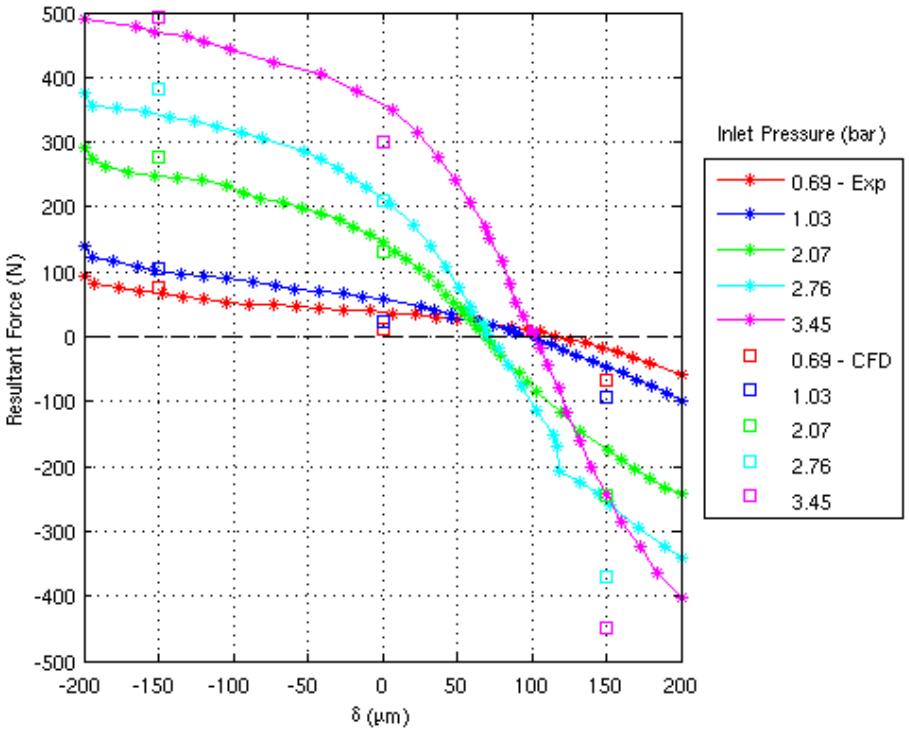


Figure 4.15: Experimental and CFD seal housing resultant force with displacement – Radial steps: h_{tsg} = 400 µm, h_{step} = 200 µm, α = 0.50, static disc

The force-displacement relationship predicted by the CFD simulations, when radial steps are employed within the seal gaps, agrees well with the experimental data. The use of these steps has ensured that the gradient is negative and an equilibrium position exists for all inlet pressures, which would give the seal a self-centring ability. There is some positive bias, as was seen in the experimental work, which moves the equilibrium position downstream with increasing inlet pressure. This indicates that this effect is not solely a result of the side leakage present in the linear test rig, although the additional leakage was a major factor. Should the position of the equilibrium position be desired at different δ, then the radial position of the secondary seal can be moved to vary the constant positive force produced by the external surfaces. Increasing the secondary seal arm thickness will lead to a greater force from the external surfaces. However, the position of maximum force-displacement gradient lies at the current equilibrium position for the three highest values of p_{HP} (Figure 4.17), which is where the seal will be most resilient to transient behaviour. For the force displacement trends observed, the equilibrium point is in the ideal position.

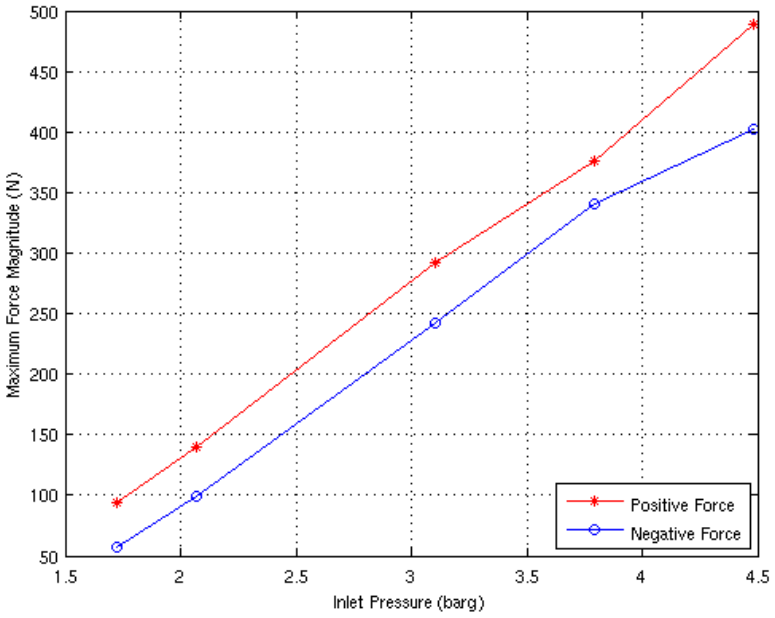


Figure 4.16: Experimental peak force magnitude

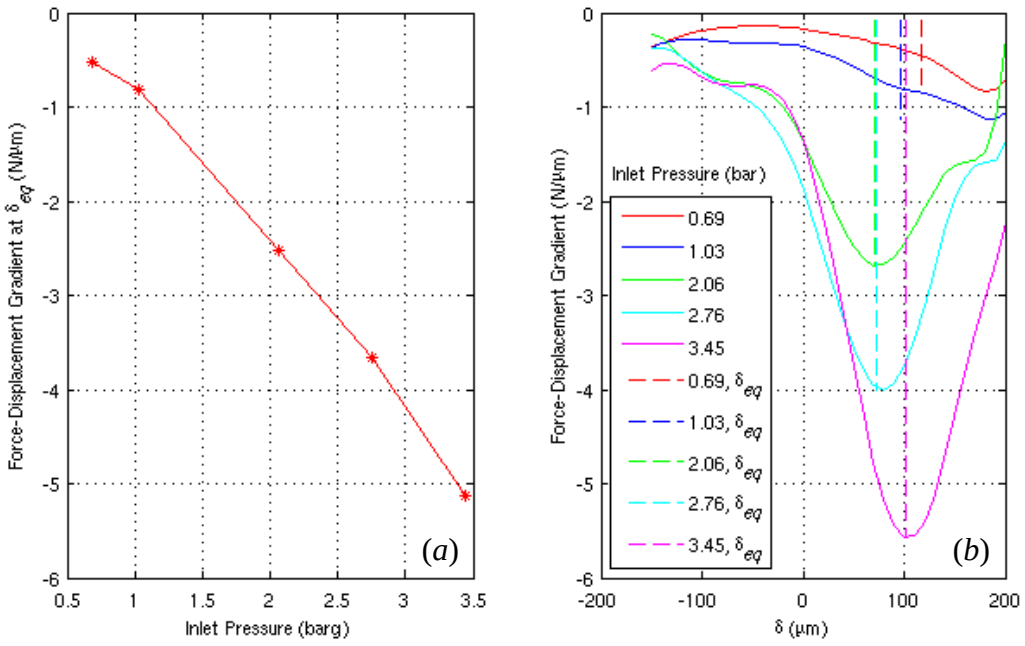


Figure 4.17: (a) Force-displacement gradient at δ_{eq} and (*b*) force-displacement gradient across displacement range with polynomial fit and δ_{eq} position shown

4.5.2.2 Seal Gap Pressure Distribution

Figure 4.18, Figure 4.19 and Figure 4.20 display the experimental (black) and CFD (red) static pressure distributions in the seal gaps with converging radial steps for δ = –150 µm, 0 µm and 150 µm respectively. The *x*-axis represents the seal gap location; 0-1 is the upstream seal gap and 1-2 represents the downstream seal gap. The radial steps were positioned at α = 0.50 and hence the step positions occur at x/L = 0.5 and 1.5. The static pressure readings are normalised by the inlet pressure p_{HP}. At δ = –150 µm where $h_u >> h_d$, there is little or no pressure drop through the upstream seal gap and the pressure remains ≈ p_{HP}, as does the IPC pressure. There is also only a very small loss as the flow enters the downstream seal gap as $h_{step} + h_u >> h_u$. When the flow reaches the step, there is a considerable drop in pressure as the flow accelerates through the minimum clearance in the primary leakage path. For inlet pressures of 0.69 bar and 1.03 bar, the viscous pressure drop downstream of the step is linear. For all other inlet pressures, the flow regime is compressible and hence the viscous pressure drops are a function of $\sqrt{\Delta x}$. For all cases, the experimental and CFD data agree well as the

losses due to acceleration are reasonably well predicted, which appears to be far more difficult to accurately model when radial steps are not present.

At δ = 0 μm, where $h_u = h_d$, the mass flow rate though the seal is greatest and hence the acceleration losses are greater. Up to 15% of the inlet pressure is lost at entry to the upstream seal gap. The largest acceleration losses occur at the step positions for all cases whereas the inlet loss to the downstream seal gap has the smallest magnitude. Viscous losses in both of the seal gaps upstream of the step are negligible though the viscous loss downstream of the step in the upstream gap is very small due to the increasing cross-sectional area with radius. Only downstream of the step in the downstream seal gap is there significant viscous pressure loss. When p_{HP} = 0.69 bar and 1.03 bar, the experimental and CFD correlation is initially good, though the CFD then over-predicts the acceleration loss at the step in the upstream seal gap. Thereafter, the CFD is effectively offset from the experimental trend. As in the parallel seal gap case, the CFD inaccurately predicted the entry losses for 0.69 bar and 1.03 bar. For the other three inlet pressures, the experimental data and CFD agree extremely well, with acceleration losses being predicted reasonably accurately. In these cases, the viscous pressure losses in the downstream seal gap beyond the step are highly nonlinear and more exaggerated as the gap cross sectional area is reducing due to the change in radius with x/L.

At δ = 150 μm (Figure 4.20), where $h_u << h_d$, the majority of the pressure drop occurs within the upstream seal gap. The experimental data shows an acceleration loss at the inlet plane of the upstream seal gap (x/L = 0) which is not seen at the inlet plane to the downstream seal gap when δ = –150 μm, when the inlet gap heights are equal. There is then a significant acceleration loss as the flow reaches the step in the upstream seal gap (the equivalent of the downstream gap when δ = –150 μm) followed by a large viscous pressure drop through the smallest clearance of the primary leakage path to the IPC. The CFD predicts that negligible

loss occurs at the upstream gap inlet and it also under-predicts the acceleration pressure drop at the upstream step. The pressure dropped across the downstream gap is much smaller than observed experimentally but it increases with inlet pressure, a trend seen in the linear work. The positive bias is significantly less, in terms of the $\frac{p_{IPC}}{p_{HP}}$ value, but nonetheless exists. The maximum magnitude is 0.15 and is much lower than the linear equivalent case exhibiting a value of 0.55. This confirms that the positive bias in the IPC is not purely caused by the linear test rig side leakage but it had a significant influence.

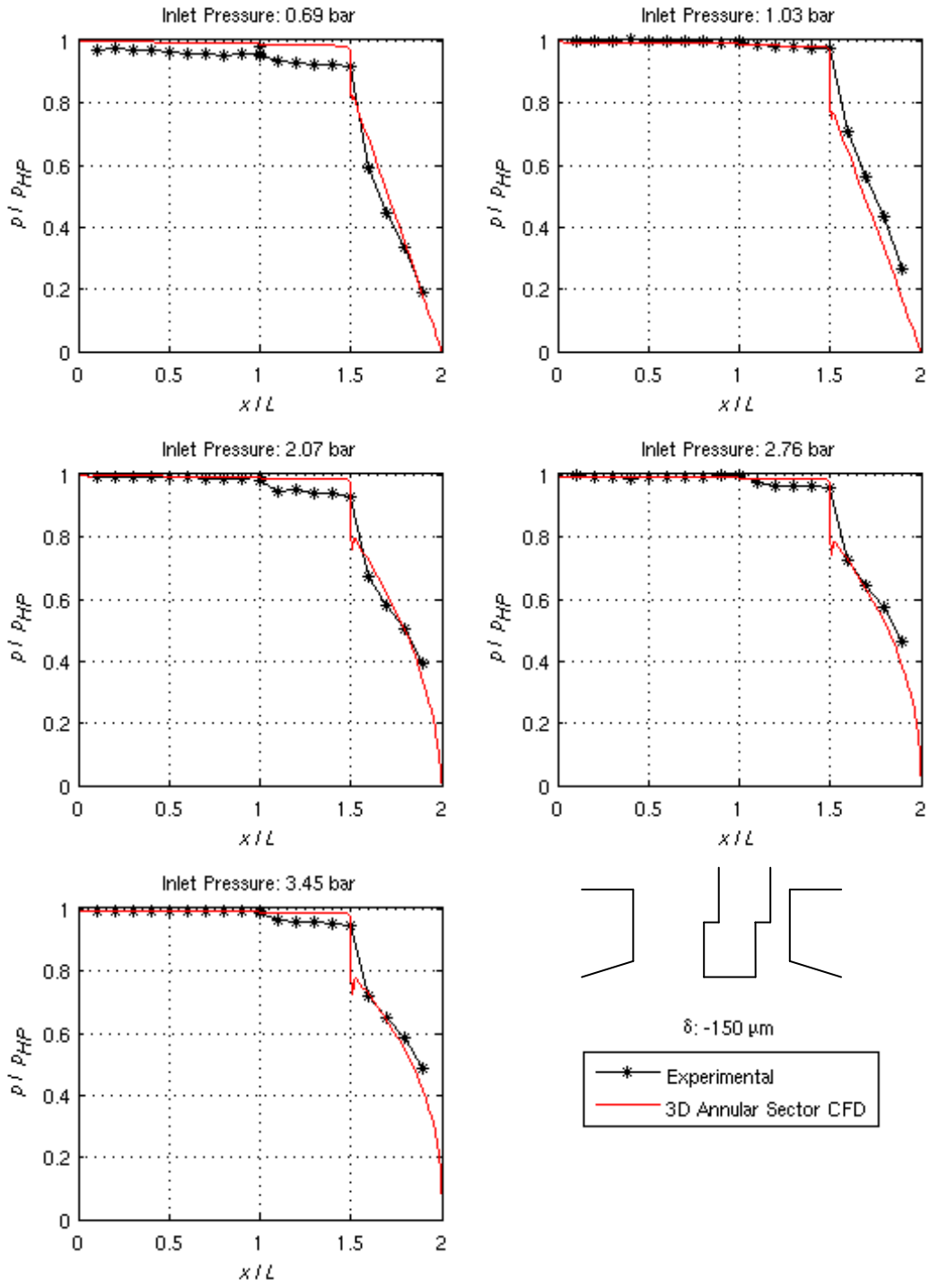


Figure 4.18: Static pressure distribution in annular seal gaps - Radial steps: h_{tsg} = 400 µm, h_{step} = 200 µm, α = 50 %, δ = -150 µm, static disc

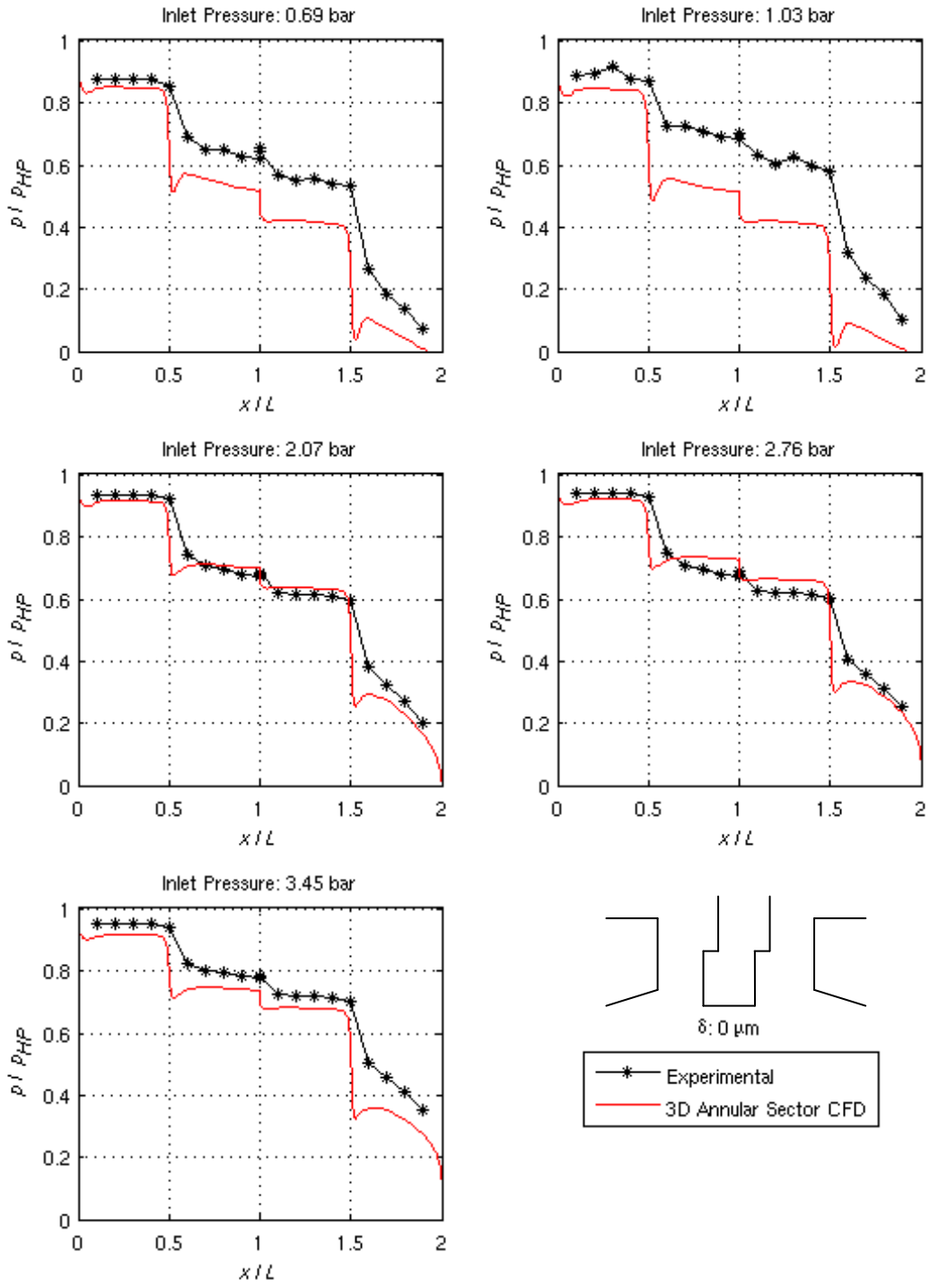


Figure 4.19: Static pressure distribution in annular seal gaps - Radial steps: h_{tsg} = 400 µm, h_{step} = 200 µm, α = 50 %, δ = 0 µm, static disc

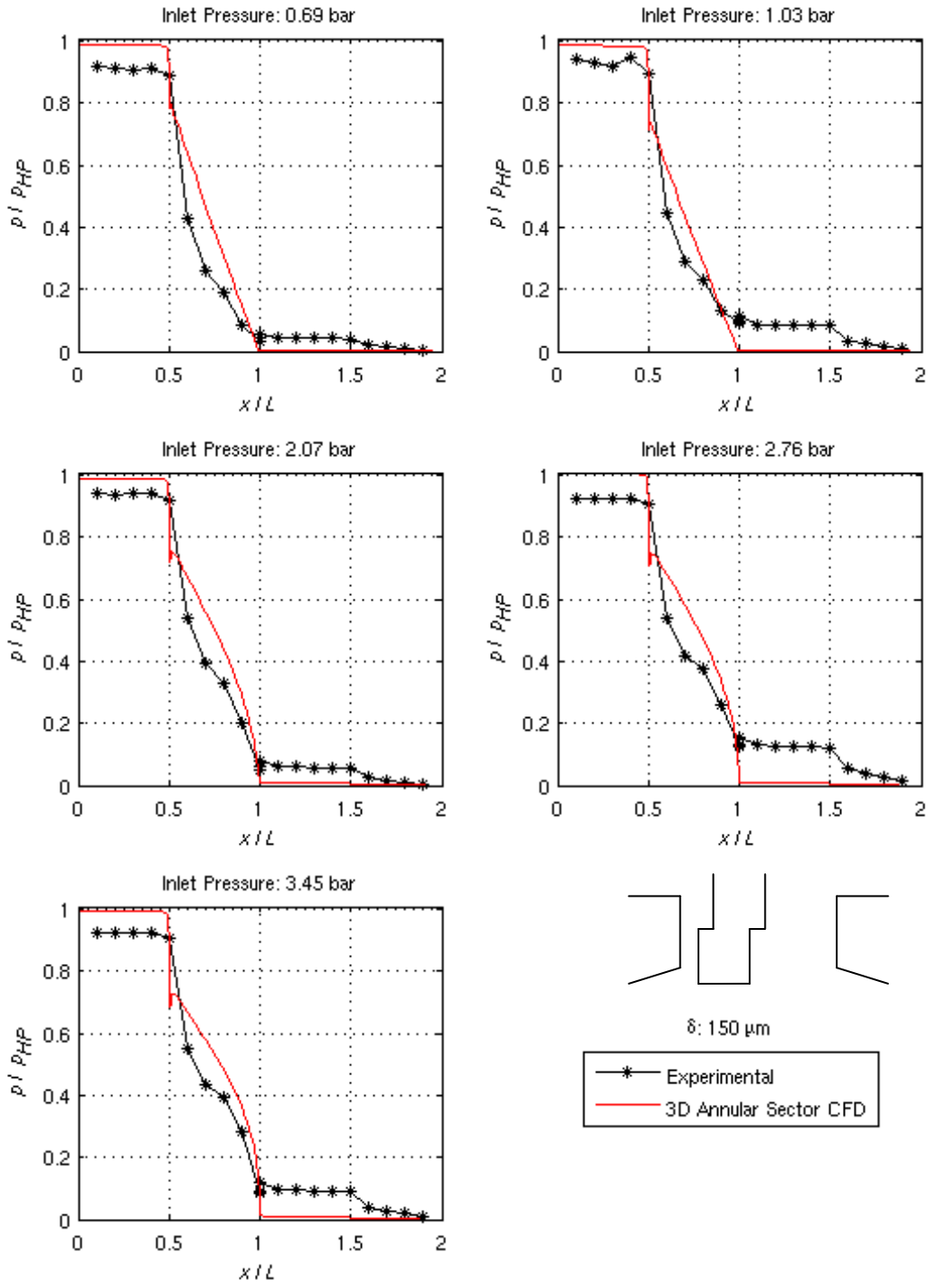


Figure 4.20: Static pressure distribution in annular seal gaps - Radial steps: h_{tsg} = 400 µm, h_{step} = 200 µm, α = 50 %, δ = +150 µm, static disc

4.5.2.3 Leakage

The experimental and CFD leakage mass flow rate data for the annular seal with radial steps are shown below in Figure 4.21 and Figure 4.22 respectively. The experimental data shows a marginal reduction in the total mass flow rate compared to the parallel face case. This is unexpected, as the average gap height has increased, but the inlet geometry may be causing the vena contractor within each seal gap to be smaller for the baseline case. The CFD data shows an increase in primary mass flow rate of approximately 10% due to the inclusion of radial steps, which is expected as the average gap height has increased. These data sets show that leakage mass flow rate through the primary leakage path is dependent on the inlet geometry and must be researched in greater detail before the leakage for a particular seal can be predicted by analytical models. The experimental seal had small chamfers on all corners (inlet planes) whereas the CFD modelled the seal as having sharp corners, which has lead to a much lower mass flow rate in the CFD for both seal gap geometries.

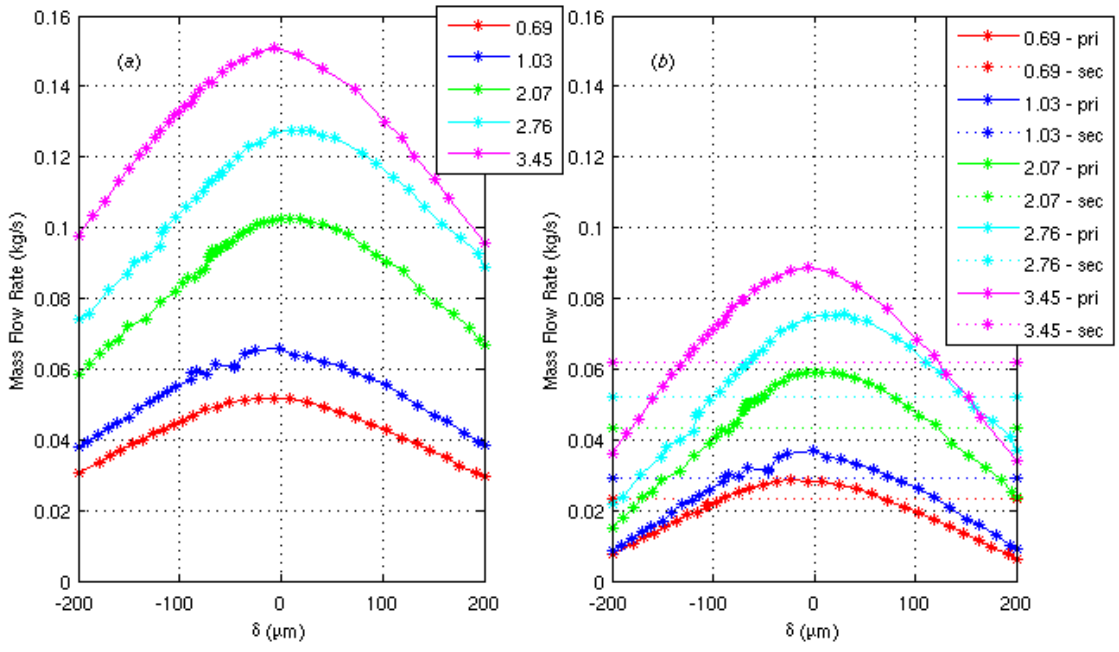


Figure 4.21: Annular experimental leakage mass flow rate – Radial steps: (*a*) – total, (*b*) – separate primary and secondary components, h_{tsg} = 400 µm, h_{step} = 200 µm, α = 0.50, static disc

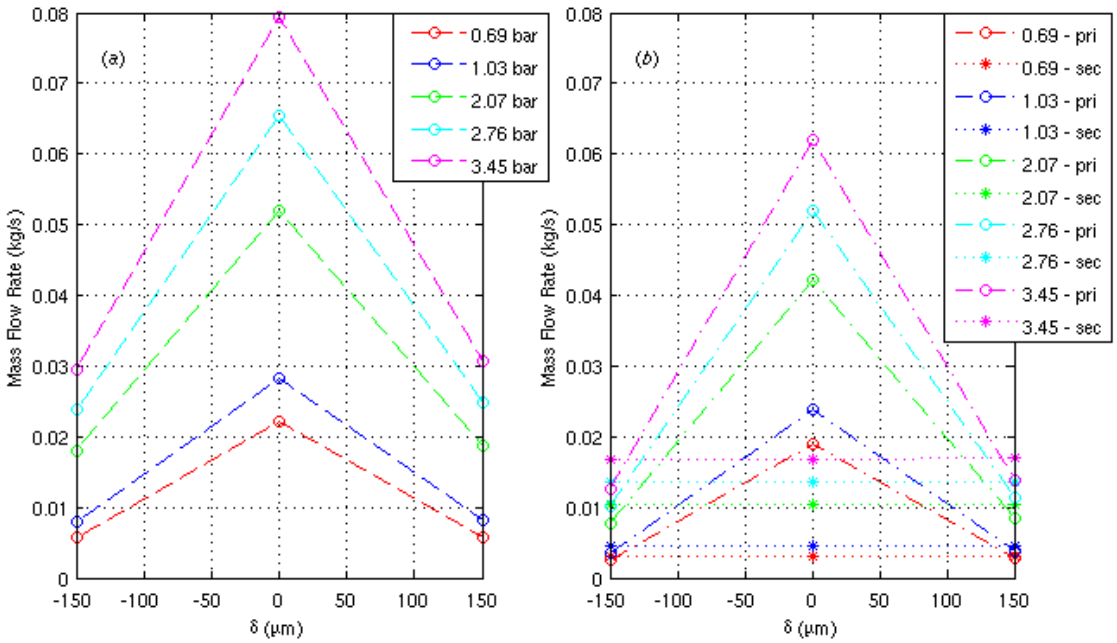


Figure 4.22: Annular CFD leakage mass flow rate – Radial steps: (*a*) – total, (*b*) – primary and secondary, h_{tsg} = 400 μm, h_{step} = 200 μm, α = 0.50

The effective clearance values for the primary leakage path with radial steps are shown in Figure 4.23. The effective clearance for the whole seal, including the secondary seal, will be higher, though as this seal only needs to deal with relative axial movement and no rotation, the leakage through the secondary seal could be minimal in comparison to the primary leakage. Effective clearance values for the LAMFS could potentially be lower than existing seals and next generation seal technologies currently under development as the maximum effective clearance observed for this seal is 0.2 mm which is the same as the best reported brush seal data.

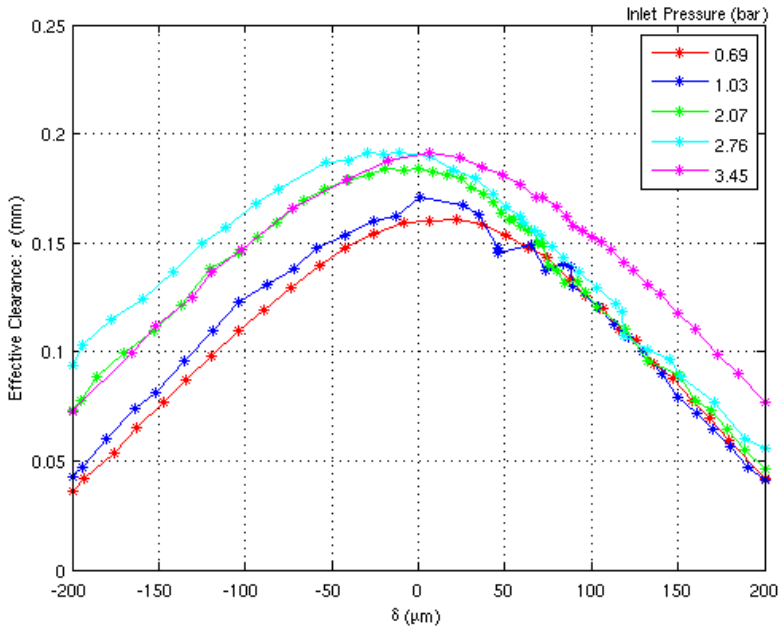


Figure 4.23: Effective clearance of primary leakage path – Radial steps: h_{tsg} = 400 µm, h_{step} = 200 µm, α = 0.50

The effective clearance at δ_{eq} is plotted below in Figure 4.24 for all inlet pressures. The peak value of e is approximately 0.153, which is less than tested values quoted for finger seals (Proctor and Delgado 2004) and leaf seals (Rolls Royce plc). This shows that the LAMFS concept, based on leakage performance alone, is a promising sealing technology.

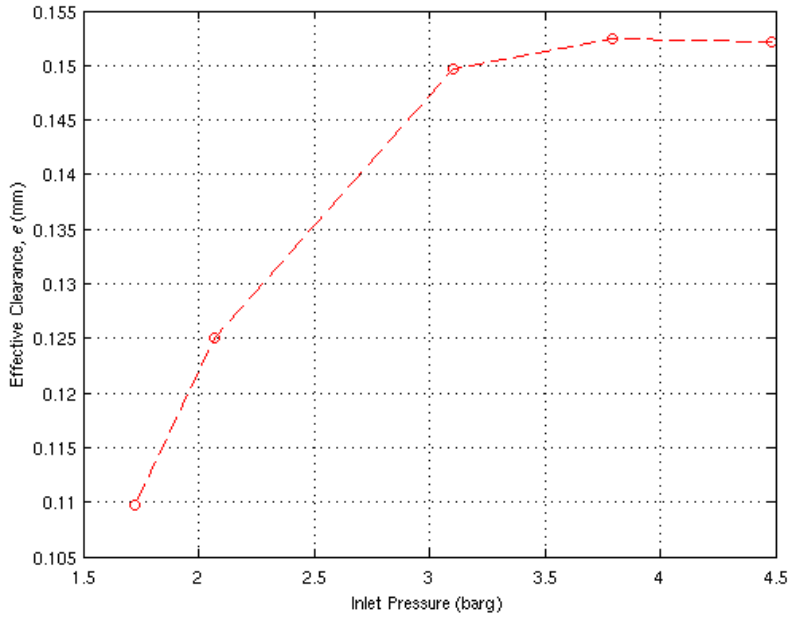


Figure 4.24: Effective clearance of primary leakage path at δ_{eq}

4.5.2.4 Rotating Disc: Radial Steps

As mentioned earlier, it was not possible to perform spinning rotor tests (though all the necessary components required for rotation were acquired or manufactured and disc failure containment calculations were performed; section A.4), however, the 3D CFD allowed an insight into the possible effects on the flow field and pressure distributions in the seal gaps caused by the moving rotor for the baseline and radial step cases. An engine representative surface speed of 100 ms^{-1} (Rolls Royce plc) was imposed at the midpoint between the radial limits of the seal surface which was achieved with a rotational speed of 1333 $rads^{-1}$ (12.7 krpm). The results showed no discernable difference between the static and rotating disc for both resultant force and leakage data. Experimental research by Li et al. (2011) reported that the flow coefficient, in this case for a labyrinth seal, was negligibly affected by the rotational speed of the rotor. Based on Reynolds equation (Equation **(**2.1**)**), the effects of relative motion between surfaces on the pressure distribution are non-existent if there is no change in gap height in the direction of motion and hence this result would be expected.

4.5.2.5 Rotating Disc: Radial Steps and Circumferential Steps

4.5.2.5.1 Seal housing Resultant Force

The influence of the circumferential steps on the seal housing's force-displacement relationship is shown in Figure 4.25. For static disc conditions, the overall trend is very similar to the case where only radial steps are present but the magnitude of the resultant force has increased significantly, by as much as 68%. The reason for this is described below using Figure 4.26 which displays the static pressure distribution on the repeatable 20° sector of the downstream seal face when p_{HP} = 3.45 bar and δ = –150 µm and hence $h_u >> h_d$.. The inclusion of the circumferential step (outlined by the black dashed lines) essentially increases the gap height (by 100 µm in this case) and hence the pressure drop across the radial step is lessened in this region, thus leading to a higher average pressure on this face. There is

negligible pressure drop across the upstream seal face as $h_u >> h_d$ and hence the circumferential (and radial) step has no effect there. Hence the restoring force is increased even when the rotor is static (left figure). The pressure distribution is also symmetric about the radial line which bisects the circumferential step sector. When the rotor is spinning, the pressure is increased marginally from 3.22 bar (static case) to 3.29 bar towards the circumferential step trailing edge where the reduction in gap height with circumferential position occurs. The pressure distribution is therefore no longer axisymmetric due to the hydrodynamic pressure generation towards the trailing edge. At this seal housing displacement, the minimum clearance is 50 µm which is larger than most hydrodynamic seal faces operate at (usually 10 µm) which may contribute to why the circumferential step has little effect on the pressure distribution. However this seal housing displacement was modelled so that it could be directly compared to all other CFD and experimental cases. For improvements to the hydrodynamic lift, smaller clearances are required and either more circumferential steps per revolution (for example, the spiral groove geometry) or tapered sectors which have a continuous change in clearance with rotation as it is the drop in clearance which induces the desired pressure fields.

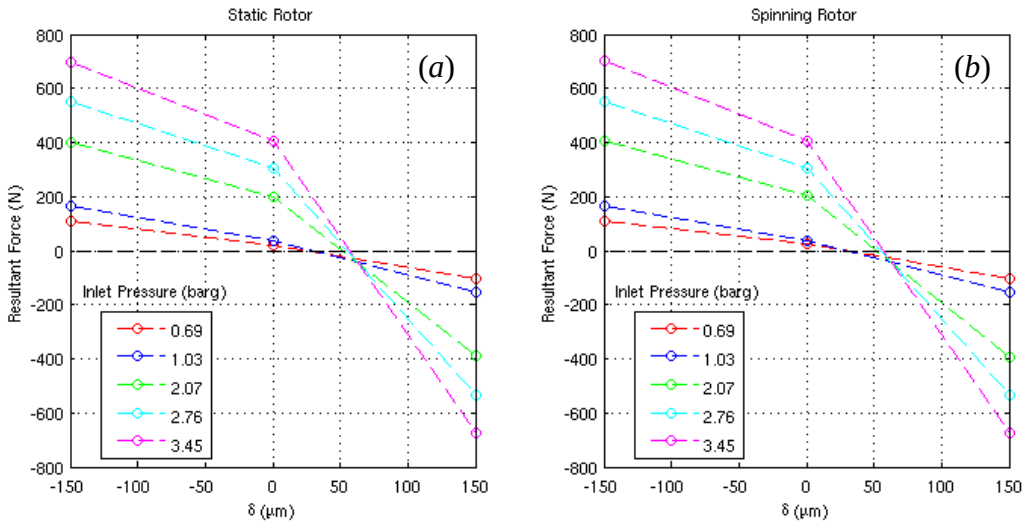


Figure 4.25: Force-displacement relationships for LAMFS with radial and circumferential steps with (*a*) - a static rotor and (*b*) - a spinning rotor, ω = 1333 rads^{-1}

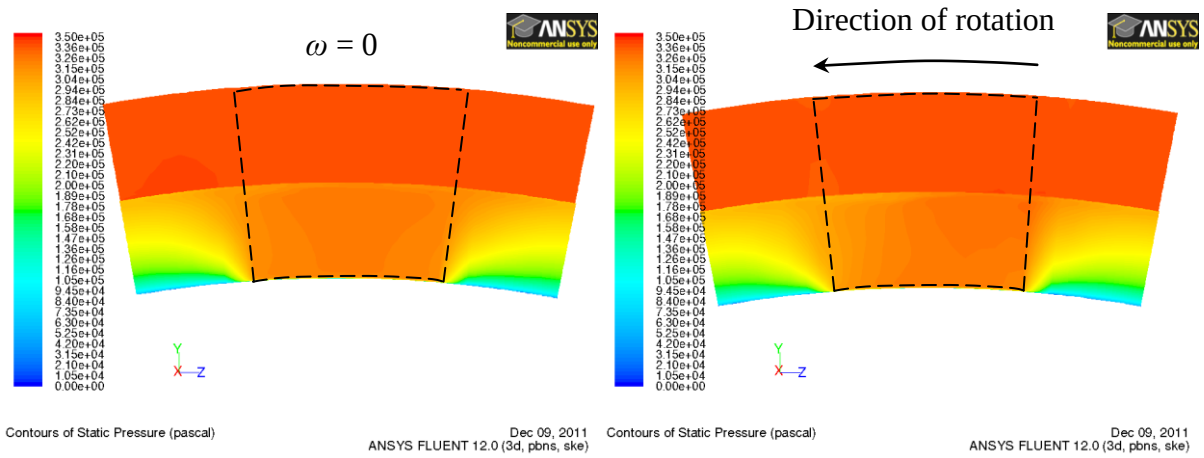


Figure 4.26: Static pressure on downstream seal face with position of circumferential step position indicated (p_{HP} = 3.45 bar, δ = -150 µm, $h_u >> h_d$)

4.5.2.5.2 Leakage Mass Flow Rate

The leakage mass flow rate for the LAMFS with radial and circumferential steps is shown below with a rotating disc. The leakage values were near identical with a static disc and are not shown. Increasing the average seal gap height by the inclusion of circumferential steps has a significant influence on the primary leakage mass flow rate and, as expected, the secondary leakage mass flow rate is unaffected. The circumferential step has a greater influence when δ = -150 µm or 150 µm as the minimum gap height within the circumferential step is increased from 50 µm to 150 µm. At these displacements, the primary leakage as a proportion of the total mass flow rate has increased from 32% (p_{HP} = 3.45 bar) to 97% (p_{HP} = 0.69 bar) leading to a total increase from 14% (p_{HP} = 3.45 bar) to 43% (p_{HP} = 0.69 bar), whereas the primary leakage is only increased by 6% (p_{HP} = 3.45 bar) to 12% (p_{HP} = 0.69 bar) when δ = 0 µm. The leakage penalty associated with the circumferential steps must be assessed against the gain in restoring force magnitude to determine whether they are beneficial. The current circumferential geometry and conditions chosen provide little improvement to the restoring forces for the leakage penalty incurred.

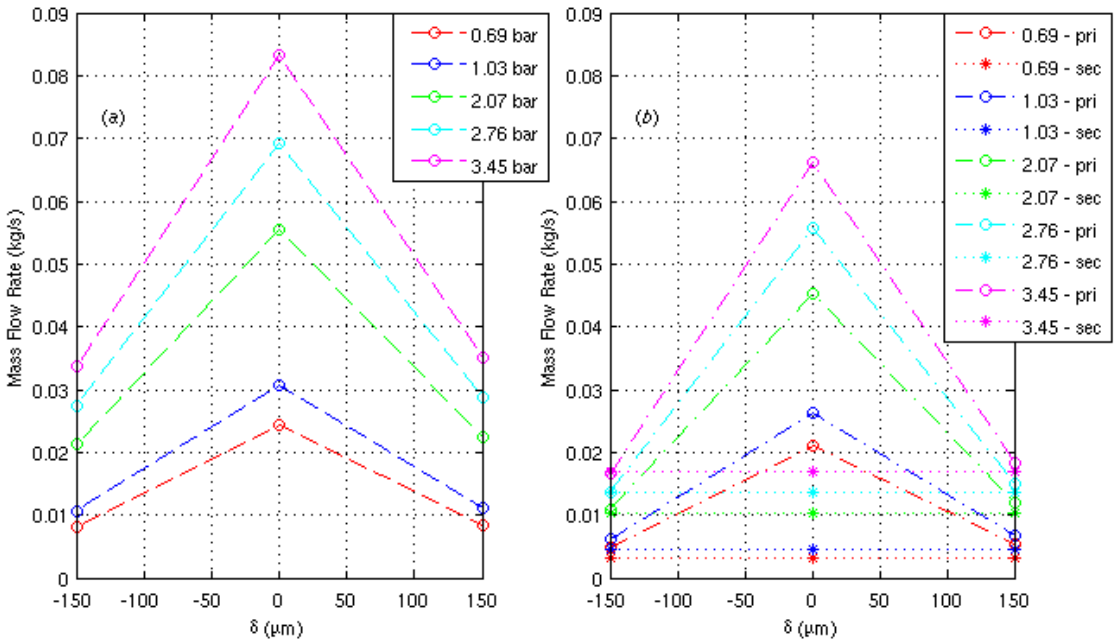


Figure 4.27: Annular CFD leakage mass flow rate – Radial and circumferential steps: (*a*) – total, (*b*) – primary and secondary, h_{tsg} = 400 µm, h_{step} = 200 µm, α = 0.50, ω = 1333 rads^{-1}

4.5.3 Dynamic Behaviour

The tight tolerance between the disc and seal housing surfaces (h_{tsg} = 400 µm) necessitates the control of the axial position of the seal housing relative to the disc to have a rapid response to accommodate any relative movement under highly transient conditions. Dynamic modelling of the annular seal was performed using the experimental data for the seal housing resultant force-displacement relationships for the radial step case. This was included as a look up table. During an engine flight cycle, the seal is likely to be at its equilibrium position, δ_{eq}, under steady state conditions when it then experiences a transient in the rotor's axial position. The dynamic model was used to assess the maximum change in axial position of the rotor to which the seal housing can respond and prevent contact. The equilibrium positions for all values of p_{HP} are in the positive range of displacement ($h_u < h_d$) thus the relative movement was modelled in the direction of minimum distance to contact (seal housing moves downstream; positive δ), which would be the limiting case. This is equivalent to perturbing the seal housing from δ_{eq} at a particular velocity and assessing the response over time.

Standard equations of linear motion including Newton's Second Law were used to predict the seal housing displacement over time. The seal housing acceleration, velocity and position are given by the following equations

$$\ddot{\delta}_j = \frac{F(\delta)}{m} \tag{4.1}$$

$$\dot{\delta}_{j+1} = \dot{\delta}_j + \ddot{\delta}_j t_{step} + O(t_{step}) \tag{4.2}$$

$$\delta_{j+1} = \delta_j + \dot{\delta}_j t_{step} + O(t_{step}) \tag{4.3}$$

where $F(\delta)$ is the resultant force as a function of the seal housing displacement obtained from the experimental results and $O(t_{step})$ is the discretisation error. The damping factor of the seal housing would need to be acquired from experimental tests for the real behaviour, but for the purpose of a basic understanding the potential of this seal to accommodate transient conditions, a damping factor was not included. The displacement of the seal housing over time is shown in Figure 4.28. All p_{HP} cases are plotted where for each, $\delta = \delta_{eq}$ at $t = 0$ and the velocities are as in Table 4.2 below. The mass of the seal housing is 5.65 kg.

p_{HP} (barg)	Maximum Velocity
0.69	75 mms^{-1}
1.03	125 mms^{-1}
2.06	230 mms^{-1}
2.76	270 mms^{-1}
3.45	250 mms^{-1}

Table 4.2: Seal housing maximum velocity from δ_{eq}

For all values of p_{HP}, the seal housing was moved at a maximum velocity before contact occurred, hence the displacement-time traces begin at the equilibrium position and move downstream (positive δ) close to the limit of displacement. What is observed about the seal housing dynamic behaviour is that the natural frequency (Equation **(**4.4**)**) increases with p_{HP}. This is because the stiffness of the seal (Equation **(**4.5**)**) increases with p_{HP} (i.e. gradient of the

force-displacement relationships). The seal therefore becomes more resilient as the pressure drop across it increases as the magnitude of the restoring resultant force increases. The dynamic response of the seal housing can also be improved by reducing the housing mass. As stated earlier in this thesis, the cross sectional area of the seal housing, and hence its mass, could be reduced provided the housing does not deform under the stresses induced by the static pressure loading on it.

Natural frequency:

$$f_n = \frac{1}{2\pi}\sqrt{\frac{k}{m}} \tag{4.4}$$

Seal stiffness:

$$k = \frac{F(\delta)}{\delta} \tag{4.5}$$

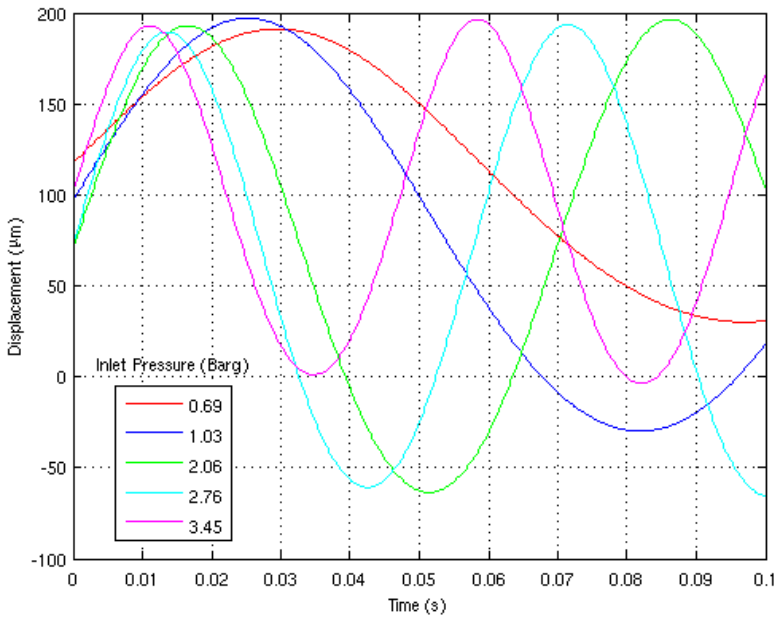


Figure 4.28: Dynamic response of annular seal (based on experimental $F(\delta)$) when displaced downstream from δ_{eq} at maximum possible velocity whilst avoiding disc contact

4.5.3.1 Squeeze film effect

When two surfaces of a similar profile are in close proximity and move closer together, a form of damping can occur by an increase in pressure above the ambient conditions as the fluid between the two surfaces takes time to evacuate the gap due to the fluid's viscosity. There is also a reduction in the pressure between the surfaces below ambient as they move apart while the fluid fills the increase in volume within the gap. This can provide a useful damping effect under highly transient conditions. This is known as the squeeze film effect and its significance on the seal's dynamic behaviour was evaluated using Reynolds 1D equation and the governing equation is shown below (equation **(**4.6**)**). This is equation **(**3.1**)** but includes a term for the variation in pressure and gap height over time, which is as follows

$$\frac{\partial}{\partial x}\left(\frac{h^3}{\mu}\frac{\partial p^2}{\partial x}\right) = \frac{\partial (ph)}{\partial t}, \tag{4.6}$$

and therefore

$$\frac{h^3}{\mu}\frac{\partial^2 p^2}{\partial x^2} = \frac{\partial (ph)}{\partial t}. \tag{4.7}$$

Let $p = Pp_{atm}$

$h = Hh_0$

$x = XL$

$t = Tt_{step}$

where p_{atm} is atmospheric pressure, h_0 is a reference gap height and is the seal gap height at zero displacement (i.e. $h_u = h_d$), L is the seal gap length and t_{step} is the time step. Equation **(**4.7**)** then becomes

$$H^3\frac{\partial^2 P^2}{\partial X^2} = \Lambda\frac{\partial (PH)}{\partial T} \tag{4.8}$$

Where

$$\Lambda = \frac{\mu L^2}{h_0^2 p_{atm} t_{step}}. \tag{4.9}$$

Employing a central difference method to the left hand side of equation **(**4.8**)** and a rearward difference method for the right hand side gives

$$\frac{H_j^3}{(\Delta x)^2}\left\{P_{i+1,j}^2 - 2P_{i,j}^2 + P_{i-1,j}^2\right\} = \Lambda\left\{\frac{P_{i,j}H_j - P_{i,j-1}H_{j-1}}{\Delta t}\right\} \quad \textbf{(4.10)}$$

where *i* and *j* relate to the position along the radial length of the seal face and the position in time respectively. The equation for the normalised induced pressure due to the squeeze film effect, $P_{i,j}$, is then

$$aP_{i,j}^2 + bP_{i,j} + c = 0 \quad \textbf{(4.11)}$$

where

$$a = 1$$

$$b = \frac{\Lambda(\Delta x)^2}{2\Delta t H_j^2}$$

$$c = -\frac{1}{2}\left\{\frac{\Lambda(\Delta x)^2}{\Delta t H_j^3}P_{i,j-1}H_{j-1} + P_{i+1,j}^2 + P_{i-1,j}^2\right\},$$

and hence

$$P_{i,j} = \frac{-b \pm \sqrt{b^2 - 4ac}}{2a} \quad \textbf{(4.12)}$$

The pressure profile induced, $P_{i,j}$, is raised above the ambient conditions as the clearance height, H_j, decreases and vice versa. To assess the potential damping benefits from the squeeze film effect, the maximum induced pressure fields on the seal faces was evaluated from all inlet pressure cases in the dynamic modelling above. Three different lengths for the seal surfaces' radial dimension, L = 0.011 m (test rig geometry), 10L and 100L, were analysed with the identical dynamic conditions (position, velocity and acceleration) held constant. The induced pressure profiles are shown in Figure 4.29. For a seal gap radial length equal to the test rig (engine representative scale), the change in pressure above ambient conditions is negligible. It is only when L is increased by a factor of 100 that a significant variation in pressure on the seal faces occurs. A peak change of 3% in the pressure distribution from

ambient is predicted, but an L of 1.1 m is entirely impractical and hence the squeeze film effect was deemed to be ineffective in the dynamic behaviour of the LAMFS.

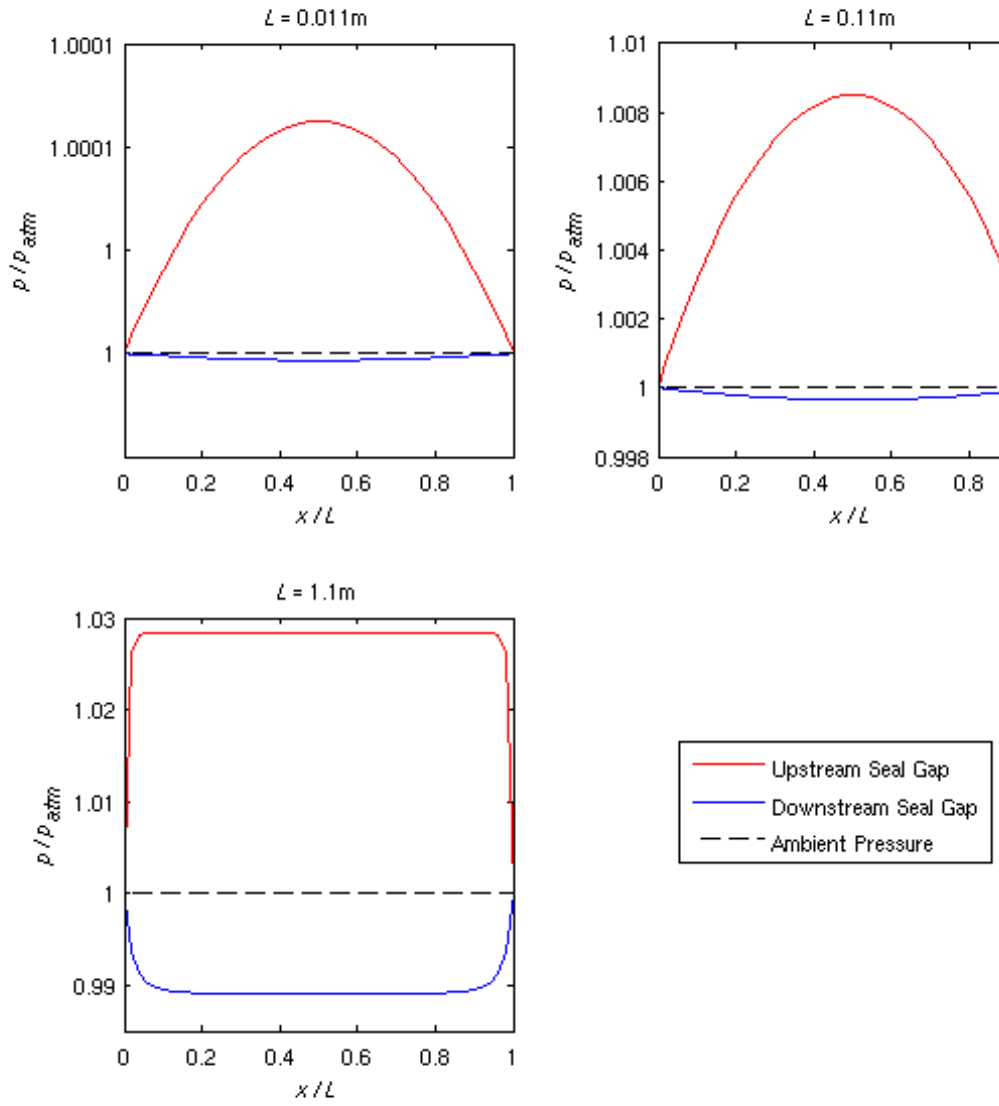


Figure 4.29: Normalised induced pressure for parallel seal surfaces – L = 0.011 m, 0.11 m, 1.1m

4.6 Summary

This chapter has confirmed the results from the linear LAMFS test rig in showing that the large axial movement face seal can possess the self-centring ability required purely from the seal gap static pressure distribution when in a fully annular form. The test rig designed, built

and commissioned at Oxford allowed for force-displacement relationships, leakage-displacement relationships and seal gap static pressure distributions to be measured. A baseline geometry of parallel seal faces was tested initially, which exhibited an undesirable, unstable seal housing behaviour as seen in the linear LAMFS work in chapter 3. The inclusion of converging radial steps proved to be essential in creating a stable, self-centring seal housing. One geometric case with h_{tsg} = 400 μm, h_{step} = 200 μm and $\alpha = 0.50$ was tested and, as predicted, the radial steps determine the location at which the majority of the pressure drop occurs within a given seal gap. For a particular seal gap where the height is small relative to the other, such that most of the pressure drop through the primary leakage path occurs here, delaying the pressure drop effectively increases the average pressure on this face. This was proven to lead to a resultant force on the seal housing that increases the clearance of the gap whose height is tending to zero.

Computational fluid dynamics software agreed well with the experimental data from the step geometry case but was less accurate for the baseline, parallel seal face geometry where it seems that, as was reported in the linear LAMFS work, predicting the losses at entry to the seal gaps is difficult. Seal gap static pressure distributions for the radial step case were far more accurate when compared to the experimental data and this was reflected in the force-displacement relationships. Rotating the disc was not possible in the experimental test rig but the CFD showed that, when there is no variation in gap height with circumferential position, the rotation has no discernable effect on the static pressure distribution. This is also expected analytically. The attempt to generate hydrodynamic lift to improve the self-centring ability of the seal housing was unsuccessful but the geometry and clearance were inadequate for these effects to be significant. This is an important observation, as it may be possible to achieve good seal design *without* having to replicate dangerous high rotational speeds.

The dynamic behaviour of the annular version of the seal was also assessed using an analytical model. It was observed that the gradient of the force-displacement increased with inlet pressure which results in the seal being able to accommodate larger sudden relative axial movement whilst avoiding contact with the disc *i.e.* the stiffness of the seal increases with inlet pressure. Any inherent damping of the seal housing would need to be evaluated from experiments and is suggested for future work. Once the extent of any inherent damping is known, any further damping required can be incorporated into the seal design, for example in the secondary seal.

The self-centring ability of the LAMFS concept as a fully annular seal has been proven to have great potential as a non-contacting, passively controlled, low leakage seal. A stable, self-centring ability can be achieved purely from the static pressure distribution on the internal and external faces of the seal housing. Effective clearance values were shown to be considerably less than the current in-service sealing technology. However, more investigation is required before this seal can enter into service. Further optimisation of the seal gap geometry can be performed and experimentation to ensure that the dynamic behaviour of the seal housing is acceptable is necessary. This data can all be acquired on the LAMFS test rig produced at Oxford for this program.

5 Fluidic Seal

5.1 Introduction

The concept of a fluidic or aerodynamic seal and its use in gas turbine applications has existed for many years where, potentially, the mass flow rate through a leakage path could be reduced by aerodynamic flow features, such as jets or a 'curtain' of air (Curtis, et al. 2009). The seal is intended to work by introducing blockage (reducing the effective leakage path cross-sectional area) and creating loss from the interaction and mixing between the leakage flow and the sealing flow, rather than using physical barriers to restrict the flow as in a brush seal. For this concept to be beneficial, the reduction in leakage mass flow rate must be greater than that of the sealing mass flow rate. Another important consideration is that the sealing mass flow rate will have been bled from the compressor and will not pass through the turbine to produce shaft work. As the sealing flow is likely to be at a higher pressure than the mainstream flow, the improvement in sealing efficiency must produce an improvement in specific thrust.

Relatively very little research has been conducted on the fluidic seal concept despite the awareness of its potential as a non-contacting sealing method, however a large quantity of research data has been obtained on impingement cooling; using jets of air to penetrate a cross flow to impinge on, and cool, a target surface. In this field, jets ideally penetrate through a cross flow with minimal interaction and hence reach the target plate relatively unaffected, thus maximising the cooling effect. The opposite is required in the case of the fluidic seal as a greater interaction between the jets and main leakage flow leads to a higher jet drag and greater mixing and dissipation of energy. Another benefit may come from an improved ability

to maintain a desired pressure difference across the leakage path. Hence, while impingement cooling flow characteristics can be applied to this concept, any feasible design is likely to lie beyond the range of currently investigated cooling systems.

This chapter describes the achievements of a parametric study involving experiments, CFD and an analytical model. In conjunction with investigating the total mass flow rate, the energy lost through the seal from the two flows is quantified by assessing the power entering and leaving the seal. An engine realistic aspect of the fluidic seal for designers to consider, which is not within the scope of this thesis, is the effect of shaft rotation. The presence of a moving rotor will introduce a whirl component to the flow field, which will vary with rotational speed. The whirl component magnitude will also vary with radial position; from the shaft rotational speed at the shaft surface to zero at the casing. This flow feature would need to be considered in the future development of this seal but in this thesis, the two flows were at the same temperature conditions and the ‘rotor’ was static.

5.1.1 Jet and Mainstream Flow Interactions

Figure 5.1 below shows how the interaction of a single jet and mainstream flow varies with the momentum flux ratio of the two flows. The dominant structure of the flow is the mutual deflection of the jet and mainstream flow. The jet is turned towards the mainstream direction and the mainstream flow is deflected as if the outer streamlines of the jet form a solid boundary, except the jet entrains some of the mainstream fluid. For a low momentum flux ratio, the mainstream flow covers the upstream part of the hole and the jet flow therefore is released from the downstream part. The mainstream lifts over the jet, tending to push the jet towards the surface. For a high momentum ratio of 4.0 the jet is only weakly affected by the mainstream flow and penetrates into the mainstream flow before its trajectory is turned

towards the mainstream direction. A complicated separation region forms downstream of the jet in both cases and reversed flow can occur.

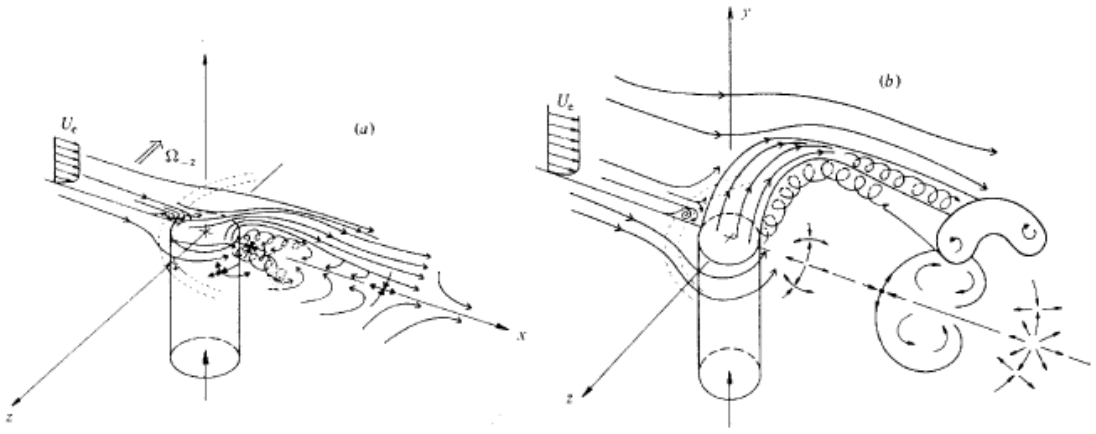


Figure 5.1: Jet and mainstream flow interaction for low, 0.25, (*a*) and high, 4.0, (*b*) momentum flux ratios (Andreopoulos and Rodi 1984)

5.2 Relevant Previous Work

5.2.1 Impingement Cooling

5.2.1.1 Discharge Coefficient

The discharge coefficient, C_d, is the ratio of the mass flow rate passing through an orifice over the mass flow rate expanding through an ideal nozzle of the same cross-sectional area with an identical working fluid, to and from the same conditions. This can vary depending on many parameters; the mainstream to jet mass velocity ratio (product of density and velocity) G_m/G_j, the pressure ratio across the hole, the hole inclination to the mainstream flow, the jet hole cross-sectional shape and filleting the hole inlet and exit edges (Hay, Lampard and Benmansour 1983). For Reynolds numbers in excess of 10,000 the peak C_d occurs at around $l / d = 2$ (Lichtarowicz, Duggins and Markland 1965). The discharge coefficient can also be influenced by channel confinement. The blockage provided by a jet causes a local acceleration in the mainstream flow around it, which lowers the mainstream local static pressure and hence the pressure difference across the hole is increased. A model to correct for

the variation in C_d due to channel confinement was developed and validated by Callaghan et al. (1949) which modifies the zero mainstream flow discharge coefficient to incorporate the effects of the drop in local channel static pressure. Chambers (2003) combined the empirical formulae from work by Callaghan et al. (1949) and Florshuetz et al. (1982) resulting in three different relationships for C_d depending on G_m/G_j.

$$C_d = 0.8 \times \sqrt{1 + \left(\frac{hd}{A - hd}\right)^2 \left(\frac{G_m}{G_j}\right)^2} \qquad 0 \leq \frac{G_m}{G_j} < 0.54 \qquad \textbf{(5.1)}$$

$$C_d = 0.893 - 0.169\left(\frac{G_m}{G_j}\right) \times C_d^* \sqrt{1 + \left(\frac{hd}{A - hd}\right)^2 \left(\frac{G_m}{G_j}\right)^2} \qquad 0.54 \leq \frac{G_m}{G_j} < 1.5 \qquad \textbf{(5.2)}$$

$$C_d = \boldsymbol{\xi}\left(G_m/G_j\right) \times \sqrt{1 + \left(\frac{hd}{A - hd}\right)^2 \left(\frac{G_m}{G_j}\right)^2} \qquad 1.5 < \frac{G_m}{G_j} \qquad \textbf{(5.3)}$$

Where

$$\boldsymbol{\xi}\left(G_m/G_j\right) = \frac{1.06}{\left(\frac{G_m}{G_j} + 0.806\right)^{0.602}} \qquad \textbf{(5.4)}$$

C_d^* = zero cross flow discharge coefficient

h = channel height

d = jet hole diameter

A = channel cross-sectional area

5.2.1.2 Channel Friction Factor

For most impingement arrays the effect of surface friction is considered to be small compared to other sources of pressure drop and hence it was deemed acceptable by Florshuetz et al. (1982) to use standard correlations for smooth ducts of constant cross-sectional area to estimate the channel friction factor. The correlations are shown below in Table 5.1.

C_f	Reynolds Number Range
$24/\mathrm{Re_c}$	$\mathrm{Re_c} < 2{,}000$
$0.079/\mathrm{Re_c^{0.25}}$	$2{,}000 < \mathrm{Re_c} < 30{,}000$
$0.46/\mathrm{Re_c^{0.25}}$	$\mathrm{Re_c} > 30{,}000$
where $\mathrm{Re_c}$ is the channel Reynolds number based on the channel hydraulic diameter.	

Table 5.1: Channel friction factor correlations (Florshuetz, et al. 1982)

5.2.1.3 Potential Core Length

A relationship for the length of a jet's potential core was derived by Chambers (2003) using the experimental data from injecting hot gas into a cold cross flow obtained by Platten et al. (1968) and is shown in Equation **(**5.5). It is a function of mass velocity ratio but is only valid for $0 \leq G_c/G_j \leq 2$ due to the experimental data available. It is also independent of the jet Reynolds number and shows that the jet potential core length in zero cross flow conditions is five hole diameters.

$$\frac{L_{pc}}{d} = 5 \times \exp\left(-1.93\frac{G_c}{G_j}\right) \tag{5.5}$$

5.2.1.4 Impingement Jet Cross Sectional Geometry

Comprehensive studies of trajectories of jets issuing from various shapes of orifices in the presence of a cross flow have been made by Ruggeri et al. (1950) where a hot jet was ejected from a shaped orifice and its penetration into the cross flow measured with a thermocouple rake as a function of downstream position. Various shaped jet holes such as circular, square and elliptical with an aspect ratio of 2:1 and 4:1 were tested and comparisons were made between them. The most effective jets for penetrating a cross flow was found to be a function of the velocity ratio between the jet and cross flow, with the square jets providing optimal performance at low velocity ratios and 2:1 aspect ratio elliptical jets were best at higher velocity ratios. Similar work on jet trajectories of elliptical holes of various aspect ratios and

target plate spacing to jet diameter ratios (*h/d*) carried out by Quinn (1989) and Hoe et al. (1987) showed that the jets twisted about their axes as a result of the formation of vortices which narrowed the jet and thus changed its major axis. Other geometries of interest may be multiple slots, or one slot spanning the entire leakage path, to provide a more uniform coverage than a row of discrete jets.

5.2.2 Theoretical Jet Analysis

Attempts have been made to predict the trajectory of a jet and it's interaction with a mainstream flow using an analytical approach. Chambers (2003) combined the work of multiple sources to produce a model validated by his experimental data. To create the model, he used an empirical formula for the entrainment of the jet mass flow produced by Hill (1972), the potential core length of a free jet in mainstream flow dependent on the mass velocity ratio, G_m/G_j, measured by Platten et al. (1968), the variation in jet shape with centreline distance and velocity ratio (mainstream / jet) from work by Wooler et al. (1967), Abramovich (1963) and Stoy et al.(1973). Another theoretical analysis was performed by Yang et al. (2005) where the turbulent three-dimensional Navier-Stokes and energy equations were solved numerically (using a finite-difference scheme) combined with the continuity equation to simulate the thermal and turbulent flow fields using an eddy viscosity model to account for the turbulent effects. The results of the model were compared to and agreed well with Nakabe (1998).

5.2.3 Fluidic Seals

The aerodynamic seal devised by Klomp (1969), shown in Figure 5.2, involves directing some of the mainstream flow from the high pressure region (HP) to be used as the sealing flow. In order to raise the pressure of the sealing flow above that of the mainstream flow, a

pump, P, is placed upstream of the jet nozzle, which directs the sealing flow back upstream, opposing the mainstream flow (flowing right to left – HP to LP). A simpler way of achieving this would be by bleeding air from the compressor at the desired pressure to be used as the sealing flow as an annular pump as indicated in the diagram would not be feasible to install and power. The total pressure difference between the jet and mainstream flow then drives the jet flow.

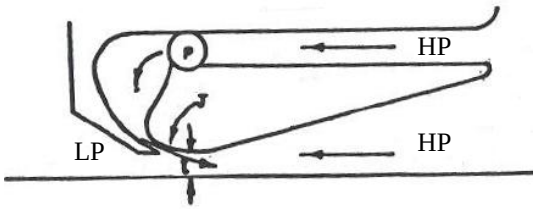


Figure 5.2: Schematic of seal proposed by Klomp (1969): (*a*) – Original design, (*b*) – Design with diffuser instead of pump

CFD investigations were performed by Hogg et al. (2011) into a fluidic seal with discrete jets at 90° and 150° (60° upstream) to the mainstream direction. Three jets were modelled in the domain using meshes of 500,000 cells with a mainstream leakage path height of 1 mm. The 90° case exhibited an increase in total mass flow rate for all jet to mainstream absolute pressure ratios (p_{0j}/p_{0m}) from 1 to 2. Increasing the angle to 150° such that the jets were pointing upstream resulted in a modest net reduction in total mass flow rate of between 5% and 10% at a pressure ratio of 1.4 (the maximum tested for this geometry).

5.2.3.1 Fluidic Labyrinth Seals

A recent patent created by Turnquist (2009) from the General Electric Company presents the fluidic seal idea incorporated into existing labyrinth seals, which generally exhibit relatively poor leakage characteristics and thus could be greatly improved. Instead of using higher pressure air for the sealing flow, some of the main leakage flow is channelled through a secondary leakage path and is injected further downstream through the main leakage path where the pressure is lower than upstream of the seal and hence the required pressure gradient

for the sealing flow is achieved. Many different configurations were listed, one of which is shown below in Figure 5.3.

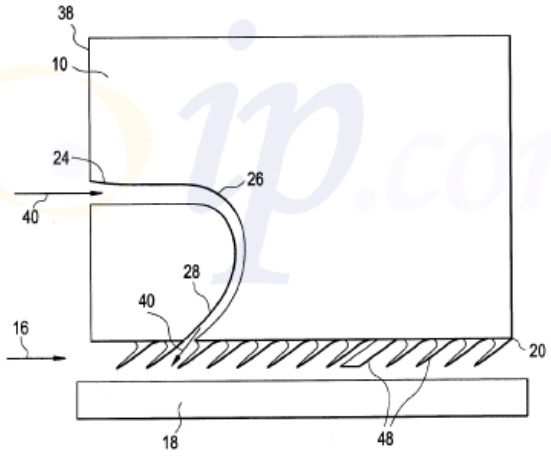


Figure 5.3: General Electric Company Fluidic Seal Patent (Turnquist 2009)

Hogg et al. (2011) also modelled a fluidic labyrinth seal using two dimensional CFD simulations. In this case, the discrete jets become a continuous slot. The labyrinth seal geometry used had three teeth with the central tooth angled upstream at 45° to the mainstream direction with the jet mass flow introduced on the upstream side of the central tooth. The jet flow angle was the same as that of the central tooth. The pressure ratio, defined differently to the plain leakage path cases, was related to the outlet static pressure and was defined as $p_r = \frac{p_{0j} - p_{out}}{p_{0m} - p_{out}}$, using steam turbine pressure boundary conditions. For both high pressure and low pressure steam turbine locations, a reduction of 25% was observed in the total mass flow rate from the baseline conditions (no jet flow).

5.2.3.2 Shrouded Turbine Blade Tip Leakage Sealing

A significant number of patents exist on sealing the leakage path between the tip of a turbine blade and the surrounding casing using the fluidic seal concept. Early patents were granted to Auyer (1954), on inclined jets injected over an unshrouded rotor with the intention of reducing the tip leakage flow, and Smile et al. (1960), on feeding a high pressure supply

through an orifice and into labyrinth style seals on the rotor shroud. Unsworth et al. (1971) had a patent accepted where an inclined jet was directed upstream against the tip leakage flow over the shroud. A patent was granted to Minoda et al. (1988) for an array of discrete jets which were angled radially inwards over an unshrouded rotor.

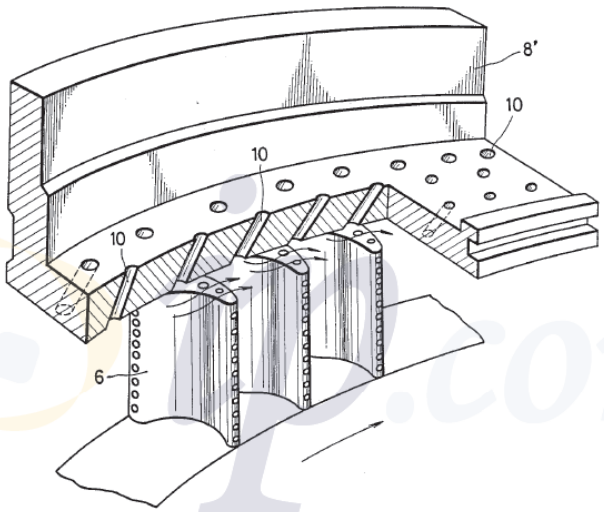


Figure 5.4: Turbine tip sealing with fluidic concept (Minoda, et al. 1988)

An experimental investigation into the use of jets and various fin combinations in a linear cascade were performed by Rusthon (2003). He concluded that the stagnation pressure loss related to the tip leakage could be reduced by 0.5% for a seal flow of 0.9% of the mainstream flow by using an inclined jet released from the casing which impinged on the blade shroud. Further work by Curtis et al. (2009) at the University of Cambridge assessed the viability of an air-curtain introduced from the casing around a shrouded turbine rotor. It was shown that, using 3.5% of the mainstream flow, the air-curtain could completely seal the over-shroud leakage path (Figure 5.5) but this would lead to a drop of approximately 0.6% in the turbine efficiency. However, a lower sealing flow of 1.2% of the mainstream flow would provide the peak increase of 0.4% in turbine efficiency. The efficiency of the turbine is defined below in Equation **(**5.6**)**, which takes account of the work that can be extracted from both the mainstream gas and the sealing flow as the denominator.

$$\eta = \frac{\Gamma \times \omega}{\dot{m}_m c_p T_{0m}\left[1 - \left(\frac{p_{0exit}}{p_{0inlet}}\right)^{\frac{\gamma-1}{\gamma}}\right] + \dot{m}_j c_p T_{0j}\left[1 - \left(\frac{p_{0exit}}{p_{0j}}\right)^{\frac{\gamma-1}{\gamma}}\right]} \tag{5.6}$$

where Γ is the brake torque of the rotor and ω is the angular velocity.

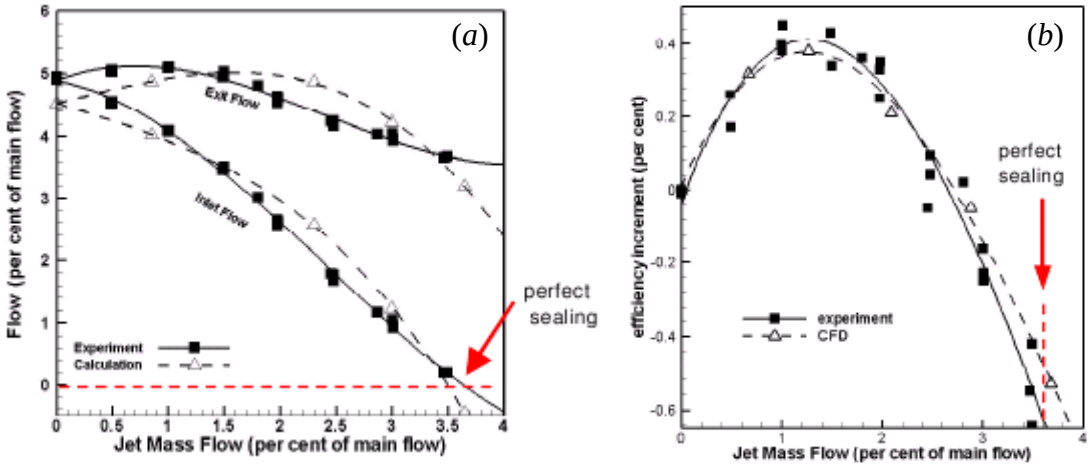


Figure 5.5: Inlet and exit mass flow rates to the shroud cavity with jet mass flow rate (*a*) and turbine efficiency with jet mass flow rate (*b*) (Curtis, et al. 2009)

A patent application filed by Hogg (2010) utilises the fluidic seal within interstage labyrinth seals to reduce vane root leakage. This is also applied to the blade tip as investigated by Curtis et al. (2009). The idea incorporates devices to recover the dynamic head from the whirl component of the leakage flow. A pressure difference across the jet holes exists due to the pressure drop in the mainstream flow across an initial labyrinth tooth which is then increased by the dynamic head recovery devices. This configuration intends to negate the requirement of higher pressure air bled from the compressor for the sealing flow and the associated loss of shaft work.

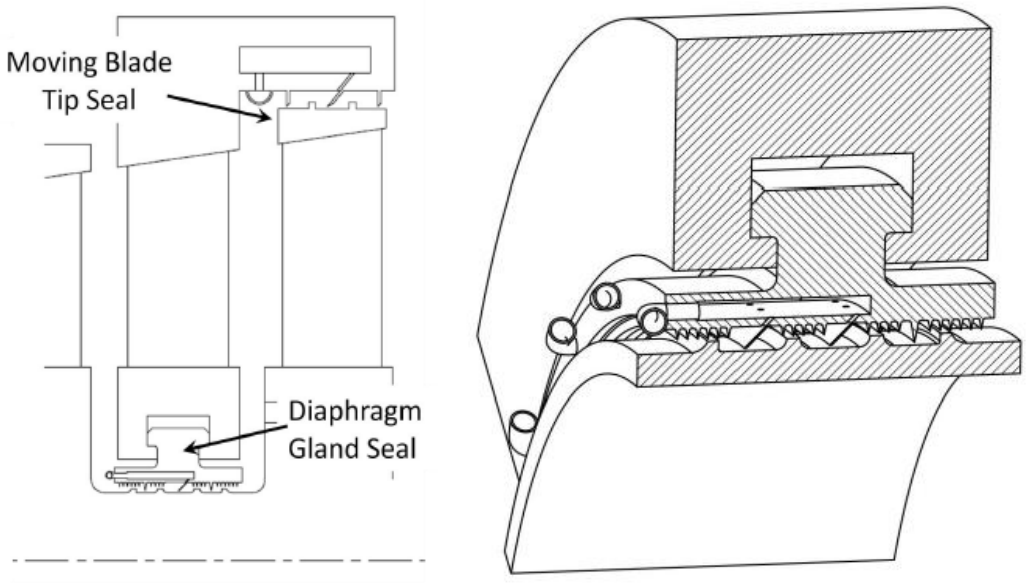


Figure 5.6: Labyrinth-fluidic concept used as interstage seals (Hogg 2010)

5.3 Experimental Test Rig

The linear test rig created to evaluate the fluidic seal concept is shown below in Figure 5.7. Assuming the mainstream gap height is much smaller than the radius ($h << r$), a linear test section provides an adequate representative geometry for performing preliminary, static investigations. The front, rear, side, top and base plates form the main pressure vessel to contain the mainstream flow and are sealed between each other with silicone sealant. A hole cut in the top plate allows for the primary insert to slot into the pressure vessel, which forms part of the mainstream inlet and outlet plena and the test section channel between them (see Figure 5.8). The main insert also contains the jet hole geometry in a removable insert and part of the jet inlet plenum. An O-ring seals between the primary insert and the top plate allowing it to be removed easily to replace the jet geometry insert to an alternative geometry, reducing the down time between tests. The jet inlet plenum is also sealed with silicone sealant on the contact areas.

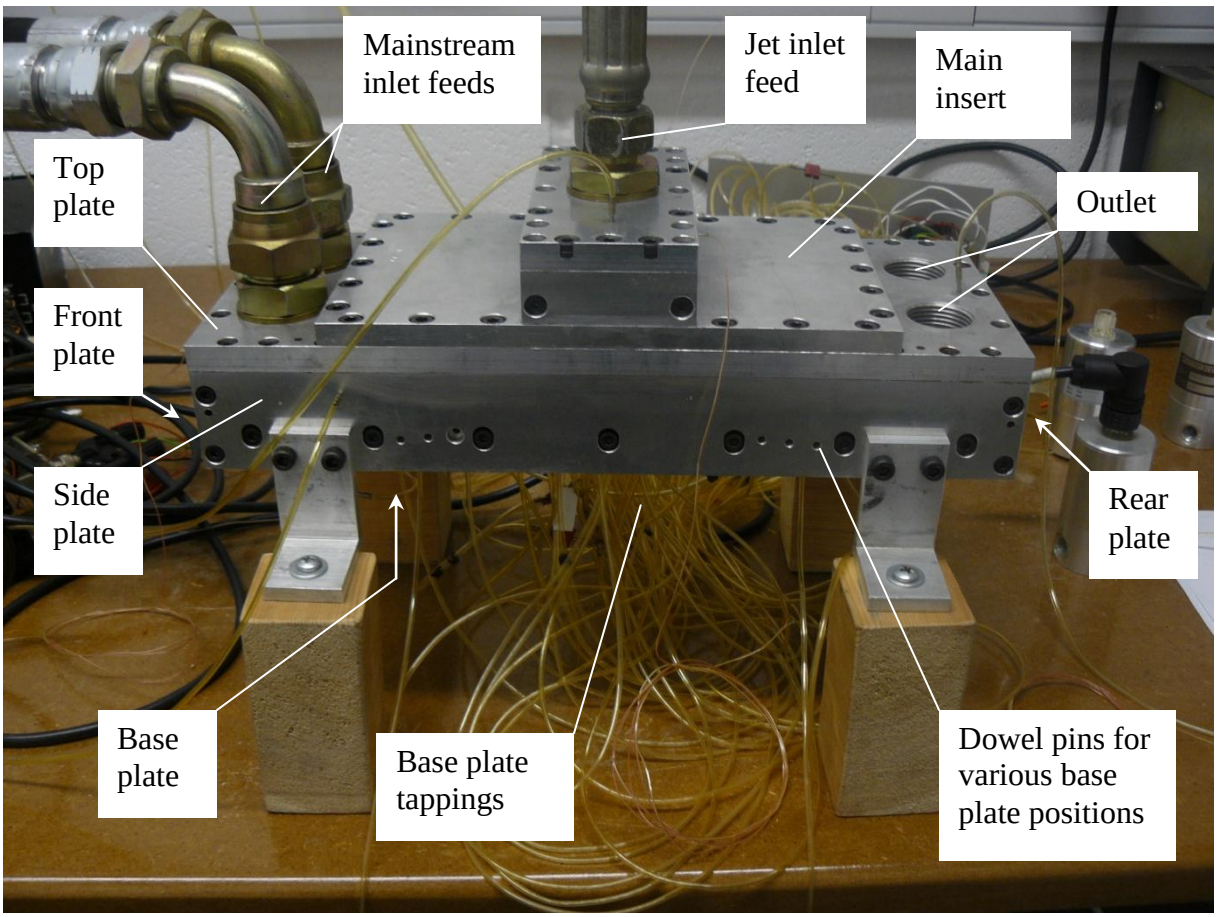


Figure 5.7 Fluidic seal test rig external view

To improve the uniformity of the mainstream flow entering the test section, the mainstream inlet feed is split into two before entering the mainstream inlet plenum. The flow then impinges on a baffle plate and is turned before reaching the inlet to the test section. Stress calculations were performed when designing the rig using the formulae from Young et al. (2002). Figure 5.8 shows the cross section of the test rig along with annotated dimensions. The mainstream flow enters the rig through the top plate into the mainstream inlet plenum before entering the test section. The jet flow enters the jet inlet plenum, which is attached to the primary insert, leading to the jet holes location at 50% of the test section length.

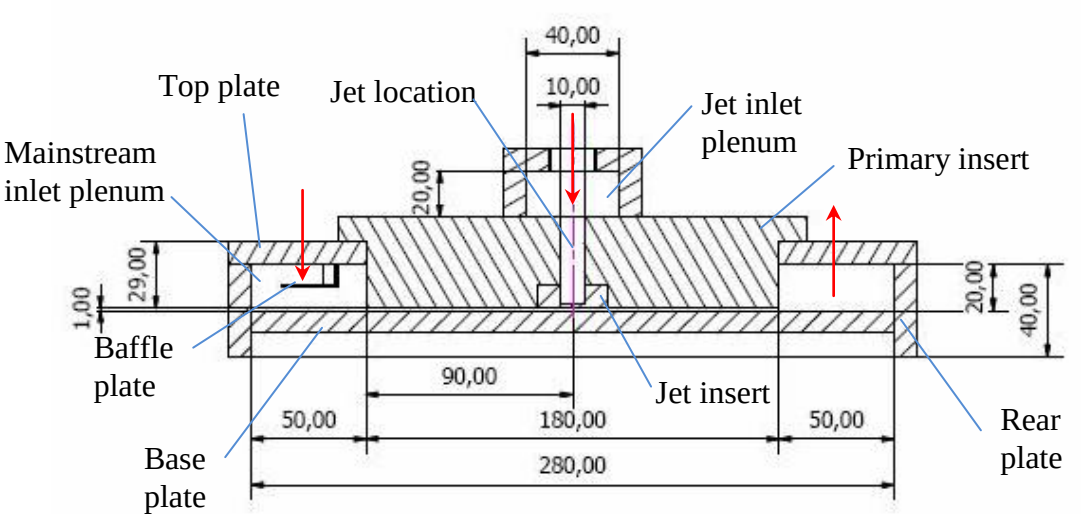


Figure 5.8: Fluidic seal test rig cross-section at mid span (dimensions in millimetres)

5.3.1 Test section geometry

The test section is 180 mm long and 100 mm wide which were constant for all tests. The length was chosen to ensure the flow was well developed by the point of reaching the row of jets, which were located equidistant from the test section inlet and outlet. The height of the test section was a parameter of interest and hence could be varied by positioning the base plate with dowel pins in the side, front and end plates. The test section width was chosen so as to ensure edge effects from flow interacting with the side plates would be negligible *i.e.* the test section span was much greater than the channel height.

5.3.2 Air System

Both the mainstream flow and jet inlet feeds are supplied by the laboratory's 100psi line. A 1" BSP fitting was taken from it and passed through a valve before being split into the two separate feeds. The flow sent to the mainstream inlet is then controlled by a *Norgren 11-808-960* pilot operated regulator in conjunction with a *Norgren 11 400/20AL-X* conventional pilot regulator before passing through an orifice meter to measure the cross-flow mass flow rate entering the test rig. The 1" BSP pipe size is split into two ¾" BSP pipes prior to being fed into the mainstream inlet plenum in order to improve the uniformity of the flow upstream of

the test section. The jet flow is controlled by a Norgren L20AG-X4G/PJ100 conventional pilot regulator and passes through a separate orifice meter, then into the jet inlet plenum via a single ¾" BSP pipe. The outlet plenum vents the exhaust flow directly to atmosphere.

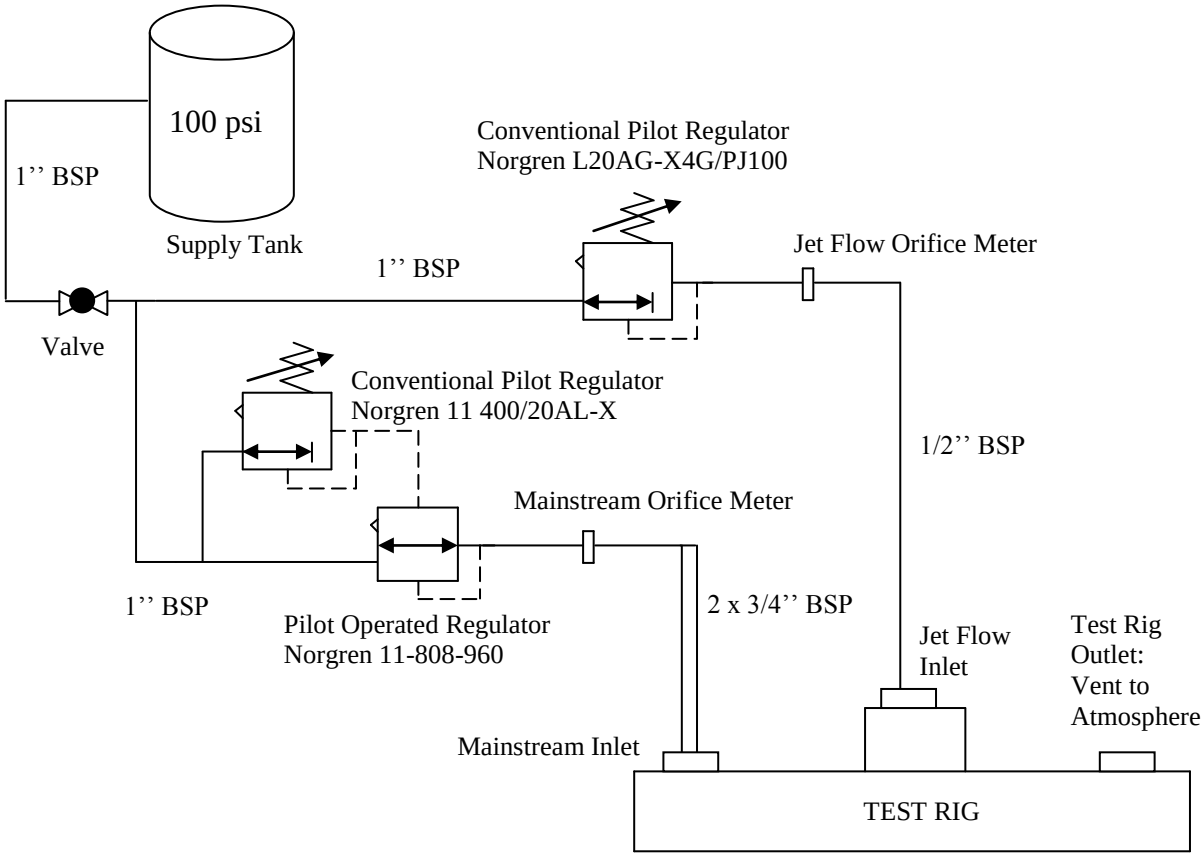


Figure 5.9: Schematic of fluidic seal test rig air supply system

5.3.3 Instrumentation

The fluidic seal test rig employs one *NI PCI-6053E* 16 bit data acquisition card. Pressure transducers were connected directly to the DAQ card via an *NI BNC 2110* shielded connector block with 8 analogue inputs. Various differential transducers from the *BTE5000* range (0 - 25 mbar, 0 - 70 mbar, 0 - 350 mbar), the *BTEM5000* range (0 - 2 bar, 0 - 5 bar) and the *PTE5000* range (0 - 15 psi) were used. Thermocouples were directly connected to an *NI USB-9211* 4 channel thermocouple reader which was transmitted to the data acquisition PC through a USB port.

5.3.3.1 Test Section

In order to assess the variation in flow conditions across the width of the test section due to possible non-uniform mainstream inlet flow and edge effects, static pressure tappings were located in the span-wise direction 20 mm apart. 33 static pressure tappings were located down the centreline of the test section, equidistant from the side plates as shown in Figure 5.10, with the tapping density increasing around the axial location of the jets. For the 10 mm upstream and downstream of the jet injection point, there is a high density array (HDA) of tappings, where one is located every millimetre in the stream-wise direction, though as the holes are 1 mm in diameter, a span-wise spacing was required (5 mm). The static pressure was taken for all the tappings on the test section centreline and the remaining tappings in the HDA were measured with a differential transducer with the low pressure port connected to the downstream-most tapping in the HDA (marked with a cross) and the high pressure port connected to the tapping in question.

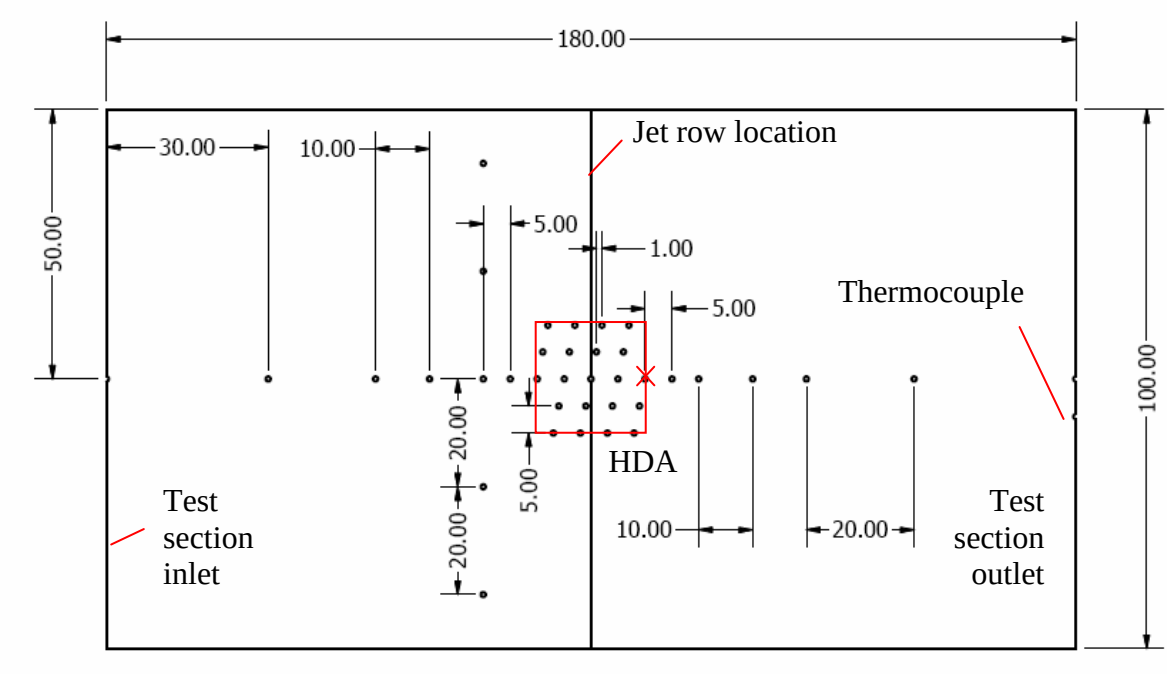


Figure 5.10: Test section pressure tapping layout (dimensions in mm)

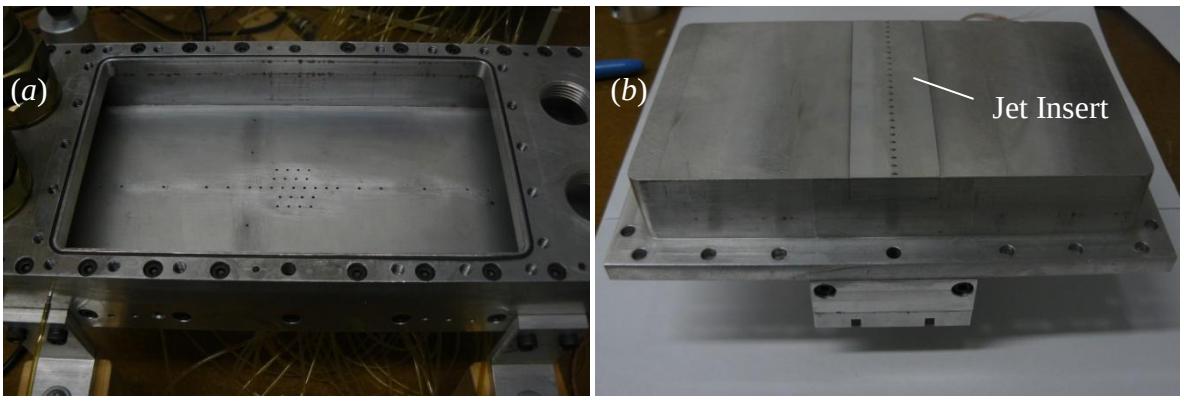


Figure 5.11: (*a*) – Fluidic seal test rig test section (primary insert removed), (*b*) – Underside of primary insert

5.3.3.2 Further Instrumentation

The pressure was measured in the mainstream inlet plenum and the jet inlet plenum in order to set the correct boundary conditions for the each test. K-type thermocouples were also present in each plenum to measure the inlet total temperature for the two inlet flows. To measure the pressure difference across the mainstream flow (leakage path), the static pressure was taken at the test section exit. A further two pressure readings, upstream and downstream of the orifice plate, and a K-type thermocouple were required for each of the two orifice meters (one for each inlet flow).

5.3.4 Parameters of interest

5.3.4.1 Pressure difference (Δp)

This is the driving pressure for the mainstream leakage flow. The pressure drops across seals in an aero engine can be 5 bar, which was higher than was tested in this facility, but the initial investigation into the feasibility of this concept could be carried out at lower pressures. Tests were performed on pressure drops of 0.5 and 1 bar.

5.3.4.2 Pressure ratio (p_r)

This is determined as the ratio of the absolute inlet total pressure for the jet inlet plenum over the absolute inlet total pressure of the mainstream inlet plenum: p_{0j}/p_{0m}. Higher pressure ratios raise the pressure difference across the jet holes and hence the jet flow momentum, potentially creating greater mixing loss and reducing the mainstream leakage further. The pressure ratios tested ranged from 1 to 2.6. Pressure ratios of 2 and above may be difficult to achieve within an engine but this research also aims to explore the performance of the seal within the compressible flow regime.

5.3.4.3 Channel height (h)

The channel height is the distance between the test section surfaces (primary insert and base plate). Larger channel heights would result in greater mainstream momentum for a given set of boundary conditions and hence the ratio of the jet to the mainstream momentum would vary with channel height. The test rig was designed to be easily reconfigured to test channel heights of 1, 2 and 3 mm.

5.3.4.4 Jet angle: (θ)

The extent of mixing between the jet flow and mainstream flow, and hence the drag on the jet, can be heavily influenced by the angle of jet flow trajectory with respect to the mainstream flow direction (Holdeman 1991). Furthermore, to exploit the jet momentum in restricting and reducing the mainstream mass flow, the jet angle is also an important parameter and hence was investigated in detail. Jet angles, relative to the mainstream direction, of 90°, 120°, 135° and 150° were investigated.

5.3.4.5 Jet spacing (*s*)

The jet diameter was fixed at 1 mm for all tests and hence varying the distance between the jet holes, *s*, affects the jet density (jet to mainstream area ratio). This greatly affects the mass flow rate that is used for the jet flow per unit span and the effective leakage path cross-sectional area reduction by the jets. A higher jet density increases the potential for the mainstream mass flow rate to be reduced, although the total mass flow through the seal may be greater. An optimum jet spacing, *s*, will give the maximum reduction in mainstream mass flow rate per unit of sealing mass flow rate. The tests in this thesis involved two jet spacing values of 2*d* and 4*d* where *d* is the jet hole cross-sectional diameter.

5.3.4.6 Other Parameters

Further parameters of interest, which have not been investigated in this thesis, are the hole shape, hole pattern and the effectiveness of the jets as the whirl component of the mainstream flow varies due to shaft rotation. In terms of the hole pattern, multiple rows can be introduced which may be staggered and each row could have a different 'whirl angles' i.e. crossing paths, for example. A variation on the circular cross-section hole is briefly investigated in this thesis and is described in section 5.5.2.

5.3.4.7 Labyrinth Seal

As described in section 1.3.1, the labyrinth seal is the most widely used seal within gas and steam turbines currently in service. There is therefore great potential to raise the overall efficiency by improving the leakage characteristics of each labyrinth seal. Incorporating a fluidic seal within a labyrinth seal, such as in Turnquist (2009), is a potential solution. To investigate the viability of such an idea, a simplified labyrinth seal, including a fluidic seal, was created by Skouby (2011) and was tested at the Osney Laboratory, Oxford. The geometry of the labyrinth-fluidic seal tested by Skouby (2011) was based on the two dimensional CFD work performed at Durham University (Hogg and Gomez Ruiz 2011) and is shown below in

Figure 5.12. The labyrinth seal created for the Oxford fluidic test rig contained 3 teeth, the roots of which were equally spaced at 14 mm. The central tooth was angled upstream at 45˚ and the row of jets was introduced at the same angle immediately upstream of the central tooth. The clearance between the teeth tips and the base plate was equal for all 3 teeth at 1 mm.

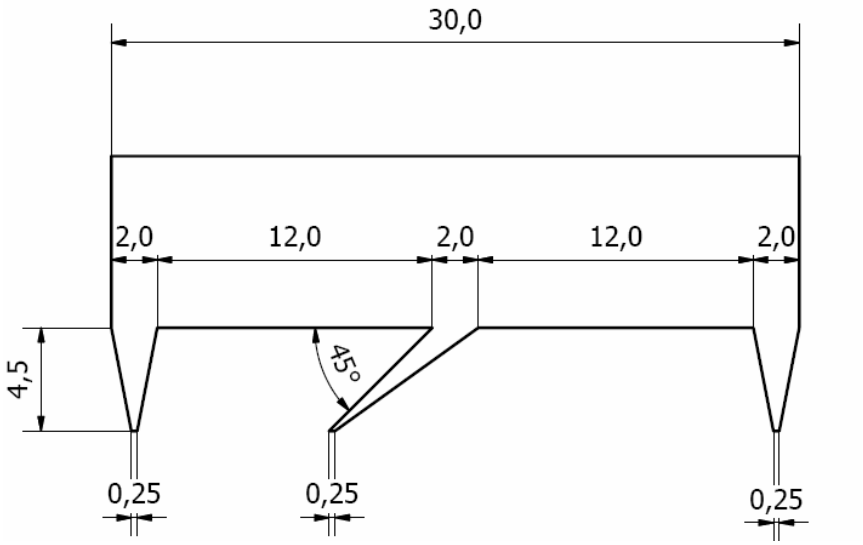


Figure 5.12: Labyrinth-fluidic seal insert geometry tested at Oxford (Skouby 2011)

Fluidic Seal Placement

If the desired requirement of the seal is to maximise the loss through it and minimise the total leakage, as oppose to controlling it for the benefit of maintaining an optimum coolant flow, for example, then the placement of the fluidic device in relation to the central fin could be a parameter of interest when the flow field within a labyrinth seal is considered. When leakage flow passes through a labyrinth seal, it accelerates under each tooth tip and forms a vortex within each cavity between neighbouring fins as shown in Figure 5.13. Therefore, depending on which side of the fin the sealing flow is ejected from, the jets could be assisted or impeded by the respective cavity vortex before they have reached the fin tip where they will interact with the mainstream leakage flow.

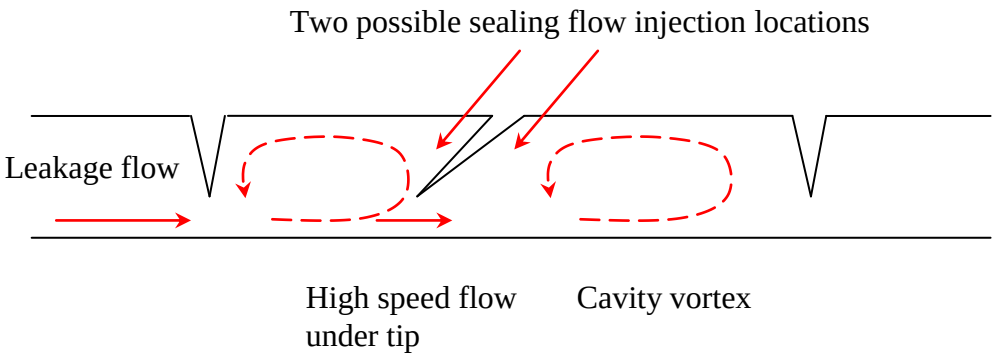


Figure 5.13: Possible sealing flow locations and flow field in a fluidic-labyrinth seal

5.3.5 Cases Tested

Table 5.2 and Table 5.3 list all the circular hole and plain mainstream path geometry cases that were tested on the Oxford fluidic seal rig for pressure differences of 0.5 bar and 1 bar respectively. Table 5.4 shows which boundary conditions were tested with the fluidic-labyrinth seal geometry. All tests are with 1 mm diameter holes and the pressure ratios tested are from 1 up to the listed value in increments of 0.2. Air system limitations or reversed mainstream flow (perfect sealing) are the reasons for why the desired peak pressure ratio of 2.6 was not achievable for some cases. The jet angle, θ, is measured between the mainstream leakage flow direction and the jet flow direction and hence 90˚ corresponds to vertical jets normal to the mainstream flow as shown in Figure 5.14. The units of jet spacing is in number of hole diameters (equivalent to millimetres) and is measured between the jet axes.

Jet Spacing (diameters)	h (mm)	ϑ (degrees)			
		90	120	135	150
2	1	2.0	-	-	-
	2	-	-	-	-
	3	-	-	-	2.6
4	1	2.0	2.6	2.4	2.2
	2	-	2.6	2.6	2.6
	3	-	2.6	2.6	3.0

Table 5.2: Maximum experimental pressure ratios tested at Δp = 0.5 bar

Jet Spacing (diameters)	h (mm)	ϑ (degrees)			
		90	120	135	150
2	1	2.0	-	-	-
	2	-	-	-	-
	3	-	-	-	2.2
4	1	2.0	2.6	2.6	2.6
	2	-	2.6	2.6	2.6
	3	-	2.6	2.6	2.6

Table 5.3: Maximum experimental pressure ratios tested at Δp = 1 bar

Jet Spacing (diameters)	h (mm)	ϑ (degrees)			
		90	120	135	150
4	1	-	-	2.6	-

Table 5.4: Maximum pressure ratios tested at on labyrinth-fluidic seal at Δp = 0.5 and 1 bar

5.3.6 Uncertainty

Direct Measurements

The individual uncertainties of the transducers involved in the Oxford fluidic test rig are shown below in Table 5.5. For the method used to derive the random and systematic uncertainty, see section 3.3.2.3.

Measurement	Systematic Uncertainty	Random Uncertainty
Pressure (25 mbar)	20.5 Pa	17.4 Pa
Pressure (70 mbar)	61.5 Pa	52.4 Pa
Pressure (350 mbar)	261.1 Pa	243.6 Pa
Pressure (15 psi)	0.111 psi	0.104 psi
Pressure (2 bar)	1480 Pa	1392 Pa
Pressure (5 bar)	3700 Pa	3480 Pa
Temperature	2.89 K	0.154 K

Table 5.5: Oxford fluidic test rig transducer uncertainties

Computed Measurements

The mass flow rate data and the power loss factor are derived quantities and hence jitter programs, as described in section 3.3.2.3, were employed to calculate the respective

uncertainties. The maximum uncertainty for the mass flow rate and power loss factors were calculated at 3.8% and 5.4% respectively.

5.4 Analytical Model

The analytical model used by the author was based on one created by Ruiz (2010) and incorporated correlations for skin friction coefficients (5.2.1.2) and discharge coefficients (5.2.1.1) for jets in a cross flow. The control volume for this model is shown in Figure 5.14 and is solved using an iterative process on a momentum balance. Mainstream leakage flow and jet flow enter the seal from their respective inlet plena. The two mass flows leave the domain through the exit on the right hand side. The jets enter the control volume at a distance L_{mu} downstream from the test section inlet and a distance L_{md} upstream of the test section outlet. L_w represents the test section width and h the height. The length of jet holes is L_j and the jet hole diameter is shown as d. $\dot{m}_m$ is the mainstream mass flow rate, $\dot{m}_j$ is the jet mass flow rate, p_{0m} is the mainstream inlet total pressure, p_{0j} is the jet flow inlet total pressure and p_{out} is the outlet static pressure. The angle of the jets relative to the mainstream direction is represented by θ. N is used for the number of jet holes across the test section width. The full list of equations which constitute the model are shown in section A.5.

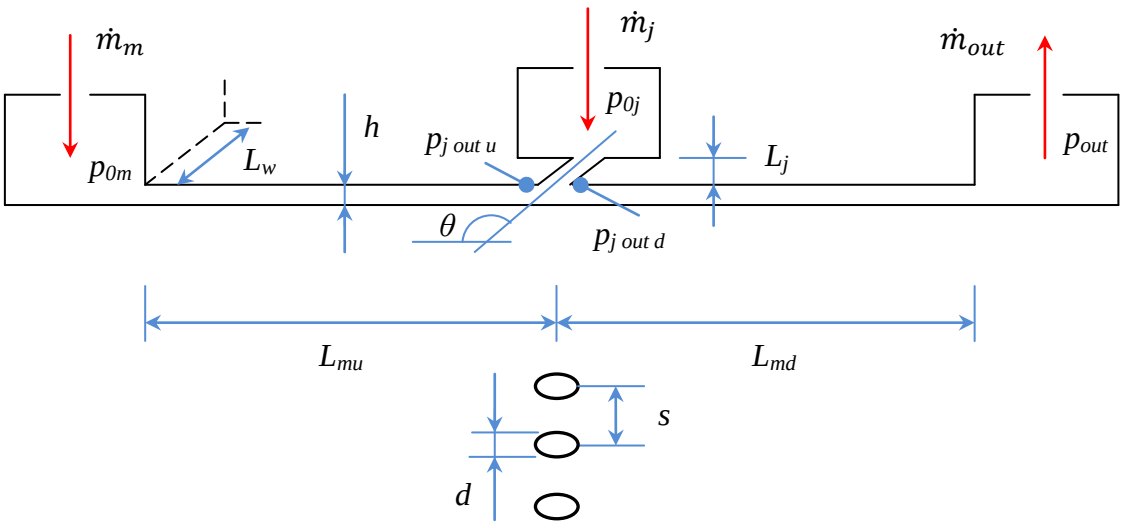


Figure 5.14: Analytical model control volume

The model was run for the number of iterations required for the Frobenius norm of the difference between subsequent iterations to fall below the desired threshold.

5.5 CFD

3D CFD studies were performed on three variations of the fluidic seal; the circular cross-section jet geometry, a novel jet geometry to achieve a continuous jet in the spanwise direction as in the case of a slot (console), and the circular jet geometry incorporated into a labyrinth seal. The details of each are described below.

5.5.1 Circular Holes

Four parameters were varied in the plain hole study to compare with the experimental data. These were the pressure ratio (p_r = 1, 1.8 and 2.6), channel height (h = 1, 2 and 3 mm), jet spacing (4d, 2d and 1.5d, where d = 1 mm) and jet angle (θ = 120°, 135°, and 150°). The pressure difference across the mainstream path was constant at 1 bar. All combinations of these parameters were created and solved for. Meshes contained approximately 400,000 cells deemed sufficient by a mesh sensitivity study.

5.5.2 Console

The console (***Con***verging ***S***lot H***ole***) jet geometry consists of an elliptical inlet (created by a circular hole inclined to the surface) and a slot exit with a reducing cross sectional area. The inlet areas are therefore directly comparable to the plain hole cases. The consoles were initially developed to create a laterally-uniform film cooling flow from a discrete set of inlets in order to maintain structural integrity when applied to turbine blade and vane applications. This idea can be applied to the fluidic seal to impede the mainstream leakage flow with a ‘curtain’ of air as attempted by Curtis et al. (2009). As the change to the domain volume was small between the console and respective circular cases, the mesh sizes were identical that stated above.

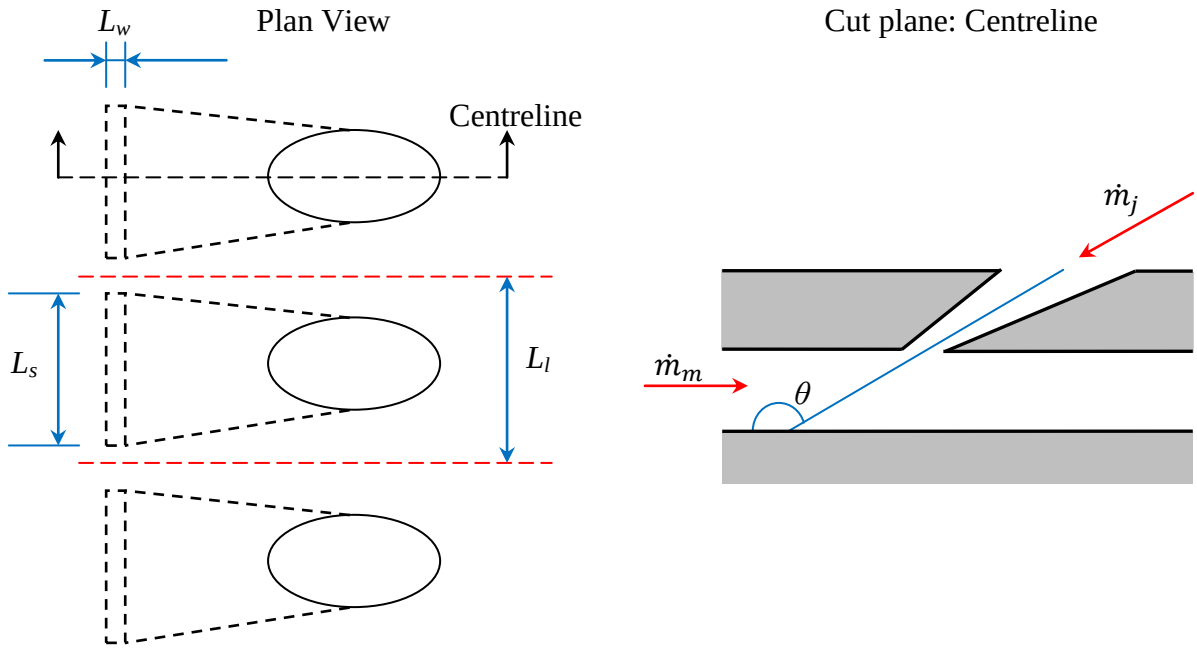


Figure 5.15: Console Geometry

The parameters varied in this study were the jet spacing, *s*, the jet-to-mainstream inlet pressure ratio (absolute and total), p_j/p_m, the jet angle, θ, the slot to ellipse (exit to inlet) area ratio, A_s/A_e, and the slot to spacing ratio, L_s/s. The cases for which data was obtained are shown below in Table 5.6. The third row represents the baseline case and all the varied parameters described above are in bold. For all other cases, one parameter is varied from the baseline case which has been shown in bold. The final two columns detail the slot dimensions; the slot length, L_s, and the slot width, L_w.

p_{0j}/p_{0m}	s (d)	θ (°)	h (mm)	A_s/A_e	L_s/s	L_s (mm)	L_w (mm)
1	2	150	3	0.8	1	2	0.628
1.8	2	150	3	0.8	1	2	0.628
2.6	**2**	**150**	**3**	**0.8**	**1**	2	0.628
2.6	2	150	**2**	0.8	1	2	0.628
2.6	2	150	**1**	0.8	1	2	0.628
2.6	2	**120**	3	0.8	1	2	0.363
2.6	2	**90**	3	0.8	1	2	0.314
2.6	**4**	150	3	0.8	1	4	0.157
2.6	2	150	3	0.8	**0.9**	1.8	0.698
2.6	2	150	3	**1**	1	2	0.785

Table 5.6: Console jet geometry CFD cases (console baseline case: 3rd row)

5.5.3 Labyrinth-fluidic Seal

Three dimensional CFD was also performed on the labyrinth-fluidic seal by Skouby (2011) and the domain geometry is shown below in Figure 5.16. The inlet plena for the mainstream and jet flows are modelled whilst the outlet is taken at the exit plane of the test section and all are given pressure boundary conditions. The domain encompasses the entire length of the test section and the width of two jets up to the midpoint between their respective neighbouring jets where symmetry boundary conditions are applied. Meshes ranged from 450,000 to 500,000 cells and were deemed sufficient in size by a mesh dependency study. Cells were deliberately concentrated around the labyrinth teeth where the resolution was required. The method and settings used to solve the CFD cases were as used in section 3.4.4.3 for the linear LAMFS.

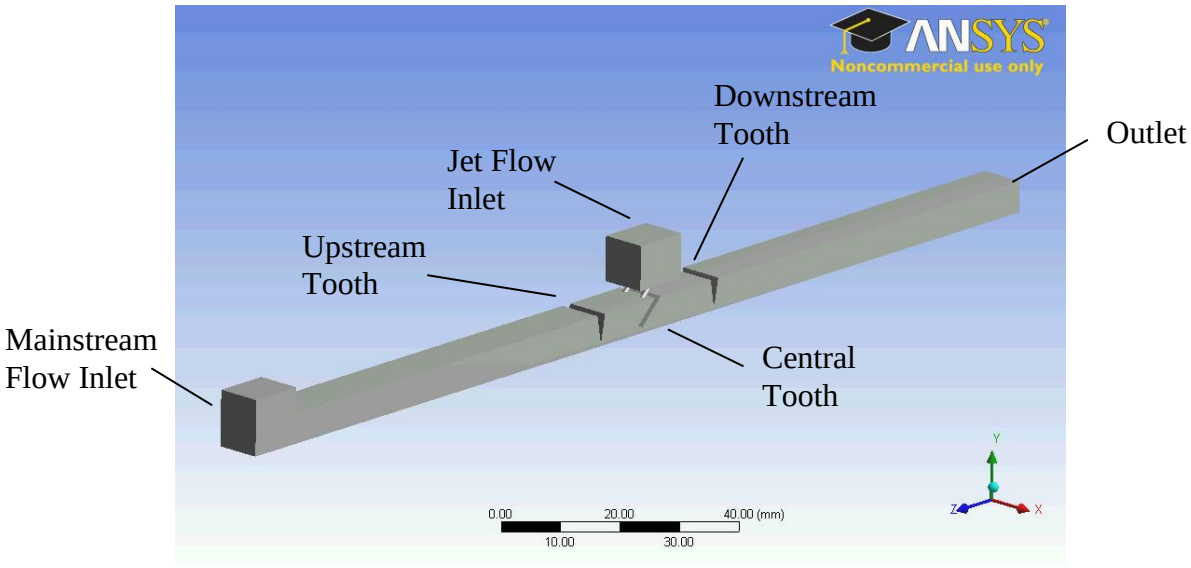


Figure 5.16: Labyrinth-fluidc seal CFD domain (Skouby 2011)

5.6 Results

This section describes the results obtained experimentally, from CFD and from the analytical model. First, the mainstream flow, jet and total mass flow rates are presented for a selection of cases for the simple geometry along with the analytical prediction, followed by further analysis of the data in terms of the energy dissipated from the interaction of the two flows. Interaction plots, which assess the influence of the various parameters on each other in terms

of normalised mass flow rate and energy dissipation are then analysed, and finally, the fluidic-labyrinth seal geometry mass flow rate results are then presented and discussed.

5.6.1 Circular Jets - Mass flow rate

Testing began with the jets angled at 90˚ to the cross flow to investigate whether the channel cross-sectional area reduction provided by the jets and jet drag and interaction with the cross flow were sufficient to reduce the total mass flow rate without taking advantage of the jet momentum. Mass flow rate figures display mainstream, jet and total mass flow rates against the pressure ratio. On each figure, the horizontal black line represents the mass flow rate of the baseline case, when only the mainstream flow is present and there is no jet flow, although the jet hole geometry has not been replaced with a 'blank', smooth alternative. The red, blue and green data points refer to the mainstream, jet flow and sum total of the two flows respectively. Therefore if the green data points are below the baseline case, a reduction in total mass flow rate has been achieved by including jet flow.

5.6.1.1 Jet Angle (θ): 90°

Figure 5.17 shows the mass flow rate for jets at 90° to the cross flow direction when Δp = 0.5 bar, h = 1 mm and $s = 4d$. Immediately once the jets are introduced, from p_r = 1, there is a reduction in the mainstream mass flow rate and is reduced further as the pressure ratio rises. When p_r = 1, there is a reduction of 14% in mainstream mass flow rate from the baseline case, however the jet mass flow rate is 19% of the baseline case and hence results in a 5% increase in the total mass flow rate, which only worsens as the pressure ratio increases. This trend is also seen for a pressure drop of 1 bar. These results show that the jets are providing a restriction which is seen by a reduction in mainstream mass flow rate for all pressure ratios but this is insufficient in reducing the total mass flow rate below the baseline case.

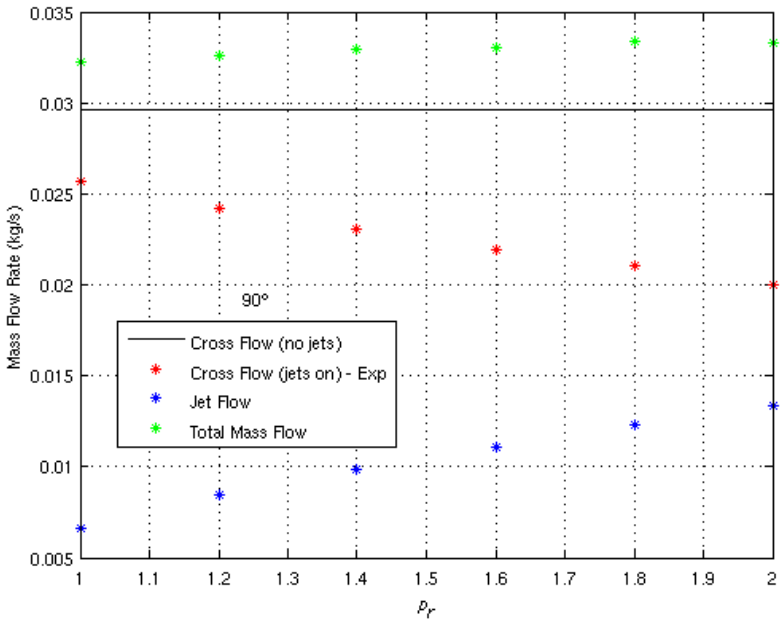


Figure 5.17: Experimental mass flow rate: h = 1 mm, θ = 90°, Δp = 0.5 bar, s = 4d

5.6.1.2 Experimental Data vs. Analytical Model

The accuracy of the analytical model is assessed below against the experimental data for the three different channel heights at θ = 150°, Δp = 1 bar and s = 4d. Channel heights of 3, 2 and 1 mm are compared in sections 5.6.1.2.1, 5.6.1.2.2 and 5.6.1.2.3 respectively.

5.6.1.2.1 h = 3 mm

Figure 5.18 shows the mass flow rate for the case where h = 3 mm. For this case, the mainstream mass flow rate is reduced by 11% at p_r = 1 to 41% at p_r = 2.6 which is slightly less effective than at Δp = 0.5 bar. The total mass flow rate has reduced by a maximum of 22% which is also slightly poorer than at Δp = 0.5 bar. The trends predicted by the analytical model are in good agreement with the experimental data though less so than when Δp = 0.5 bar. As p_r increases, the rate of cross flow reduction is near identical to the experimental data which suggests that the skin friction coefficient may be inaccurate for these conditions, whilst the jet mass flow discrepancy reduces. Overall, the total mass flow rate is under-predicted across the p_r range by a maximum of 7%.

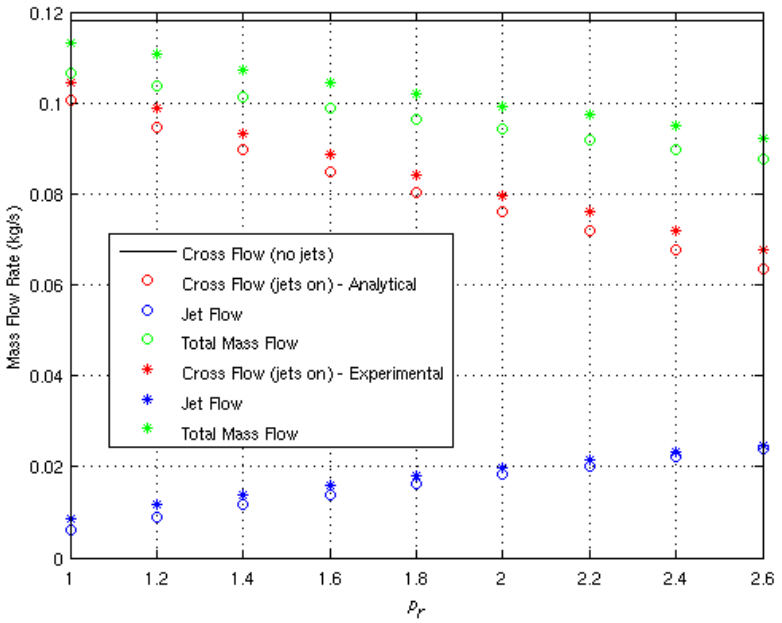


Figure 5.18: Experimental and analytical mass flow rates: h = 3 mm, θ = 150°, Δp = 1 bar, s = 4d

5.6.1.2.2 h = 2 mm

When h is reduced to 2 mm, whilst all other parameters remain unchanged (θ = 150°, Δp = 1 bar, s = 4d), the effectiveness of the jets at reducing the mainstream flow is improved. The mass flow rates for these conditions are shown in Figure 5.19. The baseline mass flow rate (no jet flow) has reduced from by 39% from 0.118 kgs^{-1} to 0.0725 kgs^{-1}, more than by the area reduction (33%) as the friction from the channel walls becomes more influential at lower hydraulic diameters. For all pressure ratios, the jet mass flow rate is identical to when h = 3 mm, as the pressure boundary conditions across the jet hole do not vary, however the mainstream is reduced by 17% when p_r = 1 to 66% less at p_r = 2.6 which shows that the jet flow is much more effective than when h = 3mm perhaps due to the lower mainstream flow momentum which affects the jet-mainstream interaction (momentum ratio). At p_r = 1, the total mass flow is reduced by a similar percentage to when h = 3 mm but the jets become more effective as the pressure ratio increases. At p_r = 2.6, the jet flow is almost equivalent to the mainstream and hence almost half of the total mass flow. The analytical model under-predicts both the cross flow and jet flow, which leads to a significant under estimate of the total mass

flow rate through the seal, though the general trends of each mass flow rate with pressure ratio are reasonably accurate.

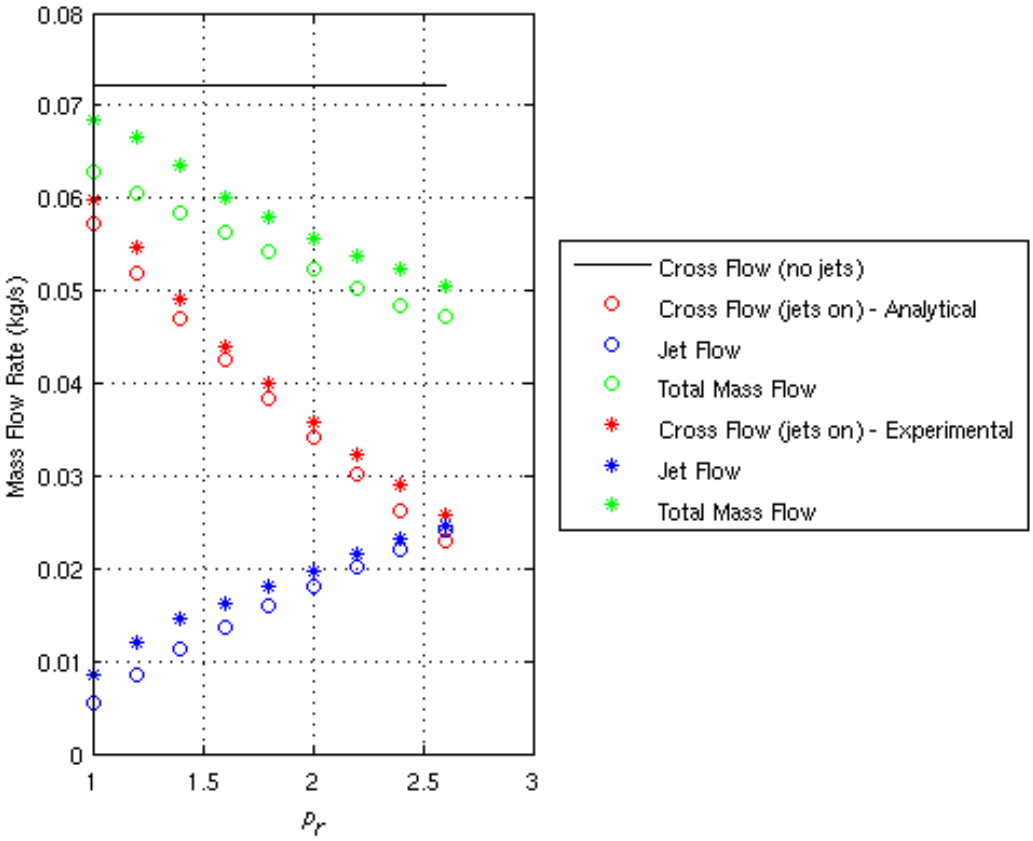


Figure 5.19: Experimental and analytical mass flow rates: h = 2 mm, θ = 150°, Δp = 1 bar, s = 4d

5.6.1.2.3 h = 1 mm

At h = 1 mm (θ = 150°, Δp = 1 bar, s = 4d), the baseline mass flow rate is less than the reduction in cross sectional area (50%) from h = 2 mm at 0.0325 kgs^{-1} caused by the more influential friction from the channel walls and subsequently lower hydraulic diameter. This is shown in Figure 5.20. This channel height has significantly changed the performance of the seal with varying pressure ratio. For channel heights of 2 and 3 mm, the limit of the reduction in cross flow by the jets is not achieved within the pressure ratio range tested, but for h = 1 mm, the total mass flow rate reaches a minimum at $p_r \approx 2.2$ and worsens at higher pressure ratios. The seal also does not reduce the total mass flow rate below the baseline for all pressure ratios as it is greater by 1.5% at p_r = 1. At this pressure ratio, the jet mass flow rate is

lower than for when h = 2 and 3 mm but reaches 0.023 kgs^{-1} at p_r = 2.6 as it does for h = 2 and 3 mm.

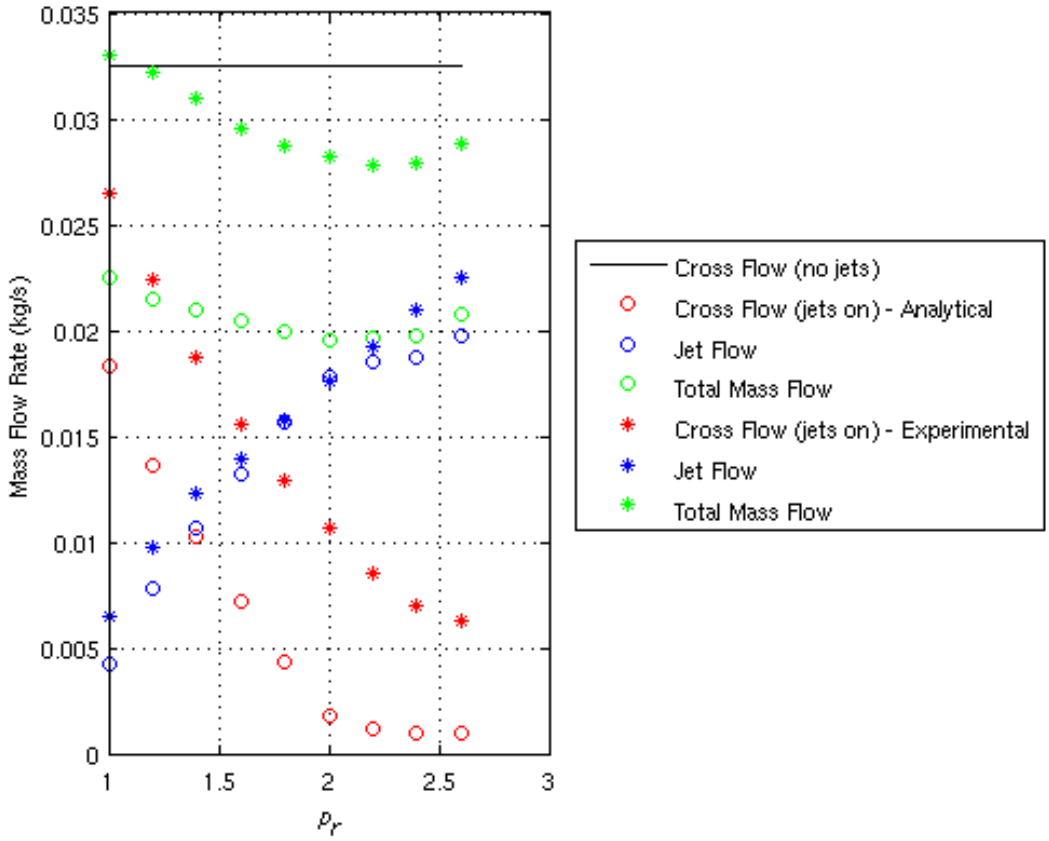


Figure 5.20: Experimental and analytical mass flow rates: h = 1 mm, θ = 150°, Δp = 1 bar, s = 4d

For this channel height, the analytical model is highly inaccurate. The cross flow is greatly under-predicted from the lowest pressure ratio, but the trend is similar to the experimental data, suggesting that either the channel friction factor is over estimated or the effectiveness of the jet flow is over predicted as the simple model cannot account for an effect caused by the complex flow field where some of the jet momentum may be wasted as they impinge on the base plate. This could be seen to a much lesser extent when h = 2 mm.

5.6.1.3 Normalised Mass Flow Rate

The experimental mass flow rates, normalised to their respective baseline cases, for all circular hole and plain channel geometry cases are displayed in Figure 5.21. A normalised mass flow rate of below 1 indicates the total mass flow rate is less than the baseline case (no

jets) and is thus described as an improvement in sealing. Each subplot represents a particular value for h and the three jet angles, 120°, 135° and 150° are shown in red, blue and green respectively. When h = 1 mm and Δp = 0.5 bar, data for certain pressure ratios is not displayed as at these conditions (p_r = 2.6 when θ = 135°, p_r = 2.4 & 2.6 when θ = 150°) the mainstream flow was reversed (perfect sealing). For all pressure drops and jet angles at h = 1 mm, the seal has a detrimental effect when compared to the baseline case at p_r = 1. For θ = 120° and Δp = 0.5 bar, only from $1.4 \leq p_r \leq 2.2$ there improvement in sealing up to a maximum of 3%. At Δp = 1 bar, a benefit is seen from p_r = 1.6 onwards though only by 1% maximum. A maximum improvement in sealing exists for all cases when h = 1 mm within the pressure ratios tested and the sealing performance improves with increasing jet angle. Increasing the pressure ratio beyond the point of maximum sealing improvement, and the limit of the jet effectiveness, leads to more jet mass flow introduced into the seal with no sealing benefit. At h = 1 mm and high pressure ratios, the jets will be strongly impinging on the base plate and some jet energy may be dissipated which would otherwise influence the mainstream flow. For both pressure drop cases, the θ = 150° outperforms the 135° case, which itself is also an improvement on the 120° case. There is also a greater gain in performance between the θ = 120°and 135° cases than between the θ = 135° and 150° cases corresponding to the relative differences in the mainstream direction component of the jet flow momentum between these angles. For a given jet angle, the Δp = 0.5 bar cases consistently outperform the Δp = 1 bar cases in sealing performance. The maximum improvement in sealing at h = 1 mm is 16% by the θ = 150°, Δp = 0.5 bar case at p_r = 2.

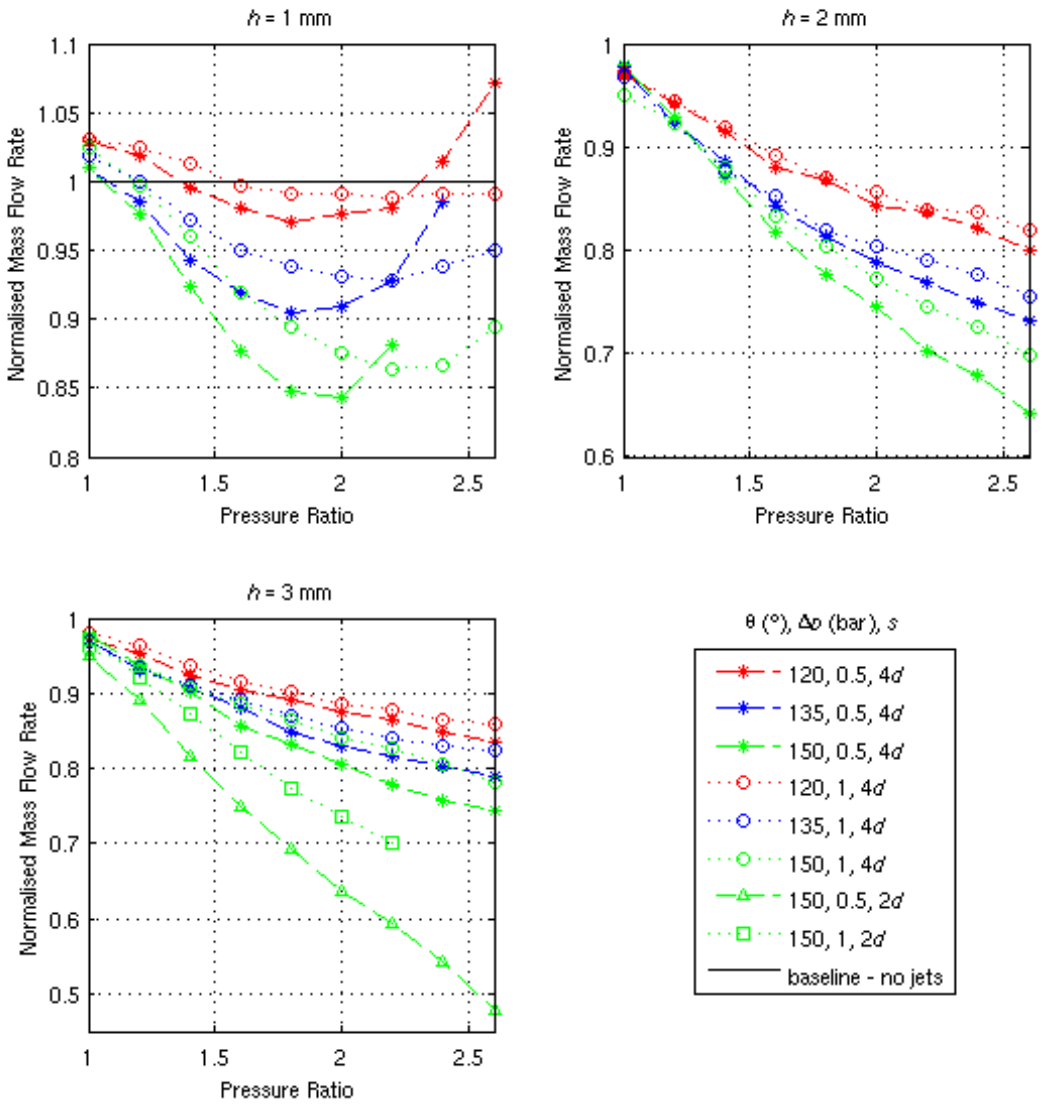


Figure 5.21: Normalised total mass flow (sum of mainstream and jet flow) rate for experimental data

When the channel height is increased to 2 mm, a limit in sealing performance is no longer reached within the range of pressure ratios tested and a performance gain is achieved from the lowest pressure ratio (p_r = 1). The sealing improvement ranges from approximately 3 or 4% for all geometric cases, which increases with pressure ratio up to between 18% and 36% at p_r = 2.6. For all cases, the gradient of the drop in total mass flow rate with pressure ratio is greatest initially up to p_r = 1.6 and then reduces slightly, though a minimum seems far from being reached. The reduction in gradient of sealing improvement from between 1.6 < p_r < 1.8 and beyond may be due to compressibility and choking of the jet mass flow rate. The jet mass flow rate increases with p_r beyond this point (as seen in Figure 5.19 for example), however,

due to the increase of p_{0j} and, subsequently, the jet flow density. Again, the Δp = 0.5 bar cases outperform the Δp = 1 bar cases for any given value of θ and p_r.

At h = 3 mm, the mass flow rate trends observed due to jet angle and pressure drop variation are also present, however the sealing improvement at p_r = 2.6 is between 13% and 26% for the equivalent cases when h = 2 mm, which shows that of the three channel heights, the fluidic seal performs best at h = 2 mm for a given jet angle and mainstream pressure difference. Two more cases are included on the h = 3 mm plot and they are θ = 150° with a hole spacing of 2d (double the hole density) instead of 4d. Again, the Δp = 0.5 bar case outperforms the Δp = 1 bar case but the sealing improvement is considerably greater than cases with s = 4d. When θ = 90°, the addition of jet flow only increases the total mass flow rate and hence doubling the jet hole density worsened the sealing performance. However when the jets are angled upstream at θ = 150°, the sealing performance is improved further by increasing the jet density. The pressure ratio only reached 2.2 for Δp = 1 bar as the inlet feed from the air system limited the jet mass flow rate. At p_r = 1, the performance gains are negligible with a double jet density, but at p_r = 2.6, the sealing improvement is 52% for Δp = 0.5 bar and 30% at p_r = 2.2 for Δp = 1 bar. The encouraging aspect of this result is that there are regions within an engine where large clearances are required due to the possibility of extreme relative growth and/or displacement, which leads to a high leakage mass flow rate penalty. With this result the overall leakage can be greatly reduced whilst maintaining sufficient clearance between the rotor and stator.

5.6.1.3.1 Normalised Mass Flow Rate: 3D CFD

All CFD cases were modelled at Δp = 1 bar. The CFD predictions for mass flow rate agree well with the experimental data. Noteworthy trends, which confirm those seen experimentally, are that increasing the angle of injection, θ, and reducing the hole spacing, s,

improve the seal performance. When h = 1 mm and p_r = 1, a net increase in mass flow rate from the baseline (mainstream only) is observed by up to 5%, as is shown in the experimental data. Higher pressure ratios result in a sealing improvement. The CFD over-predicts the effectiveness of the jets as the mainstream flow is reversed at p_r = 2.6, which does not occur experimentally at Δp = 1 bar, only at Δp = 0.5 bar. At this channel height, reversed mainstream flow is predicted (hence no data) from at least p_r = 1.8 when s = 1.5d and 2d. The peak sealing improvement is almost 14% for the θ = 150°, s = 4d case at p_r = 1.8 which is remarkably similar to the 15% drop seen experimentally.

When h = 2 mm, sealing improvement is observed for all geometric cases for the full range of pressure ratios, as is observed in the experimental data. The s = 4d cases agree well with the experimental data and as the hole spacing is shortened to 2d and 1.5d, further reductions are seen in the total mass flow rate. s = 1.5d cases all show reversed mainstream flow for 1.8 < p_r < 2.6. At these higher pressure ratios this channel height outperforms the h = 3 mm equivalent cases as seen experimentally but to a lesser extent.

Increasing the channel height to 3 mm raises the mainstream momentum such that reversed flow is not achieved for any cases. The CFD simulations over-predict the effectiveness of the jets at p_r = 1 but much more closely resemble the experimental results at p_r = 2.6. Experimental uncertainties are higher at lower mass flow rates (jets) and this will lead to the total mass flow rate also having a higher uncertainty for the lowest values of p_r which may explain this discrepancy. Based on the CFD predictions, when Δp = 1 bar, the maximum increase in sealing performance achievable is approximately 45% when h = 2 mm, s = 2d, p_r = 2.6 and θ = 150°.

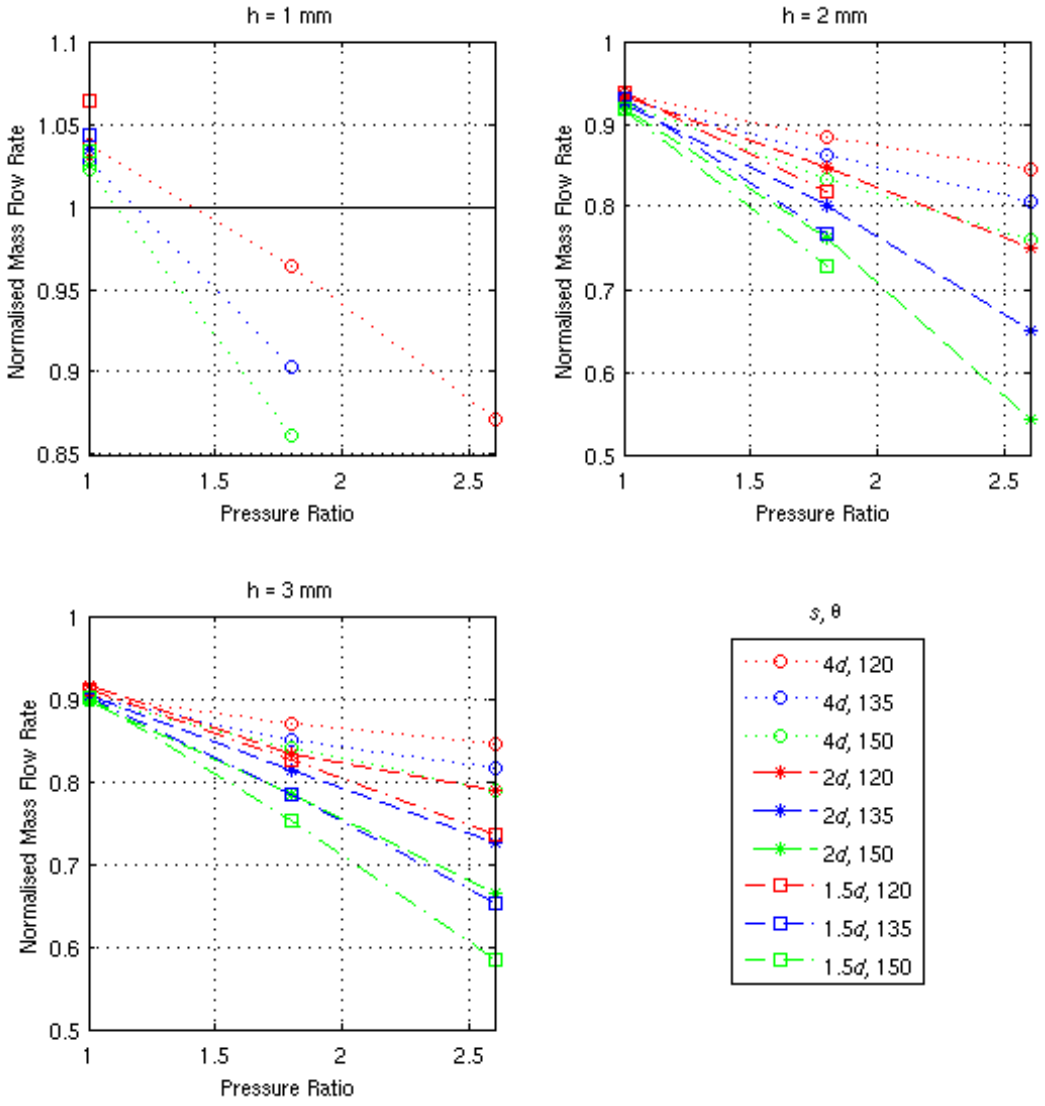


Figure 5.22: Normalised mass flow rate for CFD data

5.6.1.3.2 Interactions: Normalised Mass Flow Rate

Interaction plots are used to determine what the combined effects are from input variables on a given output variable. The effects of input variables can be coupled in their influence on an output variable which is indicated when the effect of a variable on the response (in this case, the mass flow rate) changes depending on the value of another variable. Thus convergent, divergent or crossed lines illustrate an interaction between two variables. Lines which overlay one another suggest no interaction is present. There are five input variables used in the interaction plot shown in Figure 5.23 where the output variable is normalised mass flow rate. The leading diagonal subplots refer to a specific variable. For a given subplot, the *x*-axis

represents the variable from the leading diagonal in the same column and the *y*-axis represents the variable from the leading diagonal in the same row, whilst all other variables are constant at the baseline case, which is: Δp = 1 bar, θ = 150°, s = 4d, h = 3 mm and p_{0j}/p_{0m} = 2. There is a variation in the intensity of interaction throughout the combination of variables.

- **Hole spacing, *s*, and pressure ratio, p_r** – A strong interaction occurs between the pressure ratio and the hole spacing as at low pressure ratios, the normalised mass flow rates are almost identical with the 2d case being slightly higher, but as the pressure ratio is increased, the two curves diverge and the sealing improvement for the 2d case is significantly higher than for s = 4d. This was observed in the normalised mass flow rate data (Figure 5.21). This result is to be expected as the jet mass flow rate is very low at p_r = 1and hence the difference between the two values of s is negligible.
- **Pressure ratio, p_r, and channel height, *h*** – There is also a strong interaction between the pressure ratio and the channel height. At low pressure ratios, the normalised mass flow rate is similar for h = 2 mm and 3 mm but is considerably higher at h = 1 mm. As the pressure ratio is increased, the h = 1 mm and 3 mm curves converge before diverging at p_r = 2.2, whilst the h = 2 mm and 3 mm curves continually diverge. This plot also shows that the h = 2 mm case performs best of the three channel heights.
- **Hole spacing, *s*** – The hole spacing s appears to have a significant interaction with all other variables. A limited number of cases were performed at s = 2d and hence only single points appear on some subplots. It can be seen, however, that there is a reasonably strong interaction between hole spacing and pressure drop as the difference in mass flow rate between the two pressure drops is greater at the smaller hole spacing. The mainstream-jet flow interactions from one jet may be influencing the neighbouring jets when s is reduced.
- **Pressure drop, Δp, and pressure ratio, p_r** – There is a significant interaction between the pressure drop and the pressure ratio as at low pressure ratios the two curves

overlay each other, but as the pressure ratio increases, the curves diverge, but not to the extent of the pressure ratio and hole spacing curves. At low pressure ratios, effects of the jets are small and hence larger effects on mass flow rate are seen as the pressure ratio increases. Thus the mass flow rate curves for all variables diverge to some extent as the pressure ratio increases.

- **Channel height, *h*, and jet angle, θ** – Channel height and jet angle interact with each other to have a significant effect on the mass flow rate which can most easily be seen when jet angle is on the *x*-axis. $\theta = 90°$ was only tested at $h = 1$ mm and hence the red curve has an extra data point. As the jet angle increases, the $h = 1$ mm and 3 mm curves converge, whilst the $h = 2$ mm and 3 mm curves diverge. This shows that the effects of increasing the jet angle depend on the channel height, especially when $h = 1$ mm as the increasing angle has a more pronounced improvement because the jets are not impinging so strongly on the base plate and dissipating energy. Increasing θ for $h = 2$ mm and $h = 3$mm leads to a divergence in curves. The improvement in sealing with θ is greater when $h = 2$ mm than $h = 3$ mm. This figure also shows that the $h = 1$ mm case tends to a similar performance at $\theta = 150°$.
- **Pressure drop, Δp, and channel height, *h*** –The pressure drop and channel height are an example of negligible interaction between two variables as the curves remain parallel across the *x*-axis range for both subplots.

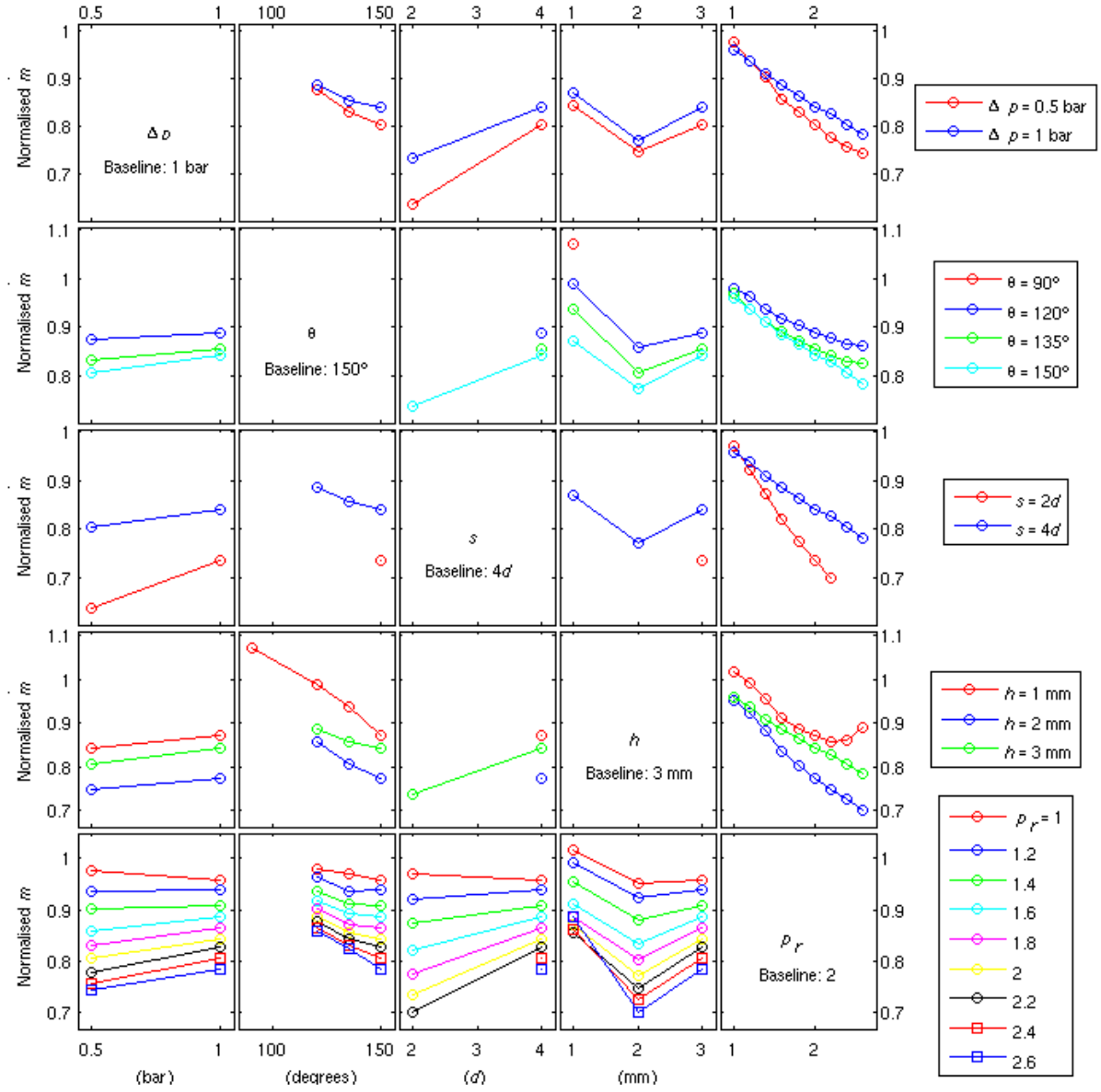


Figure 5.23: Normalised mass flow rate interaction plot

5.6.2 Circular Jets - Centreline static pressure distribution

In order to aid the understanding of the mass flow rate trends measured experimentally, a selection of static pressure profiles from the test section centreline are analysed below. Firstly, the case of θ = 90° is presented where the jet momentum was not utilised in restricting the mainstream flow and, as a result, the sealing performance worsened for all values of p_r. A typical centreline static pressure profile is then shown for a case where an improvement in sealing performance is observed.

5.6.2.1 Unexploited Jet Momentum: $\theta = 90°$

Orientating the jets at 90° gave an increased overall mass flow rate for all pressure ratios (Figure 5.17) which is confirmed from the centreline static pressure profiles in Figure 5.24. The baseline case (zero jet flow - black), which has the largest mainstream mass flow rate, experiences the largest pressure drop at the test section inlet due to mainstream acceleration (discontinuity in static pressure gradient between tapping 1 and 3). The subsequent pressure loss through the channel is due to viscous effects and, due to the higher mass flow rate and velocity, the gradient of the viscous loss is greatest for the baseline case upstream of the jet injection location. Once the jet flow is included and the mainstream mass flow is impeded with increasing pressure ratio, the inlet losses reduce (1^{st} and 2^{nd} tapping difference) and the subsequent gradient of viscous loss up to the jet location also lessens with the lower mainstream mass flow rates. Once the mainstream flow reaches the jet location, the acceleration of flow through the smaller cross-sectional area, due to the jet blockage, leads to a sudden drop in static pressure at $x / L = 0.5$. Downstream of the jet location, the static pressure is higher than the baseline case and increasingly so with pressure ratio and hence the gradient of viscous loss is greater to reach the same pressure boundary condition at the outlet. This distribution corresponds to a greater mass flow rate than the baseline case from the jet location onwards which was observed in the mass flow rate data. This case showed that an improvement in sealing performance cannot be achieved solely by causing blockage within the channel.

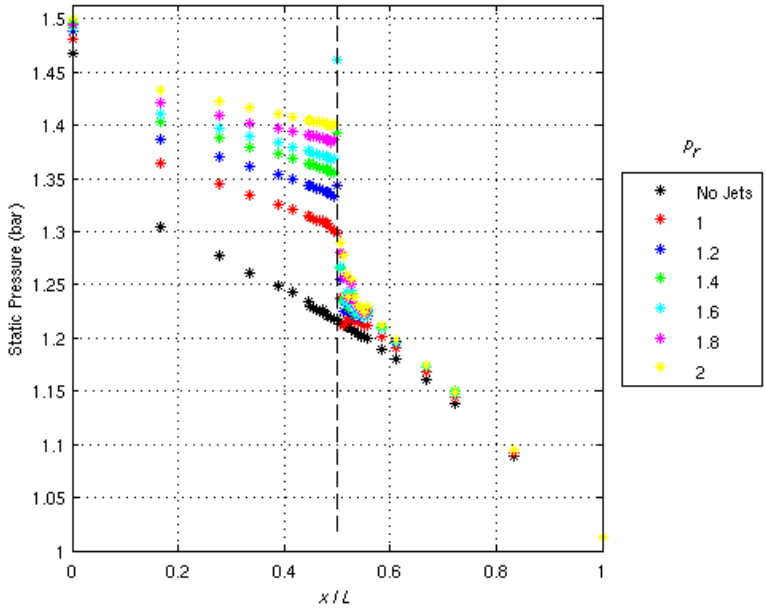


Figure 5.24: Centreline static pressure distribution – Δp = 0.5 bar, θ = 90°, h = 1 mm, s = 4d

5.6.2.2 Jets Angled Upstream

The static pressure profiles for a case where the jets are angled upstream are shown here in Figure 5.25. This set of seal parameters yields sealing improvement over all pressure ratios tested. The geometry and boundary conditions are as follows; Δp = 0.5 bar, θ = 150°, h = 3 mm, s = 4d. By introducing the jet flow into the system, a reduction in the viscous pressure drop upstream of the jet location compared to the baseline case is observed due to the fall in mainstream mass flow rate. This is caused by the blockage introduced by the jet flow. The gradient is reduced further as the pressure ratio increases until p_r = 2.6 where the viscous pressure drop upstream of the jet location is almost non-existent. The mainstream mass flow has been reduced to nearly zero. At the axial position of the jet row, there is a sudden drop in static pressure as the flow accelerates between the jets. The gradient of the viscous pressure drop on the downstream side of the jet location is lower with increasing p_r, which indicates that the mass flow rate passing through the channel from the jet location onwards is lower than the baseline case and an improvement in the sealing ability increases with pressure ratio.

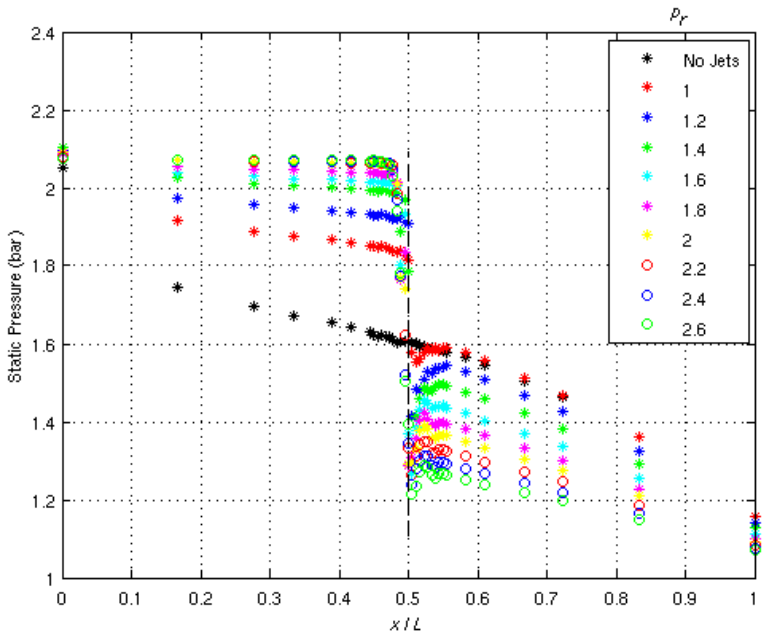


Figure 5.25: Centreline static pressure distribution – Δp = 0.5 bar, θ = 150°, h = 3 mm, s = 4d

5.6.3 An Alternative Method to Evaluate Fluidic Seal Performance

When the jets are angled upstream, the fluidic seal becomes beneficial in terms of reducing the total mass flow rate through the leakage path. Generally, the effectiveness of the seal increases with pressure ratio, however in an engine case, the use of higher pressure air for the jet flow must be accounted for in evaluating the overall benefit of the seal. A penalty is incurred by using higher pressure air as more work is taken from the turbine to reach that pressure and it will not pass through the combustor and subsequently expand through the turbine to produce work. The efficiency gain from reducing the leakage mass flow rate must outweigh the loss in efficiency from bleeding compressor flow for this seal to be deemed beneficial. The method for assessing the overall performance of the seal by accounting for the power loss is described below.

This method evaluates the power that is lost through the seal from the individual jet and mainstream flows from their respective inlets to the outlet. The total available power entering and leaving the system is therefore accounted for. In some cases, such as in coolant flow

paths, the quantity of energy lost must be limited, and a certain total pressure maintained in order that there is a sufficient pressure difference across the internal geometry of the vanes or blades to maintain a desired mass flow rate of coolant, which is critical to a cooled component's life. To compare the amount of power that is lost as a proportion of the total power entering the seal for a range of geometric configurations and boundary conditions, a power loss factor is useful and is defined as follows. The reduction in power within the flow from the jet inlet plenum to the outlet is given by

$$PL_j = \dot{m}_j c_p T_{0j} \left[1 - \left(\frac{p_{out}}{p_{0j}} \right)^{\frac{\gamma-1}{\gamma}} \right], \tag{5.7}$$

as in equation **(**5.6) (Curtis, et al. 2009). The power lost in the flow from the mainstream inlet to the outlet is therefore

$$PL_m = \dot{m}_m c_p T_{0m} \left[1 - \left(\frac{p_{out}}{p_{0m}} \right)^{\frac{\gamma-1}{\gamma}} \right]. \tag{5.8}$$

The total power loss through the seal is therefore the sum of the jet and mainstream power losses

$$PL_{seal} = PL_m + PL_j \, . \tag{5.9}$$

The power loss in the baseline case (no jets) is

$$PL_{mb} = \dot{m}_{mb} c_p T_{0mb} \left[1 - \left(\frac{p_{out}}{p_{0mb}} \right)^{\frac{\gamma-1}{\gamma}} \right]. \tag{5.10}$$

The power loss factor is then defined as the power lost in the system over the power loss for the baseline case, which is as follows;

$$\varepsilon_p = \frac{PL_{seal}}{PL_{mb}} = \frac{\dot{m}_j c_p T_{0j} \left[1 - \left(\frac{p_{out}}{p_{0j}} \right)^{\frac{\gamma-1}{\gamma}} \right] + \dot{m}_m c_p T_{0m} \left[1 - \left(\frac{p_{out}}{p_{0m}} \right)^{\frac{\gamma-1}{\gamma}} \right]}{\dot{m}_{mb} c_p T_{0mb} \left[1 - \left(\frac{p_{out}}{p_{0mb}} \right)^{\frac{\gamma-1}{\gamma}} \right]}. \tag{5.11}$$

Thus ε_p is a ratio of the power lost for the seal compared to its baseline case (no jets present).

5.6.3.1 Power loss results

The power loss factor is first plotted against pressure ratio to assess the proportion of the total power entering the seal that is dissipated through mixing as the jet energy and momentum vary. Figure 5.26 shows the power loss against pressure ratio for all Δp = 0.5 bar cases. Channel heights of 1, 2 and 3 mm are represented by red, blue and green data points respectively. When p_r = 1, ε_p for all cases is approximately 1 with the losses for the h = 1 mm channel height cases being slightly higher than the h = 2 mm and 3 mm cases. As the pressure ratio increases, clear trends begin to emerge. As the channel height decreases, the amount of power loss increases. For all the s = 4d and θ = 120, 135 and 150° cases, this trend is displayed consistently. The power loss is greatest when h = 1 mm, less so when h = 2 mm and least when h = 3 mm, though the difference in power loss between the three channel heights is greatest between h = 1 and 2 mm compared to h = 2 and 3 mm. As the channel height reduces, the jet mass flow rate becomes a larger percentage of the total mass flow rate for a given p_r. As the jet flow is at a higher pressure, the power lost from the jets per kilogram of flow is greater than the mainstream flow, leading to a greater overall power loss. When p_r tends to 2.6 at h = 1 mm, the jet flow accounts for the majority of the total mass flow rate though the seal and hence the power lost is over twice the baseline case. There is also a consistent trend with the variation of θ for a given value of h. As the jet angle increases, ε_p drops marginally which is unexpected, though the power loss factor is relatively only a weak function of θ. However, the jet flow angled at 90° yields a considerable reduction in ε_p from the interaction of the two flows, though the increase in total mass flow rate makes this configuration useless. For the same hole spacing (s = 4d), the trend of power loss reduction with jet angle is consistent across all channel heights. The effect of reducing the hole spacing to s = 2d (square data points) significantly increases ε_p. For θ = 90°, h = 1 mm, halving the hole spacing from 4d to 2d leads to an increase in ε_p by a factor of 2 at p_r = 2 compared to only an 18% increase when halved for θ = 150°, h = 3 mm at p_r = 2.6. When s = 4d, the distance between holes is 3d

which is a relatively large distance allowing for the mainstream flow passing equidistant between two neighbouring holes to be relatively unaffected. Reducing the hole spacing leads to an inter-jet distance of 1*d* and the effect on the two flows is an increase in the power loss. This is due to the cross-sectional area reduction and associated non-linear jet drag and mixing.

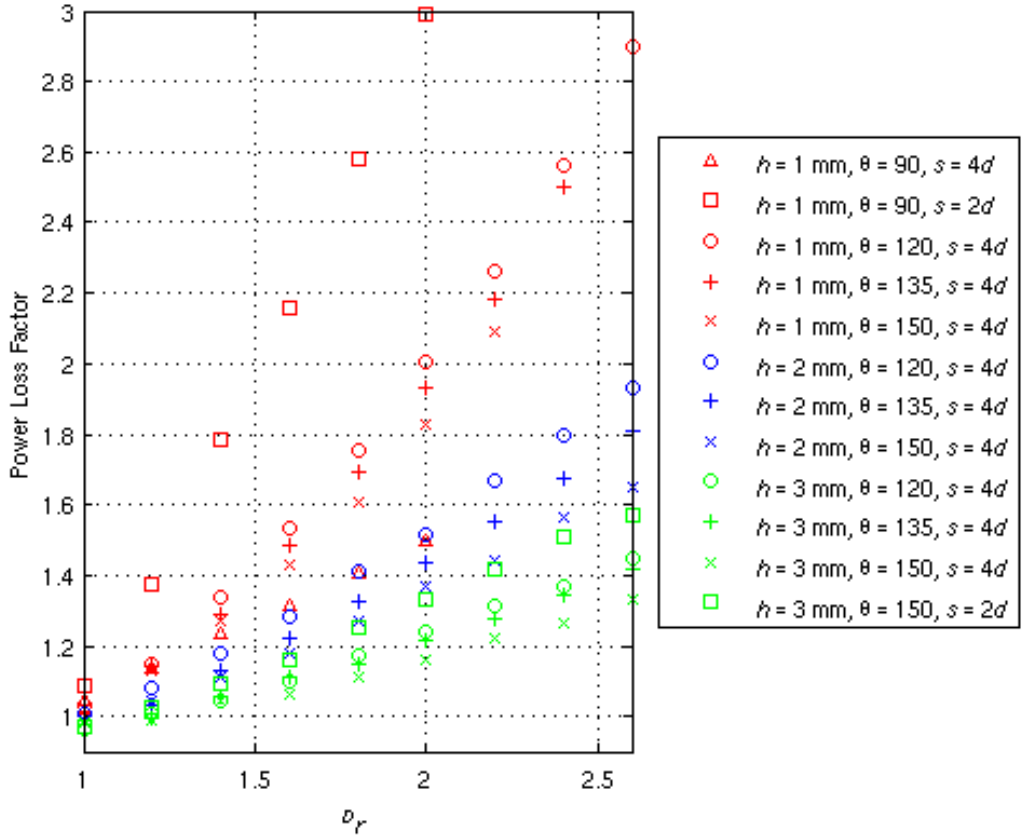


Figure 5.26: Power loss factor against pressure ratio: Δ*p* = 0.5 bar

When the pressure drop is raised to 1 bar, Figure 5.27, the trends seen at Δ*p* = 0.5 bar are consistent at this pressure drop but the magnitude of the power loss has dropped. Comparing cases where *s* = 4*d*, the power loss for the *h* = 1 mm curves are greatest, followed by *h* = 2 mm and then *h* = 3 mm yields the least power loss. At p_r = 1, ε_p is very similar Δ*p* = 0.5 bar at approximately 1, but at the highest values of pr, ε_p is up to 20% less. Having the jets angled further upstream leads to a lower ε_p. Halving the hole spacing to 2*d* also significantly increases the power loss as seen when Δ*p* = 0.5 bar. A maximum pressure ratio of only 2.2 is reached for *h* = 3 mm, θ = 150°, *s* = 2*d* due to the limit in jet mass flow rate by the air system.

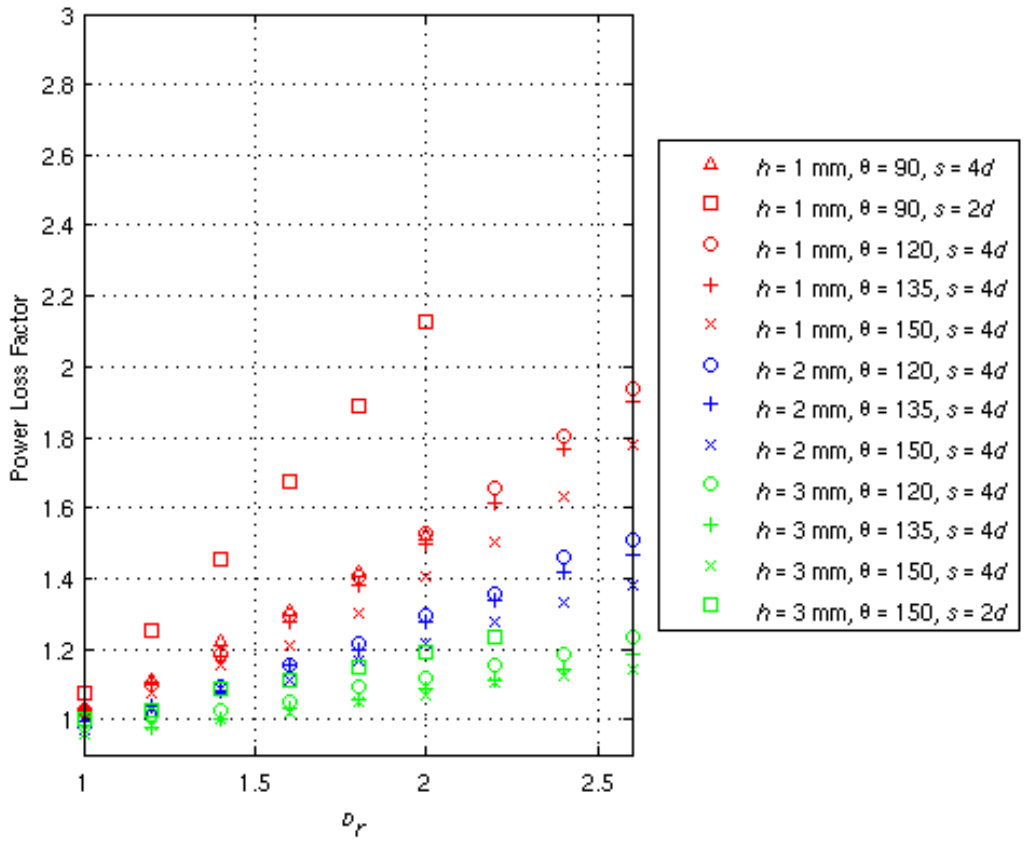


Figure 5.27: Power loss factor against pressure ratio: Δp = 1 bar

5.6.3.1.1 Power Loss vs. Mass Flow Rate

Depending on the application for the fluidic seal, the desired proportion of power entering the seal that is lost due to the mixing of the two flows may vary. If the outlet flow is then being directed to be used as coolant in a particular part of the engine, a certain amount of power will be required within the cooling flow to overcome further losses en-route to its destination and for the cooling process. For example, high pressure turbine stator vanes and rotating blades have complex internal geometries to enhance mixing and hence heat transfer, which results in losses and require a certain mass flow rate to be effective. Therefore a seal with zero outlet power would be undesirable in this application. Other sealing locations within an engine may desire minimum leakage and outlet flow power, or a trade off may be necessary to satisfy leakage and power loss requirements. Figure 5.28 and Figure 5.29 show the power loss factor

against mass flow rate for Δp = 0.5 bar and 1 bar respectively. The effect of pressure ratio can also be seen on these figures as annotated.

For the primary purpose of the seal, to reduce the leakage mass flow rate below the baseline case, the section of the plot left of, and hence less than, '1' on the *x*-axis is one constraint for the desirable region in which to set the design point for a fluidic seal. Analysing Figure 5.28, θ = 90° cases obviously have no benefit in terms of mass flow rate but also result in significant power loss and would not be considered for any application. In most applications, the clearance between the rotor and casing, *h*, will be predetermined by the expected relative growth of the rotor and casing that needs to be accommodated. If the dimension of *h* is fixed, increasing the operating pressure ratio leads to a greater power loss. Increasing the angle of the jets reduces ε_p slightly and also more significantly reduces the mass flow rate. This importantly shows that a gain of reducing the mass flow rate comes at no expense in power loss and hence a designer should maximise the jet angle where possible. For the best sealing performance and minimum power loss, the *h* = 3mm, θ = 150°, *s* = 2*d* case clearly the optimum for all pressure ratios. When minimising two functions (mass flow rate and power loss) there becomes a range of possibilities which arise by the use of Pareto efficiency, η_p, *i.e.* improving one parameter has a detrimental effect on the other. Within a set of data, the boundary of the data set at which Pareto efficiency has been achieved is known as a Pareto frontier. For all Δp = 0.5 bar cases, the Pareto frontier is essentially the *h* = 3mm, θ = 150°, *s* = 2*d*, $1 \leq p_r \leq 2.6$ case.

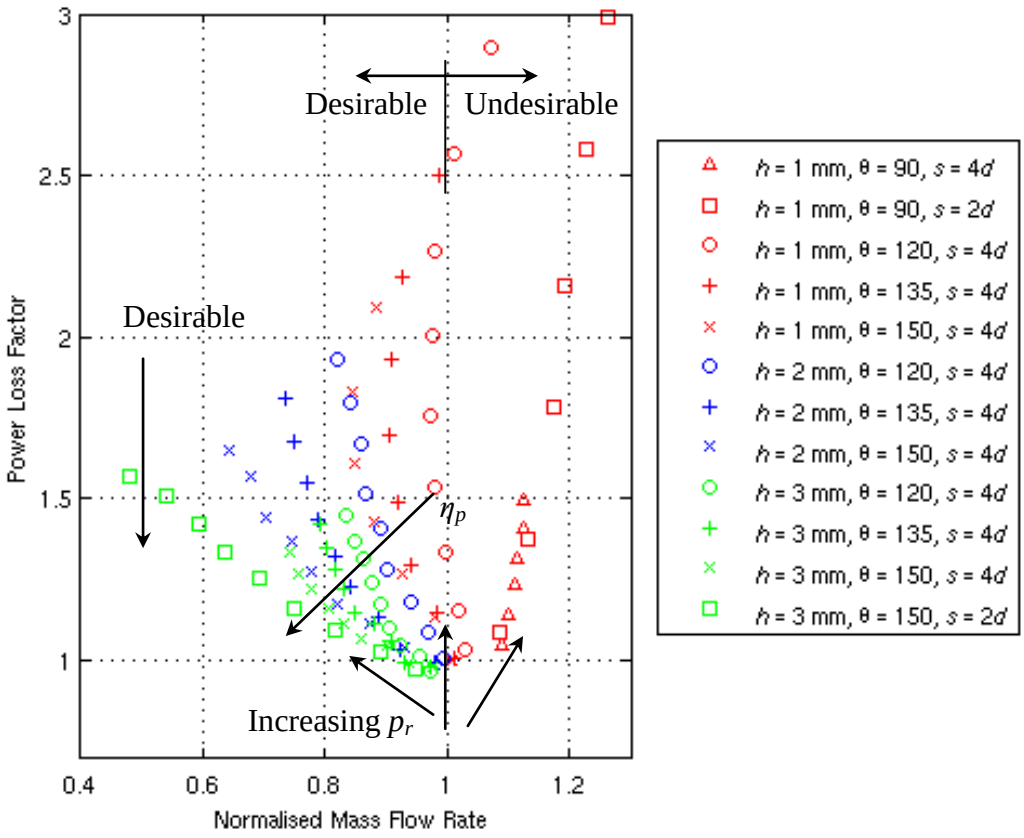


Figure 5.28: Power loss factor against normalised mass flow rate: Δ*p* = 0.5 bar

The power loss against mass flow rate data for Δ*p* = 1 bar is plotted in Figure 5.29 on the same axis limits as the Δ*p* = 0.5 bar data in Figure 5.28 to aid comparison. The range of space occupied by the Δ*p* = 1 bar data is considerably different as the generally higher mass flow rates (and lower in the cases where θ = 90°) lead to a convergence towards the normalised mass flow rate = 1 line. The power losses are significantly lower and thus the data occupies a much smaller space. All the cases at *h* = 1 mm show a lower power loss for a given pressure ratio, whilst also delivering little or no sealing improvement for low pressure ratios. The *h* = 2 mm cases give the lowest mass flow rate for *s* = 4*d* but their power loss is significantly higher than *h* = 3 mm. For a maximum sealing improvement and minimum power loss, the *h* = 3 mm, θ = 150°, *s* = 2*d* and 4*d* cases give the best compromise and hence form the Pareto frontier for this set of data (Δ*p* = 1 bar).

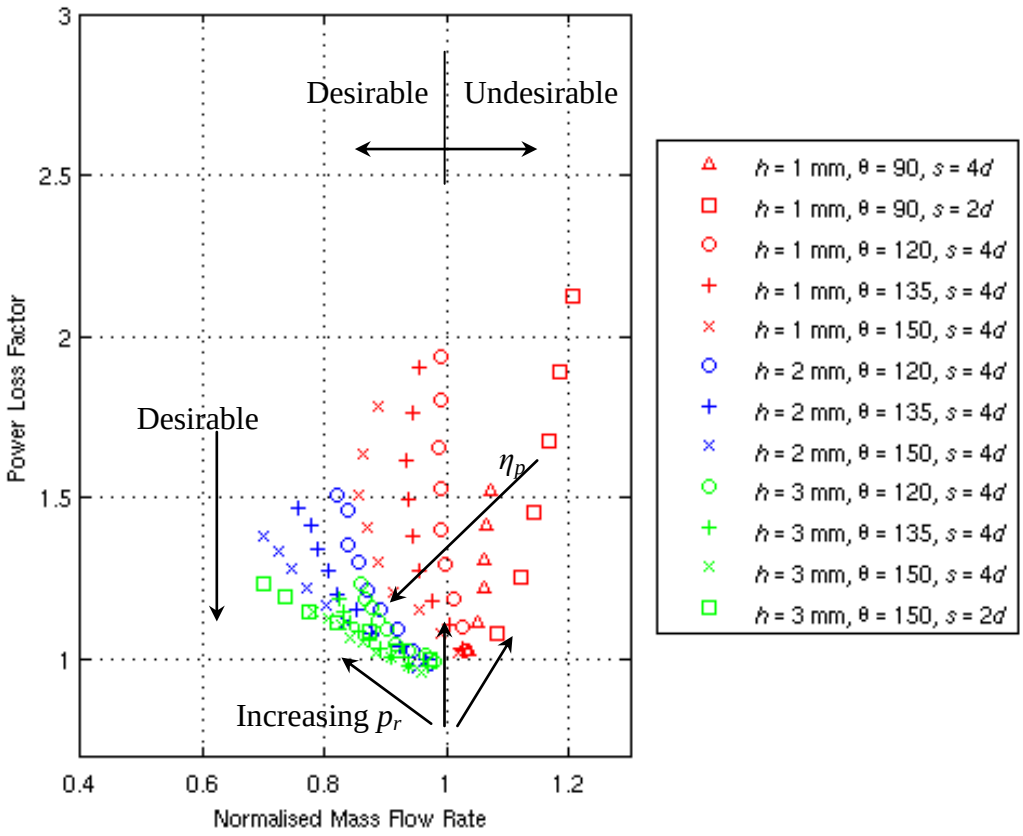


Figure 5.29: Power loss factor against normalised mass flow rate: Δ*p* = 1 bar

5.6.3.1.2 Power Loss Interaction Plot

The power loss interaction plot for the fluidic seal based on standard channel geometry is shown in Figure 5.30 where the baseline case is set at Δp = 1 bar, θ = 150°, s = 4d, h = 3 mm, p_j / p_m = 2 (identical baseline parameter values for the normalised mass flow rate interaction plot).

- **Pressure ratio, p_r** –The strongest interactions occur with the variation of pressure ratio. Both jet spacing and channel height strongly interact with pressure ratio. At p_r = 1, there is no discernable difference between the power loss at s = 2d and 4d but as the pressure ratio increases, the two data sets diverge (s = 2d has fewer data points as the maximum pressure ratio that could be reached was only 2.2). At p_r = 1, the jet mass flow rate is small and hence any variations in jet parameters have a negligible effect, as doubling the jet mass flow rate by halving the hole spacing yields an identical power loss. The interaction between the pressure ratio and channel height follows a

similar trend in that at p_r = 1, the three data sets are similar and diverge with increasing pressure ratio. At p_r = 1, h = 1 mm yields the greatest power loss, followed by 2 mm and then 3 mm. As the pressure ratio increases, the three data sets diverge, as the power loss has a nonlinear relationship with pressure ratio. This interaction is due to the increasing power entering the seal in the form of mainstream flow as h increases and thus the total loss from the jet flow as a proportion of the overall power entering decreases. As the channel height reduces and the pressure ratio increases, the jet potential core length and the likelihood of it reaching the base plate increases and so does the power loss.

- **Pressure ratio, p_r, and pressure drop, Δp** – A considerable interaction between the pressure ratio and pressure drop exists such that the two data sets diverge with increasing pressure ratio. At p_r = 1, there is a negligible difference but as the p_r increases, the Δp = 1 cases exhibit a lower power loss. The pressure ratio has a weak interaction with jet angle such the influence of the different angles is more apparent at the higher values of p_r. Increasing the angle results in a lower power loss and also a lower mass flow rate. The jet angle should then always be maximised.
- **Pressure drop, Δp, and hole spacing, s** – A weak interaction exists between the pressure drop and the holes spacing, such that the increase in hole spacing (2d to 4d) yields less of a difference between the two Δp cases. The nonlinear variation in cross-sectional area reduction by the jet flow presence with hole spacing and the greater mainstream flow momentum may lead to increased mixing. The higher pressure difference results in higher mainstream flow momentum for a given pressure ratio, leading to greater mixing losses. This may also lead to the weak interaction between channel height and pressure drop.

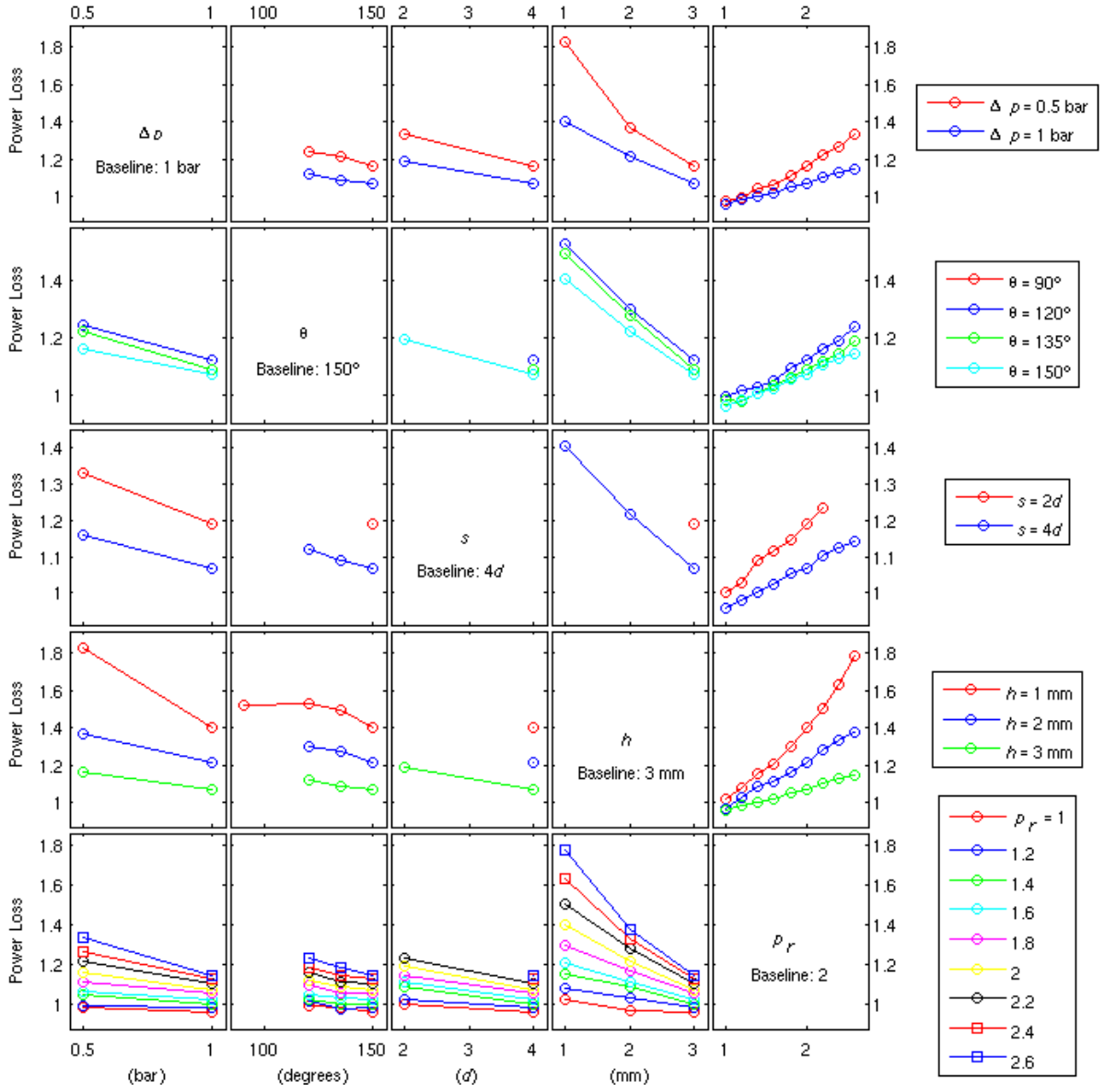


Figure 5.30: Power loss interaction plot

5.6.4 Console Jets

The normalised mass flow rate data for the console cases are shown below in Table 5.7. All cases are compared to their circular-hole equivalent, matching the hole spacing, *s*, channel height, *h*, jet angle, θ, and pressure ratio, p_r. Apart from the case where θ = 90°, all the circular equivalent hole cases resulted in a reduction in the mass flow rate from their baseline mass flow rates. Here the console is assessed by whether it is an improvement over the circular geometry and all cases are normalised against their circular hole counterparts. Only one particular console case exhibited a lower total mass flow rate compared to its circular

equivalent by 0.6% which was the 1:1 area ratio (highlighted in red). The larger exit area led to an increased jet mass flow rate and improved the effectiveness of the jets. The inlet to exit area ratio of 0.8 was chosen to accelerate the flow further and increase the mixing of the two fluid flows but this was less effective. In fact, it worsened, in comparison to the circular case, as the pressure ratio increased. The jet momentum (in the upstream direction) is clearly important when reducing the mainstream mass flow rate effectively. Generally, there is little difference between the circular and console cases in terms of the total mass flow rate leaving the domain.

p_j/p_m	s (d)	θ (°)	h (mm)	A_s/A_e	L_s/L_l	*Normalised* $\dot{m}$
1	2	150	3	0.8	1	1.014
1.8	2	150	3	0.8	1	1.027
2.6	**2**	**150**	**3**	**0.8**	**1**	1.046
2.6	2	150	**2**	0.8	1	1.080
2.6	2	150	**1**	0.8	1	-
2.6	2	**120**	3	0.8	1	1.077
2.6	2	**90**	3	0.8	1	1.011
2.6	**4**	150	3	0.8	1	1.030
2.6	2	150	3	0.8	**0.9**	1.046
2.6	2	150	3	**1**	1	0.994

Table 5.7: Total mass flow rates for console geometry normalised against circular hole equivalent geometry total mass flow rate

The flow field using particle pathlines is shown below in Figure 5.31 for the console case; p_r = 2.6, s = 2d, h = 3mm, θ = 150°, A_s/A_e = 0.8, L_s/L_l = 1. The jet flow is entrained downstream by the mainstream flow and very little mixing appears to take place. The full spanwise coverage of the jets leads to the entirety of the mainstream flow being squeezed under the turning jet 'curtain' and accelerating through the throat formed. The flow then diffuses downstream. A vortex is set up immediately behind the jet injection point which is attached to the casing wall. The pathlines in Figure 5.32 show that the majority of the jet flow's maximum penetration is approximately 50% of the channel height whereas the flow exiting the slots at the sides is more successful in penetrating the flow due to the interaction of the jet

flow with its neighbouring jet flow. This preliminary study suggests that the console can marginally outperform the circular holes using an inlet to exit area ratio of 1. However, the sealing ability could be improved further if discrete surface geometry was mounted on the rotor in the region of the highest flow velocity which could introduce large mixing losses. These could be of the order of 1 mm radially when the channel height is 3 mm (as shown).

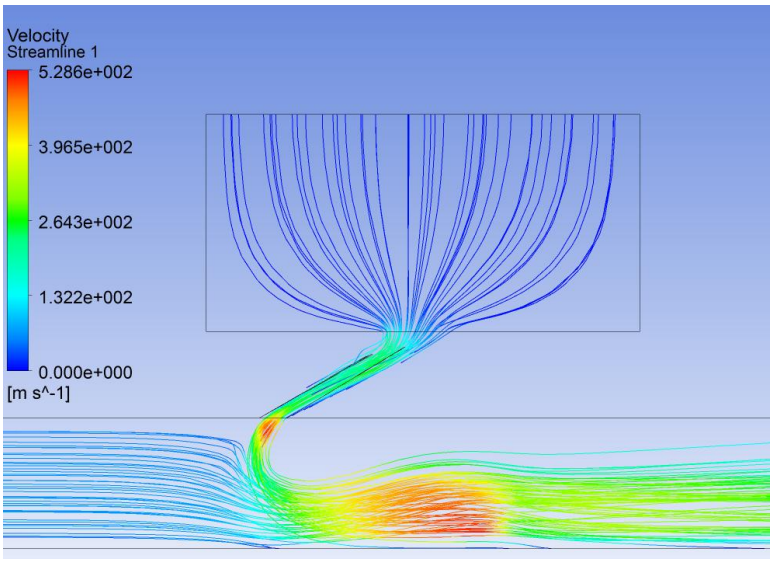


Figure 5.31: Streamlines for console jet geometry (circumferential view): p_r = 2.6, s = 2d, h = 3mm, θ = 150°, A_s/A_e = 0.8, L_s/L_l = 1

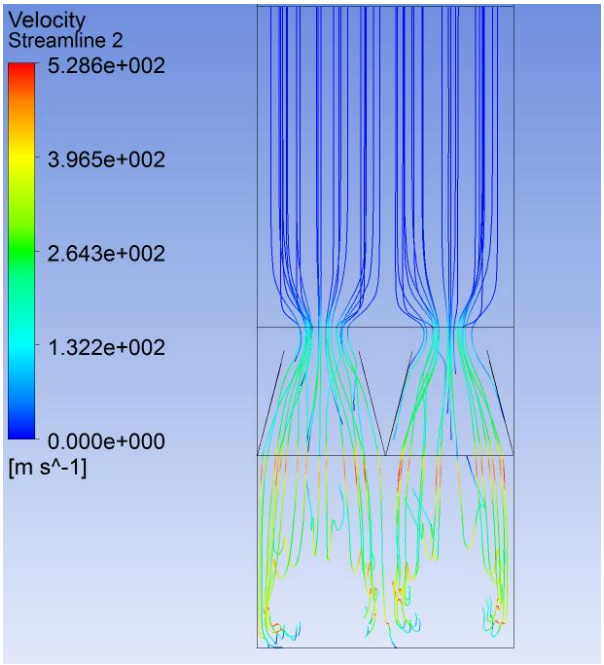


Figure 5.32: Streamlines for console jet geometry (axial view): p_r = 2.6, s = 2d, h = 3mm, θ = 150°, A_s/A_e = 0.8, L_s/L_l = 1

5.6.5 Labyrinth-fluidic seal: Jets upstream – Mass flow rate

5.6.5.1 Δp = 0.5 bar

The mass flow rate data obtained by *Skouby* (Sealing of Jet Engines 2011) is shown in Figure 5.33 and Figure 5.34 for the Δp = 0.5 bar and 1 bar cases respectively. The mainstream flow for the Δp = 0.5 bar case shows a rapid decline with increasing pressure ratio up to p_r = 1.4 where the gradient reduces thereafter. At this pressure ratio, the gradient of the jet flow with pressure ratio reduces. A change in the flow regime occurs between p_r = 1.4 and 1.6 where the jets have sufficient momentum to bridge the gap between the central tooth tip and the base plate. The mainstream flow is reduced by 90% at p_r = 2.6. and hence the total mass flow comprises mostly of jet leakage. Over the range of pressure ratios, the total mass flow varies from 106% down to 87%. The labyrinth-fluidic seal combination is slightly more effective than 1 mm regular channel height clearance as the minimum mass flow is at 90% of the baseline for the same jet angle, θ = 45°. The labyrinth-fluidic seal at these conditions has almost reversed the mainstream flow. In fact, as in the equivalent plain channel case, p_r = 2.6 produced reversed mainstream flow and hence a data point was not taken for this pressure ratio. The CFD data predicts an almost identical baseline flow rate. There is a flow regime change at the same pressure ratio, between 1.4 and 1.6, (much more pronounced than in the experimental case) and the magnitude is very similar, which is most easily observed in the mainstream flow. The jet flow, however, is greatly under-predicted and hence the total mass flow rate and seal performance appears to be better than in the experimental case – sealing performance between 1% and 25% over pressure ratio range.

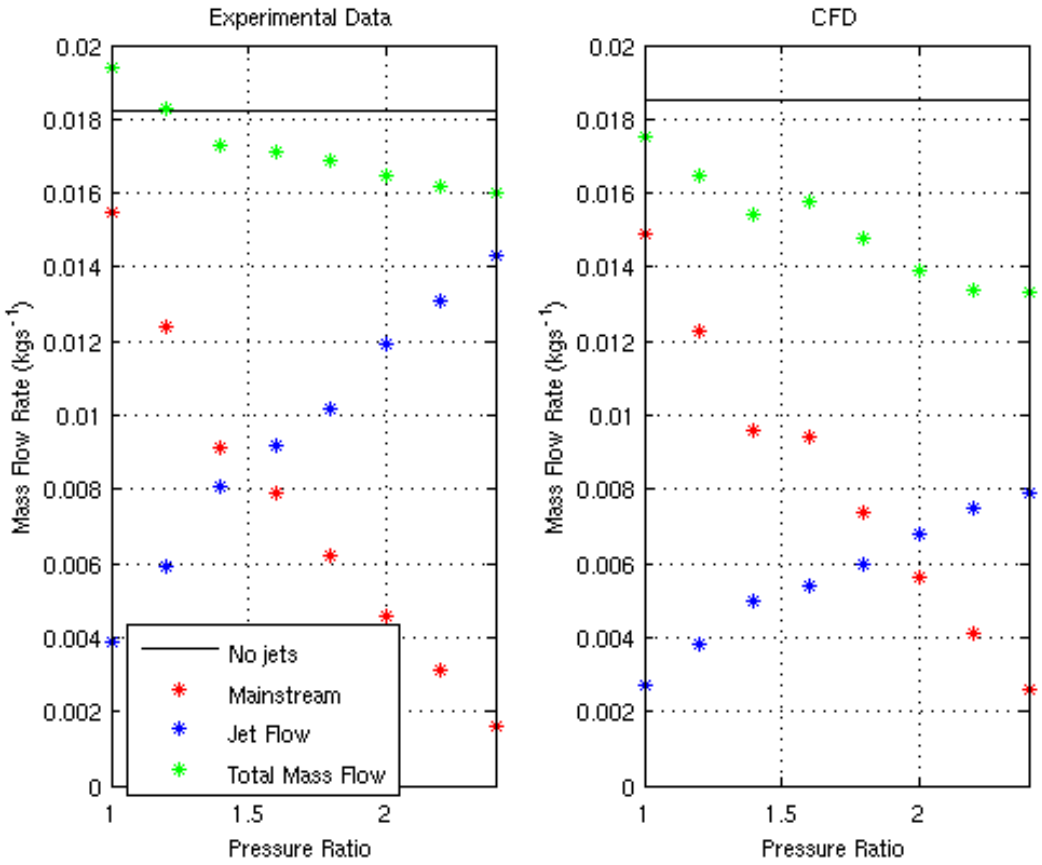


Figure 5.33: Mass flow rate for labyrinth-fluidic seal – jets upstream, Δ*p* = 0.5 bar (Skouby 2011)

5.6.5.2 Δ*p* = 1 bar

When the pressure difference across the seal is 1bar, the experimental data shows a change in the flow regime between p_r = 1.6 and 1.8 which is indicated by the kink in mainstream flow gradient between these pressure ratios, where the jets begin to bridge the tooth clearance and impinge on the base plate. At this pressure difference, the mainstream momentum is higher with the increased mass flow rate and hence raises the difficulty for the jets to penetrate through the flow accelerating under the tooth tip. The jet flow gradient also changes at this point. The effectiveness of the jet penetration through the high velocity mainstream flow increases which impedes the mainstream leading to a higher cavity pressure. Hence the pressure differential across the jet holes is slightly reduced and, consequently, the jet mass flow rate with it. Again, the CFD simulations predict much lower jet flow and similar mainstream flow and hence a lower combined mass flow rate. The experiment shows the seal

only becomes effective at p_r = 1.6 and above whereas the CFD predicts all pressure ratios to be effective.

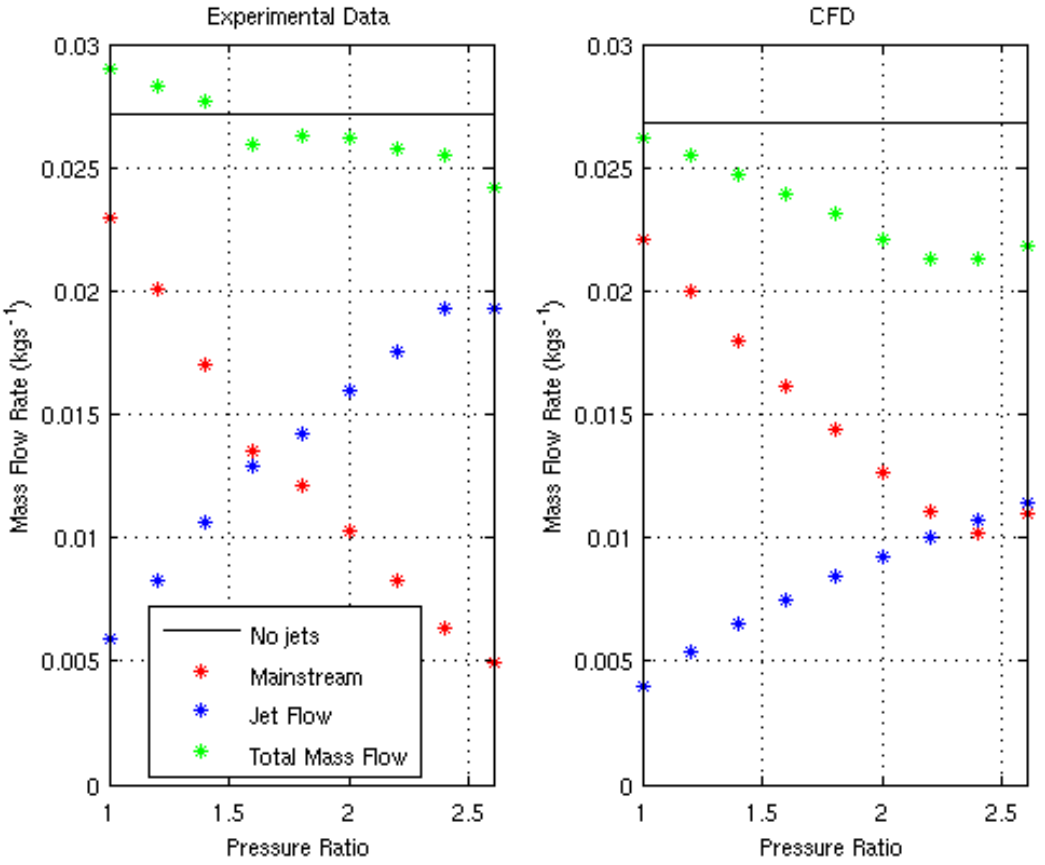


Figure 5.34: Mass flow rate for labyrinth-fluidic seal – jets downstream, Δ*p* = 1 bar (Skouby 2011)

5.6.6 Labyrinth-fluidic seal: Jets upstream – Static pressure distribution

5.6.6.1 Δ*p* = 0.5 bar

The baseline pressure distribution (black data points) shows a drop across the upstream and downstream teeth but not the central one. The flow accelerates under the upstream tooth and decelerates towards the central tooth tip which appears to have little influence on the pressure profile. This is due to the proximity of the central tooth tip to the upstream tooth tip. The flow then enters the downstream cavity where most of dynamic head will be lost before the combined flow reaccelerates under the downstream tooth resulting in a further drop to

atmospheric conditions. Once the flow has decelerated after passing under the central tooth and a small amount of pressure is recovered, the pressure within the downstream cavity is approximately 50% of the total pressure drop. As the jet mass flow rate is increased, the pressure in the upstream cavity also increases from baseline, as jet flow causes a reduction in mainstream mass flow rate and hence the mainstream velocity under the upstream tooth is lower leading to a smaller pressure drop across the upstream tooth. This therefore alters the jet driving pressure ratio from the inlet plena pressure ratio. Beyond p_r = 1.2, the jets clearly impinge on the base plate due to the peak pressures on either side of x / L = 0.46 and this is increasingly intense with pressure ratio. The pressure downstream of the central tooth tip is at the level of the baseline case for pressure ratios up to 1.2 before dropping significantly lower at higher pressure ratios, which corresponds to the point at which the jets begin to bridge the clearance between the central tooth tip and the base plate and there is an improvement in the sealing ability compared with the baseline.

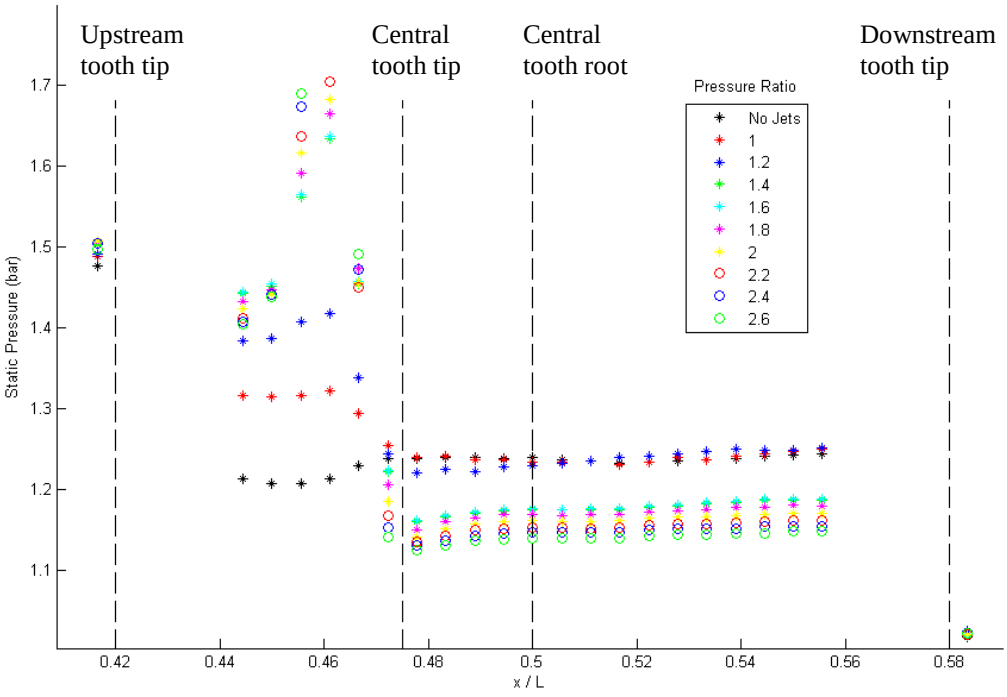


Figure 5.35: Static pressure distribution for labyrinth-fluidic seal – jets upstream, Δ*p* = 0.5 bar (Skouby 2011)

5.6.6.2 Δp = 1 bar

As when Δp = 0.5 bar, the baseline pressure distribution sees a drop across the upstream tooth, followed by a slight recovery as the flow diffuses after the central tooth tip. The pressure remains constant in the downstream cavity where some dynamic head is lost before the mainstream flow is reaccelerated and a further pressure drop under the downstream tooth to the outlet conditions is observed. At this pressure difference the flow accelerating under the upstream tooth also clears the central tooth tip.

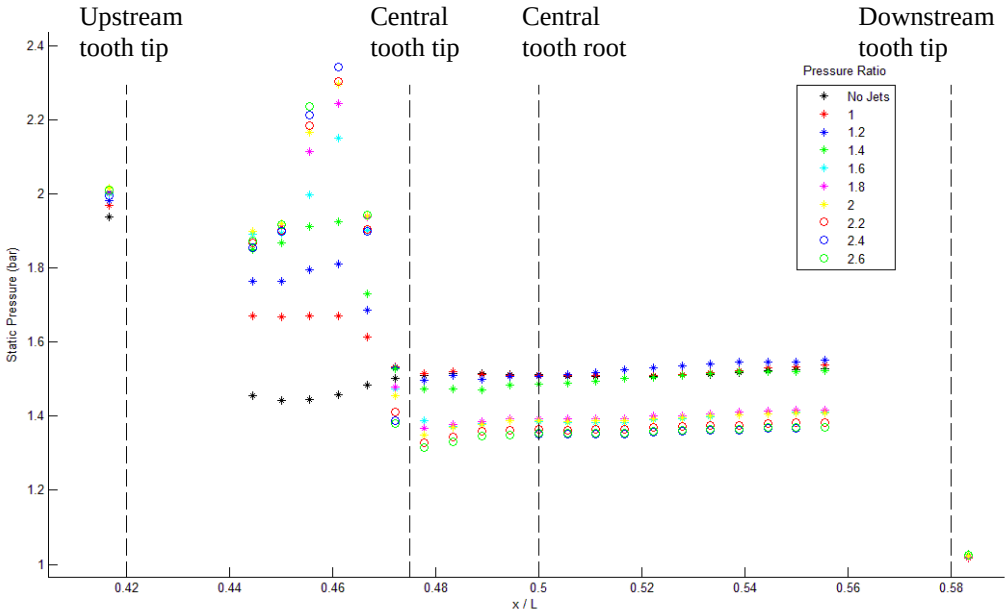


Figure 5.36: Static pressure distribution for labyrinth-fluidic seal – jets upstream, Δp = 1 bar (Skouby 2011)

From p_r = 1 there is a rise in pressure within the upstream cavity, which is due to the lower mainstream mass flow as a result of the jet mass flow, and hence a lower pressure drop occurs across the upstream tooth. The pressure drop across the upstream tooth is reduced to a minimum by p_r = 1.4, and rises slightly as flow decelerates towards the central tooth tip followed by a drop at x / L = 0.465 as flow reaccelerates underneath it. From p_r = 1.6 onwards, the jets impinge on the base plate, indicated by the static pressure rising above the mainstream inlet pressure, which reduces the cross-sectional area under the central tooth tip and hence a greater pressure drop across the central tooth occurs for pressure ratios of 1.6 and

above. Once the jets start to impinge, there is a similar trend and magnitude of the pressure profiles in the upstream and downstream cavities, though the pressure drop across the jet location (central tooth) increases slightly with pressure ratio. The static pressure in the downstream cavity is less than the baseline case for $p_r > 1.4$ which corresponds to the pressure ratio at which there is a sealing improvement.

5.6.7 Labyrinth-fluidic seal: Jets upstream – Flow field analysis (CFD)

The CFD work done by *Skouby* (2011) allowed a qualitative analysis of the flow field variation which is not attainable through experimental data. Velocity vectors are plotted in the streamwise-vertical plane at a jet axis location and the midspan between two neighbouring jets in Figure 5.37 and Figure 5.38. Path lines tracing the route taken by mainstream and jet flow particles are shown in Figure 5.39, which are coloured by velocity magnitude.

5.6.7.1 Flow Vectors - Δp = 0.5 bar, p_r = 1.2

Jet plane: The mainstream velocity under the upstream tooth is relatively high, corresponding to the pressure drop seen across it, and continues close to the base plate up to the central tooth tip where it encounters the jet flow and appears to stagnate, whilst the jet flow turns downstream and passes under the central tooth. Two counter rotating vortices are created in the upstream cavity; the larger primary vortex is expected in an inter-tooth cavity without the presence jets and a smaller secondary one exists between the primary vortex and the jet flow. The combined flow downstream of the central tooth diffuses considerably and hence a small pressure recovery is observed from $x/L > 0.48$ (Figure 5.35). Mid span: the mainstream flow accelerates to a greater velocity under the central tooth, as there is no restriction caused by the jet flow at this spanwise position, and diffuses into the downstream cavity which accounts for

the pressure drop under the central tooth followed by a slight recovery. At this low pressure ratio the mainstream flow between the jets is relatively undisturbed.

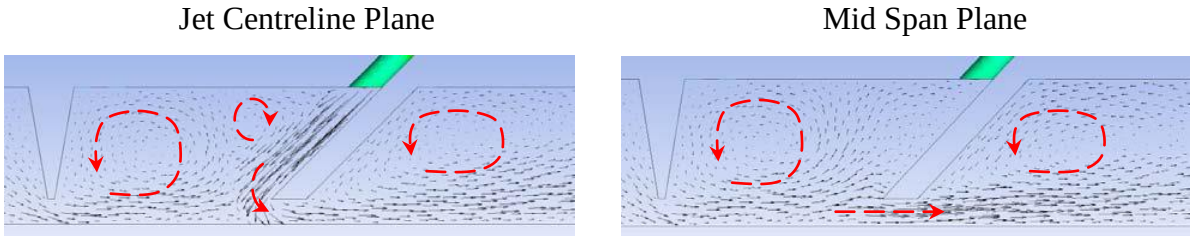


Figure 5.37: CFD flow velocity vectors for labyrinth-fluidic seal – Δp = 0.5 bar, p_r = 1.2 (Skouby 2011)

5.6.7.2 Flow Vectors - Δp = 0.5 bar, p_r = 2.6

Jet plane: at the highest pressure ratio tested of 2.6, the jets clearly reduce the mainstream mass flow rate as the flow velocity under the upstream tooth is now relatively low. The strength of the jets results in strong impingement on the base plate and the jet flow continues further upstream before stagnating and being diverted vertically with the oncoming mainstream, setting up two similarly sized counter-rotating vortices. The downstream side of the jet flow turns under the central tooth tip and accelerates through the gap before diffusing into the downstream cavity. Midspan: The influence of the jets can be seen in this plane as the mainstream flow is turned vertically by the blockage caused by the impinging jet flow spreading in the spanwise direction and hence the axial velocity immediately upstream of the central tooth tip is near zero. The mainstream flow therefore has to travel over the spanwise flow and down the upstream side of the central tooth to reach the tooth clearance where it then accelerates under the tooth and diffuses into the downstream cavity. The two counter-rotating vortices are also present in this plane.

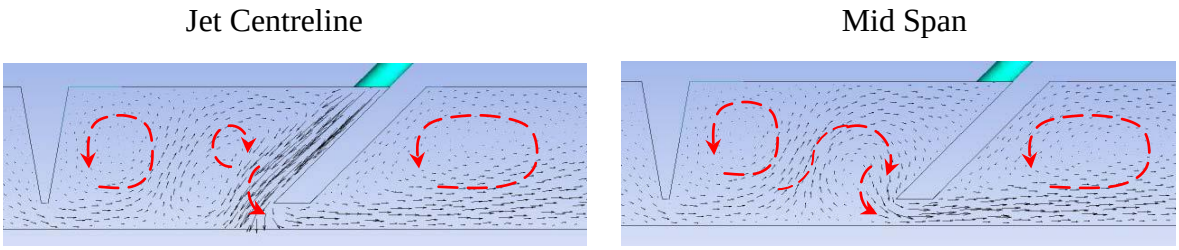
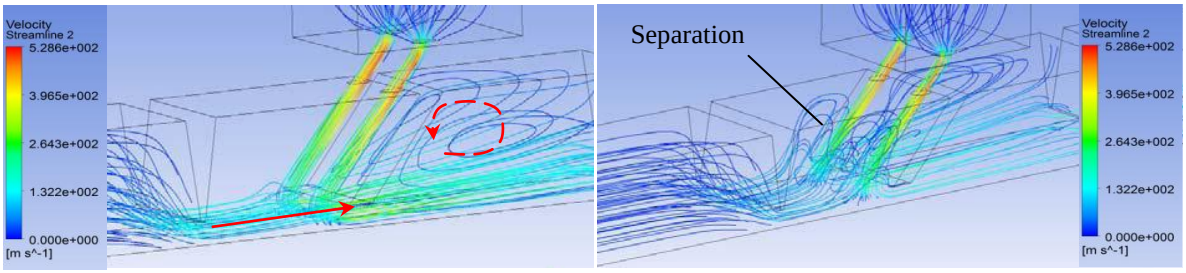


Figure 5.38: CFD flow velocity vectors for labyrinth-fluidic seal – Δp = 0.5 bar, p_r = 2.6 (Skouby 2011)

5.6.7.3 Path Lines - Δp = 1 bar, p_r = 1.2 & 2.6

The path lines in Figure 5.39 (*a*) where p_r = 1.2 show that the mainstream flow accelerates under the upstream tooth and continues under the central tooth whilst being relatively unaffected by the presence of the jet flow, which simply turns downstream once it reaches the central tooth tip. However, when the pressure ratio is raised to 2.6, Figure 5.39 (*b*), the jets clearly impinge on the base plate and spread in the spanwise direction causing the mainstream flow to lift off the base plate and circulate over the stagnation point to travel down towards the central tooth tip clearance between the jet flow. This corresponds to an improvement in sealing performance at higher pressure ratios.



(*a*) (*b*)

Figure 5.39: CFD path lines for labyrinth-fluidic seal – Δp = 1 bar, (*a*): p_r = 1.2, (*b*): p_r = 2.6 (Skouby 2011)

5.6.8 Labyrinth-fluidic seal: Jets downstream – Mass flow rate

5.6.8.1 Δp = 0.5 bar

There is a change in mainstream gradient from p_r = 1.8 to 2 onwards which is due to the sufficient momentum of jets to impinge on the base plate and hence reducing the cross

sectional area of the clearance between the central tooth tip and the base plate for the mainstream flow to pass through (Figure 5.40). The flow regime therefore changes at this pressure ratio. Compared to the upstream configuration, the jets are less able to penetrate the mainstream flow when released from the downstream side of the central tooth. The mainstream flow has passed under the central tooth and has accelerated up to maximum velocity before the jets interact with it, leading to the jet flow turning downstream instead of mixing as effectively as the upstream injection arrangement. The total mass flow rate shows that jets placed on the downstream side of the central tooth are less effective than when located on the upstream side. A sealing improvement occurs after $p_r = 2$ and is at a maximum of 14% at $p_r = 2.6$, which is almost identical to the drop in total mass flow rate of 13% for the upstream arrangement at $p_r = 2.6$. However, the upstream arrangement is beneficial in terms of sealing improvement across a greater range of pressure ratios. The downstream arrangement would need to be run at $p_r > 2$ to achieve a reduction in total mass flow rate. Reversal of the mainstream flow occurred at $p_r = 2.6$. The CFD modelling reassuringly predicts a near identical baseline mass flow rate and captures the flow field regime change seen in the experimental data though the modelled data is far more distinct. A change in the mainstream flow gradient exists between $p_r = 1.6/1.8$ where the jets become more effective for higher pressure ratios. The mainstream flow predicted by the CFD is similar in magnitude to the experimental data but the jet flow is greatly under-predicted and hence the total mass flow appears more favourable from the CFD simulations. The centreline pressure profiles obtained experimentally (section 5.6.9) agree well with the mass flow rate measurements giving further confidence in the experimental data.

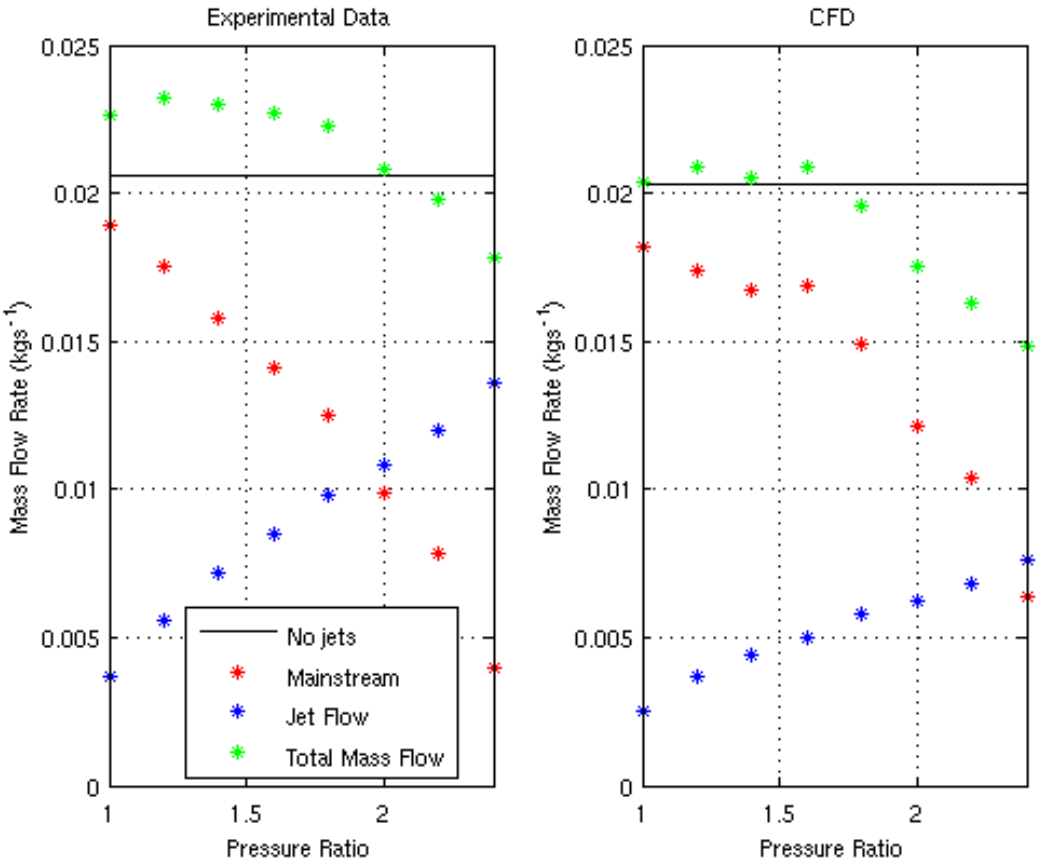


Figure 5.40: Mass flow rate for labyrinth-fluidic seal – jets downstream, Δ*p* = 0.5 bar (Skouby 2011)

5.6.8.2 Δ*p* = 1 bar

When the pressure difference is 1 bar (Figure 5.41) there is a relatively large reduction in mainstream flow from p_r = 1 to 1.2 followed by a much shallower gradient which steepens with pressure ratio between p_r = 1.2 and 2. At p_r = 2.2 there is a discontinuity in the mass flow gradient which is caused by the jets having sufficient momentum to penetrate through the high velocity mainstream flow under the central tooth tip and start to cause blockage in the gap under the central tooth. This occurs at a higher pressure ratio for the Δp = 1 bar case due to the much greater mainstream momentum. The experimental data shows that there is no sealing improvement at Δp = 1 bar across the entire range of pressure ratios tested. The total mass flow rate shows a drop from p_r = 1 to 1.2, caused by the mainstream flow, then rises up to a peak around p_r = 1.6, after which it reduces with pressure ratio where the minimum total mass flow rate occurs at p_r = 2.6. The CFD modelling captures the exact same trend for the

total mass flow rate but suggests the magnitude is much less and predicts a sealing improvement across all pressure ratios. The jet flow is again under-predicted and its effectiveness at reducing the mainstream flow is also over-predicted, giving a much lower total mass flow rate than the experimental data.

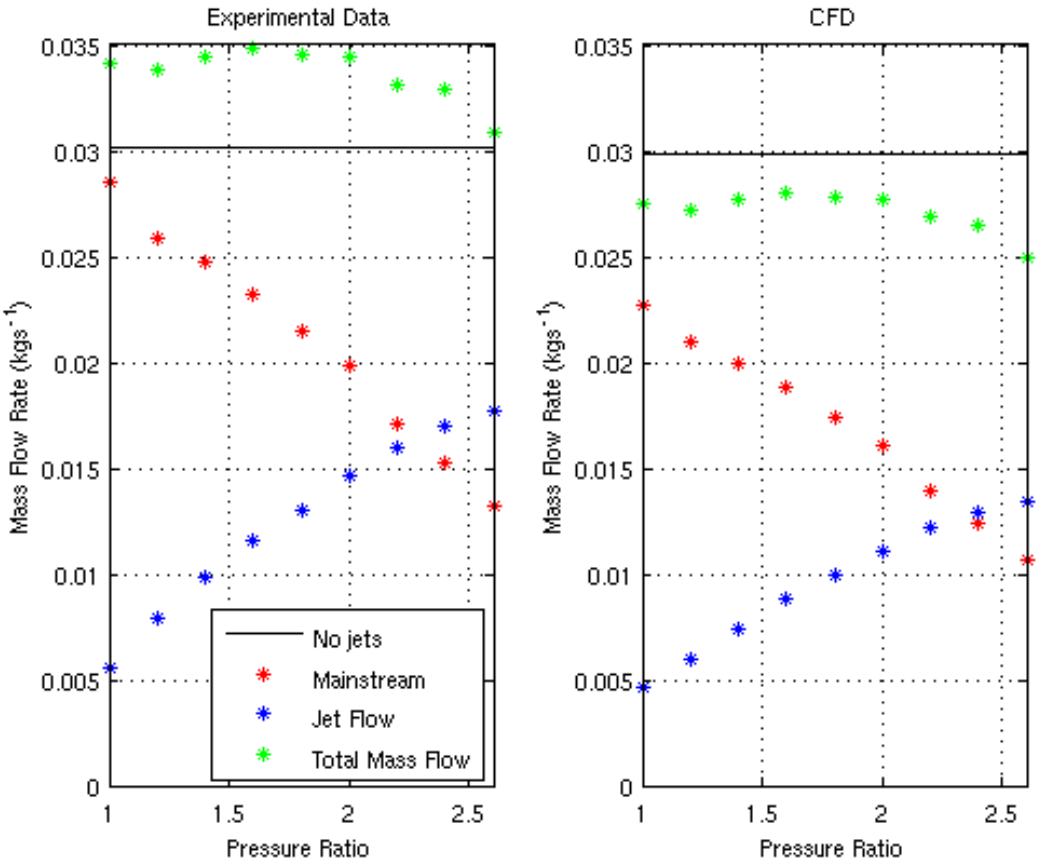


Figure 5.41: Mass flow rate for labyrinth-fluidic seal – jets downstream, Δ*p* = 1 bar (Skouby 2011)

5.6.9 Labyrinth-fluidic seal: Jets downstream – Static pressure distribution

5.6.9.1 Δ*p* = 0.5 bar

The static pressure distribution for the Δ*p* = 0.5 bar case is shown in Figure 5.42. The baseline pressure distribution is very similar to the upstream jet configuration as there is no change in geometry apart from the jet hole location, the influence of which should be negligible when there is no jet flow emanating from them. Downstream of the pressure drop accelerating the mainstream flow under the upstream tooth, there is some static pressure recovery as the

mainstream flow decelerates and the static pressure reaches a plateau within the downstream cavity where the flow has diffused into the larger area. Once the jet flow is included, the associated reduction in mainstream mass flow means the pressure drop across the upstream tooth reduces with increasing p_r until p_r = 2.6 where the pressure in the upstream cavity is almost equal to the inlet pressure. For all values of p_r, the pressure recovers steadily through the upstream cavity until the central tooth tip has been passed, where the interaction with the jets cause a significant pressure drop. The peak static pressure for $p_r \geq 2$ is indicative of the jets beginning to impinge on the base plate and hence the cross-sectional area of the leakage path is reduced, giving a much larger pressure drop at the jet interaction point which corresponds to the change in the trend of the leakage mass flow rate at this pressure ratio. The trend of the total mass flow rate seen in Figure 5.40 is reproduced by the pressure within the downstream cavity (rise to p_r = 1.4 - 1.6 then drop thereafter). The pressure within downstream cavity for p_r = 2.2 to 2.6 is below baseline which correspond to the only pressure ratios that result in improved sealing. This is reflected in the mass flow rate measurements. At the maximum pressure ratio, there is almost no pressure drop across the upstream tooth as the mainstream mass flow rate is tending to zero.

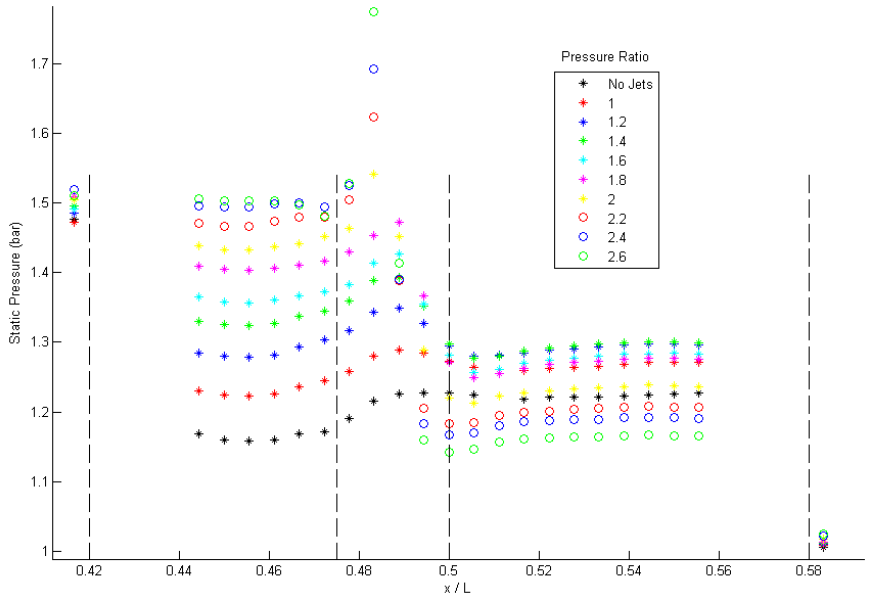


Figure 5.42: Static pressure distribution for labyrinth-fluidic seal – jets downstream, Δ*p* = 0.5 bar (Skouby 2011)

5.6.9.2 Δp = 1 bar

When Δp = 1 bar (Figure 5.43), the pressure lost across the upstream tooth for the baseline case is around 60% (around 80% when Δp = 0.5 bar) which is also followed by a slight pressure recovery after the central tooth tip location as flow decelerates towards the restriction caused by the jets and into the downstream cavity. Introducing the jet flow causes the mainstream flow to reduce and hence the pressure drop across the upstream tooth lessens. There is some pressure recovered as the high speed flow, having accelerated under the upstream tooth, slows as it passes under the central tooth before the jets interact and cause the mainstream flow to reaccelerate.

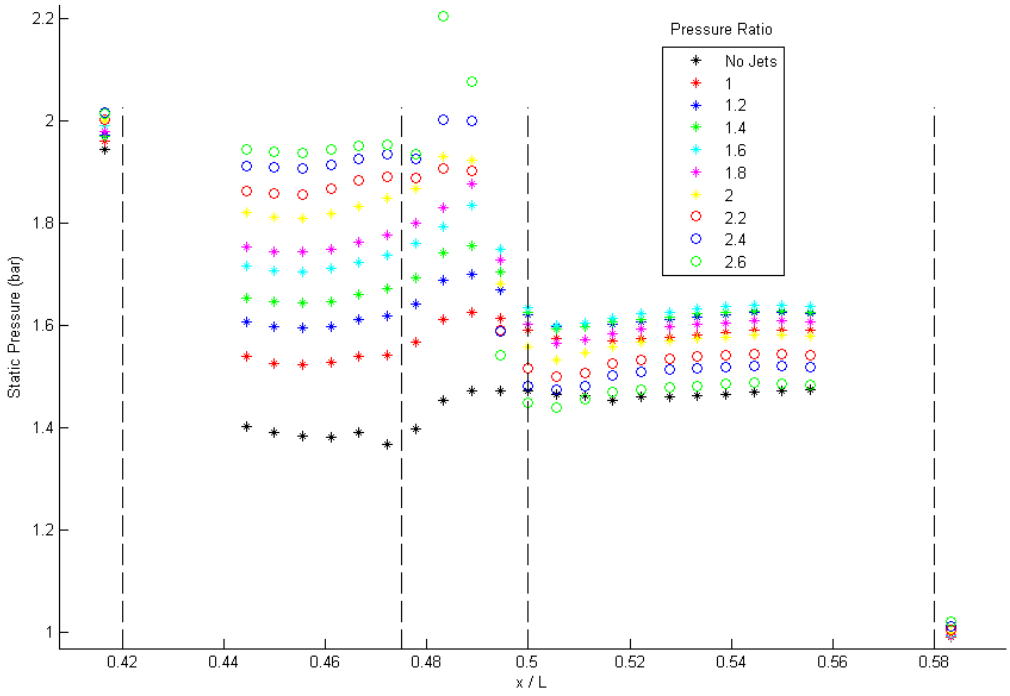


Figure 5.43: Static pressure distribution for labyrinth-fluidic seal – jets downstream, Δp = 1 bar (Skouby 2011)

As the pressure ratio, and hence jet momentum, increase further, the jets begin to fully penetrate the mainstream flow and impinge slightly on the base plate at p_r = 2.4 and 2.6, which is slightly higher than the Δp = 0.5 bar case as the mainstream velocity under the central tooth is much higher. The pressure in the downstream cavity is higher in relation to the baseline case for all pressure ratios at Δp = 1 bar so the pressure drop across the first two teeth

is no larger than the baseline, corresponding to no total mass flow rate reduction across the pressure ratio range. The relative magnitude of the pressure in the downstream cavity for all the pressure ratios relates well to the mass flow rate trend.

5.6.10 Labyrinth-fluidic seal: Jets downstream – Flow field analysis (CFD)

Figure 5.44 and Figure 5.45 show the path line analyses for the downstream jet arrangement labyrinth-fluidic seal at Δp = 1 bar and p_r = 1.2 and 2.6 respectively. At the lower pressure ratio, the mainstream flow accelerates under the upstream tooth and directly under the central tooth before decelerating into the downstream cavity. There is also subsequent acceleration under the downstream tooth. The jet flow slows considerably by the point of reaching the mainstream flow and simply turns downstream with very little interaction.

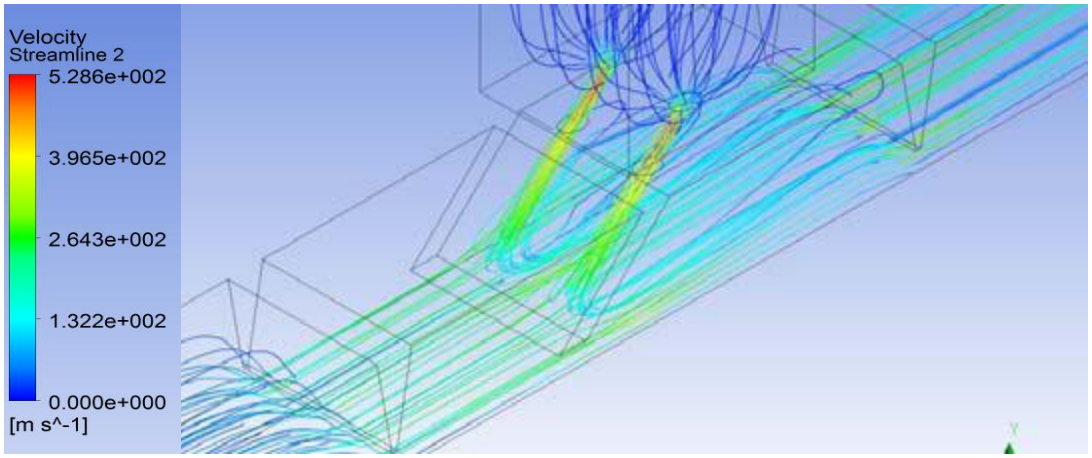


Figure 5.44: Path lines for labyrinth-fluidic seal: Jets downstream, Δp = 1 bar, p_r = 1.2 (Skouby 2011)

When p_r = 2.6, the jets have sufficient momentum to impinge on the base plate and cause a much more disturbed flow field. The mainstream flow has been reduced considerably and hence the velocity leading up to the central tooth tip is very low (dark blue) and some of the flow is forced to circulate in a vortex before passing under the central tooth. On the downstream side of the central tooth, there is a highly turbulent flow field as the two high

velocity streams mix. After mixing, the combined flow accelerates under the downstream tooth to the outlet.

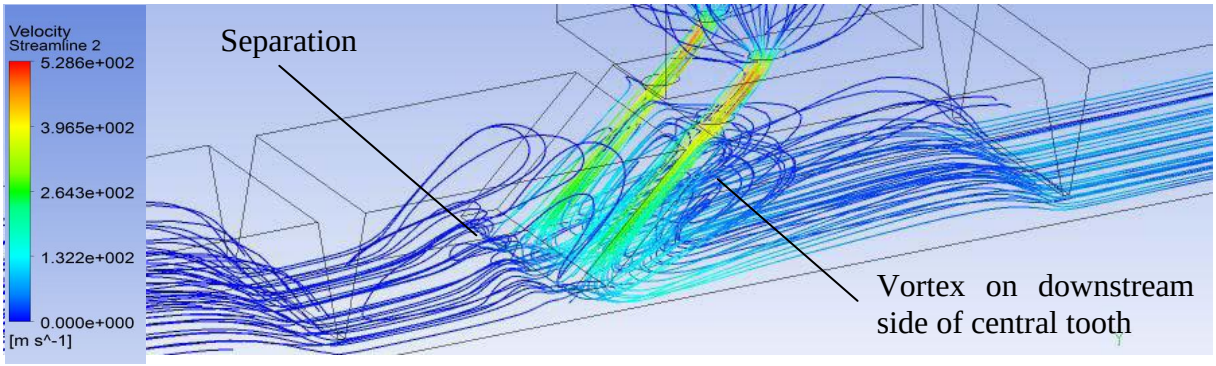


Figure 5.45: Path lines for labyrinth-fluidic seal: Jets downstream, Δp = 1 bar, p_r = 2.6 (Skouby 2011)

5.6.11 Labyrinth-fluidic seal – Power Loss

Figure 5.46 shows the power loss against pressure ratio across the labyrinth-fluidic seals and the plain channel equivalent. For p_r = 1, all cases exhibit a power loss very similar in magnitude to their respective baseline cases. The loss in the plain channel seal is very similar to the labyrinth seal geometry with upstream injection for a given Δp and p_r. All Δp = 0.5 bar cases exhibit higher loss factors than their Δp = 1 bar counterparts. The power loss relationship is nonlinear for all cases and as the pressure ratio increases, the position of the jets becomes more significant in the labyrinth-fluidic seal. For a particular pressure difference, the jets located upstream of the central tooth yield a greater power loss than the downstream arrangement, which is increasingly apparent as the pressure ratio rises. This trend corresponds to the results of the mass flow rate data, where the upstream arrangement leads to greater sealing improvement from a stronger interaction between the two flows. It was initially thought that the downstream arrangement would provide more loss as the central tooth would provide protection for the jets until they interact with the faster flowing mainstream flow which has accelerated under the central tooth. This is the same reason why film coolant flow for turbine vanes is introduced near the leading edge before the flow accelerates up to the peak velocity at the throat to minimise the loss penalty from the

interaction of the two flows. Instead, for a given Δp and for all values of p_r, the downstream arrangement has the lowest loss with the upstream arrangement giving the highest loss and the plain channel case is between the two labyrinth-fluidic cases.

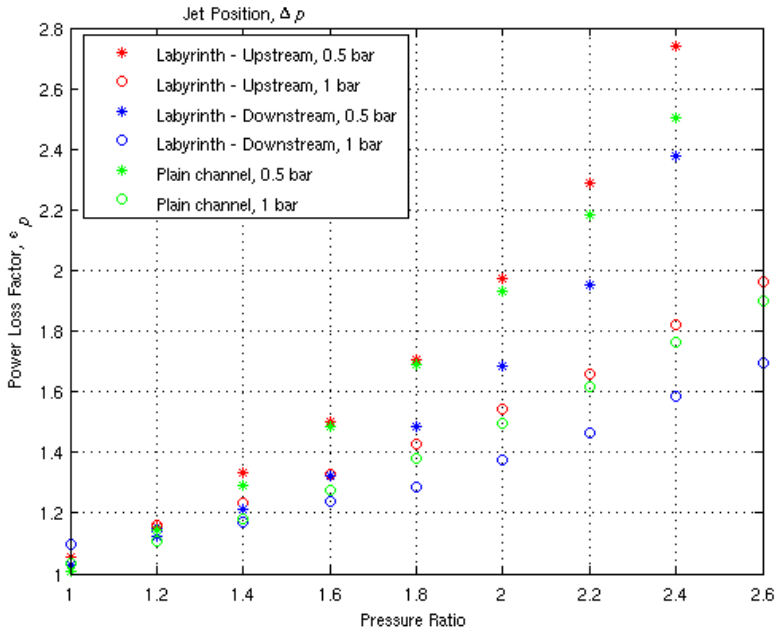


Figure 5.46: Fluidic-labyrinth seal and plain channel power loss: h = 1 mm, θ = 135°, s = 4d

The variation of power loss with normalised mass flow rate is shown below in Figure 5.47. The downstream injection arrangement is generally undesirable as the total mass flow rate is higher than the baseline value and thus no sealing benefit is observed. It may only be considered at p_r = 2.4 and Δp = 0.5 bar. The upstream arrangement and the plain channel case show sealing improvement for most of the values of p_r. A designer will generally want to minimise both the mass flow rate and power loss, and the data suggests that the upstream arrangement and the plain channel cases at Δp = 0.5 bar give the best compromise forming the Pareto frontier for this data set. The downstream arrangement at the same pressure difference exhibits the greatest sealing performance improvement but is only of use at p_r = 2.4, Δp = 0.5 bar; below this pressure ratio the mass flow rate increases significantly, and above this pressure ratio ($p_r \geq 2.6$) the mainstream flow is reversed to achieve perfect sealing.

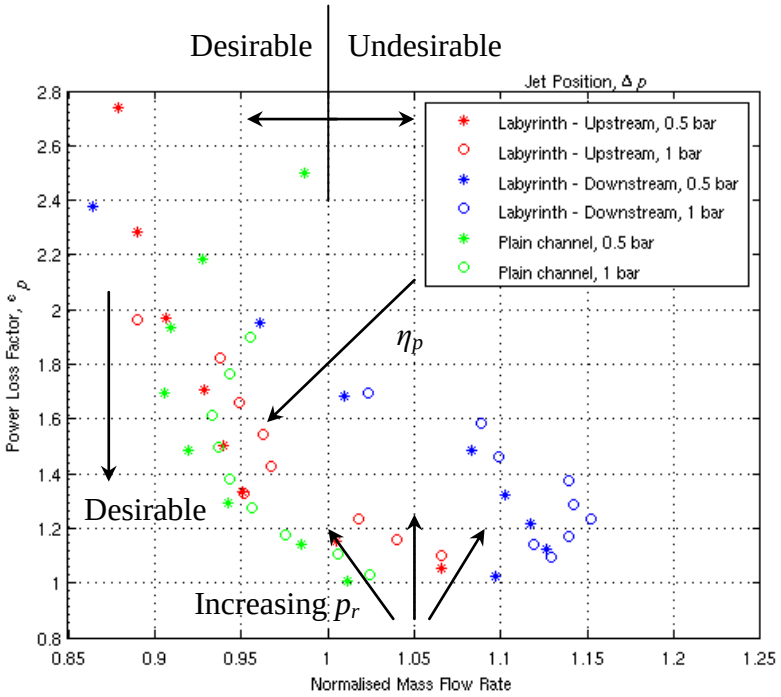


Figure 5.47: Fluidic-labyrinth seal and plain channel experimental power loss vs. normalised mass flow rate: h = 1 mm, θ = 135°, s = 4d

5.7 Summary

The work carried out in this chapter has provided a considerable step forward in assessing the potential, and improving the understanding of, the fluidic seal concept. Very few experimental studies have been performed on this sealing method and the parametric study carried out in this research program has been the first of its kind in terms of sealing.

The test rig for this experimental parametric study was designed and manufactured at the Osney Thermofluids Laboratory, Oxford. Assuming that the main leakage path clearance was much smaller than the radius of a rotor that this seal may be applied to, the test rig contained a linear version of the seal. This test rig therefore could not assess the effect on the seal's performance due to the circumferential velocity component in main leakage flow as a result of

shaft rotation, but an understanding of which parameters are most influential in providing an improvement to sealing performance is required first. Five parameters were investigated during this study on a plain channel geometry using circular cross section holes at 1 mm diameter; the pressure drop across the main leakage path (mainstream), the jet to mainstream total pressure ratio, the injection angle, the jet spanwise spacing in terms of hole diameters and the channel height.

The results of the experimental study showed that a reduction in total mass flow by including the jet flow can only be achieved if the jet momentum is exploited by directing the jets upstream to oppose the mainstream leakage flow. Increasing the angle such that the jet axial velocity component increased accordingly led to improvements in sealing ability. The maximum angle of 150° to the mainstream leakage direction outperformed all other angles tested (with all other parameters held constant). Of the three channel heights investigated (h = 1, 2 and 3 mm), a height of 2 mm produced the lowest normalised mass flow rate observed. A lower pressure drop across the mainstream path also led to a better performing seal in terms a reduction in the total leakage from the baseline case. The two most influential parameters in improving the sealing performance were the jet to mainstream pressure ratio and the hole spacing. Although at h = 1 mm the peak sealing performance occurred at a pressure ratio of approximately 2, the maximum pressure ratio of 2.6 lead to the best performing seal for channel heights of 2 and 3 mm. Two values of hole spacing were investigated and the smaller spacing led to a significant increase in the jet mass flow rate. Doubling the jet hole density from $s = 4d$ to $s = 2d$ enhanced the improvement or exacerbated the detriment of the effect from introducing jet flow, depending on the injection angle.

The fluidic seal concept was also evaluated in terms of the penalty resulting from taking extra energy from the compressor to increase the jet flow total pressure, thus diverting air from the

combustor and wasting usable work. The increase in engine efficiency must therefore outweigh the reduction in shaft work associated. Power loss results for the fluidic seal were heavily dependent on the pressure ratio, channel height and hole spacing. Ideally the loss would be minimised whilst also minimising the leakage mass flow rate, though in reality a Pareto efficiency is required *i.e.* a trade-off.

An analytical model of the fluidic seal was created based on a momentum balance which incorporated empirical data for discharge coefficients. The performance of the model was found to be in reasonable agreement with the experimental data for a channel height of 3 mm but the accuracy of the model diminished with decreasing channel height. At a channel height of 1 mm, the model was highly inaccurate which may have been due to the dissipation of jet energy as a result of impingement on the base plate and the losses associated with this, which was not accounted for by the model. An inaccurate channel friction factor may be exacerbated as the hydraulic diameter drops.

3D CFD was also applied to the circular hole, plain channel fluidic seal and reasonably accurately predicted the mass flow rates for most cases. Some of the experimental data were replicated for validation but the majority of the new cases assessed the hole spacing parameter in greater detail. Values of 4*d* (also achieved experimentally), 2*d* (limited experimental cases performed) and 1.5*d* (solely CFD) were simulated, which all indicated that decreasing the hole spacing only improved the sealing performance. These results therefore suggested that a continuous jet from a slot could provide the best performing fluidic seal.

A specific jet hole design called the console, originally designed for film cooling applications, was employed to achieve a full coverage in the spanwise direction from discrete inlet holes. The inlets were based on 1 mm diameter circular cross-section holes to ensure an appropriate

comparison for performance evaluation. Various parameters were investigated, with only one case providing an improvement over the circular holes; an inlet to exit area ratio of 1 as opposed to 0.8. It was originally thought that decreasing the exit area would accelerate the jet flow and promote mixing losses but this just restricted the jet mass flow rate. Very little mixing was observed for this jet geometry, thus the higher jet mass flow rate was required to improve upon the cylindrical hole cases.

The fluidic seal was also incorporated into a current in-service seal, the labyrinth seal. Experimental and CFD data were collected for a 3 tooth labyrinth seal with the central tooth angled upstream at 45° to the mainstream direction. The jets were circular in cross section as tested on the plain channel cases. The jets were introduced on the upstream and downstream faces of the central tooth and their leakage and power loss performances were compared to the plain channel geometry with the same jet hole parameters and boundary conditions. Sealing performance for the fluidic-labyrinth seal was shown to improve with upstream injection over downstream injection, confirmed by the static pressure data. No significant improvement was seen in the sealing performance over the equivalent plain channel case. The power loss data supported the leakage data indicating that the upstream injection was the favourable method.

This chapter has shown great potential to reduce the mass flow rate through a leakage path by the use of a fluidic seal, which can easily allow for large axial and radial relative movement and is inherently non-contacting. Further work is required before a fluidic seal can enter service, but this study aims to take a step towards achieving this goal.

6 Summary and Further Work

Stringent efficiency targets for gas turbines, particularly in the commercial aviation industry have lead to designers seeking to achieve performance gains from components other than the major constituent parts; the compressor, combustor and turbine. A relative lack of research time and financial investment has been made into sealing technology to date and subsequently large reductions can be made to specific fuel consumption in a cost-effective manner, providing the motivation for this research program. Current in-service sealing technology either possesses inherently poor leakage characteristics or the leakage performance degrades over time as the seal is contacting in nature. Contacting seals also lead to power dissipation in the form of heat, which can raise the temperature, thus reducing the effectiveness, of coolant flow. Large axial and radial relative growth cannot be easily accommodated without incurring increased leakage or wear. The aim of this research was to develop two non-contacting sealing technologies, the LAMFS (Rolls-Royce concept) and fluidic seals. This thesis reports the experimental, analytical and CFD investigations into these seal concepts leading to a greater understanding of the feasibility and potential of both.

A comprehensive literature review has been undertaken into novel non-contacting sealing technologies which are either still in the first stages of research development or have progressed to prototypes being reviewed within test engines. Each sealing method is assessed in its potential to meet the criteria discussed above. Various researchers used Reynolds compressible flow equation to analytically model the flow between two close clearance surfaces in either one or two dimensions with great success. This also proved to be an extremely useful tool for the author. A large quantity of research was discovered which

assessed the ability to generate hydrodynamic pressure fields between two moving surfaces in close proximity as a method of preventing contact between the seal and rotor surfaces. An inherent problem with these seals exists at start-up and shutdown cycle phases when the magnitude of hydrodynamic forces separating the surfaces would diminish such that contact would be made. Over multiple cycles, these seals would experience wear which this research aims to eliminate. The review of experimental research into these non-contacting sealing methods was especially interesting as it demonstrated that the induced pressure force separating the two surfaces during rotation could be very large whilst satisfying the non-contacting criterion for next generation seals.

A test rig containing a linear version of the LAMFS was manufactured by Rolls Royce in order to evaluate the forces on the seal housing as a result of the static pressure distribution alone. After a limited number of experiments, this test rig was delivered to the Osney Thermofluids Laboratory, Oxford, where it was re-commissioned for further experimental investigations as part of this research program. Tests were conducted initially on the simplest geometry, the baseline case, which gave an unstable force-displacement relationship for the seal housing. This was confirmed by two dimensional CFD simulations and an analytical model using Reynolds 1D equation (assuming no pressure variation in the 'circumferential' direction), although the trends were quite different. This was due to the inability to accurately predict the inlet losses to the seal gaps with computational modelling. The analytical model then allowed the author to derive coefficients for these inlet losses as a function of the Reynolds number at the seal gap inlets which improved the accuracy of the model considerably. Geometry modifications (converging radial steps) were made within the seal gaps which proved to be essential for the seal housing to possess a self-centring ability. Parameters such as the step height and the radial position were investigated. The reason for these geometry alterations affecting the seal housing behaviour could be seen when analysing

the static pressure distribution within the seal gaps. Leakage mass flow rates were obtained though these were heavily influenced by the secondary leakage component between the side plates and the seal housing. The analytical prediction for the leakage mass flow rate matched well with the experimental results when the secondary leakage was eliminated. A positive bias observed in the intermediate pressure chamber, and subsequently the force-displacement relationships, was partly attributed to this side leakage. This test rig, using stereolithography rotor components, allows for the influence of seal gap geometry on the force-displacement relationship of the seal housing to be evaluated easily. Although the positive bias described above influences the results observed in this test rig, any further parametric studies into other potential seal gap geometry which may improve upon the converging radial steps could easily be tested on this rig.

A test rig containing a fully annular version of the LAMFS to prove the concept was manufactured at the Osney laboratory with an identical seal housing cross section to that of the seal in the linear test rig. The cross sectional dimensions of the major features were engine representative though the radius of the rotor was significantly lower than any locations where it would potentially be installed. Inherently, with this fully annular seal, the seal gaps of the baseline geometry (parallel faces) have varying cross-sectional areas due to the change in radius with seal gap streamwise position. The experimental test results confirmed that this area change with radius only had a very minor effect and the baseline geometry still exhibited an unstable behaviour. One particular permutation of the radial steps tested on the linear LAMFS test rig was then introduced and this seal gap geometry changed the force-displacement relationship for the seal housing as was observed in the linear test rig. This proved that a stable, self-centring seal housing behaviour could be obtained purely from the static pressure distributions in the seal gaps. Tests with a rotating disc were unable to be performed due to safety concerns but CFD gave an insight into rotational effects. As

expected, a constant gap height with circumferential position yields negligible difference to the static pressure distribution or the radial leakage. Should the performance of rotating tests be desired to assess potential improvements to the seal housing behaviour as a result of hydrodynamic-induced pressure generation, the test rig must be modified. However, the results show that the magnitude of the restoring force generated from the seal gap static pressure distributions alone are extremely large and rotation-induced pressure forces may not be necessary. The dynamic behaviour of the seal was then modelled to assess this statement using the force-displacement relationships observed from the experiments performed. Results showed that, due to the large resultant forces and the relatively small mass of the seal housing, the seal housing axial acceleration could be extremely large, exhibiting a fast response to shaft axial movement. The dynamic coefficients, such as the inherent damping factor, would need to be obtained and, if necessary, modified to ensure an acceptable dynamic behaviour before entering service. Increased damping could be provided by using a brush seal as the secondary seal, which could be adjusted by varying the contact frictional force due to blow-down with the bristle lay angle.

As this particular research program into the LAMFS reached its end, tests were performed on the linear LAMFS test rig by another member of the Osney laboratory. Using a Perspex endplate and a high frame rate camera, the dynamic response of the seal housing when released from a maximum displacement away from the equilibrium position, was observed. Early results showed that the seal housing possesses inherent damping though this will be tested on the annular seal for confirmation that this is not side leakage-induced. Another important consideration is relative thermal expansion between the disc and seal housing when the sum of the two seal gap heights is of the order of 0.5 mm. The air and metal temperatures within the regions of gas and steam turbines can be extremely high. There is ample clearance within the intermediate pressure chamber for radial growth but axial growth may be an issue

with such tight tolerances. Perhaps materials with different coefficients of thermal expansion could be considered to ensure that the total seal gap height increases rather than tending to zero. The method of installing the seal housing within a gas turbine such that it has axial freedom has not been investigated but based on the data obtained, the seal housing axis should not be constrained in an attempt to avoid seal-rotor axis misalignment. The self-centring ability of the seal housing is such that restoring forces will be generated if the seal housing displacement does not lie on the equilibrium position, which will occur at any point around the circumference of the seal *i.e.* due to axis misalignment. A total seal height of 400 μm over a large shaft diameter will be susceptible to build tolerances, hence it is therefore suggested that the weight of the seal housing is supported, but is given freedom of axial position and seal axis orientation as the passive control system devised will maintain seal-rotor axis alignment.

The aforementioned fluidic seal was evaluated with a test rig manufactured at the Osney laboratory. The effect on the total mass flow rate by parameters such as mainstream pressure difference, jet to mainstream inlet total pressure ratio, jet angle, channel height and spacing were investigated. Results showed that orientating the jets upstream and exploiting the jet momentum could reduce the total mass flow rate significantly. The maximum angle tested from the mainstream direction was 150° (60° upstream from the vertical) which gave a 35% total mass flow rate reduction at a jet spacing of 4 diameters. An optimum channel height of 2 mm was discovered as at 1 mm a large proportion of the jet energy is dissipated on the channel wall and at 3mm, the mainstream momentum becomes sufficiently high such that the jets are less effective overall. Reducing the jet spacing to 2 diameters instead of 4 (doubling the jet density) significantly reduced the total mass flow rate further when the jets were angled upstream. However, when the jets were at 90° (vertical), the increase in total mass flow worsened at all pressure ratios by halving the hole spacing. Another method of quantifying the

interaction of the two flows was by considering the power entering the seal in the form of the two separate flows and how much is lost by the system exit. Depending on whether the leakage flow is being used for cooling purposes or not, the amount of total pressure required at the exit of the seal may vary, especially for internal and impingement cooling applications. Power loss results indicated that a trade-off must be made between mass flow rate reduction and minimising power consumption.

A variation in the hole geometry was investigated using the console (circular inlet to slot exit). CFD results showed that a fully spanwise coverage could be obtained from a discrete set of inlets. The console was only shown to improve, in terms of sealing performance, when the inlet to outlet area ratio was at a value of 1. Other cases with a ratio of 0.8, designed to accelerate the flow and increase jet momentum, were less effective. Another variant on the fluidic seal concept was incorporating this concept into the labyrinth seal, a widely used in-service seal, to improve its leakage characteristics. Experimental and CFD data showed that placing the row of jets either upstream or downstream of the angled central tooth has a considerable effect on the interaction of the two flows. A recommendation for further work would focus on an experimental investigation into optimising the jet geometry. A reduction in the jet spacing leads to a better sealing performance which may be due to the increased number of shear layers and resulting mixing. Multiple rows with different injection angles to the axial direction (whirl) could also be assessed. The whirl component within a gas turbine due to the moving rotor should also be considered. For these tests a fully annular seal would be required. A test rig could be designed with a removable axial section of the casing (a ring), containing the jet geometry, allowing multiple jet configurations to be tested as was done with the linear fluidic seal. The effects of shaft rotation, such as mainstream leakage whirl component velocity variation with radial position, could then also be assessed.

The two seal concepts researched in this thesis have been shown to have great potential in gas and steam turbine applications as they have the ability to accommodate large axial and radial relative movement between the rotor and casing and both are non-contacting alternatives to current technology. Considerable research is still required before these seal concepts could be entered into service but a significant contribution has been made into this research area as both demonstrate the ability to deal with rotor-seal relative movement whilst eliminating wear.

7 Bibliography

Abernathy, R B, R P Benedict, and R B Dowdell. “ASME measurement uncertainty.” ASME Journal of Fluids Engineering, 107:161-164, 1985.

Abramovich, G. N. *The Theory of Turbulent Jets.* Cambridge, Massachusetts: The M.I.T. Press, 1963.

Abramowitz, M, and I A Stegun. *Handbook of Mathematical Functions.* New York: Dover Publications, 1965.

Aksit, M. F., and J. A. Tichy. “Wear of Brush Seals: Background and New Modeling.” *Tribology Transactions*, 1998: 368-374.

Anderson, W. J. “Analysis of an All Metallic Resilient Pad Gas Lubricated Thrust Bearing.” (Journal of Lubrication Technology, ASME) 1975.

Andreopoulos, J., and W. Rodi. “Experimental Investigation of Jets in a Crossflow.” *Journal of Fluid Mechanics*, 1984: 138: 93-127.

Andres, L. S., and J. Baker. “Measurements of Leakage and Power Loss in a Hybrid Brush Seal.” *Proceedings of ASME Turbo Expo, Power for Land, Sea and Air.* Berlin, 2008.

Arora, G. K., M. P. Proctor, B. M. Steinetz, and I. R. Delgado. “Pressure Balanced, Low Hysteresis, Finger Seal Test Results.” *35th Joint Propulsion Conference and Exhibit.* AIAA (AIAA-99-2686), 1999.

Ausman, J. S., E. E. Bisson, and W. J. Anderson. *Gas Lubricated Bearings.* NASA SP-38, pp. 109-138, 1964.

Auyer. US 2685429. 1954.

Basu, P., P. Datta, A. Johnson, R. Loewerithal, and J. Short. “Hysteresis and Bristle Stiffening Effects of Conventional Brush Seals.” (Journal of Propulsion and Power) 110, no. 4 pp. 569-575 (1994).

Bayley, F. J., and C. A. Long. “A Combined Experimental and Theoretical Study of Flow and Pressure Distributions in a Brush Seal.” *Journal of Engineering for Gas Turbines and Power, Vol. 115*, 1993: 404-410.

Braun, M., H. Pierson, D. Deng, F. Choy, M. Proctor, and B. Steinetz. “Structural and Dynamic Considerations Towards the Design of a Padded Finger Seal.” *AIAA Paper 2003-4698.* 2003.

Brewe, D. R., D. P. Fleming, F. Dimote, and R. C. Hendricks. *Fluid Film Lubrication.* Chapter 8 of Tribolgy for Aerospace Applications STLE Special Publications, 1997.

Callaghan, E., and T. Bowden. *Investigation of Flow Coefficient of Circular, Square and Elliptical Orifices at High Pressure Ratios.* Ohio: Lewis Flight Propulsion Laboratory, NACA Technical Note: 1947, 1949.

Chambers, A. C. *An Investigation of Impingement Cooling Applied to Turbine Blade Cooling Passages.* DPhil Thesis, 2003.

Chupp, R. E., and P. Nelson. “Evaluation of Brush Seals for Limited-Life Engines.” *AIAA-Journal of Propulsion and Power*, 1993: 113-118.

Chupp, R. E., F. Ghrasripoor, N. A. Turnquist, and M., Aksit, M. F. Demiroglu. “Advanced Seals for Industrial Turbine Applications: Dynamic Seal Development.” (Journal of Propulsion and Power) 18, no. 6 (2002).

Chupp, R. E., M. F. Aksit, F. Ghasripoor, N. A. Turnquist, and M. Demiroglu. *Advanced Seals for Industrial Turbine Applications.* AIAA Paper No. 2001-3626, 2001.

Chupp, R. E., R. C. Hendricks, S. C. Lattime, and B. M. Steinetz. *Sealing in Turbomachinery.* NASA/TM-20060214341, 2006.

Chupp, R. E., R. J. Prior, R. G. Loewenthal, and R. P. Menendez. *Advanced Seal Development for Large Industrial Gas Turbines.* AIAA-Paper 97-2731, 1997.

Curtis, E. M., J. D. Denton, J. P. Longley, and B Rosic. “Controlling Tip Leakage Flow Over a Shrouded Turbine Rotor Using an Air-Curtain.” Orlando, Florida, USA: ASME Turbo Expo, GT2009-59411, 2009.

Delgado, A., and L. San Andres. “Identification of Structural Stiffness and Damping Coefficients of a Shoed-Brush Seal.” 2007.

Delgado, A., L. San Andres, and J. Justak. “Analysis of Performance and Rotordynamic Force Coefficients of Brush Seals with Reverse Rotation Ability.” *ASME Paper No. GT 2004-53614.* 2004.

—. “Identification of Stiffness and Damping Coefficients in a Shoed Brush Seal.” *Proceedings of the VII Congreso y Exposicion Latinoamericana de Turbomaquinaria.* Veracruz, Mexico, 2003.

Dinc., S., et al. “Fundamental Design Issues of Brush Seals for Industrial Applications.” *ASME Journal of Turbomachinery, 124,* 2002: 293-300.

Dogu, Y., M. F. Aksit, and M. Demiroglu. “Evaluation of Flow Behaviour for Clearance Brush Seals.” *Journal of Engineering for Gas Turbines and Power, Vol. 130, 012507-1,* 2008.

Etsion, I., and I. Green. “Dynamic Analysis of a Cantilever-Mounted Gas-Lubricated Thrust Bearing.” (Journal of Lubrication Technology, ASME) 1977.

Ferguson, J.G. “Brushes as High Performance Gas Turbine Seals.” (ASME, 88-GT-182) 1988.

Florshuetz, L. W., D. E. Metzger, D. I. Takeuichi, and R. C. Berry. *Multiple Jet Impingement Distributions and Heat Transfer Characteristics - Effects of Initial Crossflow and Nonuniform Array Geometry.* NASA - report 3630, 1982.

Fluent User Guide. “Fluent Inc.” 2005.

Franceschini, Gervas. *Shaft Seals for Turbine Engines.* Oxford: Oxford University, 2005.

Glahn, J. A., and P. M Munsell. United States Patent US 2009/0212501 A1. 2009.

Guardino, C., J. W. Chew, and N. J. Hills. “Calculation of Surface Roughness Effects on Air-Riding Seals .” (Journal of Engineering for Gas Turbines and Power, ASME) 2004.

Hay, N., D. Lampard, and S Benmansour. “Effect of Crossflows on the Discharge Coefficient on Film Cooling Holes.” (AMSE Journal of Power Engineering) 105 pp 243-248 (1983).

Hendricks, R. C., T. A. Griffin, Kline T., Csavina K. R., Pancholi A., and D. Sood. *Relative Performance Comparison Between Baseline Labyrinth and Dual Brush Compressor Discharge Seals in a T-700 Engine Test.* NASA TM-106360, 1994.

Heshmat, H., and W. Shapiro. “Advanced Development of Air-Lubricated Thrust Bearings.” (ASLE Lubrication Engineering, 40, no. 1, pp. 21-6) 1984.

Heshmat, H., C. A. Heshmat, and D.S. Xu. “Analysis of Gas Lubricated Foil Thrust Bearings Using Coupled Finite Element and Finite Difference Methods.” (Journal of Tribology, ASME) 2000.

Hill, B. J. *Measurement of Local Entrainment Rate in the Initial Region of Axisymmetric Turbulent Jets.* Journal of Fluid Mechanics, Volume 179, pp 383-405, 1972.

Hoe, C. M., and E. Gutmark. “Vortex induction and mass entrainment in a small aspect ratio elliptical jet.” *383-405.* Vol. 179. Journal of Fluid Mechanicss, 1987.

Hogg, S. I. Sealing Device for Reducing Fluid Leakage in Turbine Applications. Patent UK Patent Application No. 1017525.5. 2010.

Hogg, S. I., and I. Gomez Ruiz. “Fluidic Jet Barriers for Sealing Applications, GT2011-45353.” *Proceedings of ASME Turbo Expo 2011.* Vancouver, British Columbia, Canada, 2011.

Hogg, S. I., T. V. Jones, A. Baker, and P. Withers. “Two Dimensional Effects in Gas Dynamic Journal Bearings.” *ISABE 89-7078,* 1989.

Holdeman, J. D. “Mixing of Multiple Jets with a Confined Subsonic Crossflow.” *27th Joint Propulsion Conference.* Sacremento, California, 1991. NASA Technical Memorandum 104412.

Howard, S. A,, and L. S. Andres. “A New Analysis Tool Assessment for Rotordynamic Modelling ofGas Foil Bearings, GT2011-022505, Vol 133.” *Journal of Engineering for Gas Turbines and Power*, 2011.

Hughes, S. J., S. I. Hogg, and T. V. Jones. “Analysis of a Gas Lubricated Hydrodynamic Thrust Bearing.” (ASME Journal of Tribology) 1996.

ISO5167-2. “Measurement of fluid flow by means of pressure differential devices inserted in circular cross-section conduits running full.” London: British Standards Institution, March 2003.

Jahanmir, S., H. Heshmat, and C. Heshmat. “Evaluation of DLC Coatings for High-Temperature Foil Bearing Application .” *Journal of Tribology, Vol. 131, 011301,* 2009.

Jahn, I. H. J. *Leaf Seals for Gas and Steam Turbines - DPhil Thesis.* University of Oxford, 2008.

Jahn, I. H. J., G. Franceschini, A. K. Owen, and D. R. H. Gillespie. “Negative Stiffness in Gas Turbine Leaf Seals.” *ASME Turbo Expo GT2011-46483.* Vancouver, 2011.

Johnson, M. C., and E. G. Medlin. Laminated Finger Seal with Logarithmic Curvature. US Patent 5,108,116. April 1992.

Justak, J. *Non-Contacting Seal Developments.* NASA Seal/Secondary Air System Workshop, 2004.

Kim, T. H., and L. San Andres. “Heavily Loaded Gas Foil Bearings: A Model Anchored to Test Data.” (Journal of Engineering for Gas Turbines and Power, GT2008-012504) 130 (2008).

Kim, T. H., and L. San Andres. “Heavily Loaded Gas Foil Bearings: A Model Anchored to Test Data.” *ASME Paper No. GT2005-68486,* 2005.

Kim, T. H., and L. San Andres. “Limits for High Speed Operation of Gas Foil Bearings.” *ASME Journal of Tribology, 128 (3),* 2006: 670-673.

Klomp, E. D. “Note on an Aerodynamic Seal.” Michigan: General Motors Corporation, 1969.

Laurent, R., M. Arghir, O. Bonneau, and P. Matta. “Experimental Analyses of a First Generation Foil Bearing: Startup Torque and Dynamic Coefficients.” (Journal of Engineering for Gas Turbines and Power) 133 (2011).

Le Lez, S., M. Arghir, and J. Frene. “A New Bump-Type Foil Bearing Structure Analytical Model.” *Journal of Engineering for Gas Turbines and Power*, 2007: 1047-1057.

Lee, D., and D. Kim. “Design and Performance of Hybrid Air Foil Thrust Bearings.” *Journal of Engineering for Gas Turbines and Power, Vol. 133, 042501*, 2011.

Lepetit, F. A. *The Study of Hydrodynamic Effects at the Rotor Interface in Brush Seals.* D.Phil. Thesis, University of Oxford, 2001.

Li, H., and M. J. Braun. “The Sealing Behaviour and Force Analysis of a Double-Laminate Single-Padded Finger Seal.” *Proceedings of ASME Turbo Expo (GT2007-28171).* 2007.

Li, Z., J. Li, X. Yan, and Z. Feng. “Effects of Pressure Ratio and Rotational Speed on Leakage Flow and Cavity Pressure in the Staggered Labyrinth Seal, Vol 133, 114503.” *Journal of Engineering for Gas Turbines and Power*, 2011: 1-6.

Lichtarowicz, A., R. K. Duggins, and E. Markland. “Discharge Coefficients for Incompressible Non-Cavitating Flow Through Long Orifices.” (Journal Mechanical Engineering Science) 7, no. 2 (1965).

Lipschitz, A. “A Zero Leakage Film Riding Face Seal.” ASME, 1984.

Ludwig, L. P. *Self-Acting Shaft Seals.* NASA TM-73856, 1980.

McGreehan, W. F., and M. J. Schotsch. “Flow Charcteristics of Long Orifices with Rotation and Corner Radiusing.” *Journal of Turbomachinery - Transaction of the ASME, Vol. 110*, 1988: 213-217.

Minoda, M., S. Inoue, H. Usui, and H. Nouse. Air Sealed Turbine Blades, US 4732531. Japan. 1988.

Moffat, R J. “Contributions to the theory of single-sample uncertainty analysis.” ASME Journal of Fluids Engineering, 104:250-260, 1982.

—. “Describing the uncertainties in experimental results.” Experimental Thermal and Fluid Science, 107:3-17, 1988.

Moore, A. “Gas Turbine Internal Air Systems - A Review of the Requirements and the Problems.” (ASME paper, 75-WA/FT-1) 1975.

Morgan, J. J. “Cantilevered Floating Ring Seal.” (United States Patent, US2004/0150164 A1) 2004.

Munson, J. “Development of Film Riding Face Seals for a Gas Turbine Engine.” (Tribology Transactions) 35, pp. 65-70 (1992).

Munson, J. “Testing of a High Performance Compressor Discharge Seal.” (AIAA) 1993.

Munson, J., D. Grant, and G. Agrawal. “Foil Face Seal Proof-of-Concept Demonstrating Testing.” (AIAA 2002-3791) 2002.

Nakabe, K., A. Higashio, W. Chen, K. Suzuki, and J. H. Kim. “An Experimental Study on the Flow and the Heat Transfer Characteristics of Longitudinal Vortices Induced by an Inclined Impinging Jet into a Crossflow.” *11th International Heat Transfer Conference, vol. 5, pp. 439-444.* 1998.

Nakane, H., et al. “The Development of High-Performance Leaf Seals.” (ASME Journal of Engineering and Gas Turbines and Power) 126 pp. 342-350 (2004).

Neef, M., N. Surken, E. Sulda, and J. Walkenhorst. “Design Features and Performance Details of Brush Seals for Turbine Applications.” *Power for Land, Sea and Air.* Barcelona: ASME Turbo Expo, GT2006-90404, 2006.

Nemeth, Z. N. *Operating Characteristics of a Cantilever-Mounted Resilient-Pad Gas-Lubricated Thrust Bearing.* NASA TP-1438, 1979.

Peng, Z. C., and M. M. Khonsari. “Hydrodynamic Analysis of Compliant Foil Bearings With Compressible Air Flow.” *Journal of Tribology.* 2004. 542-546.

Platten, J. L., and J. F. Keffer. *Entrainment in Deflected Axisymmetric Jets at Various Angles to the Stream* . University of Toronto: UTME-TP-6808, 1968.

Proctor, M. P., and B. M. Steinetz. Non-Contacting Finger Seal. U.S. Patent 6,811,154. November 2004.

Proctor, M. P., and I. R. Delgado. “Leakage and Power Loss Test Results for Competing Turbine Engine Seals.” *ASME Turbo Expo (GT2004-53935).* 2004.

PTC19.1. “Performance Test Codes PTC 19.1-2005 Test Uncertainty.” New York: ASME PTC, 2005.

Quinn, W. R. “On mixing in an elliptical turbulence free jet.” Vol. 208. no. 257-320. Journal of Fluid Mechanics, 1989.

Rolls Royce plc. Derby, United Kingdom.

Ruggeri, R., E. Callaghan, and D. Bowden. “Penetration of Air Jets Issuing from Circular, Square and Elliptical Orifices Directed Perpenticularly to an Air Stream.” *NACA Technical Note: 2019.* Cleveland, Ohio: Lewis Flight Propulsion Laboratory, 1950.

Ruiz, I. G. *Fluidic Seals for Applications in Turbomachinery.* Durham University, 2010.

Rusthon, G.J. “High Pressure Shround Leakage.” (PhD Thesis) 2003.

Saheli, M., E. Swanson, and H. Heshmatt. “Thermal Features of Compliant Foil Bearings - Theory and Experiments .” (ASME Journal of Tribology) 123 (2001).

Saheli, M., H. Heshat, and J. F. Walton. *Non-contacting Comliant Foil Seal for Gas Turbine Engine.* NASA Secondary Seal Workshop, 2002.

Salehi, M., H. Heshmat, J. F. Walton, and S. Cruszen. “The Application of Foil Seals to a Gas Turbine Engine.” (AIAA Paper 99-2821) 1999.

San Andres, L., and Kim. T. H. “Improvements to the Analysis of Gas Foil Bearings: Integration of Top Foil 1D and 2D Structural Models.” *ASME Paper No. GT2007-27249*, 2007.

San Andres, L., J. Baker, and A. Delgado. “Rotordynamic Force Coefficients of a Hybrid Brush Seal: Measurements and Predictions.” *Journal of Engineering for Gas Turbines and Power, Vol. 132, 042503*, 2010.

Sayma, A. I., C. Breard, M. Vahdati, and M. Tmregun. “Aeroelasticity Analysis of Air-Riding Seals for Aero-Engine Applications.” (Journal of Tribology, ASME) 2002.

Skouby, Alex. *Sealing of Jet Engines.* 4th Year Undergraduate Project, 2011.

Smile, H. J., and Paulson E. E. US 2963268. 1960.

Smith, C. J. *Unique Propulsion Systems - Advanced Subsonic Technologies Evaluation and Analysis.* Task 14 Interim Report Document, Contract NAS3-25953, 1994.

Steinetz, B. M., and R. C. Hendricks. “Aircraft Engine Seals.” (Chapter 9 of Tribology for Aerospace Applications, STLE Special Publication SP-37) 1997.

Stocker, B. M., D. M Cox, and G. F. Holle. *Aerodynamic Performance of Conventional and Advanced Design Labyrinth Seals with Solid, Smooth, Abradable and Honeycomb Lands - Gas Turbine Engines.* NASA CR-135307, 1977.

Stoy, R. L., and Y. Ben-Haim. “Turbulent Jets in Crossflow.” (Journal of Fluids Engineering, Paper No. 73-FE-15, pp. 551-556) 1973.

Turnquist, N. A. US 2009/0297341 A1 Fluidic Sealing for Turbomachinery. General Electric Company. 2009.

Unsworth, R. G., and R. K. Burton. US 3597102. 1971.

Vasco, V. M. B. I. *Development of a Cantilevered Floating Ring Seal.* D. Phil. Thesis, University of Oxford, 2009.

Webster, J. R. *Preliminary Evaluation of the Pressure Balanced Seal Concept, Document Number: DNS 78832.* Derby: Rolls-Royce Strategic Research Centre, 2001.

Webster, John. Patent US 7249769 B2, Seal Apparatus . 2007.

Willenborg, K., Kim. S., and S. Wittig. “Effects of Reynolds Number and Pressure Ratio on Leakage Loss and Heat Transfer in a Stepped Labyrinth Seal.” Journal of Turbomachinery, ASME, 2001.

Wood, P. E. *An Investigation of Contact Forces, Flow, Pressure, Hysteresis and Frictional Effects in Brush Seals.* D.Phil. Thesis, University of Oxford, 1998.

Wood, P. E., and T. V. Jones. “A Test Facility for the Measurement of Torques at the Shaft to Seal Interfaces in Brush Seals.” *ASME-Paper 97-2731.* 1997.

Wooler, P. T., G. H. Burghart, and J. T. Gallagher. “Pressure Distributions on a Rectangular Wing with a Jet Exhausting Normally Into and Air System.” (Journal of Aircraft, Vol. 4, pp 537-543) 1967.

WP0875.104. “Work Practice Experimental Assembly & Test: Measurement and Uncertainty Analysis.” Rolls-Royce Corporation, 2005.

Wright, C. Resilient Strip Seal Arrangement. United States Patent (6,267,381B1). 1999.

Yang, Y. T., and Y. X Wang. “Three-Dimensional numerical simulation of an inclined jet with cross-flow.” (International Journal of Heat and Mass Transfer, Volume 48, Issues 19-20, pp. 4019-4027) 2005.

Young, W. C., and R. G. Budynas. *Roark's Formulas for Stress and Strain ISBN 0-07-072542.* Singapore: McGraw-Hill, 2002.

Zaretsky, E. V. “Tribology for Aersopace Applications.” (STLE SP-37) 1997.

Zhang, H., R. G. Landers, and B. A. Miller. “Adaptive Controls of Mechanical Face Seals with Rotor Runout and Static Stator Misalignment.” *Journal of Dynamic Systems, Measurements and Control, Vol. 132, 041009,* 2010.

Zheng, X. “Parametric Study of Hydrodynamic Seal Using 2D Design Code and Comparing with a 3D Model.” (ASME Turbo Expo (GT2005-68915)) 2005.

Zhou, J, B Gu, and Y Chen. “An Improved Design of a Spiral Groove Mechanical Seal.” (ASME) 2007.

8 Appendix

8.1 Derivation of Reynolds 1D Flow Equation

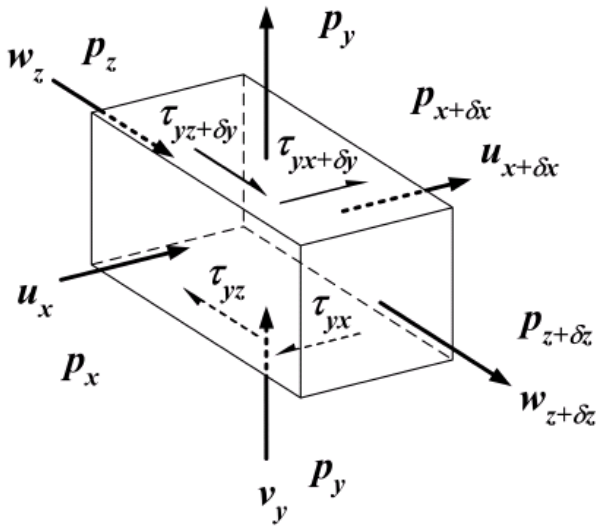


Figure A.1: Elemental volume for seal gap flow (Franceschini 2005)

Consider an elemental volume of fluid δx, δy, δz where the fluid velocities are u, v, w as shown in Figure A.1. By applying conservation of mass, the continuity equation gives

$$\frac{\partial \rho}{\partial t} + \frac{\partial}{\partial x}(\rho u) + \frac{\partial}{\partial y}(\rho v) + \frac{\partial}{\partial z}(\rho w) = 0\,. \tag{A.1}$$

and under steady conditions $\left(\frac{\partial \rho}{\partial t} = 0\right)$, this simplifies to

$$\frac{\partial}{\partial x}(\rho u) + \frac{\partial}{\partial y}(\rho v) + \frac{\partial}{\partial z}(\rho w) = 0\,. \tag{A.2}$$

Applying the momentum equation for the case of steady flow and no body forces in the x direction gives

$$\frac{1}{\rho}\left(\frac{\partial \tau_{yx}}{\partial y} - \frac{\partial p}{\partial x}\right) = \frac{u\partial u}{\partial x} + \frac{v\partial u}{\partial y} + \frac{w\partial u}{\partial z} \tag{A.3}$$

If the fluid is Newtonian, $\frac{\partial \tau_{yx}}{\partial y} = \mu \frac{\partial^2 u}{\partial y^2}$, then we may write

$$u\frac{\partial u}{\partial x}+v\frac{\partial u}{\partial y}+w\frac{\partial u}{\partial z}=-\frac{1}{\rho}\frac{\partial p}{\partial x}+\frac{\mu}{\rho}\frac{\partial^2 u}{\partial y^2}, \tag{A.4}$$

and a similar equation in the *z* direction:

$$u\frac{\partial w}{\partial x}+v\frac{\partial w}{\partial y}+w\frac{\partial w}{\partial z}=-\frac{1}{\rho}\frac{\partial p}{\partial z}+\frac{\mu}{\rho}\frac{\partial^2 w}{\partial z^2}. \tag{A.5}$$

An assumption is made here that convective acceleration terms are negligible compared to pressure and viscous terms, and hence equations (A.4) and (A.5) reduce to

$$\frac{\partial p}{\partial x}=\mu\frac{\partial^2 u}{\partial y^2} \tag{A.6}$$

and

$$\frac{\partial p}{\partial z}=\mu\frac{\partial^2 w}{\partial y^2} \tag{A.7}$$

respectively. Integrating with respect to *y* ($\frac{\partial p}{\partial x}$ and $\frac{\partial p}{\partial z}$ do not vary with *y*) gives

$$\mu u=\frac{\partial p}{\partial x}\frac{y^2}{2}+\mathrm{A}y+\mathrm{B} \tag{A.8}$$

and

$$\mu w=\frac{\partial p}{\partial z}\frac{y^2}{2}+\mathrm{C}y+\mathrm{D}\,. \tag{A.9}$$

Let the boundary conditions be $u = U$, $w = W$ at $y = 0$ and $u = 0$, $w = 0$ at $y = h$. *U* and *W* are zero for the two dimensional LAMFS test rig but are left non-zero for completeness.

$$u=\frac{1}{2\mu}\frac{\partial p}{\partial x}(y^2-hy)+U\left(1-\frac{y}{h}\right) \tag{A.10}$$

$$w=\frac{1}{2\mu}\frac{\partial p}{\partial z}(y^2-hy)+W\left(1-\frac{y}{h}\right) \tag{A.11}$$

Continuity (equation (A.1)) is integrated with respect to *y* as

$$[\rho v]_0^{h(x,z)}=-\int_0^{h(x,z)}\frac{\partial}{\partial x}(\rho u)\mathrm{d}y-\int_0^{h(x,z)}\frac{\partial}{\partial z}(\rho w)\mathrm{d}y\,. \tag{A.12}$$

Since *h* only varies spatially, *v* evaluated at the boundary will be zero

$$0 = -\int_0^{h(x,z)} \frac{\partial}{\partial x}(\rho u)\mathrm{d}y - \int_0^{h(x,z)} \frac{\partial}{\partial z}(\rho w)\mathrm{d}y \tag{A.13}$$

Substituting equations A.10 and A.11 into A.13 gives

$$0 = -\int_0^{h(x,z)} \frac{\partial}{\partial x}\left(\frac{\rho}{2\mu}\frac{\partial p}{\partial x}(y^2 - hy) + \rho U\left(1 - \frac{y}{h}\right)\right)\mathrm{d}y$$

$$-\int_0^{h(x,z)} \frac{\partial}{\partial z}\left(\frac{\rho}{2\mu}\frac{\partial p}{\partial z}(y^2 - hy) + \rho W\left(1 - \frac{y}{h}\right)\right)\mathrm{d}y\,. \tag{A.14}$$

The best approach from this point is to apply Leibniz's Theorem for differentiation of an integral (equation A.15 taken from (Abramowitz and Stegun 1965))

$$\frac{\mathrm{d}}{\mathrm{d}c}\int_{a(c)}^{b(c)} f(x,c)\mathrm{d}x = \int_{a(c)}^{b(c)} \frac{\partial}{\partial c}f(x,c)\mathrm{d}x + f(b,c)\frac{\mathrm{d}b}{\mathrm{d}c} - f(a,c)\frac{\mathrm{d}a}{\mathrm{d}c} \tag{A.15}$$

so that

$$\frac{\partial}{\partial x}\int_0^{h(x,z)}\left(\frac{\rho}{2\mu}\frac{\partial p}{\partial x}(y^2 - hy) + \left(1 - \frac{y}{h}\right)\right)\mathrm{d}y$$

$$= \int_0^{h(x,z)} \frac{\partial}{\partial x}\left(\frac{\rho}{2\mu}\frac{\partial p}{\partial x}(y^2 - hy) + \left(1 - \frac{y}{h}\right)\right)dy$$

$$+\left(\frac{\rho}{2\mu}\frac{\partial p}{\partial x}(h^2 - hh) + \left(1 - \frac{h}{h}\right)\right)\frac{\mathrm{d}h}{\mathrm{d}x}$$

$$-\left(\frac{\rho}{2\mu}\frac{\partial p}{\partial x}(0^2 - h0) + \left(1 - \frac{0}{h}\right)\right)\frac{\mathrm{d}0}{\mathrm{d}x}. \tag{A.16}$$

Provided μ and ρ can be considered as independent of y, the integral becomes

$$0 = -\int_0^{h(x,z)} \frac{\partial}{\partial x}\left(\frac{\rho}{2\mu}\frac{\partial p}{\partial x}(y^2 - hy) + \rho U\left(1 - \frac{y}{h}\right)\right)\mathrm{d}y$$

$$-\int_0^{h(x,z)} \frac{\partial}{\partial z}\left(\frac{\rho}{2\mu}\frac{\partial p}{\partial z}(y^2 - hy) + \rho W\left(1 - \frac{y}{h}\right)\right)\mathrm{d}y$$

$$0 = -\frac{\partial}{\partial x}\int_0^{h(x,z)}\left(\frac{\rho}{2\mu}\frac{\partial p}{\partial x}(y^2 - hy) + \rho U\left(1 - \frac{y}{h}\right)\right)\mathrm{d}y$$

$$-\frac{\partial}{\partial z}\int_0^{h(x,z)}\left(\frac{\rho}{2\mu}\frac{\partial p}{\partial z}(y^2 - hy) + \rho W\left(1 - \frac{y}{h}\right)\right)\mathrm{d}y$$

$$0 = -\frac{\partial}{\partial x}\left(\frac{\rho}{2\mu}\frac{\partial p}{\partial x}\left(-\frac{h^3}{6}\right) + \rho U\frac{h}{2}\right) - \frac{\partial}{\partial z}\left(\frac{\rho}{2\mu}\frac{\partial p}{\partial z}\left(-\frac{h^3}{6}\right) + \rho W\frac{h}{2}\right)$$

$$0 = \frac{1}{12}\frac{\partial}{\partial x}\left(\frac{\rho h^3}{\mu}\frac{\partial p}{\partial x}\right) - \frac{1}{2}\frac{\partial}{\partial x}(\rho U h) + \frac{1}{12}\frac{\partial}{\partial z}\left(\frac{\rho h^3}{\mu}\frac{\partial p}{\partial z}\right) - \frac{1}{2}\frac{\partial}{\partial z}(\rho W h)\,. \tag{A.17}$$

Hence the governing partial differential equation is

$$\frac{\partial}{\partial x}\left(\frac{\rho h^3}{\mu}\frac{\partial p}{\partial x}\right) + \frac{\partial}{\partial z}\left(\frac{\rho h^3}{\mu}\frac{\partial p}{\partial z}\right) = 6U\frac{\partial}{\partial x}(\rho h) + 6W\frac{\partial}{\partial z}(\rho h)\,. \tag{A.18}$$

By introducing the equation of state, we get

$$\frac{\partial}{\partial x}\left(\frac{p h^3}{\mu R T}\frac{\partial p}{\partial x}\right) + \frac{\partial}{\partial z}\left(\frac{p h^3}{\mu R T}\frac{\partial p}{\partial z}\right) = 6U\frac{\partial}{\partial x}\left(\frac{ph}{RT}\right) + 6W\frac{\partial}{\partial z}\left(\frac{ph}{RT}\right). \tag{A.19}$$

which simplifies slightly to

$$\frac{\partial}{\partial x}\left(\frac{h^3}{\mu T}\frac{\partial p^2}{\partial x}\right) + \frac{\partial}{\partial z}\left(\frac{h^3}{\mu T}\frac{\partial p^2}{\partial z}\right) = 12U\frac{\partial}{\partial x}\left(\frac{ph}{T}\right) + 12W\frac{\partial}{\partial z}\left(\frac{ph}{T}\right). \tag{A.20}$$

If the assumption that conditions are isothermal within the domain is possible, then the equation reduces to

$$\frac{\partial}{\partial x}\left(\frac{h^3}{\mu}\frac{\partial p^2}{\partial x}\right) + \frac{\partial}{\partial z}\left(\frac{h^3}{\mu}\frac{\partial p^2}{\partial z}\right) = 12U\frac{\partial}{\partial x}(ph) + 12W\frac{\partial}{\partial z}(ph)\,. \tag{A.21}$$

In the case of the test rig described in this chapter, the seal surfaces can only move relative to the disc surface in the *y* direction and hence *U* and *W* are zero. Although edge effects may be present from leakage paths between the end plates and the seal housing side walls, it is assumed that they are negligible and there is no flow component in the *z* direction. The equation therefore simplifies to

$$\frac{\partial}{\partial x}\left(\frac{h^3}{\mu}\frac{\partial p^2}{\partial x}\right) = 0\,, \tag{A.22}$$

which then becomes

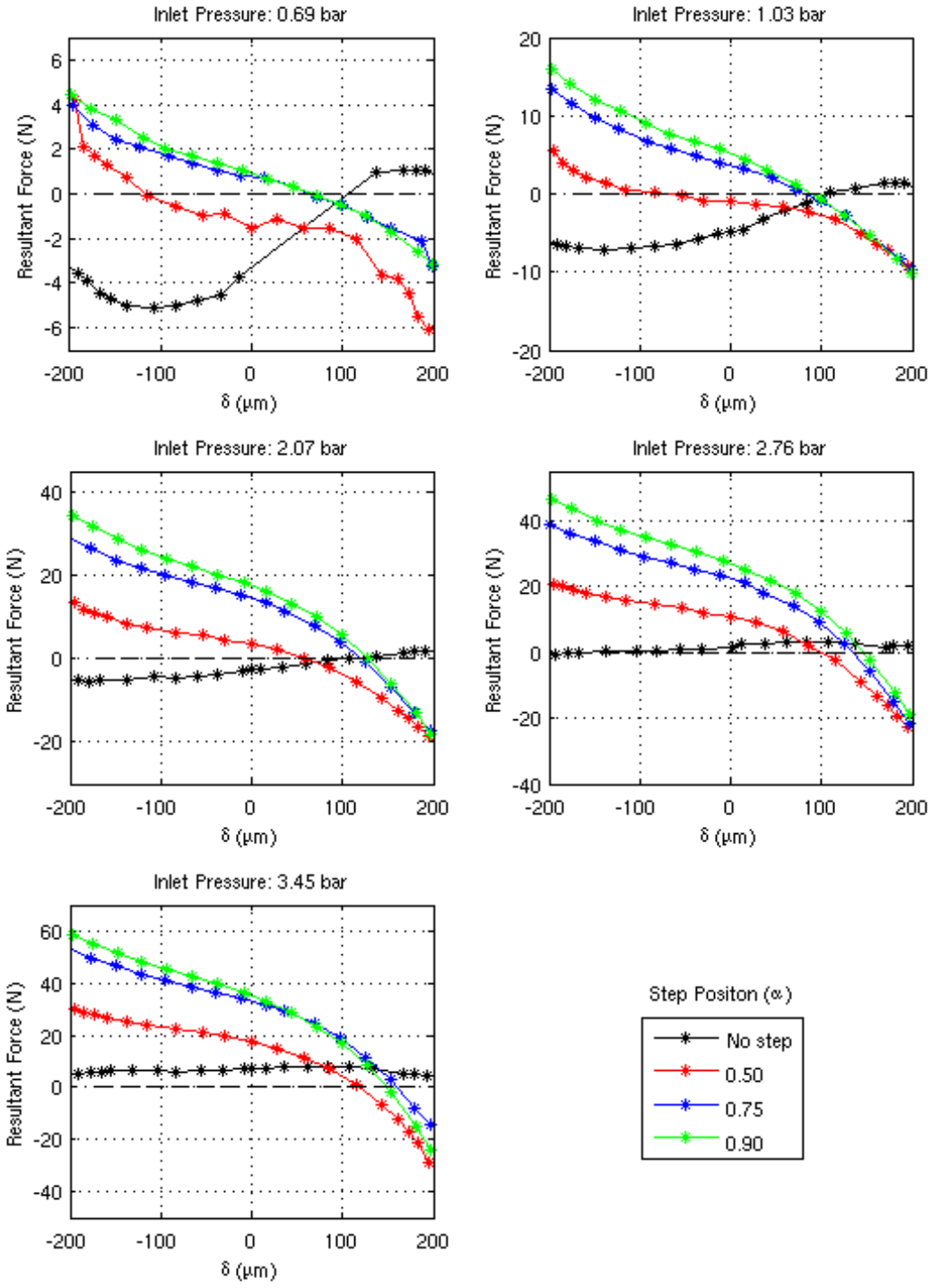
$$\frac{\partial p^2}{\partial x} = \mathrm{Q}\frac{\mu}{h^3}, \tag{A.23}$$

and evaluates to

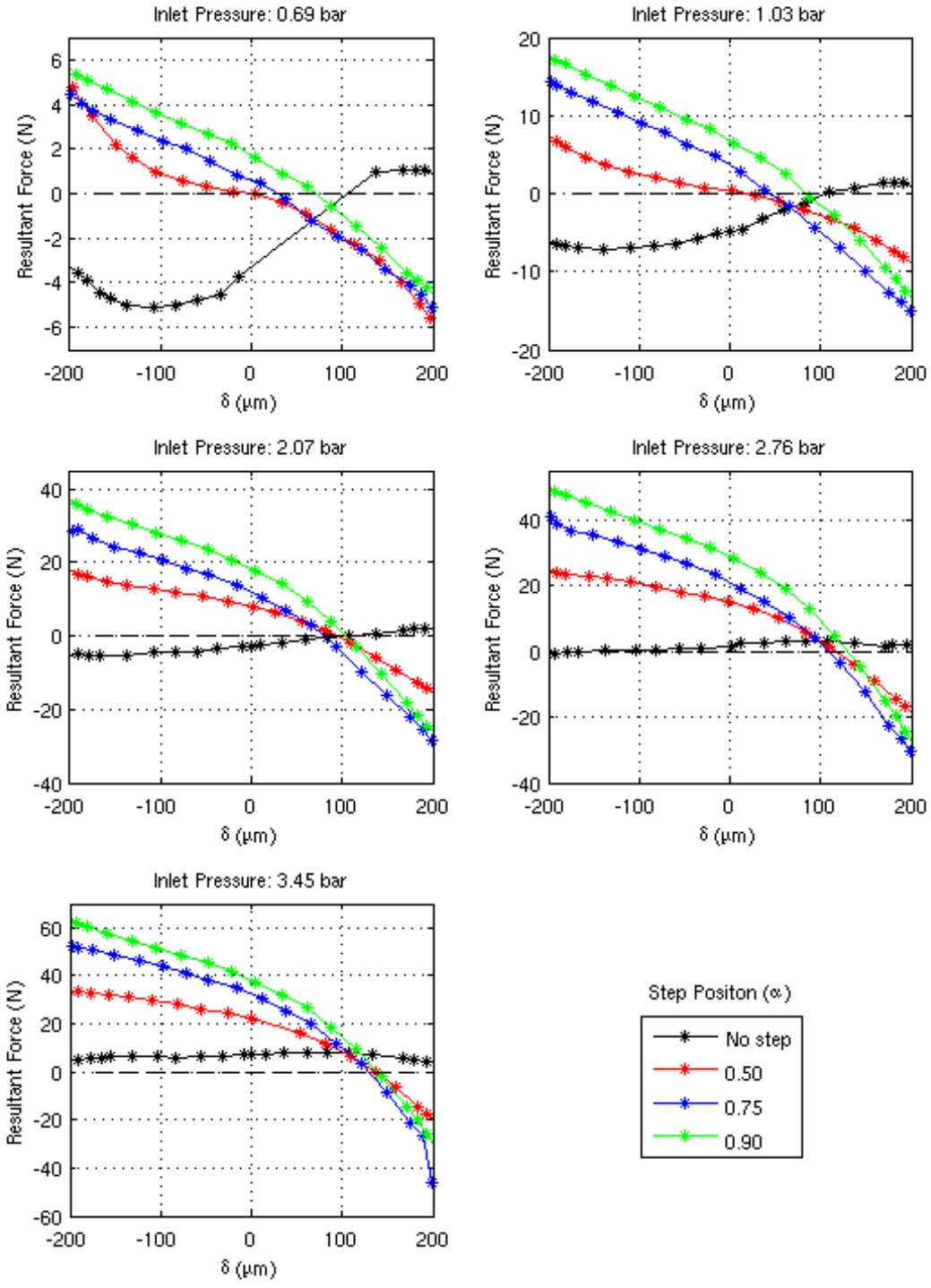
$$p_2^2 - p_1^2 = \left[\frac{\mathrm{Q}\mu x}{h^3}\right]_{x_1}^{x_2}. \tag{A.24}$$

giving the governing equation for one dimensional, compressible flow from an upstream pressure p_1 to a downstream pressure p_1 through a gap of height h length x.

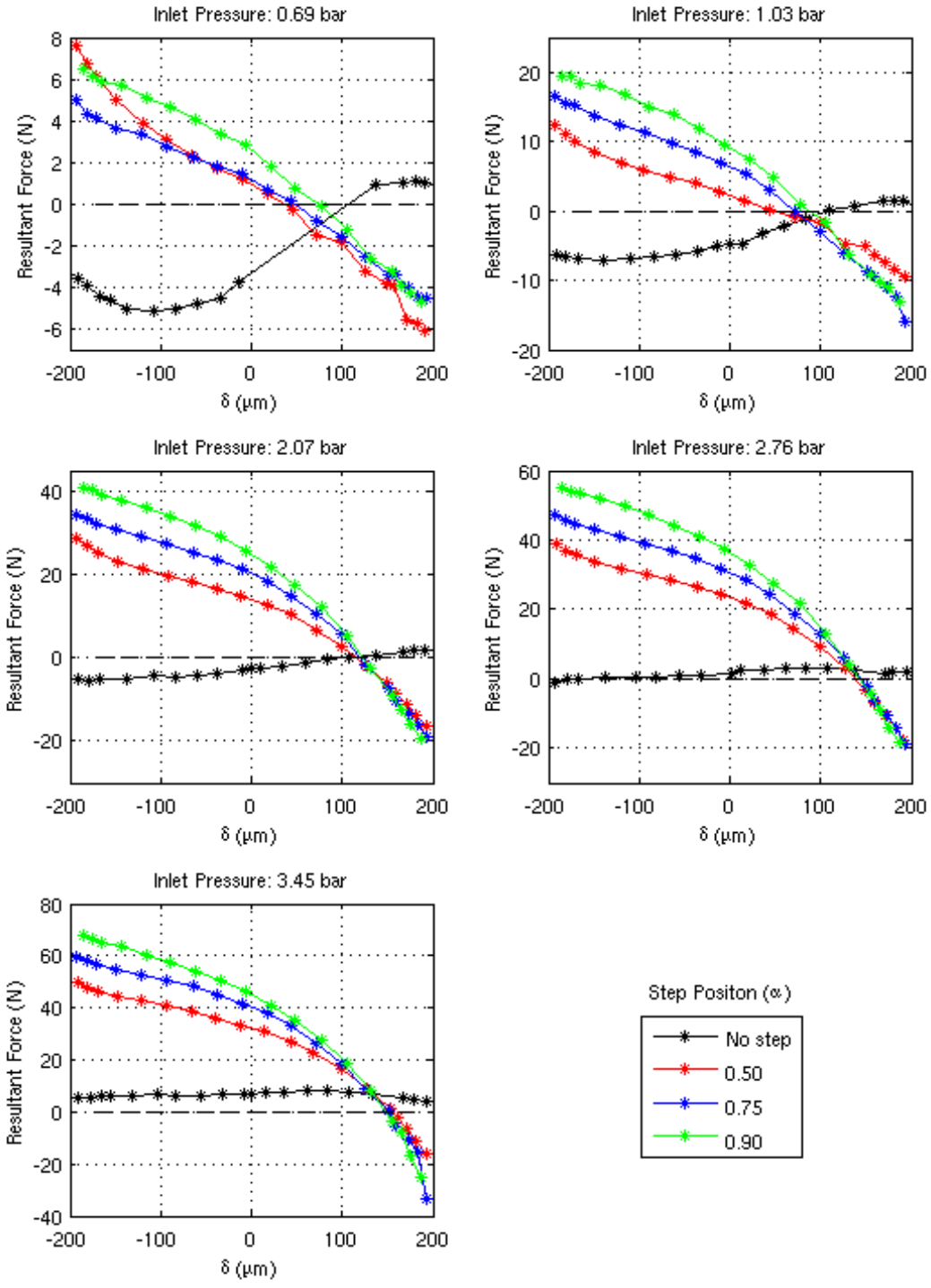
8.2 Seal Housing Resultant Force



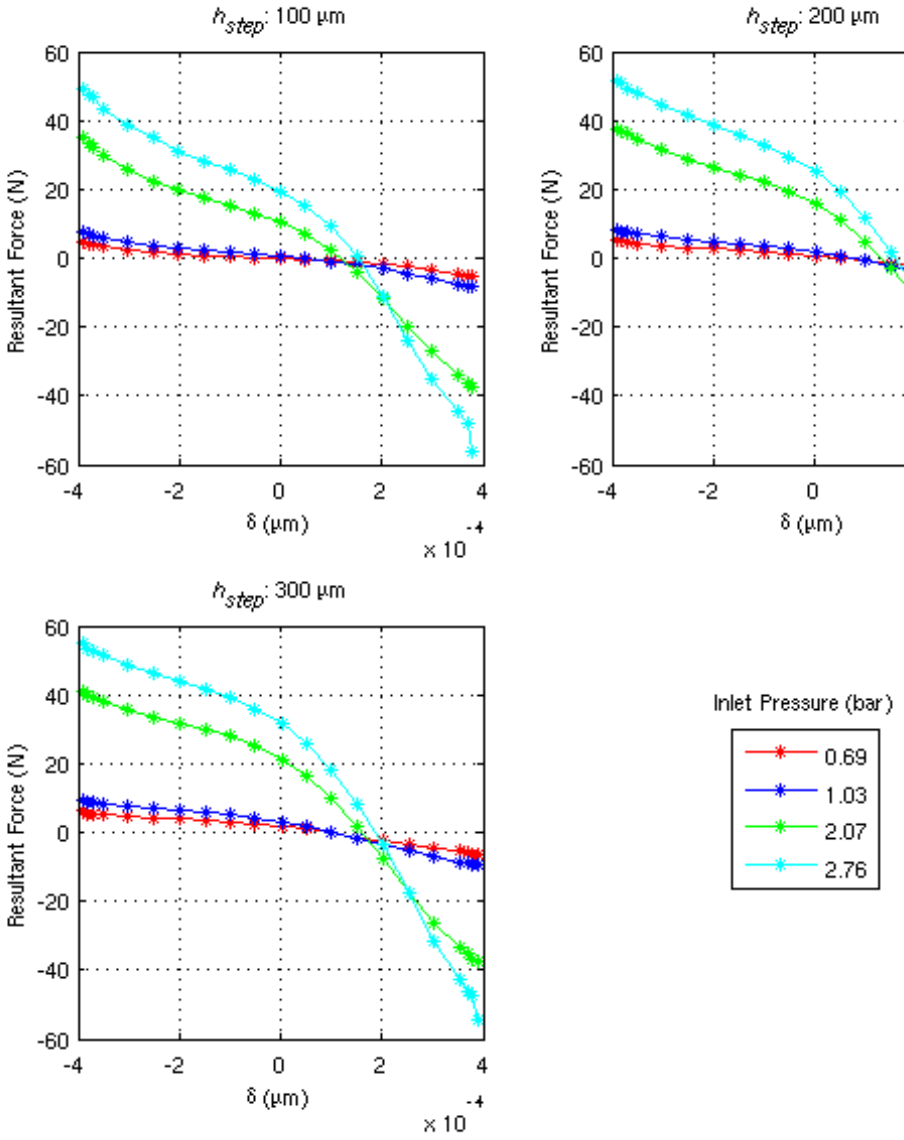
Seal housing resultant force with displacement: h_{tsg} = 400, h_{step} = 100 µm



Seal housing resultant force with displacement: h_{tsg} = 400 μm, h_{step} = 200 μm

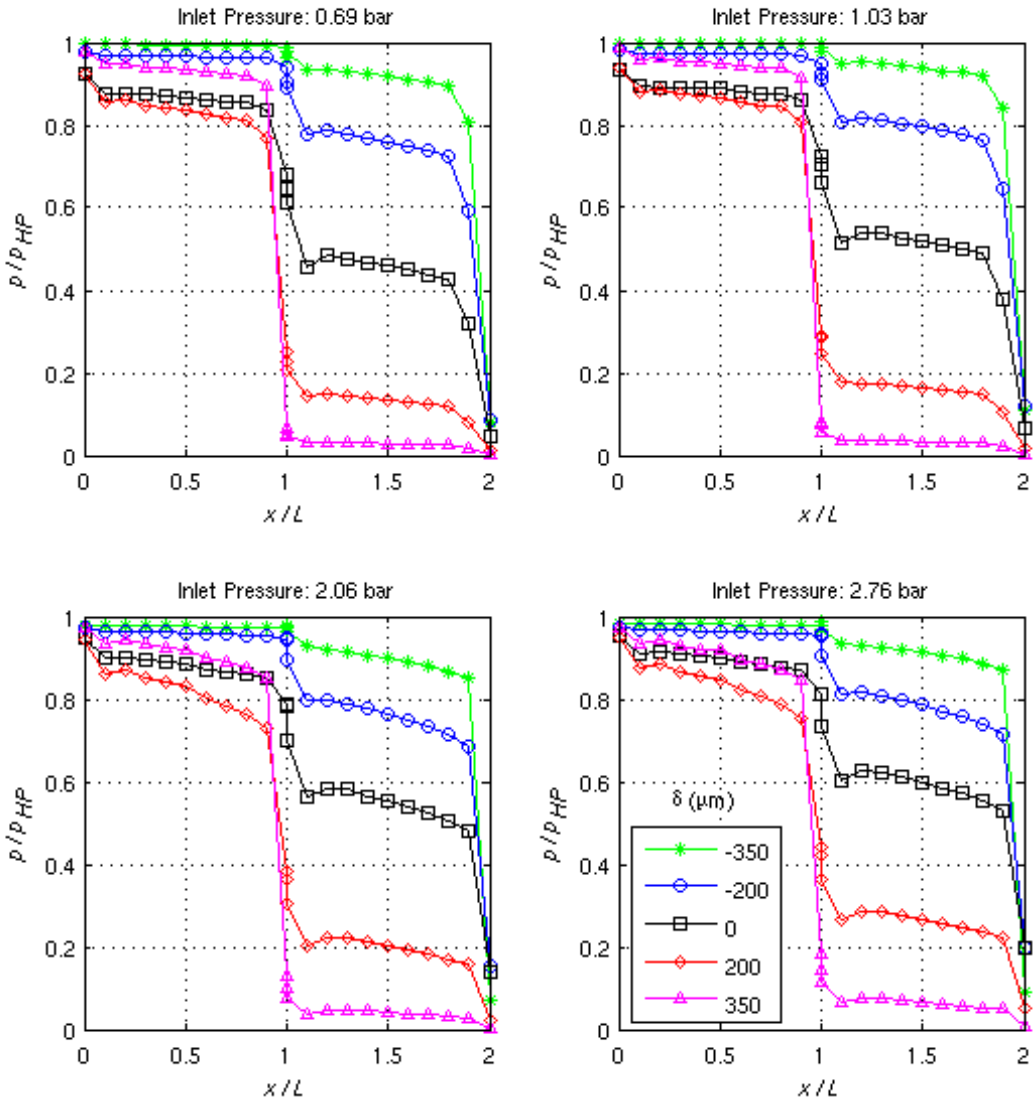


Seal housing resultant force with displacement: h_{tsg} = 400 µm, h_{step} = 300 µm

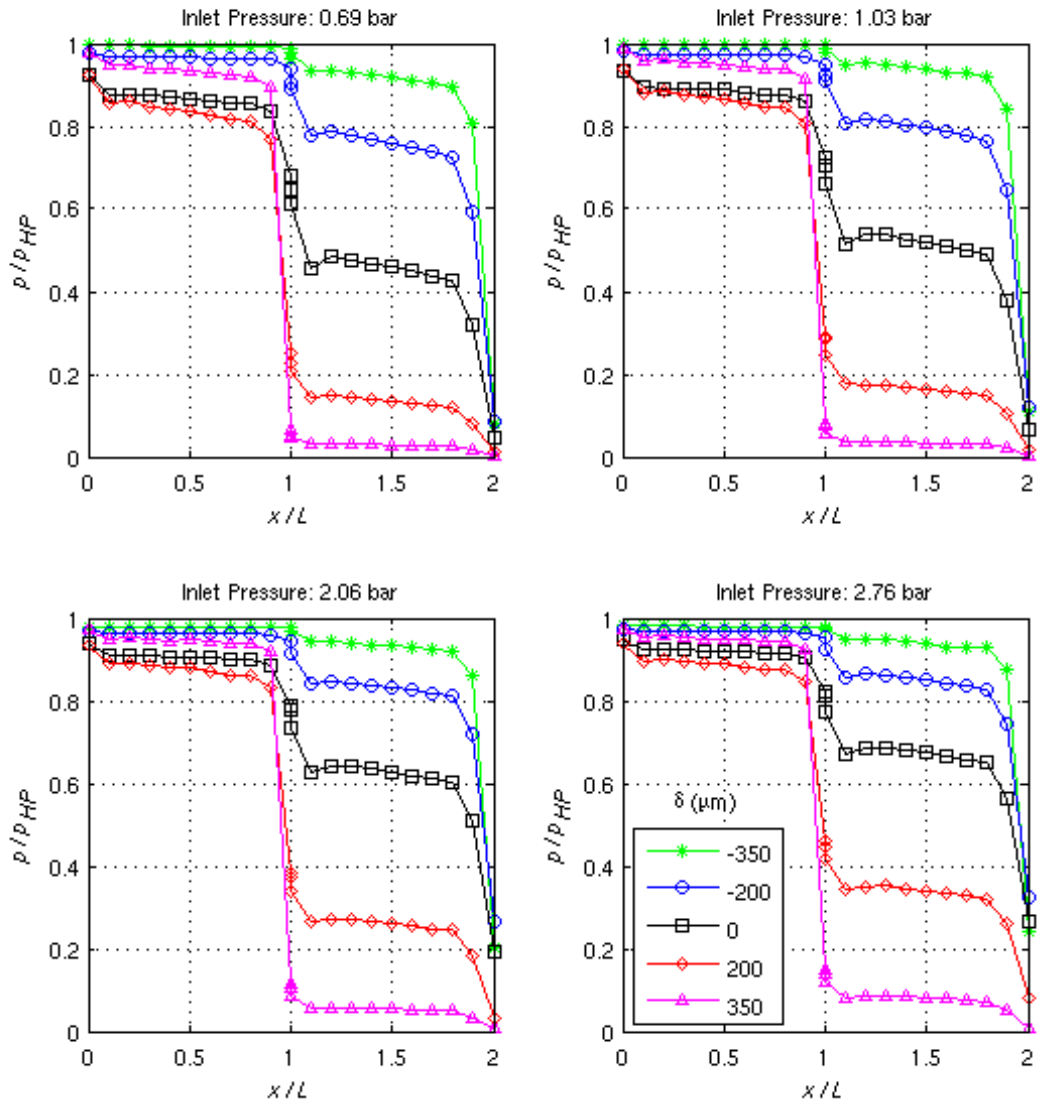


Seal housing resultant force with displacement: h_{tsg} = 800 µm, α = 0.90

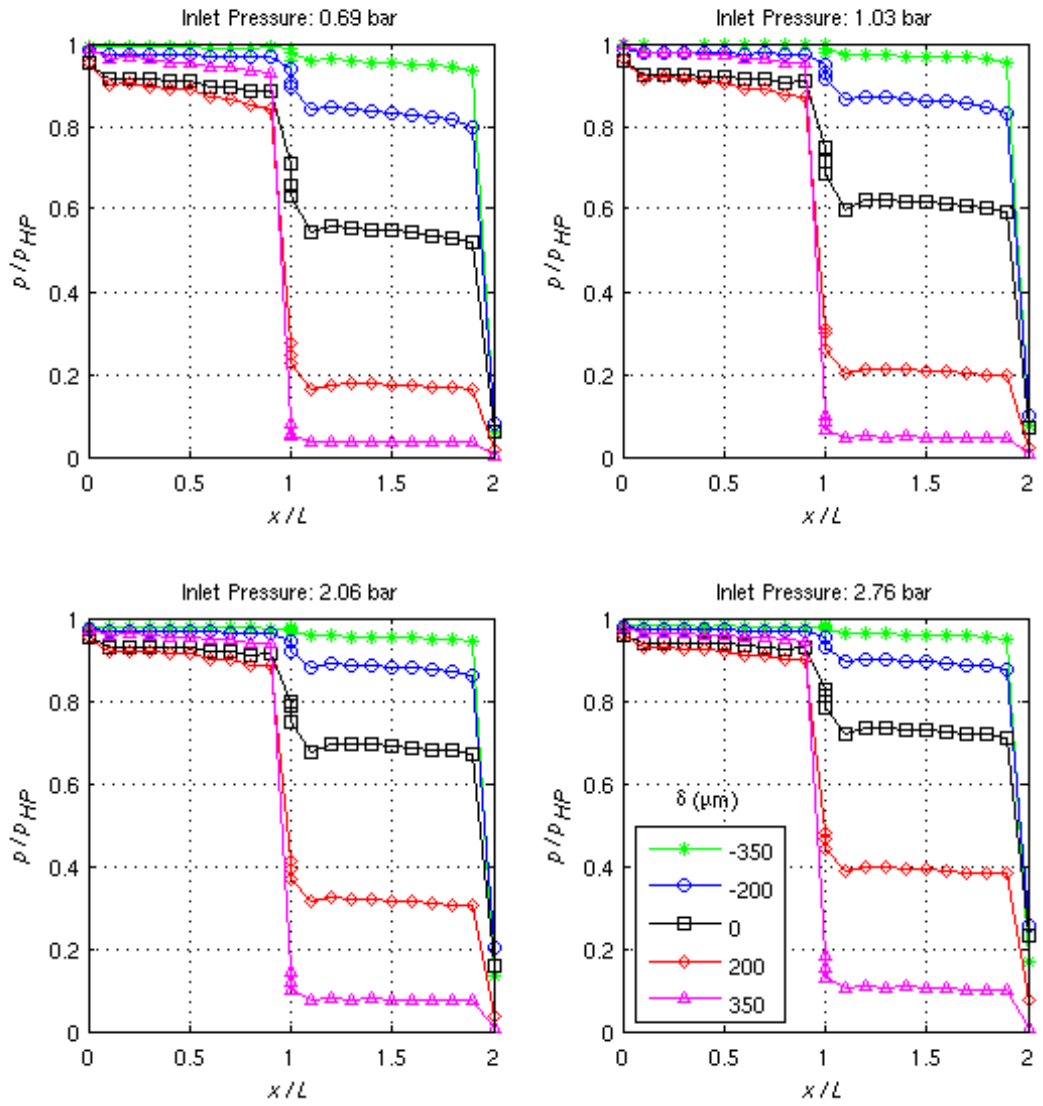
8.3 Linear LAMFS Primary Leakage Path Static Pressure Distribution



Primary leakage path static pressure distribution (h_{tsg} = 800 µm, h_{step} = 100 µm)



Primary leakage path static pressure distribution (h_{tsg} = 800 µm, h_{step} = 200 µm)



Primary leakage path static pressure distribution (h_{tsg} = 800 µm, h_{step} = 300 µm)

8.4 Rotating Component Containment

The disc is mounted on a shaft which was manufactured within the laboratory workshop. It possesses a flat surface where the disc is attached to and is held by two bearings, one at each end. Due to the pressure loading on the disc in the downstream direction, axial load bearings were required and a pair of *SNFA Super Precision SEB25 7CE1 DUL* 15° bearings were used. The bearings were tightly fit within an aluminium bearing housing which was mounted on supports to locate the disc's axis at the height desired. Rotating component containment

When the disc spins at between 10 krpm and 25 krpm, there is a large amount of kinetic energy stored in it and hence an uncontained disc failure would be extremely dangerous to persons nearby. A system of containment consisting of alternating layers of high yield stainless steel and neoprene sheet has been designed based on the method outlined in Goodisman et. al. The design process for the disc containment is shown below.

First the energy stored in the disc is calculated. The second moment of area of the disc is

$$I = \frac{1}{2}mr^2 = \frac{1}{2} \times 1.785 \times 0.085^2$$

$$I = 6.45 \times 10^{-3}\text{kgm}^3 .$$

The maximum speed of the disc (plus a 25% safety factor) is based on the maximum motor speed and is

$$\omega = 25{,}000 \times 1.25 = 31{,}250 \text{ rpm}$$

$$\omega = 3272 \text{ rad s}^{-1} .$$

The rotational kinetic energy stored at this speed is therefore

$$KE = \frac{1}{2}I\omega^2 = \frac{1}{2} \times 6.45 \times 10^{-3} \times 3272^2$$

$$KE = 34.5 \text{ kJ} .$$

The containment material chosen is austenitic stainless sheet steel, BS 304S15. The mechanical properties are shown below:

σ_y = 195 MPa (min)

UTS = 500 MPa (min)

Strain at yield (e) = 0.45 (min)

Energy, E, absorbed by containment per unit volume, D:

$$\frac{E}{D} = \frac{(\sigma_y + \sigma_{UTS})e}{2} = \frac{(195 \times 10^6 + 500 \times 10^6) \times 0.45}{2} = 139 \text{ MJm}^{-3}$$

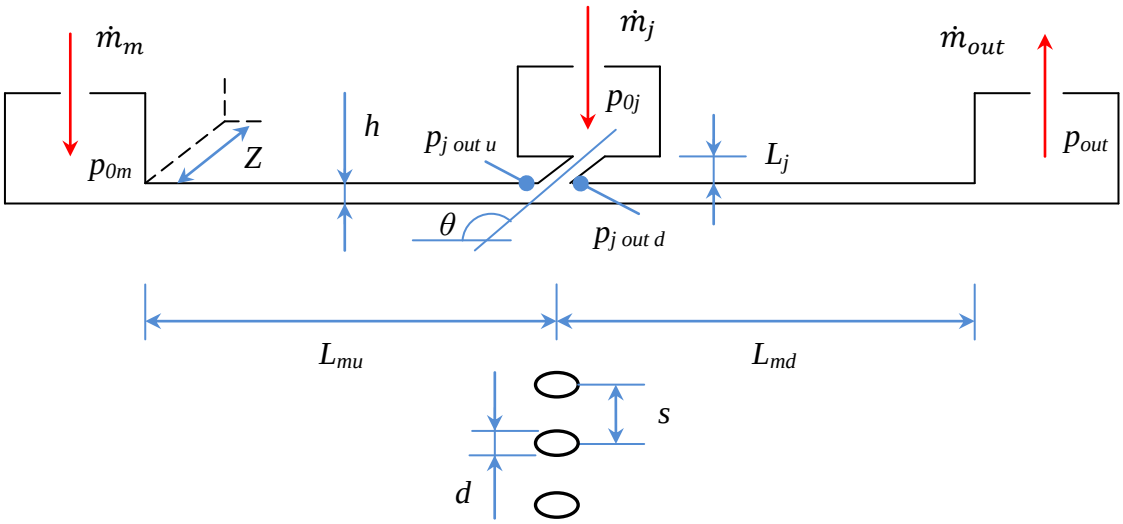
Using BS 304S15 sheet at 0.914 mm thick and 0.2 m wide, the total volume required is:

$$\left(\frac{E}{V}\right) D = KE \times safety\ factor = KE \times 10$$

$$D = \frac{34.5 \times 10^4}{139 \times 10^6} = 2.48 \times 10^{-3}\text{m}^3$$

which gives a length of 13.8 m of sheet steel of the cross section dimensions above.

8.5 Fluidic Seal Analytical Model



The cross-sectional areas of the test section and the row of jets are therefore

$$A_m = Zh \tag{A.25}$$

$$A_j = \pi d^2 N \tag{A.26}$$

respectively, where N is the number of jets in the row. An iterative process is required to achieve a solution for the mainstream and jet leakage mass flow rates for a given set of boundary conditions which are known; the mainstream inlet total pressure, p_{0m}, the jet inlet total pressure, p_{0j}, the outlet static pressure, p_{out}, the mainstream inlet total temperature, T_{0m},

and the jet inlet total temperature, T_{0j}. For each iteration of the mainstream mass flow rate, $\dot{m}_m$, there are four stages, beginning with solving the conditions for the inlet. To begin, an initial guess is required for $\dot{m}_m$, the Mach number at the inlet plane of the test section, M_m, the static pressure at the inlet to the jet holes, p_j, and the Mach number at the exit plane of the test section, M_{out}.

Stage 1

The first step involves an iterative loop to solve for the conditions at the mainstream inlet, which requires the initial guess for M_m. Iterative loop 1, Equation A.27 to A.31, includes isentropic flow relations and the ideal gas equation.

$$p_m = p_{0m}\left\{1 + \frac{1}{2}(\gamma - 1)M_m^2\right\}^{\frac{\gamma}{1-\gamma}} \tag{A.27}$$

$$T_m = \frac{T_{0m}}{\left\{1 + \frac{1}{2}(\gamma - 1)M_m^2\right\}} \tag{A.28}$$

$$\rho_m = \frac{p_m}{RT_m} \tag{A.29}$$

$$v_m = \frac{\dot{m}_{m(n)}}{\rho_m A_m} \tag{A.30}$$

$$M_m = \frac{v_m}{\sqrt{\gamma RT_m}} \tag{A.31}$$

Once the iterative loop has converged to give a solution to the mainstream inlet conditions for this iteration of $\dot{m}_m$, the inlet Reynolds number, Re_m, the coefficient of friction (depending on the Reynolds number, which determines c_1 and c_2), C_{fm}, and hence the static pressure in the leakage channel immediately upstream of the row of jets, $p_{jout\,u}$, is calculated.

$$Re_m = \frac{\rho_m v_m D_H}{\mu} \tag{A.32}$$

$$D_H = \frac{4A_m}{2(Z+h)} \tag{A.33}$$

$$C_{fm} = c_1 Re_m^{-c_2} \tag{A.34}$$

$$p_{jout\,u} = p_m - \left(\frac{2(W+h)L_{mu}C_{fm}}{A_m}\right)\left(\frac{1}{2}\rho_m v_m^2\right) \tag{A.35}$$

Stage 2

The second step for each iteration of $\dot{m}_m$ is to use $p_{jout\,u}$ to iteratively solve for the conditions at the inlet to the row of jets using the initial guess for p_j. This iterative loop finds a solution for p_j based on the inlet conditions and the boundary conditions p_{0j} and T_{0j}.

$$M_j = \sqrt{\frac{2}{\gamma-1}\left[\left(\frac{p_{0j}}{p_j}\right)^{\frac{\gamma-1}{\gamma}} - 1\right]} \tag{A.36}$$

$$T_j = \frac{T_{0j}}{\left\{1 + \frac{1}{2}(\gamma-1)M_j^2\right\}} \tag{A.37}$$

$$\rho_j = \frac{p_j}{RT_j} \tag{A.38}$$

$$u_j = M_j\sqrt{\gamma R T_j} \tag{A.39}$$

$$\dot{m}_j = C_d \rho_j A_j u_j \tag{A.40}$$

$$Re_j = \frac{\rho_j u_j d_j}{\mu} \tag{A.41}$$

$$C_{fj} = c_1 Re_j^{c_2} \tag{A.42}$$

$$p_j = p_{jout\,u} + \left(C_{fj}\left(\frac{4L_j}{d_j}\right) + C_{IL}\right)\left(\frac{1}{2}\rho_j u_j^2\right) \tag{A.43}$$

where C_{IL} is a static pressure loss coefficient at the inlet to the jet holes based on the dynamic head and C_d is the discharge coefficient for jets in a cross flow based on Equations (5.1) to **(**5.4). Once stage two has been completed, a value for the jet mass flow rate, $\dot{m}_j$, is achieved.

Stage 3

The third step involves continuity to assess the total mass flow leaving the domain

$$\dot{m}_{out} = \dot{m}_{m(n)} + \dot{m}_j \tag{A.44}$$

The steady flow energy equation gives the total temperature at the domain exit as

$$T_{0out} = \frac{\dot{m}_{m(n)} T_{0m} + \dot{m}_j T_{0j}}{\dot{m}_{out}} \tag{A.45}$$

A third iterative loop then gives the flow conditions at the domain outlet using a guess for the outlet Mach number, M_{out}.

$$T_{out} = \frac{T_{0out}}{\left\{1 + \frac{1}{2}(\gamma - 1) M_{out}^2\right\}} \tag{A.46}$$

$$\rho_{out} = \frac{p_{out}}{R T_{out}} \tag{A.47}$$

$$v_{out} = \frac{\dot{m}_{out}}{\rho_{out} A_m} \tag{A.48}$$

$$M_{out} = \frac{u_{out}}{\sqrt{\gamma R T_{out}}} \tag{A.49}$$

Once converged, the static pressure immediately downstream of the row of jets is calculated by use of the following equations

$$Re_{out} = \frac{\rho_{out} v_{out} D_H}{\mu} \tag{A.50}$$

$$C_{fout} = c_1 Re_{out}^{c_2} \tag{A.51}$$

$$p_{jout\,d} = p_{out} + \left(\frac{2(Z+h)L_{out}C_{fout}}{A_m}\right)\left(\frac{1}{2}\rho_{out}v_{out}^2\right) \tag{A.52}$$

Stage 4

The final part of the main iterative loop is to use a momentum balance on the control volume to achieve an updated value for the mainstream mass flow rate, $\dot{m}_{m(n+1)}$. The pressure forces on the control volume are

$$F_P = p_m A_m - p_{out}A_m + \left(p_j - C_{IL}\frac{1}{2}\rho_j v_j^2\right)A_j cos\theta \tag{A.53}$$

The frictional forces on the internal walls are

$$F_F = -\rho_m v_m^2 C_{fm}(Z+h)L_m - \rho_{out}v_{out}^2 C_{fout}(Z+h)L_{md} - \frac{1}{2}\rho_j v_j^2 C_{fj}\pi d L_j N cos\theta \tag{A.54}$$

The momentum balance is then

$$\dot{m}_{out}v_{out} - \dot{m}_m v_m - \dot{m}_j v_j cos\theta - F_P - F_F = 0 \tag{A.55}$$

which becomes

$$\left(\dot{m}_m + \dot{m}_j\right)v_{out} - \dot{m}_m v_m = F_P + F_F + \dot{m}_j v_j cos\theta \tag{A.56}$$

and finally the updated mainstream mass flow rate is given by

$$\dot{m}_{m(n+1)} = \frac{F_P + F_F - \dot{m}_j v_{out} + \dot{m}_j v_j cos\theta}{v_{out} - v_m} \tag{A.57}$$

Equations A.27 to A.57 constitute one iteration of $\dot{m}_m$. This process was run for the number of iterations required for the Frobenius norm to fall below the desired threshold.